DOCTOR OF PHILOSOPHY

# Laser-Driven Acceleration of Ions: Biological Effects at Ultra-High Dose Rates

Gwynne, Deborah

*Award date:*
2018

*Awarding institution:*
Queen's University Belfast

# Laser-Driven Acceleration of Ions: Biological Effects at Ultra-High Dose Rates

**Deborah Caroline Gwynne**
**MSci Physics**

Centre for Plasma Physics, School of Mathematics and Physics

Queen's University Belfast

This thesis is submitted in partial fulfilment of the requirements for the degree of

*Doctor of Philosophy*

Centre for Plasma Physics 7th March 2018

# Acknowledgements

I would like to thank my supervisor Prof. Marco Borghesi for his continued support and guidance throughout my project.

I would like to thank friends and colleagues from the Borghesi Plasma Physics group in the Centre for Plasma Physics including Aarón Alejo, Fiona Hanton, Kealan Naughton, Clare Scullion, Dr Hamad Ahmed, Dr Domenico Doria and Dr Satya Kar, as well as friends and colleagues from the Prise Radiobiology Group in the Centre for Cancer Research and Cell Biology including Dominique French, Carla Maiorino, Thomas Marshall, Gaurang Patel, Emma Waring, Dr Pankaj Chaudhray, Dr Miheala Ghita and my second supervisor Prof. Kevin M. Prise. Technical and clerical staff from the School of Maths and Physics including Maurice Macartney, Neil Meharg, Jackie Patrick, Christopher Smyth, Jennifer Wheeler, Dr. Dan Marlow, Dr. Gagik Nersissyan and Dr. Philip Orr, link Scientists Nicola Booth and David Carroll from the Central Laser Facility, Marianne Grognot, Dr. Lorenzo Romagnai and Dr. Marie-Claire Schanne-Klein from École Polytechnique, Franesca Perozziello and Dr. Lorenzo Manti from the University of Napoli, Giacomo Candiano, Renata Leanza and Antonella Tramontana from Catania, Stephen Barnard and Graham Holliman from Public Health England, Hersimerjit Padda and Prof. Paul McKenna from the University of Strathclyde, Dr. Giuseppe Schettino of the National Physical Laboratory, Prof. Stan Botchway from the Resrach Complex at Harwell, the staff of the Central Laser Facility, the staff of LULI2000, the mechanical engineering staff of Queen's University Belfast and the EPSRC and ASAIL for their continued funding.

I would also like to thank Matthew England, Haroon Rafique, Rory Garland, Natalie Mayhead, Greame McKendirck, Nicholas Millington, Prof. Roger Barlow, Prof. Dino Jarozynski and Prof. Karen Kirkby from the Centre for Doctoral Training in Next Generation Accelerators.

Finally I would like to thank my family, my dad Robert, mum Carole, sister Stephanie and fiancé Matthew for their continued and unwavering support throughout my PhD.

In loving memory of my father.

Robert William Albert Gwynne

23rd September 1941 - 11th Septmeber 2014

# Contents

**Contents** **iv**

**List of Figures** **viii**

**List of Tables** **xxi**

**1 Introduction** **1**

1.1 Motivation . . . . . 1

1.2 Thesis Aims . . . . . 3

1.3 Thesis Overview . . . . . 6

1.4 Role of the Author . . . . . 8

**2 Physical Concepts of Laser Interactions** **11**

2.1 Laser-Matter Interactions . . . . . 11

2.2 Electron Motion and the Ponderomotive Force . . . . . 14

2.2.1 Electron Motion . . . . . 14

2.2.2 The Ponderomotive Force . . . . . 15

2.3 Absorption Mechanisms . . . . . 18

2.3.1 Inverse Bremsstrahlung . . . . . 18

2.3.2 Resonance Absorption . . . . . 20

2.3.3 Vacuum Heating - Brunel Absorption . . . . . 22

2.3.4 j X B Heating . . . . . 23
2.3.5 Hot Electron Transport . . . . . 24
2.4 Laser-Driven Ion Acceleration . . . . . 26
2.4.1 Target Normal Sheath Acceleration . . . . . 26
2.4.2 Radiation Pressure Acceleration . . . . . 29
2.5 Research . . . . . 32

**3 Experimental Tools and Techniques 40**
3.1 Chirped Pulse Amplification . . . . . 40
3.1.1 Laser Contrast . . . . . 44
3.2 High Power CPA Laser Systems . . . . . 47
3.2.1 Vulcan . . . . . 47
3.2.2 LULI2000 . . . . . 50
3.2.3 TARANIS . . . . . 52
3.2.4 Astra-Gemini . . . . . 54
3.3 Diagnostics and Detectors . . . . . 55
3.3.1 Thomson Parabola Spectrometer . . . . . 56
3.3.2 Image Plate Detectors . . . . . 65
3.3.3 Radiochromic Films . . . . . 68
3.3.4 Ion Detection . . . . . 71

**4 Radiation Therapy 79**
4.1 Interaction of Radiation with Matter . . . . . 80
4.1.1 Photon Radiation . . . . . 82
4.1.2 Swift Charged Particles . . . . . 90
4.2 Radiation Effects on Human Tissue . . . . . 93
4.2.1 Radiation Damage . . . . . 93

4.2.2 Reactive Oxygen Species . . . . . 97
4.2.3 The Cell Cycle . . . . . 100
4.2.4 Repair Pathways . . . . . 108
4.2.5 LET, RBE and OER . . . . . 113
4.2.6 The Role of Hypoxia . . . . . 118
4.3 Hadron-Therapy . . . . . 124
4.4 Laser-Driven Ion Sources for Hadron-Therapy . . . . . 127
4.4.1 Ultra-High Dose Rates . . . . . 130

**5 Biological Tools and Techniques 136**

5.1 Cell Culture . . . . . 136
5.1.1 AG01522 Cell Line . . . . . 138
5.1.2 Sub-culture Technique . . . . . 139
5.1.3 Mycoplasma Testing . . . . . 144
5.1.4 Cell Doubling . . . . . 147
5.2 Detection of DNA Damage . . . . . 150
5.2.1 $\gamma$−H2AX . . . . . 150
5.2.2 53BP1 . . . . . 153
5.3 Immunofluorescence . . . . . 155
5.3.1 Immunofluorescence Protocol . . . . . 157
5.4 Fluorescence Microscopy . . . . . 163
5.5 Hypoxia Chamber . . . . . 164
5.5.1 Design . . . . . 166
5.5.2 Physical Characterisation . . . . . 167
5.5.3 Biological Characterisation . . . . . 171
5.5.4 Conclusions . . . . . 174

**6 Biological Effects of Laser-Driven Ions 175**

6.1 Previous Work . . . 177

6.1.1 Gemini 2013 - First Carbon Ion Irradiations . . . 177

6.2 TARANIS Experiment . . . 182

6.2.1 Experimental Arrangement . . . 182

6.2.2 Irradiation Setup . . . 185

6.2.3 Data Analysis and Results . . . 188

6.3 LULI Experiment . . . 194

6.3.1 Experimental Arrangement . . . 195

6.3.2 Irradiation Setup . . . 197

6.3.3 Data Analysis and Results . . . 200

6.4 TAP 2015 Experiment . . . 210

6.4.1 Experimental Arrangement . . . 211

6.4.2 Irradiation Setup . . . 214

6.4.3 Data Analysis and Results . . . 220

6.5 Comparative X-ray Experiments . . . 232

6.5.1 Experimental Arrangement . . . 233

6.5.2 Irradiation Setup . . . 234

6.5.3 Data Analysis and Results . . . 237

6.6 Discussion of Results . . . 239

**7 Conclusions and Future Directions 253**

7.1 Conclusions . . . 253

7.1.1 Thesis Aims . . . 255

7.2 Future Work . . . 258

7.2.1 Dose and LET Dependent Cell Survival Studies . . . 259

7.2.2 Plasmid DNA Studies . . . 259

**Glossary** **261**

**References** **264**

**Appendix A Research Publications** **288**

A.1 Peer Reviewed Publications . . . . . 288

A.2 Non-peer Reviewed Publications . . . . . 289

A.3 Publications in Preparation . . . . . 290

**Appendix B Immunofluorescence Protocol** **291**

# List of Figures

1.1 The difference of dose distribution by one port between carbon ion beams and X-rays [7]. . . . . 2

2.1 **(a)** Schematic of multiphoton ionisation, **(b)** schematic of tunnelling ionisation. In multiphonton ionisation the electron escapes into the free continuum, in tunnelling ionisation the electron tunnels through the potential barrier. . . . . 12

2.2 Target Normal Sheath Acceleration reproduced from [45]. . . . . 28

2.3 Model profiles of the ion density $n_i$ (blue), electron density $n_e$ (green) and electrostatic field $E_x$ (red) at three different stages of RPA [27]. . . . . 29

2.4 Light-Sail Acceleration. . . . . 32

3.1 Schematic diagram of a CPA laser [72]. . . . . 43

3.2 A schematic of the operating principle of a plasma mirror. A laser pulse with a preceding prepulse and pedestral is incident on a AR coated glass slab. The low intensity prepulse and pedestral are transmitted until the laser intensity become sufficiently large at the leading edge of the pulse to form a plasma. Once the critical density of the plasma is reached, the laser pulse is reflected. . . . . 46

3.3 Building blocks of the Vulcan Petawatt facility reproduced from [88]. . . . 48

3.4 The MILKA interaction chamber in LULI2000 target area room 1 [94]. . . 51

3.5 Optical layout of the TARANIS laser. Image key: FI – Faraday isolator; VSF – vacuum spatial filter; TA – Teflon aperture; TP – Teflon pinhole; SA – serrated aperture; 1, 2, 3 - laser heads with Nd:Glass rods of 9 mm, 25 mm, and 50 mm diameter, respectively; $L_1L_2$, $L_3L_4$, $L_5L_6$, $L_7L_9$, $L_8L_{10}$ – relay imaging telescopes; VC1, VC2 – vacuum compressors [96]. . . . . 53

3.6 Schematic layout of the Gemini laser. Reproduced from [98]. . . . . 54

3.7 Schematic of a Thomson Parabola Spectrometer [110]. The TPS described here has the electric and magnetic fields separated by a distance D, however there are variations which have overlapping electric and magnetic fields [116]. 56

3.8 Schematic of the electric plate setup in PTRACE for calculation of the E-field [110]. . . . . 59

3.9 Comparison of the maximum energy of $A/Z$ = 2.0 resolvable for different values of $\Delta(A/Z)$ achieved with 50 x 50 mm plates at 1 x $10^6$ V/m, 50 x50 mm plates at 2 x $10^6$ V/m, and 50 x 100 mm plates at 1 x $10^6$ V/m, assuming $L_{E2}$ = 150 mm [110]. . . . . 62

3.10 Comparison between the TPS traces of several ion species (from left to right; up to 100 MeV $p^+$, up to 200 MeV $C^{6+}$, $C^{5+}$ and $C^{4+}$ ions, and up to 1000 MeV $Au^{40+}$ and $Au^{45+}$ ions) obtained using the different TPS configurations shown in the schematics. The red arrows show the ion beam direction, with the beam axis 10 mm above the bottom edge of the electric plate. For all simulated configurations $L_{E1}$ + $L_{E2}$ = 300 mm, the $B$ = 1.0 T magnets were 50 mm in length ($L_{B1}$), the distance between the magnets and electric plates was 5 mm ($D$), the electric field strength $E$ = 1.8 x $10^6$ V/m, and the electric plates were 18 mm apart ($d$ = 9 mm). The insets show a zoomed in view of the high energy portion of the ion traces. There is improved trace separation in **(b)** as comapred to **(a)**, and even better $A/Z$ resolution and trace separation is obtained in **(c)**. Some clipping of the low energy ions is observed in **(b)** and more seriously in **(c)** as shown by the dotted red line. Trapezoidally shaped electric plates, as shown in **(d)**, can be used in such high resolution spectrometers allowing the lower energy ions to pass over the top of the plate, whilst keeping the same trace separation for the high energy ions as obtained in **(c)** [110]. . . . . 63

3.11 **(a)** 3D schematic view of the TPS employed in the experiment, **(b)** data obtained by the TPS showing traces of different energy and mass-to-charge ratio ions produced by the interaction of the Vulcan laser with a 10 nm gold foil. The low energy ions are clipped by the electric plate as shown by the dotted line, **(c)** a zoomed in view of the enhanced species separation produced by the 150 mm rectangular electric plates, where the numbers represent $A/Z$ values for the ion species, such as 1.0 - $p^+$, 2.0 - $C^{6+}$ and $O^{8+}$, 2.29 - $O^{7+}$, 2.4 - $C^{5+}$, 2.67 - $O^{6+}$, 3 - $C^{4+}$, **(d)** a zoomed in view of the fine charge state separation of Au ions, which are clipped by the longer electric plate [110]. . . . . 64

3.12 Raw experimental data from the image plate scans employing different electric plate designs, as shown by the inset at the bottom right corner. The white line in **(a)** represents the clipping of the lower energy ion traces, which are not clipped when using the plate geometry shown in **(b)**. **(c)** shows a zoomed in view of the data shown in **(b)**, as marked by the orange square [112]. . . 65

3.13 The PSL process. Reproduced from [119]. . . . . 67

3.14 The structure of EBT-3 dosimetry film. The film has 28 $\mu$m active layer sandwiched between two 125 $\mu$m matte-polyester substrates. The active layer contains the active component, a marker dye, stabilisers and other components which give the film its near energy-independent response [129]. 70

3.15 MATLAB GUI TPspec with an example of an image plate showing traced proton, carbon and oxygen tracks. . . . . 73

3.16 Proton spectra obtained from three shots on 10 nm Au targets of [energy on target (J), pulse duration (ps)] of [171.54, 5.2] shown in black, [150.93, 2.3] shown in red and [147.36, 1.0] shown in blue. . . . . 74

3.17 $C^{6+}$ spectra obtained from three shots on 10 nm Au targets of [energy on target (J), pulse duration (ps)] of [171.54, 5.2] shown in black, [150.93, 2.3] shown in red and [147.36, 1.0] shown in blue. . . . . 75

3.18 $Au^{45+}$ spectra obtained from three shots on 10 nm Au targets of [energy on target (J), pulse duration (ps)] of [171.54, 5.2] shown in black, [150.93, 2.3] shown in red and [147.36, 1.0] sown in blue. . . . . 75

3.19 Peak ion energies plotted against pulse duration for the three shots summarised in Table 3.1 for TP-3/TP0 in **(a)** and TP3 in **(b)**. . . . . 77

4.1 A simplified model of the interaction of radiation with matter. Interaction A causes excitation, B causes ionisation, and C causes multiple ionisations. Each ioisation frees an electron from the atom to which it was bound. Reproduced from [134]. . . . . 81

4.2 Schematic representation of the photoelectric effect, reproduced from [135]. 85

4.3 Illustration of the Compton effect, reproduced from [138]. . . . . 86

4.4 Relative importance of photoelectric absorption, Compton scattering and pair production reproduced from [138]. . . . . 88

4.5 The different types of DNA damage [141] and the direct and indirect effects caused by ionising radiation [142]. . . . . 94

4.6 The cell cycle and the cell cycle checkpoints. The average length of the cell cycle is 16 hours: 15 hours in the interphase and 1 hour in the mitosis phase. 101

4.7 The relationship between LET, RBE and DSBs [139, 178]. . . . . 115

4.8 Comparison of the effects of low- and high-LET radiation on a population of cells [134]. . . . . 115

4.9 The relationship between LET and the cell survival curve. The width of the shoulder represents the part of the dose which is wasted, thus the higher LET radiation has a greater RBE compared to the lower LET radiation as less of the dose is wasted. . . . . 116

4.10 Radicals are either oxidated, fixing the damage, or reduced, restoring the DNA to its original form. . . . . 119

4.11 The spatial relationship between a blood vessel and a solid tumour in the context of HIF-1 and $O_2$ concentrations. In normoxic conditions of 5%, within 70 $\mu$m of the blood vessel, the HIF-1 is rapidly degraded or has a very low level of expression. Hypoxic regions exist at distances greater than 100 $\mu$m from the blood vessel, where the HIF-1 expression is increased and $O_2$ concentration is decreased [208]. . . . . 123

4.12 Advantageous energy deposition of ions and protons compared with X-ray photons [213]. . . . . 125

4.13 A conventional cyclotron based system [223] on the left compared to a conceptual laser accelerated proton therapy instrument [224] on the right. . . . 129

5.1 AG01522 human fibroblast cells at 10 x magnification. Image taken a few hours after seeding as the cells are starting to attach and spread out. . . . . 139

5.2 **(a)** Schematic of a Hemocytometer [251]. **(b)** The appearance of the counting grid visualised under the microscope [10]. **(c)** Counting system to ensure accuracy and consistency; cells within the large square and those crossing the edge on two out of the four sides are counted [252]. . . . . 143

5.3 Graph showing the total number of cells in the 2 ml samples 24, 48 and 72 hours after seeding. The samples were counted using a Coulter Counter, with the total cell number calculated using the method described in Section 5.1.2. . . . . 149

5.4 **(a)** Schematic of a chromatin containing histones [266]. **(b)** $\gamma$-H2AX foci [10]. . . . . 151

5.5 **(a)** Schematic of BRCA1 protein [273], **(b)** 53BP1 foci. . . . . 155

5.6 Screen-shot of the ImageJ Cell Counter application used to count the DNA DSB 53BP1 or $\gamma$-H2AX foci in the experimental data. . . . . 164

5.7 **(a)** The new compact hypoxia chamber. The chamber is small enough that 6 can be stored in a standard 3 shelf incubator. **(b)** Continuous measurement of the $O_2$ concentration inside the hypoxia chamber using a Rapidox 1100Z meter. **(c)** Schematic of the new hypoxia chamber. The chamber is 12.0 by 9.6 by 3.8 cm in size, with the main body constructed from PEEK and the windows from Saran. **(d)** Stainless steel and aluminium cell dish. **(e)** View of the cell dish placement inside the new hypoxia chamber. The cell dish is secured in place by an aluminium bracket. . . . . 166

5.8 **(a)** Recorded $O_2$ concentration inside 3 of the hypoxia chambers compared with the accepted levels of physiological ($< 2.0\%$ $O_2$), pathological ($< 1.0\%$ $O_2$) and radiobiological hypoxia ($< 0.4\%$ $O_2$) [197]. All 3 chambers maintained a physoxic ($< 5\%$ $O_2$) [197] environment for the full 24 hr test period. **(b)** Zoomed in view of the first 2 hrs. . . . . 169

5.9 Graph showing the dose of 225kVp X-rays deposited on the EBT-3 normal film mounted underneath the cell dish placed inside the hypoxia chamber (red), and the dose deposited when the dish and film were irradiated outside the hypoxia chamber (blue). The calibration was calculated from a set of EBT-3 films irradiated in the X-ray cabinet without being mounted on the dish, or being inside the hypoxia chamber. . . . . 170

5.10 AG01522 human skin fibroblast cells were irradiated with 15 MeV laser accelerated protons employing the petawatt arm of the Vulcan laser facility at the Rutherford Appleton Laboratory, Oxford, UK. The samples were kept inside the hypoxia chambers after the irradiations to maintain the hypoxic environment. The samples were fixed at 0.5 and 24 hrs post irradiation, then stained for HIF-1$\alpha$ to show the induction of hypoxia, 53BP1 to highlight DNA DSB damage and DAPI for detecting the cell nuclei. Images were acquired using the Carl Zeiss Axiovert 200M fluorescence microscope (at 40x magnification) with a CCD camera and the Axiovision Rel 4.8 software package, located in the Centre for Cancer Research and Cell Biology, Queen's University Belfast. . . . . 172

5.11 53BP1 foci induction and repair in AG01522 human skin fibroblast cells after exposure to 15 MeV laser accelerated protons and 225 kVp X-rays under oxic and hypoxic conditions. The initial damage is shown at 0.5 hrs and the residual damage is shown at 24 hrs post irradiation. . . . . 173

6.1 Experimental configuration used to characterise the beam. For the cellular irradiations the 0.9 T magnets were removed. . . . . 178

6.2 Temporal kinetics of phosphorylated 53BP1 foci in cells exposed to protons, carbon ions and X-rays over a 24 hr period [38]. . . . . 181

6.3 **(a)** The experimental setup of the target chamber in TA2 of the TARANIS laser facility. **(b)** A close up of the magnet and the target mount inside the chamber. . . . . 183

6.4 An example of the proton spectra of 6.85 MeV protons on the cell plane. The distance is measured from the straight edge of the reference RCF. . . . 184

6.5 **(a)** The RCF mask used to attach the un-coated EBT-3 film to the back of the hypoxia chamber. The position of the hypoxia chamber during the irradiations form **(b)** the back and **(c)** the side. . . . . 184

6.6 **(a)** Schematic of the stainless steel dish with Mylar attached to the first side with an aluminium plate and O-ring, **(b)** an aluminium plate, **(c)** and how the dish is assembled. The front layer of Mylar is cut to just below the centre line of the dish after it is assembled. . . . . 185

6.7 Example foci images obtained for the nuclei irradiated with 6.85 MeV protons. The $\gamma$-H2AX foci have been stained red, the nuclei are contrast stained blue and the hypoxia induction bio-marker HIF-1$\alpha$ has been stained green. 190

6.8 The 53BP1 foci kinetics of laser induced DNA DSBs. The values shown are the average number of foci per nucleus (with the control value of $1.98 \pm 0.78$ for oxic and $1.75 \pm 0.76$ for hypoxic samples subtracted) as the dose was unobtainable from the RCF as it was below 0.1 Gy for the majority of the shots, hence the low values for the average number of foci per nucleus. These values have the control value subtracted, hence why the value can become negative (for example the 24 hr time point error bars) if the foci count falls below the control value. . . . . 191

6.9 The percent foci remaining at each time point compared to the number of foci present 0.5 hrs post irradiation. . . . . 192

6.10 **(a)** Target chamber arrangement, showing the re-entrant tube and magnet assembly. **(b)** Aerial and **(c)** lateral detail of the target arrangement, beam transport delivery system and the position of the biological sample within the re-entrant tube. . . . . 195

6.11 Mask used to attach the RCF with the positions of the 6 MeV, 10 MeV and 15 MeV protons marked. . . . . 196

6.12 Example images of the 53BP1 foci taken at the positions irradiated by 10 MeV, 13 MeV and 15 MeV protons as indicated by the positions on the RCF mask, at the five different time points of 0.5, 1, 2, 6 and 24 hrs post irradiation and the control. . . . . 203

6.13 Average number of foci per nucleus aligned with the dose across the normal EBT-3 RCF along the 10 MeV proton line for the first 0.5 hr sample. . . . . 204

6.14 Dose response extracted from Figure 6.13 where the average number of foci per nuclei has been plotted against the dose at that position. . . . . 205

6.15 Kinetics of DNA DSB damage and repair visualised through 53BP1 immunostaining and displayed as the average number of foci per nucleus per Gy with respect to time post irradiation. . . . . 206

6.16 Percent foci remaining at the different time points with respect to the average number of foci 0.5 hrs post irradiation. . . . . 207

6.17 The relative foci induction measured as the ratio of the average number of foci per nucleus per Gy induced by the proton irradiations (10 MeV, 13 MeV and 15 MeV) compared to the average number of foci per nucleus per Gy induced by 225 kVp X-rays for each time point. . . . . 208

6.18 Shot to shot dose variation for all shots calculated from the positions for each energy line indicated from the RCF mask. . . . . 209

6.19 **(a)** The experimental arrangement used for the TAP experiment showing the different elements of the beam delivery system and shielding. **(b)** A schematic of the experimental arrangement. . . . . 213

6.20 The rail used to position the hypoxia chamber inside the insertion pipe, and the position of the pipe inside the interaction chamber. The front window of the hypoxia chamber is aligned with the flange mounted Kapton window. . 214

6.21 **(a)** The position of the hypoxia chamber before and after the irradiations and **(b)** during irradiations. . . . . 220

6.22 The average number of foci per nucleus across one cell sample aligned with the dose from the customised EBT-3. Both measurements are taken from the position of the 15 MeV proton line as indicated by the RCF mask, which is attached to the cell dish as shown. . . . . 223

6.23 AG01522 human skin fibroblast cells were irradiated with 15 MeV laser accelerated protons employing the petawatt arm of the Vulcan laser facility. The samples were kept inside the hypoxia chambers after the irradiations to maintain the hypoxic environment. The samples were fixed at 0.5 and 24 hrs post irradiation, then stained for HIF-1$\alpha$ to show the induction of hypoxia, 53BP1 to highlight DNA DSB damage and DAPI for detecting the cell nuclei. 224

6.24 The raw scanned image of the RCF which is converted to a dose map using an ImageJ Macro. The position of the 15 MeV proton line and an example image of the foci is shown. . . . . 225

6.25 Kinetics of DNA DSB damage and repair visualised through 53BP1 immunostaining for oxic irradiation conditions, displayed as the average number of foci per nucleus per Gy with respect to time post irradiation. . . . . 226

6.26 Kinetics of DNA DSB damage and repair visualised through 53BP1 immunostaining for physically hypoxic irradiation conditions, displayed as the average number of foci per nucleus per Gy with respect to time post irradiation. . . . . 226

6.27 Kinetics of DNA DSB damage and repair visualised through 53BP1 immunostaining for chemically hypoxic irradiation conditions, displayed as the average number of foci per nucleus per Gy with respect to time post irradiation. . . . . 227

6.28 Kinetics of DNA DSB damage and repair visualised through 53BP1 immunostaining for free radical scavenging irradiation conditions, displayed as the average number of foci per nucleus per Gy with respect to time post irradiation. . . . . 227

6.29 The relative foci induction for each of the irradiation conditions across all time points. . . . . 229

6.30 HRF calculated for both 15 MeV protons and 225 kVp X-rays for the physically hypoxic samples and the chemically hypoxic ($CoCl_2$) samples for all time points. The average values were 1.36 $\pm$ 0.55 and 1.95 $\pm$ 0.33 for the proton and X-ray hypoxic samples respectively, and 0.94 $\pm$ 0.26 and 1.78 $\pm$ 0.31 for the proton and X-ray $CoCl_2$ samples respectively. . . . . 230

6.31 Shot to shot dose variation across all shots for the 15 MeV proton energy line. 232

6.32 Comparison of the 15 MeV proton DNA DSB kinetic profiles for the TAP and LULI experiments. . . . . 240

6.33 The percentage of cells with 0 - 5 (blue), 6 - 10 (green), 11 - 20 (yellow), 21 - 30 (orange) and > 30 (red) foci per nucleus per Gy at 0.5 hours post irradiation for the four different irradiation environments. The percentages for 225 kVp X-rays from the CCRCB, 15 MeV laser accelerated protons (LA protons, 3.3 keV/$\mu$m) from TAP and conventionally accelerated protons from the 62 MeV beam at Istituto Nazionale di Fisica Nucleare-Laboratori Nazionali del Sud (INFN-LNS), Catania, Italy (CA protons, 1.2 keV/$\mu$m low LET at the entrance of the Bragg peak) are shown. At Catania it was not possible to perform hypoxic experiments using gassed samples at the time of the experiment. . . . . 241

6.34 The percentage of cells with 0 - 5 (blue), 6 - 10 (green), 11 - 20 (yellow), 21 - 30 (orange) and > 30 (red) foci per nucleus per Gy at 24 hours post irradiation for the four different irradiation environments. The percentages for 225 kVp X-rays from the CCRCB, 15 MeV laser accelerated protons (LA protons, 3.3 keV/$\mu$m) from TAP and conventionally accelerated protons from the 62 MeV beam at the Istituto Nazionale di Fisica Nucleare-Laboratori Nazionali del Sud (INFN-LNS), Catania, Italy (CA protons, 1.2 keV/$\mu$m low LET at the entrance of the Bragg peak) are shown. At Catania it was not possible to perform hypoxic experiments using gassed samples at the time of the experiment. . . . . 243

6.35 The percentage of cells with 0 - 5 (blue), 6 - 10 (green), 11 - 20 (yellow), 21 - 30 (orange) and > 30 (red) foci per nucleus per Gy at 0.5 and 24 hours post irradiation for the Oxic and Hypoxic irradiation environments. Values are shown for 225 kVp X-rays, 15 MeV laser accelerated protons from TAP (3.3 keV/$\mu$m) and low LET conventionally accelerated protons from the 62 MeV Catania beamline (1.2 keV/$\mu$m at the entrance of the Bragg peak). . . 245

6.36 The percentage of cells with 0 - 5 (blue), 6 - 10 (green), 11 - 20 (yellow), 21 - 30 (orange) and > 30 (red) foci per nucleus per Gy at 0.5 and 24 hours post irradiation for the $CoCl_2$ and DMSO irradiation environments. Values are shown for 225 kVp X-rays, 15 MeV laser accelerated protons from TAP (3.3 keV/$\mu$m) and low LET conventionally accelerated protons from the 62 MeV Catania beamline (1.2 keV/$\mu$m at the entrance of the Bragg peak). . . 246

6.37 Comparison of the 15 MeV proton DNA DSB kinetic profiles for the TAP and LULI experiments. . . . . 247

# List of Tables

3.1 Summary of shot details. . . . . 77

4.1 Approximate levels of oxygen corresponding to the different levels of hypoxia [184]. . . . . 121

4.2 Comparison between a conventional particle accelerator and a laser-driven accelerator [224]. . . . . 129

5.1 Incidence of Mycoplasma contamination in cell culture [255] . . . . . 145

5.2 Most common species of mycoplasma that cause cotamination [255] . . . . 146

5.3 Summary of the number of cells in each 2 ml sample from each of the two counts, average number of cell from the counts, the standard deviation and the standard error of the AG01522 cells grown on 3 $\mu$m Mylar (surface area of 16.63 $\pm$ 0.73 cm$^2$) and cell culture slide flasks (surface area of 9.2 $\pm$ 0.2 cm$^2$), measured 24, 48 and 72 hours after seeding. . . . . 148

5.4 Summary of the oxygen concentration measurements for the 3 chambers. The Rapidox 1100Z meter and the hypoxic gas supply were connected to each chamber. The chamber was gassed for approximately 15 minutes, and then the oxygen concentration was measured continuously for the next 24 hrs. The rate of change for every 4 or 5 min interval was calculated, as was the rate of change from the starting value of 0.49%, 0.27% and 0.02% for chambers A, B and C respectively. . . . . 168

6.1 Raw experimental data obtained for 10 MeV protons and 5 MeV/nucleon carbon ions [38]. . . . . 180

6.2 Summary of the TARANIS replicates for each time point and irradiation condition for 6.85 MeV protons. The values represent the number of samples successfully stained with clearly discernible foci. . . . . 189

6.3 Summary of the RFI for each time point for oxic versus hypoxic irradiation conditions for 6.85 MeV protons. . . . . 193

6.4 Summary of the LULI replicates for each time point and proton energy for the irradiations under oxic conditions. The values represent the number of samples successfully stained with clearly discernible foci. . . . . 201

6.5 The average dose calculated across all shots for each proton energy line, the maximum dose obtained for each line and the minimum dose obtained for each line. . . . . 209

6.6 Summary of the TAP replicates for each time point and irradiation environment for 15 MeV protons. The values represent the number of samples successfully stained with clearly discernible foci. . . . . 222

6.7 Summarised RFI and HRF values for the four different irradiation conditions for 15 MeV protons and 225 kVp X-rays. . . . . 229

6.8 The average dose calculated across all shots, the maximum dose obtained and the minimum dose obtained for the 15 MeV proton line. . . . . 232

6.9 Summary of the CCRCB replicates for each time point and irradiation environment for 225 kVp X-rays. The values represent the number of samples successfully stained with clearly discernible foci. . . . . 238

6.10 The average number of foci per nucleus for each time point for 15 MeV proton irradiations at LULI and TAP. These values have had the control value of $1.87 \pm 0.05$ and $1.85 \pm 0.08$ for LULI and TAP respectively, subtracted. 242

# Chapter 1

# Introduction

## 1.1 Motivation

Proton and ion beams produced during ultra-intense laser interactions with thin foils have very different properties compared to beams of comparable energy produced by conventional accelerators. As a result they have the potential to be used for a wide range of innovative applications, particularly in the areas of science, technology and medicine [1]. The properties of interest include high brightness of $\sim 10^{12}$ ions in picosecond-scale bunches [2], high laminarity and energy cut-off, ultra-short pulse durations [3], high intensity, ultra-low emittance, good collimation which increases with proton energy [4] and a high field acceleration gradient [5]. Current interest in laser-driven ion sources for medicinal purposes such as hadron therapy stems from factors such as the ease of beam production and the reduction in the facility scale required for their acceleration and delivery. Conventionally, large magnetic steering systems, called Gantries, have to be employed to enable to the irradiation of a lying position from any direction. The creation of a specialised, relatively small medical laser proton accelerator would reduce the size of the accelerator gantry set-up to approximately 2 - 3 m and a few tons, compared to existing conventional systems which are approximately 6 - 8 m in diameter, 10 - 12 m in length and weigh more than 100 tons

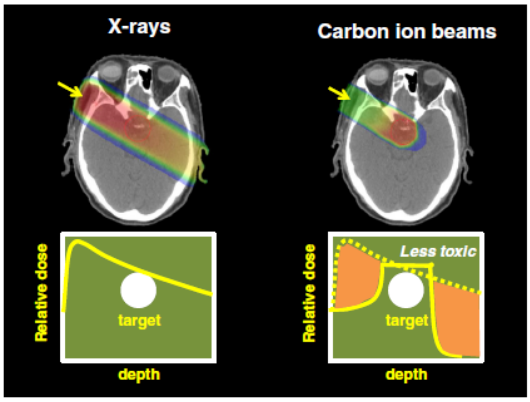


Fig. 1.1 The difference of dose distribution by one port between carbon ion beams and X-rays [7].

[6].

One of the greatest challenges of cancer radiation therapy using X-rays is the lack of contrast between normal healthy cells and the cancerous cells of the tumour. The dose delivered to a patient in a single X-ray treatment is limited and the full curative dose may be delivered over a number of treatments in a process called fractionation. The advantageous energy deposition properties of ions compared with X-rays can be exploited in radiation therapy, as ions are able to deliver a lethal amount of dose into the target tumour whilst limiting harm to the surrounding healthy tissue [5], owing to their inherent Bragg peak.

Laser-driven ion beams which are currently available have not yet sufficiently fulfilled the requirements for many of the envisaged applications, particularly in terms of the energy required for medical applications. For proton therapy for cancer treatment, beams in the energy range of 60 - 250 MeV [8] and with a bandwidth of a few per cent of the central energy are required, but the highest published laser-driven proton energy reported to date is 85 MeV [9]. The energies required for the treatment of deep seated tumours are in excess of 250 MeV, which is well beyond the capabilities of current systems. Determining the feasibility of using future high power lasers as drivers of proton acceleration for oncology still requires investigation of the scaling of laser-accelerated proton energies and yields as a

function of laser parameters such as intensity, energy and pulse duration [2].

One of the main differences between laser-driven ion beams and their conventionally produced counterparts is their ultra-short pulse length, as the ions are emitted in bursts of picosecond duration at the source. From here, the beam pulse will lengthen in time corresponding to the spread of energies and distance over which the protons travel from the source to the target, typically resulting in a pulse with duration in the range of nanoseconds. A proton pulse depositing energy on this very short time frame coupled with the inherent high flux of proton beams correlates into an ultra-high dose rate of $> 10^9$ Gys$^{-1}$ [10].Their therapeutic use may result in dose rates as many as 8 orders of magnitude higher than those normally used with conventionally accelerated protons. The biological effects of ions at these ultra-high dose rates are virtually unknown and cannot be put to any medical use until they have been carefully assessed [11].

## 1.2 Thesis Aims

Currently, one of the most important challenges facing radiotherapy is tumour hypoxia. Tumour hypoxia occurs in nearly all human solid tumours and ionising radiation depends heavily on the presence of molecular oxygen to produce cytotoxic effects [12]. The treatment of hypoxic tumours is challenging even with the most advanced X-ray based therapies, often leading to the failure of such treatments. Ion beam therapy has gained momentum as an effective modality for combating this challenge, employing protons and high LET charged particles, with several investigations reporting success in inducing cell death in cancer cells under hypoxia [13–16]. The prospect of employing laser accelerated ions as a cost effective alternative to protons and ions from conventional acceleration sources has also become more realistic with significant advances in laser technologies. In recent years the capability of high-energy lasers to generate suitable ion beams for cancer therapy has been demonstrated [17–19].

The dose rates achieved by employing laser driven ion sources may impact the oxygen dependency of the radiation response, thus it is imperative to gain an understanding and characterise the radiobiological effects at the ultra-high dose rates delivered by these short ion pulses on human cells under hypoxic conditions if the technology is to develop and advance towards clinical applications. The effectiveness of laser accelerated protons and carbon ions in the induction of DNA double strand breaks in AG01522 normal human fibroblast cells has already been shown (see Section 6.1.). Here we aim to demonstrate for the first time laser accelerated proton induced double strand breaks in human cells under physically induced hypoxia, chemically induced hypoxia and a free radical scavenging environment, as well as in an oxic environment for comparison.

What we want to know is do laser accelerated protons deposited at ultra-high dose rates produce different biological effects under oxic, physically hypoxic, chemically hypoxic and free radical scavenged conditions, as compared to X-rays and conventionally accelerated protons?

To fully understand the relationship between laser accelerated ion induced DNA damage and oxygen dependency it is necessary to have a compact and reliable device capable of maintaining hypoxia for the duration of the radiation exposure and the subsequent twenty four hours over which the DNA double strand break kinetics are observed. Several devices exist, discussed in more detail in Section 5.5, however a device compatible with the irradiation procedures and set-up required for laser accelerated ion beams did not exist. Therefore, a portable and compact hypoxia chamber was developed, suitable for characterising the biological effects of laser accelerated beams under a range of oxygen concentrations.

Experiments have been carried out employing three high-power laser systems: TARANIS at Queen's University Belfast, LULI2000 at Ecole Polytechnique Paris and the Vulcan Petawatt system at the Rutherford Appleton laboratory. Comparison X-ray experiments were carried out in the Centre for Cancer Research and Cell Biology at Queen's University

Belfast, and data from conventional proton sources was provided by colleagues from experimental campaigns at Clatterbirdge Cancer Centre, Birkenhead England and the Istituto Nazionale di Fisica Nucleare-Laboratori Nazionali del Sud (INFN-LNS), Catania Italy.

The main aim of the TARANIS experiment were to test the newly designed hypoxia chamber with laser accelerated protons as a proof of principle to develop the cell handling procedure and irradiation methods for the TAP Vulcan experiment. The effect of hypoxia on DNA double strand break induction and repair was studied by irradiating AG01522 normal human fibroblast cells inside the hypoxia chamber in hypoxic and oxic conditions for a direct comparison.

The main aim of the LULI experiment was to use the unique capabilities of the laser system carry out single shot investigations of the cellular response to proton irradiation, through ultra-fast proton dose deposition in normal cell models. The DNA double strand break formation and repair were monitored as a function of dose and time post irradiation by means of immunofluorescence.

The main aim of the TAP Vulcan experiment was demonstrate for the first time laser accelerated proton induced double strand breaks in AG01522 normal human fibroblast cells under physically induced hypoxia, chemically induced hypoxia and a free radical scavenging environment, whilst overcoming limitations in terms of the dose available in a single shot, and a need to relax the energy selection and pulse duration, highlighted by the previous Gemini (Section 6.1.1) and TARANIS (Section 6.2) campaigns. This experiment was performed using the new compact hypoxia chamber designed specifically for this experiment and tested previously employing he TARANIS laser.

Therefore the main aims of thesis can be summarised as follows:

- Demonstrate laser accelerated proton induced DNA DSB under physically induced hypoxia, chemically induced hypoxia and free radical scavenging environments for the first time

- Develop and characterise a new compact hypoxia chamber for use with laser driven ion sources
- Develop the cell handling procedure and irradiation methods associated with the use of the new hypoxia chamber
- Repeat laser accelerated proton experiments in an oxic environment for comparison
- Discover if there are different biological effects produced under the four irradiation environments as compared to X-ray and conventionally accelerated proton irradiations where data exists
- Develop a robust immunofluorescence protocol

## 1.3 Thesis Overview

There are two main areas of investigation presented in this thesis: the generation of laser-accelerated ion beams produced from thin foil interactions and their scaling dependence on pulse duration; and the biological effects of such laser-driven ion beams at ultra-high dose rates on normal human cells. The results presented are from four different experimental campaigns carried out at three different high power laser facilities: the TARANIS system at Queen's University Belfast, the LULI2000 system at École Polytechnique Paris and the Vulcan Petawatt system at the Rutherford Appleton Laboratory Oxford. Some results from previous experiments, carried out employing the Gemini laser system at the Rutherford Appleton Laboratory, are also presented as motivation for continued work in this field.

The structure of the thesis is as follows:

**Chapter 2** provides an overview of the physical processes relevant to laser solid interactions, as all the experiments involved the irradiation of thin or ultra-thin foils with high intensity laser beams. The laser ion acceleration methods at work are also discussed.

**Chapter 3** explains the different laser systems, diagnostics and detectors employed throughout the experimental campaigns. A brief description of the four high power laser systems mentioned above is followed by a description of the working principles of the three main diagnostics used: the Thomson Parabola Spectrometer (TPS), Image Plates (IP) and Radiochromic Films (RCF). A brief explanation of improvements to the standard TPS and an introduction to experimental results from ion acceleration investigation into energy scaling are also discussed.

**Chapter 4** gives an introduction to the relevant aspects of radiobiology. How radiation effects human tissue including DNA damage and repair mechanisms, reactive oxygen species, influence of the cell cycle, the role of hypoxia and the rationale for using laser-driven ion beams for next generation Cancer therapy.

**Chapter 5** explains the different biological tools and techniques employed throughout the experimental campaigns, including the design, development and validation of a new compact hypoxia chamber and the biological protocols used for cell culture and Immunofluorescence.

**Chapter 6** presents the results of three experimental campaigns carried out to investigate the biological effects of laser-driven ions at ultra-high dose rates in oxic and hypoxic conditions employing Vulcan, TARANIS and LULI2000. Previous results from the first radiobiology experiment employing the Gemini laser are also presented. These experiments focused on the induction and repair kinetics of DNA DSB damage in a variety of irradiation conditions: oxia, physical hypoxia, chemical hypoxia and free radical scavenging.

**Chapter 7** presents any conclusions derived from the experimental work and any considerations relevant for future work in the fields discussed.

## 1.4 Role of the Author

The experimental results presented in Chapter 3 regarding benchmarking the modified TPS design and ion acceleration, and the radiobiological experimental results presented in Chapter 6 were the result of collaborations with several research groups at the various different European laser facilities. The experiments carried out employing Vulcan and Astra-Gemini required essential planning and support from the staff of the Central Laser Facility, especially the Link Scientists, Target Fabrication, Engineering staff and staff members of the Research Complex at Harwell. Members of the research team at Public Health England Harwell also provided invaluable support. Experiments carried out at TARANIS and the Centre for Cancer Research and Cell Biology (CCRCB) at Queen's University Belfast benefited from expertise from the Borghesi Plasma Physics Group in the Centre for Plasma Physics, and the Prise Radiobiology Group, with special mention to Dr. Domenico Doria and Dr. Pankaj Chaudhary. Essential support was also provided by Dr. Gagik Nersissyan and Dr. Dan Marlow, and the Mechanical Workshop staff who manufactured the new hypoxia chambers. At École Polytechnique, the staff of LULI2000 and Laboratoire d'Optique et Biosciences (LOB) were extremely accommodating and helpful during the experimental run, especially Dr. Lorenzo Romagnani and Marianne Grognot.

The author has actively participated in the three main experimental campaigns presented in Chapter 6 of this thesis: the TARANIS, LULI and Vulcan radiobiology experiments, as well as the previous work carried out on Astra-Gemini and the comparison X-ray experiments carried out in the CCRCB. The author did not actively participate in the experiments which culminated in the results shown in Chapters 3, but instead carried out data analysis and simulations pre and post experiments. A more detailed account is given below.

The two separate investigations described in Section 3.3.1 of Chapter 3 were carried employing the Petawatt arm of the Vulcan laser at the Rutherford Appleton Laboratory. The author did not actively participate in either of these investigations, but instead prepared and

ran the PTRACE simulations used to design the modified Thomson Parabola Spectrometer (PTRACE written by Dr. Angelo Schiavi [20]). The first experiment verified the use of longer electric plates, the second the altered shape of the electrodes (described in more detail in Section 3.3.1 of Chapter 3). The author also carried out analysis of the image plates used in the first experiment, more detail of which is given in Section 3.3.4 of Chapter 3.

The results presented in Section 3.3.4 of Chapter 3 were obtained from the first investigation described in Section 3.3.1 of Chapter 3. The author modified an existing Matlab GUI called TPSpec (written by Dr. Satya Kar and Dr. Domenico Doria), which was used to analyse the digitised image plate scans. The GUI was then used by the author to extract the ion spectra of the species detected to determine the scaling dependence of the peak ion energy on pulse duration (more detail is given in Section 3.3.4 of Chapter 3). The author also analysed images of the laser focal spot to determine the focal spot size and thus the intensity of the laser pulse.

The author was involved in the design, development and validation of the new hypoxia chamber described in Section 5.5 of Chapter 5. The initial design was created by the author and Dr. Domenico Doria, and fine tuned by Dr. Doria. The author carried out the validation of the hypoxia chamber by physically and biologically measuring the oxygen concentration and induction of hypoxia inside the chamber in collaboration with Dr. Pankaj Chaudhary and Carla Maiorino. The author also validated the dose received inside and outside the chamber by means of a calibration produced by irradiating RCF films.

The author was actively involved in all the experiments presented in Chapter 6. The author was involved in maintaining the AG01522 cell line and preparing samples for irradiation during the Astra-Gemini experiment, and heavily involved in the subsequent data acquisition through the taking of images of the samples under the microscope and counting the number of induced DNA DSBs (more details given in Chapter 6 Section 6.1.1). The au-

thor was involved in the planning and conduction of the three main experiments employing the TARANIS laser at Queen's University Belfast, LULI2000 (pico) at École Polytechnique Paris, and Vulcan Petawatt at RAL Oxford, presented in Sections 6.2, 6.3 and 6.4 respectively of Chapter 6. The author provided minor assistance in the setting up of the laser interaction chambers, with the main focus being the maintenance of the AG01522 cell line and the preparation of samples for irradiations. The author carried out biological analysis of the samples through several permutations of the immunofluorescence technique (described in Section 5.3.1 of Chapter 5), and acquired the biological data through fluorescence microscopy and the Cell Counter application of ImageJ. The author was also responsible for building and scanning RCF stacks at Vulcan, and used the Epson Perfection V750 Pro QUB program (written by Dr. Doria) to convert the raw RCF scans to dose for all three experiments, as well as for the calibration mentioned above.

# Chapter 2

# Physical Concepts of Laser Interactions

This chapter presents a brief overview of the physics of intense laser interactions with solid targets. The different absorption mechanisms which transfer the laser energy into the target, generation and transport of hot electrons, and ion acceleration during interactions with thin foils are described.

## 2.1 Laser-Matter Interactions

When an intense laser pulse is focused onto a solid target, a sudden ionisation of the target material occurs producing a front surface plasma. Ionisation of all target materials is guaranteed when the intensity of the laser is greater than the atomic intensity of the target material, which is when the binding strength of the electron to the atom is matched to the intensity of the laser field:

$$I_a = \frac{\varepsilon_0 c E_a^2}{2} \tag{2.1}$$

where $E_a$ is the electric field strength at the Bohr radius. The target is ionised by different processes, dependent upon the laser intensity and energy, with ionisation possible below this threshold via multiphoton effects. The two main regimes of ionisation are multiphoton

ionisation and tunnelling/barrier supression ionisation, which are separated by the Keldysh parameter [21]:

$$\gamma = \omega\sqrt{\frac{2E_{ion}}{I_L}} = \sqrt{\frac{E_{ion}}{\Phi_{pond}}} \tag{2.2}$$

where

$$\Phi_{pond} = \frac{e^2E_L^2}{4m\omega_L^2} \tag{2.3}$$

which is the ponderomotive potential of the laser field and $E_{ion}$ is the ionsiation potential of the ion or atom with charge $(Z-1)$. When the laser wavelength is shorter and the intensity lower, $\gamma > 1$, and ionisation of the target occurs via multiphoton ionisation. In this regime an electron is excited from its bound state into the free continuum by simultaneously absorbing several low frequency photons or a single high frequency photon. When the laser wavelength is longer and has higher intensity, $\gamma < 1$, the laser field is strong enough to distort the Coulomb field which holds the electrons in their orbit and the target is ionised by tunnelling/barrier suppression ionisation [22, 23]. Tunnelling ionisation is the dominant ionisation mechanism in intense laser interactions with solids, where the intensities are $\geq 10^{14}$ Wcm$^{-2}$.

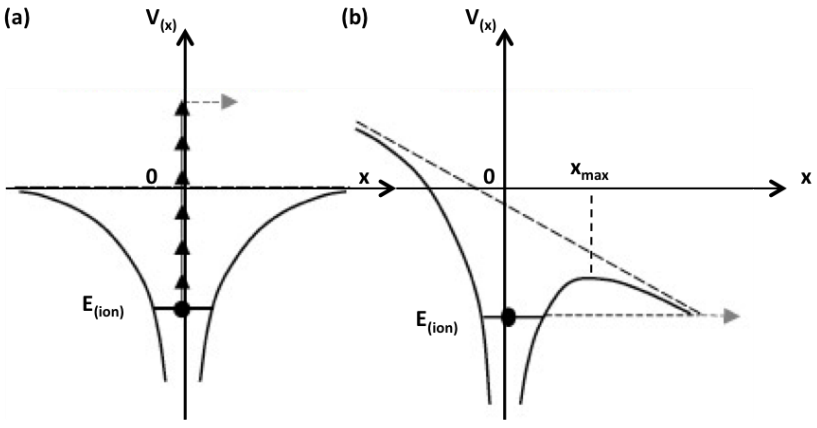


Fig. 2.1 **(a)** Schematic of multiphoton ionisation, **(b)** schematic of tunnelling ionisation. In multiphoton ionisation the electron escapes into the free continuum, in tunnelling ionisation the electron tunnels through the potential barrier.

Once this ionisation of the target surface has occurred, a plasma with ionisation state $Z^*$ and electron density $n_e = Z^* n_i$ will be formed on the front surface of the target, which starts to expand with the ion sound velocity:

$$c_s = \left( \frac{Z^* k_B T_E}{m_i} \right)^{1/2} \tag{2.4}$$

where $k_B$ is the Boltzmann constant, $T_e$ is the electron temperature and $m_i$ is the ion mass [23]. As the plasma expands, it creates large density and temperature gradients. Assuming that this expansion is isothermal (when the isothermal equation of state $p_e = n_e T_e$ is satisfied [24]), the electron density variation in the direction of the expansion can be approximated by an exponential decay:

$$n_e(x) = n_0 \exp\left( -\frac{x}{c_s t} \right) \tag{2.5}$$

where $n_0$ is the initial electron density in the target and $x$ is the distance the plasma has expanded [24]. This produces a well defined scale length of $L = c_s \tau_L$ during a laser pulse of length $\tau_L$ [25, 26].

The propagation of laser radiation at a frequency of $\omega_L$ through a cold collision-less plasma is described by the dispersion relation:

$$\omega_L^2 = \omega_p^2 + c^2 k^2 \tag{2.6}$$

where

$$\omega_p = \sqrt{\frac{n_0 e^2}{\varepsilon_0 m_e}} \tag{2.7}$$

is the plasma frequency and $k$ is the wave number. From the dispersion relation, as the laser frequency approaches the plasma frequency the wave number approaches zero, thus the laser can only propagate up to a critical density defined by the condition $\omega_p = \omega_L$. When the wave number is equal to zero, the plasma appears opaque to the laser and it is reflected.

This critical density is equal to:

$$n_c = \frac{\varepsilon_0 m_e}{e^2}\omega_L^2 \simeq \frac{1.1\times 10^{21}}{\lambda_{L\mu}^2}\ \mathrm{cm}^{-3} \tag{2.8}$$

where $\lambda_{L\mu}$ is the laser wavelength in microns. This critical density is used to classify the plasma as either over-dense $n_e > n_c$ or under-dense, $n_e < n_c$, which supports the propagation of the laser through the plasma [26].

When chirped pulse amplification is used to produce an intense laser pulse, the main pulse is usually preceded by a pedestral or pre-pulse which in general is intense enough to ionise the target surface before the arrival of the main pulse. This means the main pulse interacts predominantly with the preformed plasma rather than the target surface, and the laser energy is transferred to the electrons in the pre-plasma. It is thus important to discuss the motion of these electrons in high intensity laser fields.

## 2.2 Electron Motion and the Ponderomotive Force

### 2.2.1 Electron Motion

The equation of motion for an electron in the electric (**E**) and magnetic (**B**) fields of an electromagnetic wave is given by the Lorentz equation:

$$\frac{d\mathbf{p}}{dt} = -e\left(\mathbf{E} + \frac{\mathbf{v}\times\mathbf{B}}{c}\right) \tag{2.9}$$

together with an energy equation:

$$\frac{d}{dt}\left(\gamma m_e c^2\right) = -e\left(\mathbf{v}\,.\,\mathbf{E}\right) \tag{2.10}$$

where $\mathbf{v}$, $m_e$ and $\mathbf{p} = \gamma m\mathbf{v}$ are the electron velocity, mass and momentum, and $\gamma = (1 + \mathbf{p}^2/m_e^2c^2)^{1/2}$ is the relativistic factor. In the non-relativistic case where $\mathbf{v} \ll c$, the magnetic term in the equation becomes negligible and the electron will oscillate in the direction of the laser polarisation. The velocity of this oscillation can be derived as:

$$v_{osc} = \frac{-eE_L}{m_e\omega_L} \quad (2.11)$$

where $E_L$ and $\omega_L$ are the electric field and frequency of the laser. This allows the definition of the dimensionless laser amplitude $a_0$ as follows:

$$a_0 = \frac{v_{osc}}{c} = \frac{-eE_L}{m_e\omega_L c} \quad (2.12)$$

which can be used to distinguish if the interaction is in the relativistic or non-relativistic regime [27]. If $a_0 < 1$ the motion of the electron is non-relativistic, however if the laser field strength is such that $a_0 \geq 1$ the relativistic effect becomes important as the electrons are now oscillating at velocities comparable to the speed of light. This occurs when $\lambda \sim 1\mu$m and $I \sim 10^{18}$ Wcm$^{-2}$.

If the laser is linearly polarised, the time averaged relativistic factor can be obtained as:

$$\gamma = \sqrt{1 + \frac{a_0^2}{2}} \quad (2.13)$$

### 2.2.2 The Ponderomotive Force

The ponderomotive force is a pressure exerted on the plasma by the electromagnetic field of the laser, which arises because of the spatial variations in the intensity of the wave [28]. The electric and magnetic fields of the laser which act on the electrons contained in the plasma are oscillatory, but can still exert a time-averaged force on the electrons if the wave amplitude varies in space. If $a_0 \ll 1$, the motion of the electrons is purely an oscillation

along $E$, but if the amplitude of the field is spatially dependent and the electron reaches a region where the amplitude is smaller within a half cycle of the laser, the second half of the cycle will have a smaller amplitude and the electron will not return to its original position. The overall consequence is that the electrons will drift towards regions of the field which are less intense [24, 28], i.e. away from the center of a focused laser beam [23].

For the non-relativistic case, the time-averaged ponderomotive force can be calculated as follows using a perturbation method. If the electrons respond to a field of the form:

$$E = \mathbf{E_0}(\mathbf{r})\cos(\omega t) \tag{2.14}$$

This electric field slowly changes in space and time. The equation of motion (equation 2.9) becomes:

$$\frac{\partial \mathbf{v_1}}{\partial t} = -\frac{e}{m}\mathbf{E_0}(\mathbf{r_0})\cos(\omega t) \tag{2.15}$$

neglecting the $\mathbf{v} \times \mathbf{B}$ term in the first order, and $\mathbf{v}$ and $\mathbf{r}$ are:

$$\mathbf{v_1} = -\frac{e}{m\omega}\mathbf{E_0}(\mathbf{r_0})\sin\omega t \tag{2.16}$$

$$\mathbf{r_1} = \frac{e}{m\omega^2}\mathbf{E_0}(\mathbf{r_0})\cos\omega t \tag{2.17}$$

where $\mathbf{E}$ has been evaluated at the initial position $\mathbf{r_0}$. The $\mathbf{v_1} \times \mathbf{B_1}$ term has to be considered when going to the second order. $\mathbf{B_1}$ is given by Maxwell's equation:

$$\nabla \times \mathbf{E_0} = -\frac{\partial \mathbf{B}}{\partial t} \tag{2.18}$$

$$\mathbf{B_1} = -\frac{1}{\omega}\nabla \times \mathbf{E_0} \mid_{\mathbf{r}=\mathbf{r_0}} \sin\omega t \tag{2.19}$$

Expanding **E(r)** about $\mathbf{r_0}$ gives:

$$\mathbf{E(r)} = \mathbf{E(r_0)} + (\mathbf{r_1} \cdot \nabla)\mathbf{E}\,|_{\mathbf{r=r_0}} + ... \tag{2.20}$$

Using equations 2.14, 2.16, 2.17, 2.19 and 2.20, the second order equation of motion for the electron becomes:

$$\frac{\partial \mathbf{v_2}}{\partial t} = -\frac{e}{m}\left(\mathbf{E_0}\cos\omega t + \left[\frac{e}{m}\frac{\mathbf{E_0}}{\omega}\cos^2\omega t \cdot \nabla\right]\mathbf{E_0} + \frac{e}{m\omega^2}\sin^2\omega t\,[\mathbf{E_0} \times (\nabla \times \mathbf{E_0})]\right) \tag{2.21}$$

Taking the cycle average of this expression yields the following expression, as the $\cos\omega t$ goes to zero and $\langle\sin^2\omega t\rangle = \langle\cos^2\omega t\rangle = 1/2$:

$$\langle\frac{\partial \mathbf{v_2}}{\partial t}\rangle = -\frac{e^2}{2m^2\omega^2}\,[(\mathbf{E_0} \cdot \nabla)\mathbf{E_0} + \mathbf{E_0} \times (\nabla \times \mathbf{E_0})] \tag{2.22}$$

Using the triple vector product, this can be re-written as:

$$\langle\frac{\partial \mathbf{v_2}}{\partial t}\rangle = -\frac{e^2}{2m^2\omega^2}\nabla\langle\mathbf{E}^2\rangle \tag{2.23}$$

where $\mathbf{E_0^2} = 2\langle\mathbf{E}^2\rangle$. Multiplying by $m$ yields the ponderomotive force on the electron:

$$\mathbf{F_p} = -\frac{e^2}{4m\omega^2}\nabla\langle\mathbf{E_0^2}\rangle = -\frac{e^2}{8\pi\varepsilon_0 mc^3}\nabla\langle\mathbf{E_0^2}\rangle \tag{2.24}$$

In the relativistic case, the ponderomotive force is derived from the force equation:

$$\frac{\partial \mathbf{p}}{\partial t} + \mathbf{v} \cdot \nabla\mathbf{p} = -e\left(\mathbf{E} + \frac{\mathbf{v} \times \mathbf{B}}{c}\right) = \frac{e}{c}\frac{\partial \mathbf{A}}{\partial t} - \frac{e}{c}\mathbf{v} \times \nabla \times \mathbf{A} \tag{2.25}$$

where **A** is the vector potential. In an oscillating, quasimonochromatic electromagnetic field described by a dimensionless vector potential a(r,t) whose envelope is sufficiently smooth

in space and time, the relativistic ponderomotive force is:

$$\mathbf{F_{pr}} = -mc^2\nabla\left(1+<\mathbf{a}>^2\right)^{1/2} \tag{2.26}$$

where $\mathbf{a} = e\mathbf{A}/mc^2$.

In a typical laser pulse, the intensity profile in non-uniform such that $\mathbf{F_p} \neq 0$ and the electrons will be accelerated away from the laser axis creating a space charge field. Because of this charge separation between the electrons and the ions, a mechanical equilibrium between the electrostatic and ponderomotive forces on the electron will be established, and the whole material will experience a ponderomotive pressure, which will accelerate the ions [26].

## 2.3 Absorption Mechanisms

Laser energy can be transferred to solid targets by a variety of different mechanisms which depend on both the target parameters, such as shape, material and temperature, and laser parameters, such as wavelength, intensity and pulse duration. A selection of these mechanism will be briefly described in the following Sections.

### 2.3.1 Inverse Bremsstrahlung

Inverse Bremsstrahlung is a collisional absorption mechanism which transfers energy from the laser to the under-dense region of the plasma via electron-ion collisions. This absorption mechanism dominates at laser intensities of $10^{12}$ - $10^{14}$ Wcm$^{-2}$.

The electrons first gain energy by oscillating in the electric field of the laser, then lose part of this energy via the collisions with the ions. As a result of these interactions, the laser energy is damped and the plasma is heated. This requires the addition of a collisional

damping term to the equation of motion:

$$m\frac{\partial \mathbf{v}}{\partial t} = -e\left(E + \frac{\mathbf{v}\times\mathbf{B}}{c}\right) - mv_{ei}\mathbf{v} \tag{2.27}$$

where $v_{ei}$ is the electron-ion collision frequency given by [23]:

$$v_{ei} = \frac{4(2\pi)^{1/2}}{3}\frac{n_e Z e^4}{m^2 v_{te}^3}\ln\Lambda \tag{2.28}$$

$$\simeq 2.91\times10^{-6} Z n_e T_e^{-3/2}\ln\Lambda\ \mathrm{s}^{-1} \tag{2.29}$$

where $Z$ is the ionisation state, $n_e$ is the electron density in $\mathrm{cm}^{-3}$, $T_e$ is the electron temperature in eV and $\Lambda$ is the plasma parameter.

Assuming the electrons have a Maxwellian distribution and approximately linear scaling, the fraction of energy absorbed by this mechanism is given by [24, 29]:

$$f_{ib} = 1 - \exp\left(-\frac{32 v_{ei}^* L_n}{15c}\right) \tag{2.30}$$

where $v_{ei}^*$ is the collision frequency at critical density, as given by Equation 2.29, and $L_n$ is the scale length of the plasma.

Longer pulses (ns) produce longer scale lengths and thus lower electron temperatures [23]. The temperature of the distribution can be estimated from classical heat transport models and is given by:

$$T_e\ (\mathrm{eV}) = 119\left(\frac{n_e}{10^{23}\ \mathrm{cm}^{-3}}\right)^{1/12} Z^{1/12} I_{15}^{1/3}\tau^{1/6} \tag{2.31}$$

where the intensity is expressed as $I_N = I(\mathrm{Wcm}^{-2})/10^N$ and $\tau$ is the pulse length in units of 100 fs. Equation 2.31 shows that the temperature will increase with the intensity, therefore at intensities of approximately $10^{15}\ \mathrm{Wcm}^{-2}$ the electron-ion collisions become ineffec-

tive as the effective collision frequency becomes negligible [26]. The electron distribution can no longer be assumed to be Maxwellian at these intensities and the precise electron-ion frequency should be calculated from kinetic equations such as the Vlasov–Fokker–Planck equation [29]. Other collision-less absorption mechanisms start to play their role at these intensities.

### 2.3.2 Resonance Absorption

Laser light can excite resonant plasma oscillations at the critical density surface when obliquely incident on the plasma density gradient. An incident light wave at angle $\theta$ will be refracted by the density gradient and reflected at a density lower than the critcal density, with the turning point occurring at $n_e(\theta) = n_c \cos^2\theta$ [24, 28]. If the laser is p-polarised, a component of the electric vector oscillates electrons along the direction of the density gradient ($E$ is parallel to $\nabla n$), generating fluctuations in the charge density which can be resonantly enhanced by the plasma. The light wave will tunnel through to the critical surface of the target, where it transfers some of its energy to an electrostatic oscillation, or plasma wave at frequency $\omega = \omega_p$, in a phenomenon termed resonance absorption [30]. This wave will eventually be damped either by collisions at low intensities or by particle trapping and wave breaking at high intensities [23]. If the laser is s-polarised, there is no component of $E$ along $\nabla n$ so no plasma wave can be driven.

Even though the light wave itself reflects at a density lower then the critical density, the fields tunnel to the critical density region to excite the resonance. The amount of energy transferred to the plasma wave depends on the amplitude of the field that can tunnel from the turning point to the critical surface and drive the plasma wave. The field driving the resonance, $E_d$, is the component of the electric field of the light wave which oscillates the

electrons along the density gradient [28]. This field is equal to:

$$E_d = \frac{E_{FS}}{\sqrt{2\pi\omega L/c}}\phi(\tau) \tag{2.32}$$

where $E_{FS}$ is the value of the electric field of the light wave in free space, $\tau$ is a parameter which relates the scale length $L$ and the angle of incidence $\theta$, equal to $(\omega L/c)^{1/3}\sin\theta$, and the Denisov function $\phi(\tau) \simeq 2.3\tau\exp(-2\tau^3/3)$ describes the angular dependence of the driving field as a function of $\tau$ [23]. Since the component of the electric field along the density gradient varies as $\sin\theta$, the driving field will vanish as $\tau \to 0$. The driving field becomes very small for large angles of incidence as the distance between the critical surface and reflection surface is too large to tunnel. If $\theta$ is too small, the component of the electric field along the gradient will also be small and the electron oscillations will not be driven effectively [24, 28].

By integrating the energy lost by the light wave over the density profile, the absorption fraction is found to be [28]:

$$f_{ra} \approx \frac{\phi(\tau)^2}{2} \tag{2.33}$$

Resonance absorption is therefore most efficient at the angle of incidence which maximises the Denisov function [28]:

$$\sin\theta_{opt} \approx 0.8\left(\frac{c}{\omega L}\right)^{1/3} \tag{2.34}$$

At higher laser intensities, the angular dependence of of the absorption may be altered by the ponderomotive steepening of the density profile near the critical density. If the density profile is steeper the distance the field is required to tunnel to reach the critical surface is shortened and the resonance absorption is less sensitive to $\theta$. Effects such as rippling of the critical surface can enhance the amount of resonance absorption, by providing additional regions of the plasma where $\mathbf{E}\cdot\nabla n \neq 0$, which can lead to resonance absorption for s-

polarised light as well as p-polarised light [28].

### 2.3.3 Vacuum Heating - Brunel Absorption

In resonance absorption, a smooth density profile allows coupling between the incident laser pulse and the plasma wave, but when the density gradient of the plasma is very steep, resonance absorption ceases to work as these plasma waves cannot be initiated. This is because the field amplitude $E_p$ of the plasma wave at critical density is enhanced very little and is roughly equal to the incident laser field $E_L$. Therefore the electrons will oscillate along the density gradient with an amplitude of $x_p \simeq \varepsilon E_L/m_e\omega^2 = v_{osc}/\omega$, thus the resonance breaks down when $x_p$ exceeds the density scale length $L$ [23]. The collisional absorption process of vacuum heating comes into play at short scale lengths and moderate intensities [31].

The electrons near the edge of the abrupt plasma-vacuum interface are now directly exposed to the laser field. Thus at high enough intensities, thermal electrons will be dragged out of the target surface into the vacuum by the electric field, and accelerated back into the plasma when the field changes sign [32, 33]. As the plasma is highly over-dense, the electric field will only penetrate to a skin depth of approximately $c/\omega_p$ allowing the electron to travel unhindered into the target where it will be absorbed by collisions. Instead of the energy imparted to the electrons being transferred to the plasma wave, it is now directly imparted to the target [34].

This mechanism was first modelled by Brunel using a capacitor approximation, in which the magnetic field of the wave is ignored and the laser electric field $E_L$ has a component $E_d$ normal to the target surface which pulls the electrons back and forth across their equilibrium positions [23], thus the laser must again be p-polarised as in resonance absorption. Initially the target has a smooth mirror-like surface on which the laser light wave is incident at an angle $\theta$, producing a standing wave with a driving electric field. This driving field will pull

a layer of electrons out of the target, creating an electric field between the target and the position of this electron layer, which can be equated to the driving field. On returning to its original position, this electron layer will acquire a velocity of $v_d \simeq 2v_{osc}\sin\theta$, where $v_{osc}$ is the electron quiver velocity. The reflectivity of the surface will not be perfect, therefore the driving field will have amplitude:

$$E_d = [(1-\eta_a)^{1/2}]E_L\sin\theta \tag{2.35}$$

and the return velocities may become relativistic, thus the fractional absorption rate is given by:

$$\eta_B = \frac{1}{\pi a_0}\left[(1+f^2a_0^2\sin^2\theta - 1\right]\frac{\sin\theta}{\cos\theta} \tag{2.36}$$

where $f = 1+(1-\eta_a)^{1/2}$ is the field amplification factor and $a_0 = v_{osc}/c$ [23, 29].

For short scale lengths and high intensities, this type of absorption saturates at around 10 - 15%, but for moderate intensities, around those at which resonance absorption also occurs, the absorption can be as high as 70% [23].

### 2.3.4 j X B Heating

J x B heating is the absorption mechanism that dominates in the relativistic regime at intensities $\geq 10^{18}$ Wcm$^{-2}$. At these intensities the contribution of the Lorentz force becomes important and $v_{osc}$ will have a component along the $k$-vector of the radiation. As with the Brunel mechanism, the electrons are directly accelerated by the laser field incident on a step-like density profile, however the driving term is now the high frequency $\mathbf{v}\times\mathbf{B}$ component of the Lorentz force rather than the electric field. This component of the Lorentz force oscillates at twice the laser frequency [23, 28].

A linearly polarised light wave $E = E_0(x)\hat{y}\sin\omega t$ gives rise to a longitudinal force term:

$$f_x = -\frac{m}{4}\frac{\partial v_{osc}^2(x)}{\partial x}(1-\cos 2\omega t) \tag{2.37}$$

the first term is the usual ponderomotive force which pushes the electron density profile inwards, the second term is the high-frequency oscillating component which leads to heating of the electrons owing to the magnetic field of the laser and the transverse quivering of the electrons in the laser electric field [26]. This $\mathbf{j}\times\mathbf{B}$ term works for both s- and p- polarisations and is most efficient for normal incidence, as the laser electric field vector is perpendicular to the plasma density gradient and the electrons gain most of their energy by being accelerated across this gradient in the laser propagation direction [26]. This term does not work for circular polaristation at normal incidence as the oscillating term vanishes. $\mathbf{j}\times\mathbf{B}$ heating becomes significant with sufficiently high intensities at oblique incidence, even in addition to resonance absorption. Vacuum heating is however more important than $\mathbf{j}\times\mathbf{B}$ heating when the driving field is greater than the magnitude of the $\mathbf{j}\times\mathbf{B}$ field (when $\sin\theta > v_{osc}\omega_0/c\omega_{pe}$) [28].

### 2.3.5 Hot Electron Transport

In intense laser-plasma interactions large numbers of hot electrons are generated which are crucial for laser-driven ion acceleration. This results in a large electron current trying to propagate through the target and the plasma. There is however a limit, known as the Alfvén limit, on the maximum current which can propagate through a plasma without generating a return current, which for the relativistic case is [35]:

$$J_A = \beta\gamma\frac{mc^3}{e} \simeq 17\beta\gamma\,\mathrm{kA} \tag{2.38}$$

where $\beta = v/c$ and $(\gamma - 1)mc^2$ is the kinetic energy of the electron [23]. This limit is exceeded in typical laser interactions, and the current of fast electrons flowing into the target will rapidly heat and ionise the target creating a plasma [36]. For this fast electron current, $j_f$, to be able to propagate, local charge neutrality needs to exist in the form of a return current, $j_r$, which is both spatially coincident with the fast electron current density and nearly cancels the fast electron current to a good approximation [37], thus:

$$j_f + j_r \approx 0 \tag{2.39}$$

where $j_f \approx -en_h v_h$ and $j_r \approx -en_c v_c$ are the charge densities for the hot electrons and return current respectively, and $n_{h,c}$ and $v_{h,c}$ are the respective electron densities and velocities of the hot and cold electrons. In a hot plasma equation 2.39 is easily satisfied, since it acts like a superconductor with almost zero resistivity. In a cold solid, or cold solid density plasma, $j_r$ is very much less than $j_f$ in general owing to the finite resistivity of the material. This rapidly induces an electric field which effectively inhibits the penetration of any further hot electrons. Instead of the hot electrons freely streaming into the target, there is an electrostatic equilibrium in which the electrons are reflected back from the solid region of the target out towards the surface by the potential barrier associated with the field [23].

The return current produced may not entirely balance the hot electron current, inducing a magnetic field which will also inhibit the penetration of the hot electrons into the target. This field can be estimated by [23]:

$$B_{max} \simeq \left(\frac{\sigma_e}{10^6 \Omega^{-1} m^{-1}}\right)^{-1} \frac{\tau_L}{ps} \left(\frac{\sigma_L}{10 \mu m}\right)^{-1} \eta_a I_{17}^{2/3} \lambda_{\mu m}^{-2/3} \cdot 4 \text{ MG} \tag{2.40}$$

where $\tau_L$ is the pulse duration, $I_{17}$ is the intensity of the laser in units of $10^{17}$ Wcm$^{-2}$, $\sigma_e$ is the conductivity of the target, $\eta_a$ is the resistivity and $\lambda_L$ is the wavelength of the laser in microns [26].

In thin foil interactions, a fraction of the most energetic hot electrons will escape from the target and establish a quasi-electrostatic sheath field in the order of $10^{12}$ $\mathrm{Vm}^{-1}$ on the rear surface of the target. This field is responsible for ion acceleration in the Target Normal Sheath Acceleration mechanism which will be described in Section 2.4.1. This field is strong enough to re-inject the majority of the escaped electrons back into the target, where they travel back to the front surface where a similar sheath potential has formed. This field will then reflect the returning electrons in a process known as electron reflux or electron recirculation [38]. This occurs several times, resulting in an increase in the electron density at the rear surface of the target, as the recirculated electrons combine with the electrons reaching the target rear surface for the first time. The effect of this process increases with decreasing target thickness, thus the efficiency of the ion acceleration is also increased.

## 2.4 Laser-Driven Ion Acceleration

An important factor which influences the beams produced by laser-foil interactions is the particle acceleration mechanism at work.

### 2.4.1 Target Normal Sheath Acceleration

When a laser interacts with a thin foil, proton and ion beams will form from the layer of hydrocarbon contaminants on the target. As hydrogen atoms have a low ionisation potential and high charge to mass ratio [39], they tend to ionise first and the protons will react more quickly to the accelerating fields than the other ion species as they also have a high charge to mass ratio [40]. The protons undergo the strongest acceleration, travelling ahead of the other species, thus shielding them from the space charge field [41]. Heavier ions will not be accelerated to as high energies as the protons, as the protons deplete most of the energy provided by the accelerating mechanism. However, if the layer of hydrocarbon

contaminants on the target is removed, the signal from the protons will be suppressed and ions from the target constituents will be accelerated to higher energies. Although ions are accelerated from both the rear and front surfaces of the target, the sharp density interface at the rear causes the acceleration to be much stronger at this surface than at the front [42]. The photon pressure of the laser accelerates the electrons into the target. The electrons ionise the molecules on the back of the target, resulting in the most energetic ions emerging from the rear surface. As the cloud of electrons is emitted from the back surface they produce an electrostatic field which accelerates the protons and the ions [5]. The electrostatic field produced is typically $10^{12}$ - $10^{13}$ $\mathrm{Vm}^{-1}$ [41, 43] and accelerates the ions perpendicular to the rear surface of the target in the direction of the laser beam [42].

Typically the front surface of the target foil irradiated by the laser will become ionised ahead of the peak of the irradiating pulse. During the interaction of a high energy laser pulse (up to $10^{21}$ $\mathrm{Wcm}^{-2}$ in the laser focus, achieved by chirped pulse amplification [44], although $\sim 10^{19}$ $\mathrm{Wcm}^{-2}$ is more routinely realised [43]) with a solid target, the prepulse is sufficiently intense to transform the matter into the plasma state, thus the main pulse will interact with a highly ionised hot plasma [40].

During the high-intensity laser-plasma interaction which takes place at the peak of the pulse, the electrons will be accelerated forward into the target, owing to a number of mechanisms depending on the conditions of the target and the interaction. The typical energies of the fast electrons accelerated at the front of the target are such that their mean free path is much larger than the thickness of the targets used in this type of experiment, thus allowing the electrons to freely propagate to the rear of the target [4]. The atoms are ionised and the ions are rapidly accelerated normal to the initially unperturbed surface, as the electrostatically confined electrons on the rear surface set up a charge separation field over a Debye length $\lambda_D$ inducing strong electric fields. The accelerated ions form a dense bunch of short duration that is charge neutralised by co-moving electrons. The space-charge field produced

by the electrons is given by [39]:

$$E \approx \left( \frac{k_B T_e}{e \lambda_D} \right) \tag{2.41}$$

where

$$\lambda_D = \left( \frac{\varepsilon_0 k_B T_e}{e^2 n_e} \right)^{1/2} \tag{2.42}$$

As the rear of the target is initially a cold surface and the duration of the acceleration is extremely short, there are excellent emission properties [4].

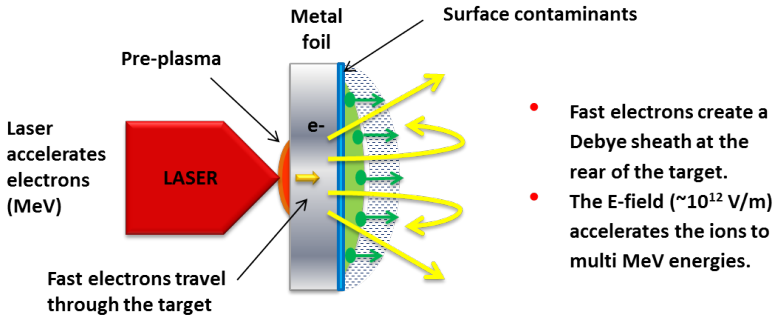


Fig. 2.2 Target Normal Sheath Acceleration reproduced from [45].

After this initial phase the ions stream into the vacuum, preceded by a Debye sheath of hot electrons. This form of acceleration is normally referred to as Target Normal Sheath Acceleration, or TNSA, and is shown in Figure 2.2.

The scaling of the maximum proton energy, $E_{proton}$, achievable with peak laser intensity, $I_0$, within the TNSA regime is;

$$E_{proton} \propto I_0^{1/2} \tag{2.43}$$

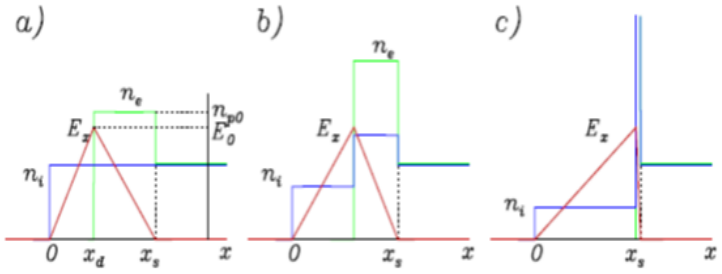


Fig. 2.3 Model profiles of the ion density $n_i$ (blue), electron density $n_e$ (green) and electrostatic field $E_x$ (red) at three different stages of RPA [27].

Unfortunately, TNSA beams are characterised by large divergence, low particle density and almost 100% energy spread which poses significant limitations for many of the envisaged applications [46, 47].

### 2.4.2 Radiation Pressure Acceleration

By contrast, ion production by the radiation pressure of intense lasers has been predicted to be a more promising route for accelerating large numbers of ions quasi-monoenergetically to the range of GeV's per nucleon in a more efficient manner than TNSA [43].

In the Radiation Pressure Acceleration (RPA) regime a superior scaling in terms of laser-ion conversion efficiency and ion energy is predicted, with similarly efficient acceleration for both protons and ions of higher mass.

In RPA the ions are accelerated by directional momentum transfer from the laser to the target via the ponderomotive force of the laser. In a plasma the electrons feel the effect of the ponderomotive force, which is then transferred to the ions via a space-charge field. The ponderomotive force acts as a snowplough on the front surface of the target and a dense ion bunch is launched into the target. Experimental evidence for RPA is scarce (some results are discussed in Section 2.5) as TNSA dominates for typical interaction conditions, but there are two known regimes; hole-boring and light-sail.

### Hole-Boring

In the hole-boring mechanism the radiation pressure instantly pushes the electrons in the skin depth and sets up a strong accelerating field for the ions to promptly follow the electrons, allowing the laser to bore through the target [47]. The hole-boring velocity is dependent on the laser intensity and the mass density of the target [47, 48]. A very high intensity laser is required to achieve high energy ion beams as the ion velocity does not increase with time after hole-boring has saturated. The maximum energy of the ions scales linearly with the intensity of the laser.

If the laser and target parameters do not vary considerably over an acceleration cycle, all ions will be accelerated up to a maximum energy and the hole-boring process, although of non-stationary nature, may be described on the average by a quasi-stationary model. The situation changes when a target is thin enough that all the ions are accelerated before the end of the laser pulse and a complete hole-boring cannot occur [49].

### Light-Sail

The term "light-sail" is appropriate to refer to a thin object of finite inertia, having low mass and large surface so that it can receive a significant boost from radiation pressure. If a target is thin enough, the hole-boring phase will cease well before the end of the laser pulse. If the target thickness is less than the product of the hole-boring velocity and the laser pulse duration, the ions will pile up at the rear surface of the target before the end of the laser pulse. As the thickness of the compressed layer becomes comparable to or less than the evanescence length of the ponderomotive force, the whole layer is cyclically accelerated [47] with high efficiency for the rest of the duration of the laser pulse, as shown in Figure 2.4.

The LS regime can be simplistically modelled as totally reflecting, perfectly rigid plane mirror boosted by a light wave which is perpendicular to its surface. As the laser follows the

ion bunch, the acceleration stage will be repeated. This model predicts that the efficiency $\eta$ of the acceleration regime , defined as the ratio between the mechanical energy of the mirror over the electromagnetic energy of the light wave pulse given by:

$$\eta = \frac{2\beta}{1+\beta} \tag{2.44}$$

where $\beta = V/c$ and $V$ is the mirror velocity, hence RPA becomes more and more efficient ($\eta$ -> 1) as $\beta$ -> 1 [50]. The assumption of the LS model that the target is a perfect mirror implies that all the ions will be accelerated to the same velocity producing a perfectly monoenergetic spectrum. This is not the case as in reality only a thin layer of the rear side of the foil is accelerated by RPA. The electrostatic pressure pushing the ions in the accelerated layer is modelled such that the equation of motion for the thin layer is the same as if the entire foil were accelerated, thus maintaining a mechanical quasi-equilibrium of the electrons. This simplistic view therefore can predict the energy of the accelerated ions, but will over estimate the fraction of the laser pulse energy transferred to the quasi-monoenergetic ions (the conversion efficiency).

As the ions become relativistic, the energy momentum transfer is very efficient. The scaling of the ion bunch energy, $E_{bunch}$, with dimensionless laser amplitude, $a_0$, pulse duration, $\tau_p$, and areal density, $\chi$, within the light-sail regime is [46];

$$E_{bunch} \propto \left(\frac{a_0^2 \tau_p}{\chi}\right)^{\alpha} \tag{2.45}$$

where $\alpha = 2$ for the non-relativistic case, and $\alpha = 1$ for the ultra-relativistic case. A full description of the parameters $a_0$, $\tau_p$ and $\chi$ will be given in Section 3.3.4. Another consideration for the ultrarelativistic case, is the impact on the surface's reflective quality. As the threshold for critical density increases it causes the laser to propagate further into the target with increasing momentum, thus decreasing the reflectivity non-linearly [51]. The laser's

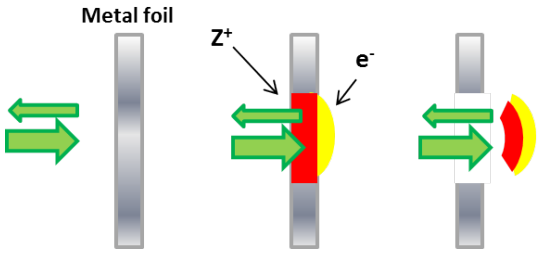


Fig. 2.4 Light-Sail Acceleration.

amplitude will also have a limit above which there will be the inception of relativistic transparency. If this limit is breached the energy attainable via RPA will be limited, with the onset of relativistically transparent effects.

Higher energies are expected from this light-sail regime as the ions are no longer screened by the background plasma. The light-sail regime is particularly promising for producing higher energy beams suitable for oncology, as they possess narrow energy spectra, reduced divergence, similarly efficient acceleration for both protons and higher mass ions, and there is a favourable dependence on fluence in the scaling of the ion energy. Although they are currently barely competitive in terms of average flux, the density of such laser accelerated ion bunches can reach almost solid density, exceeding conventional sources by many orders of magnitude [43].

## 2.5 Research

Research in the area of laser-driven ion sources has grown at a phenomenal rate, with most of the present research being motivated by the exceptional spatial and temporal qualities of the beams, the high energy and high particle numbers achievable and the application of these properties to Plasma Physics, Medicine, Technology and many other interdisciplinary areas. Research groups worldwide are striving to optimize the control of the acceleration mechanism and the beam properties [52].

There are a wide range of proposed potential applications including tumour therapy, ultra-fast radiography, isotope production and fast ignition inertial confinement fusion, which rely on a monoenergetic high-energy, large particle number ion beam with a small angular divergence. Along with TNSA, RPA using circularly polarised lasers has been regarded as the most promising and efficient route to achieving these desirable ion beams. The majority of studies have been focused on proton and light ion beams, while using RPA to produce heavy ion beams has been largely unexplored [44, 53–55]. Heavy ion beams have a much broader appeal for medical, material, nuclear fission/fusion, quantum electrodynamics and high energy density plasma applications.

Proton energies up to 85 MeV [9] and heavier ions with up to 7 MeV per nucleon have been have been measured [39]. These proton beams have a number of unique properties such as high brightness and ultra-low emittance, and a possible application of these laser-based ion beams is the production of medical isotopes for positron emission tomography (PET). To produce these intense radioisotope sources a large number of protons at $\sim$ 10 MeV is required. Normally > $10^9$ Bq of $C^{11}$ or $F^{18}$ are commonly used per patient dose [2]. Up to $10^7$ Bq of $C^{11}$ and $10^5$ Bq of $F^{18}$ produced by laser accelerated protons were measured by Ledingham *et al.* [56]. Further investigation is required to determine if this is a feasible option of high-power lasers as drivers of proton acceleration for PET isotope production.

Several experimental investigations have been carried out to investigate the maximum achievable proton energy as a function of laser parameters. Fuchs *et al.* investigated laser-driven proton production and scaling employing aluminium targets, laser pulse durations of 0.15 - 10 ps and laser intensities from $10^{18}$ to 6 x $10^{19}$ $Wcm^{-2}$ [57]. They measured the proton beam maximum energy and energy conversion efficiency as a function of varying laser and target parameters. The scaling laws achieved were favourably compared with predictions from a simple fluid based model of proton acceleration and supported by 2D

PIC simulations, with the fluid model emerging as a helpful predictive tool for high-energy and high-quality proton beams [57]. This model, Mora's plasma-explosion model, was used to predict that a proton energy of 200 MeV could be achieved with a ps laser pulse at an intensity of about 5 x $10^{20}$ $\mathrm{Wcm}^{-2}$.

Robson *et al.* extended the experimental energy and intensity range over which proton scaling is parametrically investigated up to 400 J and 6 x 10 $^{20}$ $\mathrm{Wcm}^{-2}$ [2]. They found their results for the higher energy and intensity regimes and pulse durations of up to 10 ps were not consistent with previous predictions, with the increase in maximum proton energy being much slower than previously thought. They compared their results to the same model as Fuchs, and introduced a revised form of the model, which involved two phases of electron temperature, and mimicked three-dimensional effects, and found their experimental results were in much better agreement with this revised model. At the lower end of the intensity range investigated by Robson, the measurements were in good agreement with the results reported by Fuchs, with a maximum proton energy of 20 MeV for a laser intensity of around 6 x 10 $^{19}$ to 8 x $10^{19}$ $\mathrm{Wcm}^{-2}$, however Robson found the scaling relations for proton energy and conversion efficiency reported by Fuchs to not be valid at the higher intensity regime [2].

The two main acceleration mechanisms identified as the promising routes to achieving high energy, high particle number ion beams are TNSA and RPA. Most experimental research to date has been focused on the TNSA mechanism, producing ion beams typically characterised by a broad energy spectrum, a modest conversion efficiency at high energies, a large divergence and scaling of maximum proton energy $E$ proportional to the peak laser intensity $I_0^{1/2}$. The RPA mechanism has since attracted a substantial amount of theoretical and experimental attention owing to the superior scaling of the peak ion energy and conversion efficiency predicted for this regime. The most promising sub regime of RPA is the LS regime as the beams produced by the scheme have natively narrow energy spectrum, low

divergence and a favourable dependence on fluence. This scheme also results in similarly efficient acceleration of both protons and higher mass ions. It is generally accepted that an effective implementation of the RPA scheme at relativistic irradiances is facilitated by the implementation of circularly polarised laser pulses, as this provides a constant poderomotive drive [58]. Conversely for linearly polarised lasers, the oscillating $\mathbf{j} \times \mathbf{B}$ term causes the re-circulation of the hot electrons, creating the large sheath field on the rear side of the target which accelerates the ions via TNSA, as the rapid decompression of the foil breaks the equilibrium conditions required for LS acceleration [58], thus experimental evidence of the of the LS regime is scarce as TNSA is the dominant mechanism of ion acceleration in typical interaction conditions.

Schreiber *et al.* [59] presented a general expression for the maximum ion energy observed in experiments with thin foils irradiated by high intensity laser pulses. Their analytical model was based on a radially confined surface charge set up by laser accelerated electrons on the rear side of the target. The only input parameters required for the model are the target thickness and the laser pulse properties. The model explains, and predicted, to good agreement the optimal laser pulse duration and maximum ion energies observed in a variety of existing experiments as well as dedicated studies where either the laser pulse duration or the charge-to-mass ratio of the ions was varied. They found that the highest intensity was not necessarily suitable for reaching maximum energies.

Esikepov *et al.* [60] identified a RPA dominated laser-piston regime at extremely high intensities of $> 10^{23}$ Wcm$^{-2}$. This regime produces a high density ultra-short relativistic ion beam from a thin foil by an ultra-intense EM wave, with the ion beam generation in this scheme being highly efficient and the ion energy per nucleon being proportional to the laser pulse energy. The results obtained conformed to the results of 3D PIC simulations and promote the advantage of using exawatt lasers. They distinguished two distinct stages in the laser-piston regime (i) a relativistically strong laser pulse with a significantly wide

waist to promote quasi-one-dimensional geometry irradiates a thin foil, quickly accelerating electrons via the transverse electric field pushing all the electrons forward creating a charge separation field between the electrons and ions, which accelerates the ions to relativistic energies, and (ii) the accelerated foil is regarded as a relativistic plasma mirror which co-propagates with the laser, perfectly reflecting the laser pulse, hence the plasma mirror acquires energy from the laser pulse and is accelerated by the radiation pressure. The radiation momentum is transferred to the ions through the charge separation field, providing them with a greater forward kinetic energy than the electrons [60]. The main principle of this method is that the ultra-strong radiation pressure produced is used to accelerate the ions to relativistic energies within a few cycles of the laser before the rear sheath field rapidly grows and decompresses the foil, allowing the ions and protons to catch the accelerated electrons in the accelerated plasma slab.

Zhuo *et al.* [61] also presented a dual-peaked electrostatic field acceleration using linearly polarised pulses for the production of quasi-monoenergetic ion beams, which in reality was qualitatively the same as the laser-piston regime, as they also employed a very high laser intensity of 5.5 x $10^{22}$ $\mathrm{Wcm}^{-2}$, with the proton energy reaching relativistic levels within 2 cycles of the laser. There is also a clear interest in the identification of regimes where the RPA mechanism can dominate the particle acceleration at intensities which are more easily obtainable with the currently available linearly polarised laser systems. Qiao *et al.* [58] identified a new RPA dominated regime where quasi-monoenergetic ion beams were generated by linearly polarised laser pulses at the more moderate intensities of $10^{20}$ - $10^{21}$ $\mathrm{Wcm}^{-2}$. With an appropriate coupling condition between the laser pulse duration, intensity and target foil thickness, the RPA mechanism can win the competition between the RPA and TNSA mechanisms in the hybrid acceleration stage. Qiao analytically derived and verified this coupling condition using 2D PIC simulations, showing 1.26 GeV quasi-monoenergetic $C^{6+}$ ion beams with an angular divergence of $< 5^{\circ}$ and an energy spread of $\sim 0.1$ GeV ob-

tained through irradiation of 80 nm ultra-thin foils with linearly polarised laser pulses at an intensity of $10^{21}$ Wcm$^{-2}$. The simulations also showed that a multi-species foil contributed to the stabilisation of the LS RPA component in the hybrid acceleration of lighter ions. This resulted in more pronounced spectral peaks, similar to those observed from 'pure' RPA using circularly polarised lasers.

Henig *et al.* [62] have also reported RPA effect associated spectral peaks. They preformed experimental studies using ultra-thin diamond like carbon foils irradiated with 0.7 J laser pulses of ultra-high contrast and peak intensities of 5 x $10^{19}$ Wcm$^{-2}$. These features were attributed to polarisation dependent modifications of the ion spectral profile at moderate ion energies, as a reduction in the electron heating was observed when the polarisation of the laser was switched from linear to circular, resulting in pronounced peaks in the $C^{6+}$ spectrum at an optimal target thickness of 5.3 nm. 2D PIC simulations revealed the $C^{6+}$ ions were dominantly accelerated in a phase-stable way by the laser radiation pressure for the first time [62].

Kar *et al.* also presented experimental evidence of narrow-band features in the ion spectra produced by thin foil irradiations with sub petawatt laser pulses. They presented carbon ion peaks centred at up to 7 MeV per nucleon for the first time, with a flux of nearly an order of magnitude higher than previously reported [62–64]. The scaling of the ion energy $E_{ion}$ was proportional to $(a_0^2\tau_p/\chi)^\alpha$ with $\alpha$ equal to 2 when the dimensionless fluence parameter $\varepsilon \ll 1$ and $\alpha$ equal to 1 when $\varepsilon \gg 1$ in the ultra relativistic case ($\tau_p = ct_p/\lambda$, $\chi = \rho' l/\lambda$ and $\rho' = \rho/m_p n_c$ ). The spectral features and their scaling with the target and laser parameters points to the multispecies scenario of LS acceleration. The possibility of achieving spectral peaks beyond 100 MeV per nucleon, a key requirement for hadron therapy, could become a reality by tuning currently achievable laser and target parameters as predicted by 2D PIC simulations [65].

Most current experiments rely on TNSA, which allows the production of very energetic

ion populations, although the exploration of other mechanisms has resulted from the characteristic drawbacks of TNSA beams such as the low conversion efficiency and the difficulty of obtaining a mono chromatic spectrum. This mechanism does however continue to play a fundamental role as a new generation of laser facilities come online. This will pave the way for exploring the TNSA mechanism with a new set of parameters so far unobtainable, and an extensive parametric investigation based on satisfactory theory will be required, together with detailed comparisons with experimental evidence [66], the main focus of which will be the maximum ion energy achievable. With the recent development of 100 TW Ti:sapphire, ultra-short pulse laser systems with pulse lenths around 30 fs, the hope will be to bridge the gap between the maximum achievable ion energies between table-top and single shot laser systems. Systematic studies can be performed and scaling laws for TNSA deduced with ultra-short pulses for the identification of feasible routes toward high proton energies at reasonable repetition rates [67]. Zeil *et al.* [67] presented a systematic investigation of an ultra-short pulse laser acceleration of protons that yielded a maximum proton energy of 17 MeV employing a table-top 100 TW Ti:sapphire laser. They used plain few $\mu$m thick foil targets, observing a linear scaling of the maximum proton energy with laser power, attributed to the short acceleration period close to the rear surface of the target [67]. Slight deformations in the target rear surface were found to lead to a shift in the direction of the energetic proton emission away from the target normal that could be used for better discrimination of the low energy part of the proton spectrum [67].

In the TNSA scheme the most efficient acceleration is of the hydrocarbon contaminant layer on the rear of the surface, which impedes the acceleration of the heavier target material ions. In the idealistic RPA scheme, all species would be co-accelerated with the lighter ions not impeding the heavier ions, thus efficiently accelerating the heavier ions to much higher energies. However, in a more realistic multi-dimensional view of the RPA scheme, the heavier ions have a very broad spectrum resultant from rapid Coulomb explosion, de-

ficiency of co-moving electrons and transverse instabilities [68]. Wu *et al.* proposed and demonstrated a novel RPA regime for the generation of monoenergetic, high-energy heavy ion beams by irradiation of ultrathin foils with intense laser pulses. An appropriate matching condition between the target thickness, laser intensity and the ionisation energy gap produced by the successive ionisation of high-Z atoms passing the noble gas configuration, was used to create a self-organised stable RPA regime of highly charged heavy ions close to the laser central axis [68]. A large number of electrons are also produced during the ionisation, which stabilises the beam by keeping the accelerating plasma non-transparent and suppressing the transverse instabilities. They analytically established and verified the regime using a 2D PIC simulation, which produced a 1 GeV peak energy highly charged monoenergetic $Al^{13+}$ beam with total charge above 2 nC and 5% energy spread employing a 7 x $10^{20}$ $Wcm^{-2}$ circularly polarised laser, and a 16.8 GeV peak energy $Fe^{26+}$ monoenergetic beam was obtained by increasing the laser intensity to 4 x $10^{22}$ $Wcm^{-2}$ [68].

# Chapter 3

# Experimental Tools and Techniques

This chapter describes the laser systems and detectors implemented in the experimental work presented in this thesis. Four laser systems are described; Vulcan Petawatt, LULI2000, TARANIS and Astra-Gemini. All four systems were employed for radiobiological studies of the effect of ultra-high dose rate protons on AG01522 human fibroblast cells under different irradiation conditions, and Vulcan Petawatt was also employed for laser-driven ion acceleration investigations. Details of the three different detectors used (Thomson Parabola spectrometer, image plates and radiochromic films) are given, as is a short description of how a Thomson Parabola Spectrometer was modified to enhance its functionality.

## 3.1 Chirped Pulse Amplification

Femtosecond laser pulses are prone to inducing beam distortions, non-linear effects and optical dmage to the optical components through which they propagate, owing to high peak powers and associated electric fields even in modest pulses. These effects include self-focusing and its temporal counterpart self phase modulation. In order to amplify short pulses to efficiently extract stored energy from the laser amplifier, the amplifying medium must be operated at fluences close to the saturation fluence of the material, which is not

possible with ultra-short pulses without the induction of significant self focusing and self phase modulation, resulting in significant optical damage. To overcome these non-linear limits associated with high intensity, yet still efficiently extract energy from high energy storage materials by short pulses, more complex amplification schemes must be employed which reduce the non-linearity of the gain medium and control the temporal stretching of the pulse during amplification. This can be achieved by using the Chirped Pulse Amplification (CPA) technique, which by producing short pulses only after amplification increases the extractable energy achievable from broadband materials to a level comparable to that from long pulses [69–72]. Keeping the pulse length at least at 40 ps throughout the amplifier chain allows the components time to cool through thermal conduction, thus avioding damage [23].

As laser pulse lengths become shorter, it becomes increasingly difficult to efficiently extract energy from the laser amplifier without incurring detrimental non-linear effects. This arises from the fact mentioned above that the amplifier has to be operated at close to the saturation fluence;

$$F_{sat} = \frac{hv}{\sigma} \tag{3.1}$$

where $h$ is Planck's constant, $v$ is the laser frequency and $\sigma$ is the emission cross section [70, 73]. The saturation fluence for most solid laser materials is between 1 J/cm$^2$ (Ti:Sapphire) and 6 J/cm$^2$ (Nd:glass). It is not possible to amplify ps pulses to this level because of the index of refraction;

$$n = n_0 + n_2 I \tag{3.2}$$

which is dependent on the intensity of the pulse $I$ [70]. This intensity-dependent refractive index produces a non-linear phase retardation given by the $B$ integral which represents the amount of wave-front distortion owing to the intensity dependent index of refraction, accumulated by the beam over the propagation length $l$;

$$B = \frac{2\pi}{\lambda} \int_0^l n_2 I(z) dz \tag{3.3}$$

which results in eventual catastrophic filamentation which causes damage to the amplifier. For a perfectly Gaussian beam, B will cause the whole beam to self focus above a critical power given by;

$$P_{cr} = \frac{\lambda_0^2}{2\pi n_0 n_2} \tag{3.4}$$

Small scale self focusing represents the most severe problem in the amplifier system [74, 75]. The maximum growth rate $g_m$ occurs for spatial frequencies $K_m$ given by;

$$K_m = \left(\frac{2\pi}{\lambda}\right)\left(\frac{2n_2 I}{n_0}\right)^{1/2} \tag{3.5}$$

$$g_m = \left(\frac{2\pi}{\lambda}\right)\left(\frac{n_2 I}{n_0}\right) \tag{3.6}$$

with the exponential growth rate $G_m$ over gain length $l$ being exactly equal to $B$. For laser fusion systems, the beam has to be 'cleaned 'with spatial filters every time B reaches 3, and for high-field experiments where the temporal and spatial quality of the beam are much more important, B has to be kept below 0.3 [75]. The intensity in the amplifier must remain below the critical level at which the non-linear effects become significant and distort the temporal and spatial profile of the pulse [73].

Amplifier materials which have lower cross sections, such as Nd:glass, can store up to 10,000 times more energy than dyes or excimers. However, to extract this increased amount of stored energy in a ps pulse requires a beam of intensity $\sim 10^{12}$ Wcm$^{-2}$, corresponding to a B value of a few thousand which is not possible. Therefore in order to utilise these materials with superior energy storage, the input energy needed for extraction must be increased whilst keeping the input intensity at an acceptable level, which is achieved through the process of CPA [69, 74, 75].

In CPA the pulse is primarily stretched by a factor of 1000 to 100,000 by introducing a large well characterised dispersion, or time delay, of the different spectral components

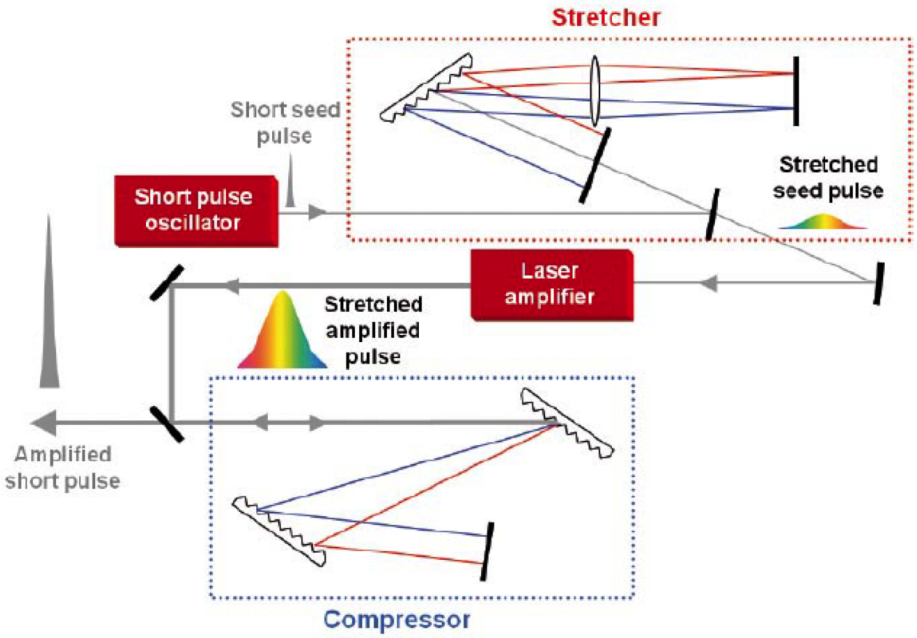


Fig. 3.1 Schematic diagram of a CPA laser [72].

of the ultra-short pulse to produce a long chirped optical pulse, without changing the input pulse energy (input fluence) or the energy extraction capability. The stretching of the pulse allows more energy to be extracted from the amplifier system than would be from a short pulse. It does however lower the input intensity by the stretching ratio and hence keeps B at a reasonable level, reducing the peak power in the amplifier below the threshold for non-linear pulse distortion. The pulse is then amplified by 6 to 12 orders of magnitude from the nJ to the mJ/kJ level and is finally recompressed by the same stretching ratio back to a duration close to its initial value, via a dispersion that closely matches the stretching dispersion but has the opposite sign [71, 72, 75, 76].

A significant portion of the energy in the pulse remains uncompressed, forming the pedestral. This pedestral originates from the non-linear chirp, the non-Gaussian pulse shape and non-linearities in the amplification process [76]. Optical recompression of the laser pulse can also be prevented through amplitude and phase distortions resultant from the CPA process [72].

Since the advent of chirped pulse amplification in 1985 by Mourou, Strickland, Maine and colleagues at the University of Rochester [69, 73], it is exploited by nearly all existing high power femtosecond laser systems. To further increase the power of these laser systems without destroying the laser components is possible through the further reduction of the pulse length employing the OPCPA, optical parametric chirped pulse amplification, technique proposed by Ross et al [77]. This technique takes a conventional laser pump beam of any wavelength and amplifies a large bandwidth of the chirped pulse and recompresses it to short pulses 10 - 20 times shorter than those produced by CPA. This would allow current PW class lasers to be upgraded to the 10 PW level without too much additional cost or reconsruction [23].

### 3.1.1 Laser Contrast

As the intensities produced by high power CPA laser systems have increased greatly over the past number of years to $10^{19}$ - $10^{22}$ Wcm$^{-2}$, the importance of good laser contrast has become increasingly evident. The laser pulse contrast ratio (LPCR) is defined as the ratio R between the peak laser pulse intensity $I_{peak}$ and any pre-pulse or pedestal intensity $I_{pre/ped}$ [23, 78];

$$R = \frac{I_{peak}}{I_{pre/ped}} \tag{3.7}$$

A reduction in the LPCR is caused by different mechanisms dependent on the timescale of the intensity temporal profile. On the ns timescale (up to 20 ns), prepulses result form insufficient contrast between the amplified laser pulse and neighbouring pulses produced in the oscillator. Below a few ns, amplification of spontaneous emission (ASE - amplified fluorescence produced by the pumped crystal during amplification of the laser pulse which propagates along the same axis as the main pulse), results in a ns plateau shaped pedestral. In the ps timescale (below a few 10's of ps), deficient manipulations of the laser spectrum resulting in imperfect pulse compression degrade the LPCR close to the peak intensity [78,

79].

When considering the effect of a low LPCR on a laser solid interaction, there are two target parameters of great importance; the ionisation threshold and the damage (ablation) threshold. An intensity of $\sim 10^{13}$ Wcm$^{-2}$ will ionise all known target materials to form a plasma even in the shortest pulses. The presence of this pre-plasma near the target surface before the arrival of the pulse peak intensity modifies the electron gradient density and the nature of the mechanisms leading to the absorption of the laser energy in the target. The damage threshold corresponds to the onset of a fluence dependent phase transition following energy deposition in the solid target resulting in a morphology change. This change affects the energy absorption process and may damage or even destroy the target [78–80].

At intensities in excess of $10^{21}$ Wcm$^{-2}$, a peak intensity to prepulse intensity contrast of greater than 1:1:$10^{-9}$ (contrast of greater than $10^{10}$) is required [**? ?** ], to prevent the change in the physical properties of the target before the arrival of the main pulse. This is very hard to achieve directly from the laser amplifier itself, for example, the inherent contrast of Astra-Gemini is $10^6$ - $10^7$, with typical sources being prepulses leaked by the Pockels cells, ASE and spectral bandwidth limitations of the main pulse itself [80, 81]. Several techniques are available to enhance the LPCR in CPA systems such as saturable absorbers, cross polarised wave generation and plasma mirrors. Incorporating a plasma mirror into the experimental set-up can increase the contrast by more than two orders of magnitude [82].

### Plasma Mirror

One method of enhancing the contrast of the laser pulse is self-induced plasma shuttering, more commonly known as a plasma mirror (PM). If a sufficiently intense laser pulse is focused onto a dielectric material, rapid ionisation takes place releasing electrons which gives rise to an overdense plasma with reflectivity close to unity. If the dielectric material is a glass slab coated with a tailored anti-reflection coating, ionisation will only occur on the

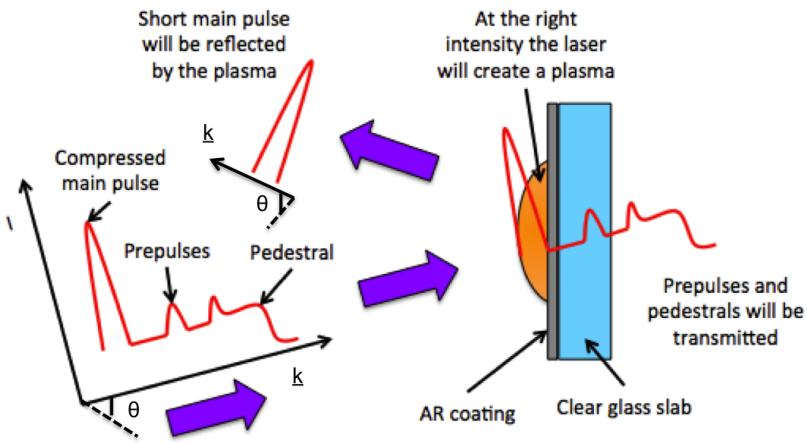


Fig. 3.2 A schematic of the operating principle of a plasma mirror. A laser pulse with a preceding prepulse and pedestral is incident on a AR coated glass slab. The low intensity prepulse and pedestral are transmitted until the laser intensity become sufficiently large at the leading edge of the pulse to form a plasma. Once the critical density of the plasma is reached, the laser pulse is reflected.

rising edge of the main pulse and the pulse peak will interact with the dense plasma. Given the rapid change in reflectivity which occurs with the rapid ionisation, the PM can be used as a laser-triggered ultrafast optical switch. The intensity of the incident laser beam is chosen such that the intensity of any prepulse energy is below the ionisation/damage threshold of the glass and experiences the cold reflectivity, while the main pulse easily ionises the target and reflects off the plasma. The majority of the prepulse and pedestral energy are transmitted through the plasma mirror [80, 81, 83, 84].

The reflectivity of a PM is maximised by operation at high intensities, as an earlier "switch on" time allows more of the main pulse to be reflected, however the prepulse and the pedestral may also be partially reflected if the switch-on is too early. Also the plasma surface will have longer to expand, thus disturbing the initial flatness and causing the beam to scatter and not be perfectly specularly reflected. To prevent the laser beam from resolving any modulations in the plasma surface, the optimum operation condition of the PM with

negligible distortion of the reflected beam is when,

$$c_s \Delta t < \lambda_{laser} \tag{3.8}$$

where $c_s$ is the sound speed and $\Delta t$ is the time from ionisation to the peak of the main pulse. If the intensity is too low, triggering may occur late or not at all [81, 83].

Use of double plasma mirror on the Astra Gemini laser system (described in Section 3.2.4) can increase the contrast between the pulse peak intensity and the ASE pedestral intensity by a factor of $\sim$ 1000 [85]. However, the laser contrast is enhanced at the expense of the energy delivered to the target. The reduction in energy is typically in the region of 15 - 30 % per PM interaction and consequently a reduction in the interaction intensity [82].

## 3.2 High Power CPA Laser Systems

The experiments described in this thesis were carried out employing three high power laser systems: Vulcan Petawatt, LULI2000 and TARANIS. Previous experimental work which contributed to this thesis was also carried out at the Astra-Gemini facility. These four systems will be described in the following Sections.

### 3.2.1 Vulcan

The Vulcan laser is a versatile high power laser system located at the Central Laser Facility, Rutherford Appleton Laboratory, Oxford, UK. It is comprised of Nd:glass amplifier chains, which can deliver up to 2.6 kJ of laser energy in long (ns range) pulses and up to 1 PW ($10^{15}$ W) in a short (500 fs) pulse at a wavelength of 1053 nm [86].

Vulcan currently has eight beamlines; six of these beamlines operate only in long pulse mode, the other two can operate in both long and short pulse modes. There are two different target areas supported by Vulcan; Target Area Petawatt (TAP) and Target Area West (TAW).

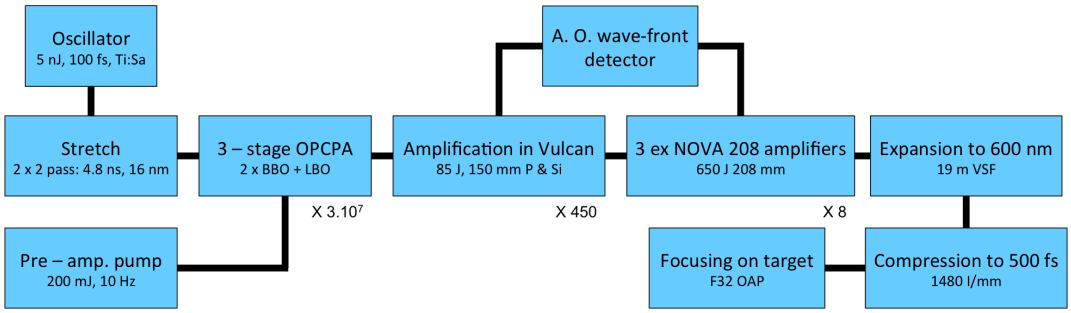


Fig. 3.3 Building blocks of the Vulcan Petawatt facility reproduced from [88].

The short- and long-pulse systems can be operated jointly and directed to the two different target areas, enabling sophisticated interaction and probing experiments. The seed sources for each target area are different; TAP is seeded by a commercial Ti:Sapphire laser and TAW is seeded by a commercial Nd:glass laser, mode locked using a saturable absorber [87].

Vulcan is capable of delivering ultra-high focused intensities greater than $10^{21}$ Wcm$^{-2}$ in its short pulse mode, achieved by amplifying a sub-picosecond pulse to hundreds of Joules and then focusing it close to its diffraction limit. This amplification is achieved by CPA. The low intensity pulse is stretched from a few femtoseconds to nanoseconds, amplified, then recompressed and focussed onto the target, producing the high intensities [86].

### Vulcan Petawatt

The CPA technique employs a pulse stretcher, amplifier and a compressor before delivery to a target. The stretcher of Vulcan is based on a double Offner triplet arrangement, which comprises two confocal equal positive lenses and one negative lens at the common focus, which has half the focal length of the positive lenses eliminating aberrations. The beam passes through one Offner then the other, being vertically displaced on each pass of the stretcher using retro-reflectors [89].

The pre-amplification of the beam employs OPCPA (optical parametric chirped pulse amplification), which generates $\sim 10$ mJ pulses at large bandwidth (1 mJ nm$^{-1}$) for injection

into the rod and disc amplifier chain. The amplifier chain is optimised for bandwidth using a combination of Nd:silicate and Nd:phosphate amplifying media. The pre-amplifier uses a 10 Hz, 2 J, 1053 nm YAG laser to generate a frequency doubled pump pulse of 4.5 ns and 200-300 mJ. This pumps a three stage optical parametric amplifier that is seeded by the stretched oscillator pulse [89].

The amplification stage comprises three ex-Nova 208 mm aperture disc amplifiers with gain isolation provided by a 208 mm aperture Faraday rotator and a single polariser at the stage input [89]. When this additional amplifier stage was added, one of the apertures was modified in order to be able to operate with Vulcan's existing pulse power system. Under the narrow bandwidth 1053 nm operation conditions, the small signal gain was measured as 2.23, falling to $\sim$ 2.0 under saturation conditions for 670 J total output, indicating a saturation fluence of 4 Jcm$^{-2}$ [89].

The use of a large 120 mm aperture adaptive optics module is essential for the Vulcan facility, as it is required to improve the wave-front quality to produce an optimum on target focal spot, and also to achieve the best possible re-compression of the stretched pulse.

The compressor (operational frequency 170 mJ cm$^{-2}$) uses a pair of gold-coated holographic 1480 line mm$^{-1}$ gratings, 940 mm in diameter, separated by 13 m with an operational angle of 48°, inside a large vacuum chamber. The compressed pulse is focused down to a 5 $\mu$m (FWHM) focal spot using an $f/3$ OAP, delivering 500 J in $\sim$ 500 fs and peak intensity of $10^{21}$ Wcm$^{-2}$. Measured 60 ps ahead of the main pulse, the pulse peak to ASE contrast ratio was found to be $10^6$ [88].

Target Area Petawatt (TAP) is configured for delivering the highest intensity of up to $10^{21}$ Wcm$^{-2}$ using the F3 focusing optic. The length and energies of the pulses are configurable on request from sub-ps to tens of ps. A single standard long pulse beam of length 0.5 ns to 8 ns and energy 50 J to 300 J depending on the operational pulse length is available in addition to the standard short pulse beamline. The beam can also be converted to the

second harmonic and the temporal shape of the beam can also be modified. The standard jitter between the two beams is 150 ps [90].

### 3.2.2 LULI2000

LULI (Laboratoire d'Utilisation des Lasers Intenses) is a large scale facility and research laboratory founded in 1988 and supported by CNRS (Centre National de la Recherche Scientifique), CEA (Commissariat à l'Énergie Atomique), Université Pierre et Marie Curie and École Polytechnique where it is located (Palaiseau, Paris, France). The LULI2000 system is unique to European academia in the field of high-energy density physics owing to the coupling of short (ps) and long (ns) high energy laser beams and the availability of auxiliary beams for pump-probe experiments [91].

Two high-power single pulse neodymium glass laser chains (NORTH and SOUTH) are contained within the laser hall. In the nano2000 configuration, each beam can deliver up to $\sim 0.8$ kJ at $\omega$ (wavelength 1053 nm) in 1.5 ns. A delay line allows the delay to be adjusted by $\pm$ 10 ns between the two chains [92]. A 10 Hz laser allows fast diagnostic alignment, but the repetition rate is limited to 1 shot every 90 minutes, equating to 4 to 6 full energy shots per day.

A second configuration, pico2000, implements CPA on the SOUTH laser chain to compress the beam in time by a factor of 1000, allowing that chain to operate in the ps regime [93]. However, the energy delivered is then limited to $\sim$ 100 J in 1 ps (100 TW) to avoid any damage to the grating.

There are two additional moderately energetic beams, the blue and black chains, which are fully synchronised and available for laser-based diagnostics such as Thomson scattering and off- or on-axis radiography. The blue chain delivers 50 J ns pulses while the black chain delivers a few J in 1 ps [92]. The NORTH, SOUTH and blue chains are also able to deliver frequency-doubled pulses ($2\omega$).

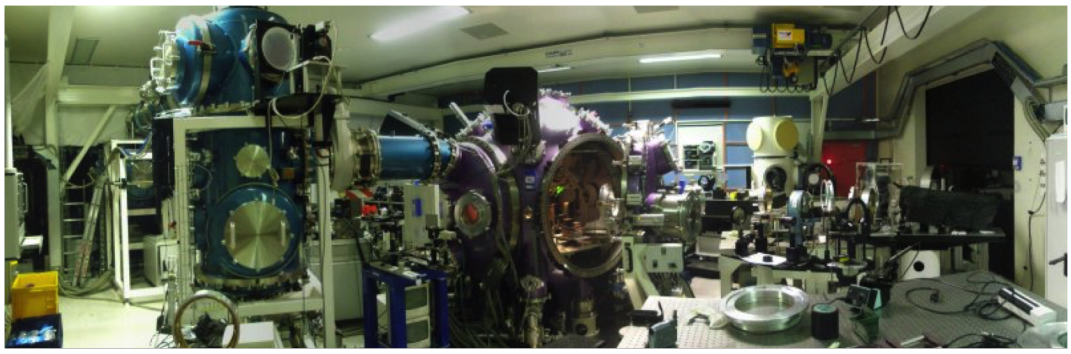

Fig. 3.4 The MILKA interaction chamber in LULI2000 target area room 1 [94].

It is possible to have on target pulses with different temporal shapes as there are three independent laser oscillators. One is for the NORTH and SOUTH chains when they are operated in the ns regime, 1 is for the SOUTH and black chains when they are operated in the ps regime, and the third is for the blue chain. The pulses may be shaped over a total duration of $\sim$ 1 to $\sim$ 10 ns when operated in the ns regime.

There are two target areas at the LULI2000 facility, each dedicated to either the nano2000 configuration (room 2) or the pico2000 configuration (room 1).

Three laser beams are available in target area room 1; the NORTH beam, the SOUTH beam and the blue beam. The NORTH beam offers 800 J in 1.5 ns at $\omega$, the SOUTH beam offers 100 J in 1 ps at $\omega$ in the pico2000 configuration and the blue beam offers 50 J in 1.5 ns at $\omega$ [94]. The spherical MILKA target chamber has an approximate diameter of 2 m, with an internal vacuum of $10^{-2}$ mbar ($10^{-4}$ Pa) achievable after 30 minutes of pumping. When the SOUTH beam is being operated in the ps regime, the room is radio-protected and radiologically controlled through the implementation of strategically placed dosimeters.

Four laser beams are available in target area room 2; the NORTH and SOUTH laser beams, the blue beam and the black beam. The NORTH and SOUTH beams are both operated at 800 J in 1.5 ns at $\omega$ in the nano2000 configuration, the blue beam offers the same specifications as those it operates at in room 1, and the black beam offers a few J in 1 ps at $\omega$ [94].

### 3.2.3 TARANIS

The Terawatt Apparatus for Relativistic And Non-linear Interdisciplinary Science (TARANIS) is located in the Centre for Plasma Physics at Queen's University Belfast. TARANIS is a hybrid Ti:Sapphire-Nd:glass system opperating in the CPA mode [95]. The front end of the laser system comprises a Ti:Sapphire oscillator, followed by a folded all reflective stretcher and a Ti:Sapphire regenerative amplifier (RA). The oscillator is a commercial Coherent Mira mode-locked system, which provides a train of 120 fs transform limited pulses at 1053 nm, with a repetition frequency of 76 MHz [96]. The wavelength is chosen to match the peak of the Nd:glass amplifiers gain curve, although the oscillator still delivers an average power of 400 mW even though the Ti:Sapphire crystal is not peaked at this wavelength. The pulse is stretched by a factor of $\sim 10^4$ within the double-pass stretcher equipped with a 1740 lines/mm diffraction grating and an $f$ = 1524 mm spherical mirror arranged in an inverting telescope configuration, producing optically chirped pulses of $\sim$ 1.2 ns [96]. The pulse is pre-amplified in the Ti:Sapphire RA, pumped by a commercial Coherent Evolution Q-switched Nd:YLF 527 nm laser. The RA delivers $\sim$ 0.6 mJ pulses, at a maximum frequency rate of 500 Hz in a $\sim$ 300 mW average power beam [96]. Pre-pulse activity and spontaneous amplified emission are controlled and limited by a double set of Pockels cells and optimisation of the Ti:Sapphire RA for amplification at 1053 nm.

Amplification of the laser pulse to multi-TW levels is achieved by a three stage flash-lamp pumped Nd:glass rod chain that amplifies two separate pulses up to $\sim$ 30 J per pulse at a repetition rate of one shot every ten minutes in the full power mode. The two pulses from the glass rod chain can be recompressed separately in two double-pass grating compressors, each with two parallel gold-coated diffraction gratings. A minimum pulse duration of 560 fs (typically 700 fs on average at high energy) can be achieved with $\sim$ 60% energy transmission through the compressors [95], and longer pulses of $\sim$ 1 ns can be obtained by by-passing the compressors.

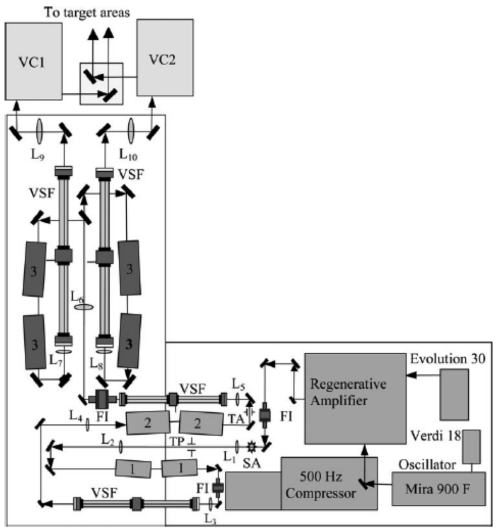


Fig. 3.5 Optical layout of the TARANIS laser. Image key: FI – Faraday isolator; VSF – vacuum spatial filter; TA – Teflon aperture; TP – Teflon pinhole; SA – serrated aperture; 1, 2, 3 - laser heads with Nd:Glass rods of 9 mm, 25 mm, and 50 mm diameter, respectively; $L_1L_2$, $L_3L_4$, $L_5L_6$, $L_7L_9$, $L_8L_{10}$ – relay imaging telescopes; VC1, VC2 – vacuum compressors [96].

A pulse picking technique using three Pockels cells with crossed polarisers is employed to reduce pre-pulse activity. One Pockels cell is before the RA, the other two are between the RA and the Nd:glass amplifying chain. The intensity contrast ratio is measured at low energy on a ns timescale, and the pre-pulse activity is recorded by a fast photodiode. The measured intensity contrast ratio is $\sim 10^7$ [96].

For experiments requiring two beams, different combinations of ns and ps pulse durations can be selected. A short pulse beam and an uncompressed long pulse beam can be delivered into TA1 (target area 1), while a combination of a short pulse and a long pulse or two short pulses can be delivered to TA2 (target area 2). A 180 mJ pulse can be extracted after the second stage of the amplifying chain and separately recompressed down to 400 fs duration in a compact double diffraction grating compressor, and can be employed as a probe pulse for time resolved optical probing measurements in either target area [96].

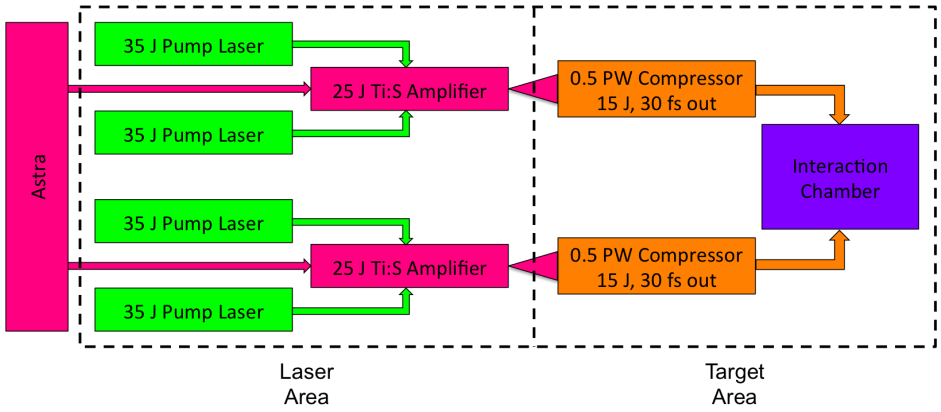


Fig. 3.6 Schematic layout of the Gemini laser. Reproduced from [98].

### 3.2.4 Astra-Gemini

The Astra Gemini laser system is also located at the Central Laser Facility. Astra is a high-repetition rate, ultra-short pulse, high power laser, which uses titanium-doped sapphire (TiS) as its active material and opperates at 800 nm [97]. Astra Gemini is an extension of Astra which transforms it from a single beam 10 TW system into a two beam Petawatt class laser, that can deliver thirty times as much energy in each of its two beams at a peak power of 0.5 PW. It is one of the most intense lasers in the world with 30 J on target, a repetition rate of three shots per minute and an intensity of greater than $10^{21}$ Wcm$^{-2}$ [97].

The source beam of Gemini is the output from the third amplifier of Astra. The Gemini system consists of a pair of TiS amplifiers, each with its own pulse compressor and pair of pump lasers. Each pump laser will produce a 35 J, 10 ns optical pulses at 527 nm, with each pair providing up to 70 J of pump energy to each amplifier seeded by the Astra system [98]. The two beam design of Gemini allows the possibility of a combination of long and short pulses, different focal lengths, variations in relative timing and mixed polarisations as both beams are independently configurable [99].

Through temporal compression each beam delivers 15 J on target in a pulse of 30 femtoseconds, with a maximum focused intensity of $\sim 10^{22}$ Wcm$^{-2}$ from each beam. Gemini

has an inherent intensity contrast of $\sim 10^7$ 20 ps before the pulse peak, as measured by a third-order scanning autocorrelator [85]. The laser system has a repetition rate of one shot every 20 seconds, which is incredibly high for a facility of this type. The beams enter the target chamber from above, providing 360° access around the chamber, and the beam polarisation can be controlled by the direction they are steered. The beams are focused onto a double plasma mirror system using an off-axis parabola (OAP), with a second identical OAP used to re-collimate the expanding beam. This arangement enhances the pulse peak to ASE pedastal intensity ratio to $\sim 10^{10}$, a factor of $\sim 1000$ improvement [85].

## 3.3 Diagnostics and Detectors

The high power laser systems described in the Section 3.2 are capable of accelerating protons and other heavier ions up to tens of MeV per nucleon via the acceleration mechanisms described in Chapter 2. Evidently these ion sources are multi species as the accelerated protons and ions originate from both the bulk target material and the contaminant layer which is present on the target surface. Protons, several charge states of carbon, oxygen and the bulk target elements, are all accelerated simultaneously, resulting in an essential demand for spectrometers which adequately discriminate between these different species. Diagnosis and characterisation of these ion beams is essential for understanding the underlying acceleration mechanisms at work, and for tailoring the experimental set-up to the beam characteristics required for specific investigations. Many diagnostics exist including Radiochromic film detectors [100, 101], image plate detectors [102–104] (discussed in Sections 3.3.3 and 3.3.2 respectively), nuclear activation techniques [105, 106], nuclear track detectors [107, 108], Faraday cups [109] and Thomson Parabola Spectrometers [110–113] (discussed in Section 3.3.1). However the most convenient to use in terms of implementation and data analysis is the Thomson Parabola Spectrometer which disperses the ion species in energy and mass-to-charge (A/Z) ratio by means of static magnetic and electric fields.

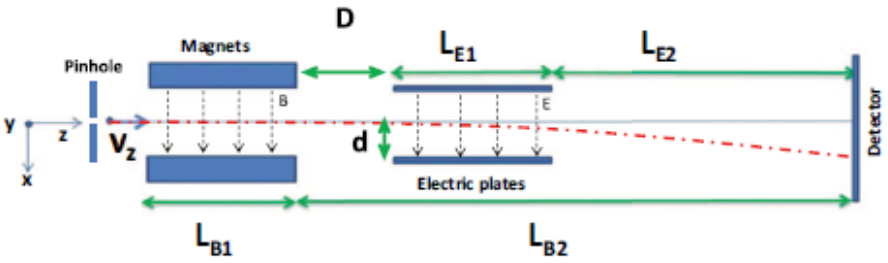


Fig. 3.7 Schematic of a Thomson Parabola Spectrometer [110]. The TPS described here has the electric and magnetic fields separated by a distance D, however there are variations which have overlapping electric and magnetic fields [116].

### 3.3.1 Thomson Parabola Spectrometer

A Thomson Parabola Spectrometer (TPS) is the most convenient diagnostic to use in terms of ease of implementation and data analysis when studying laser-driven ion beams. A schematic of a traditional TPS used in laser plasma experiments is shown in Figure 3.7. A TPS consists of a pair of rectangular permanent magnets and a pair of rectangular electrodes, which produce uniform static magnetic and electric fields, and disperse the ions according their mass-to-charge ratio and energy [114], resulting in a unique parabolic trace on the detector plane for each mass-to-charge ratio.

It is used to measure the energy spectra of different ion species in a given solid angle, and more than one TPS can be employed to gain information from different positions within the interaction chamber. From a single shot, complete information about the energy distributions of all ionisation states of the ion can be obtained for ions with charge states $q < 20$ [115].

The pinhole of the TPS selects a pencil beam of ions, which is transmitted through the magnetic and electric field regions which are parallel to each other but perpendicular to the ion's initial momentum. High energy ions are deflected less than low energy ions, whilst neutral particles will pass through un-deflected.

For uniform electric and magnetic fields, without considering fringe effects, the ion

displacements at the detector plane along the Y, $S_B$, owing to the magnetic field, and X, $S_E$, owing to the electric field, axes can be derived, respectively, for the non-relativistic case as:

$$S_B = \alpha B \left( \frac{L_{B1}^2}{2} + L_{B1} L_{B2} \right) \tag{3.9}$$

$$S_E = \alpha^2 E \frac{m}{q} \left( \frac{L_{E1}^2}{2} + L_{E1} L_{E2} \right) \tag{3.10}$$

where $\alpha = q/mv_z$ and $v_z$ is the longitudinal speed of the ion (of mass $m$ and charge $q$) at the pinhole [110], $L_{B1}$, $L_{B2}$, $L_{E1}$ and $L_{E2}$ correspond to the distances shown in Figure 3.7, and $E$ and $B$ represent the electric and magnetic field strengths respectively. These displacements are derived from the equations of motion and the Lorentz force, where the change in $v_z$ can be neglected without any loss in generality. Equations 3.9 and 3.10 can be used to define the equation of the parabolic trace described by each particle of a given $q/m$:

$$S_B^2 = \frac{qB^2}{mE} \frac{\left( \frac{L_{B1}^2}{2} + L_{B1} L_{B2} \right)^2}{\left( \frac{L_{E1}^2}{2} + L_{E1} L_{E2} \right)} S_E \tag{3.11}$$

As can be seen from Equations 3.9 and 3.10, the deflection produced has a linear dependence on the magnetic field strength and the electric field strength, but a stronger dependence on the length of either the magnets or the electric plates.

The dimensions of the various elements of the TPS, such as the field regions and the distances from the electric and magnetic fields to the detector, and the strengths of the electric and magnetic fields are what governs the dispersion of the ion species. The spectrometers need to be compact in order to fit inside the interaction chamber, but still provide sufficient A/Z resolution for heavy ions beyond several MeV/nucleon as the parabolic traces will start to overlap, making it difficult to discriminate the individual ion species towards the high energy end of the spectrum. Overlapping of the ion tracks occurs when the deflection owing

to the electric field is insufficient, even if the dispersion by the magnetic field is adequate. Species separation can primarily be improved by increasing the distance between the end of the field region and the detector plane ($L_{E2}$ and $L_{B2}$), increasing the strength of the electric field ($E$) or increasing the longitudinal extent of the electric field region ($L_{E1}$). However, increasing $L_{E2}$ results in a loss of resolution at the detector plane, increasing $E$ may result in damage to the apparatus or the low energy ions being deflected away from the detector, and increasing $L_{E1}$ results in the low energy ions being deflected into the electric plate itself. This compromises the ability of the detector to resolve the entire ion spectrum, however if the electric plates are shaped the low energy ions could be retained whilst still preventing the overlapping of the traces at the high energy end of the spectrum.

**Modification of a TPS for use with high energy, multi-species ion sources**

The 3D particle tracing code PTRACE [20] was used to study a suitable field configuration for effective charge state separation, whilst retaining the low energy ions. PTRACE is written in C++ object orientated methodology and computes the trajectory of the particle through a customised electromagnetic field region using a differential equation solver at its core. The numerical algorithm is a fourth order Runge-Kutta solver coupled with an adaptive step-size monitoring routine [110]. This approach is fast and reliable at solving the equation of motion, and it is possible to prescribe the degree of precision to which the trajectory is comptued [20].

The 3D setup of PTRACE is shown in Figure 3.7. The selected pencil beam of ions input to the TPS is defined as a very low divergence point source with a multi-energy spectrum. The magnetic field was defined as being the first field encountered by the ions. To include any fringe field effects produced by the magnets, the magnetic field region was defined according to the field profile in a conventional magnet-yoke configuration, as measured by Carroll et al [116]. This magnetic field profile along the ion propagation axis (Z-axis) was

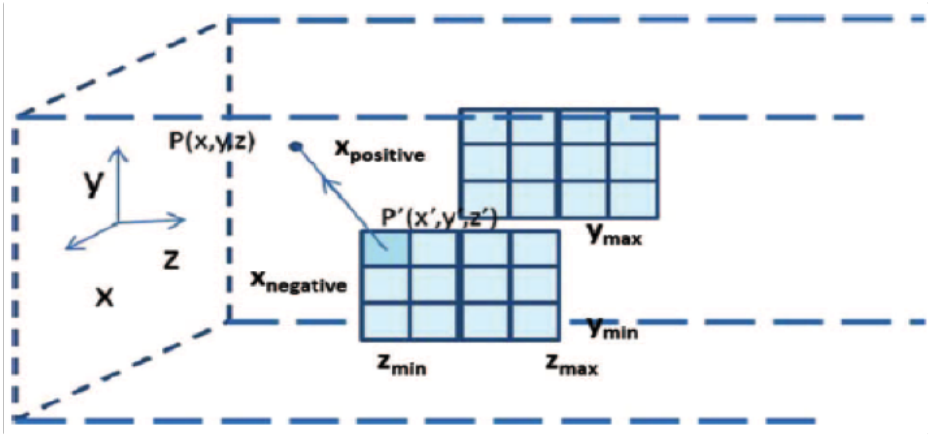


Fig. 3.8 Schematic of the electric plate setup in PTRACE for calculation of the E-field [110].

fitted with a super-Gaussian like function:

$$B(z) = B_{peak} \exp\left[-\left(\frac{z - z_{centre}}{B_{FWHM}/1.82}\right)^4\right] \tag{3.12}$$

where $B_{peak}$ is the peak magnetic field, $z_{centre}$ is the $z$ coordinate of the centre of the magnets, and $B_{FWHM}$ is the full width at half maximum of the field profile, which is approximately equal to the length of the magnets.

A simple numerical approach was chosen for the electric field calculation in order to study the effect of different electric plate geometries. The electric field at any given point in space $P(x,y,z)$ was numerically calculated by the superposition of the electric fields owing to all points on the electrodes, shown by Figure 3.8. In the case of rectangular electrode geometry, the electric field $\overrightarrow{E}$ owing to the negative electrode will be:

$$\overrightarrow{E} = K\sigma \int_{y_{min}}^{y_{max}} \int_{z_{min}}^{z_{max}} \frac{\mathrm{d}y' \mathrm{d}z' \overrightarrow{PP'}}{|\overrightarrow{PP'}|^3}\Bigg|_{x=x_{positive}} \tag{3.13}$$

where $K = 1/4\pi\varepsilon_0$, the surface charge density $\sigma = 2\varepsilon_0$ and the limits $y_{max}$, $y_{min}$, $z_{max}$, $z_{min}$ and $x_{negative}$ refer to those shown in Figure 3.8. In order to simplify the calculation, the

integration over $z$ was substituted with a summation over $z$. During the transit of the ion of a given charge, mass and energy, the main module of PTRACE accesses the electric and magnetic field objects in order to obtain the fields values at the ion's position. The trajectory of the ion is subsequently simulated by the differential equation solver, producing a two dimensional image of the simulated ion trace at the detector plane (a distance of $L_{E2}$ from the end of the electric plate).

As mentioned earlier, the species separation can be increased by three possible methods: (1) increase $L_{E2}$, (2) increase the strength of the electric field, and (3) increase $L_{E1}$. In terms of the capability of discriminating ion traces at the detector plane, the resolution of the spectrometer can be defined as follows:

$$R = \left| \frac{S_{E2} - S_{E1}}{a} \right| = \frac{E}{2a} \left| \frac{m_2}{q_2} - \frac{m_1}{q_1} \right| \alpha^2 \left( L_{E1} + 2L_{E2} \right) L_{E1} \tag{3.14}$$

where $S_{E1}$ and $S_{E2}$ stand for the electric field displacements of two ion species of charge $q_1$ and $q_2$, and masses $m_1$ and $m_2$, respectively, at a given magnetic displacement (when $q_1/m_1 v_{1z} = q_2/m_2 v_{2z}$), $a$ stands for the size of the pinhole at the entrance of the TPS, which typically defines the width of the ion traces at the detector (in a standard configuration, the pinhole to detector distance is significantly less than the distance between the ion source and the pinhole). Since $R = 1$ corresponds to the threshold for discriminating two neighbouring ion traces, equation 3.14 can be re-written as:

$$\Delta \left( \frac{A}{Z} \right) = \frac{4a[\mu\text{m}](A_i/Z_i)^2 W_i[\text{MeV/nucleon}]}{E[\text{MV/m}](L_{E1}[\text{mm}] + 2L_{E2}[\text{mm}])L_{E1}[\text{mm}]} \tag{3.15}$$

where $A_i$, $Z_i$ and $W_i$ represent the atomic mass, ionisation state, and energy per nucleon of a given charge species. Equation 3.14 indicates that the resolution increases linearly with $E$ and $L_{E2}$, whereas the dependence on electric plate length, $L_{E1}$, is quadratic. Increasing $L_{E2}$, by a significant amount, in order to improve the resolution, is normally not a viable

option as it is difficult to place a large spectrometer inside a small interaction chamber, whilst still keeping the TPS a reasonable distance from the target. However, moving the detector significantly further away from the end of the electric plates also increases the magnetic field dispersion commensurately, as it entails an increase in $L_{B2}$, which is not always desired given the finite dimensions of the detector. There will also be a decrease in the particle flux at the detector plane, as there would be with any alteration that would increase the dispersion of the ions, giving rise to a lower signal to noise ratio. The strength of the electric field can be increased by two different methods; decreasing the separation of, or, increasing the voltage to the electrodes. These methods are both limited by the onset of arcing or discharging between the electrodes, causing the elctric field to fluctuate or drop instantaneously. Typically an experimental chamber has vacuum pressure of $10^{-4}$ to $10^{-5}$ mbar allowing up to $\sim$ 2 x $10^6$ V/m to be applied to the electrodes without any significant discharge [64, 113]. Increasing the length of the electrode however is not limited by any fundamental constraints.

Equation 3.9 can be used to calculate the maximum energy $W_i$ at which a particular charge state of ion species can be resolved from adjacent traces. Figure 3.9 shows $W_i$ for $A/Z$ = 2.0 (e.g. $C^{6+}$), plotted against $\Delta(A/Z)$ for different configurations of a TPS, either doubling the electric field strength or doubling the length of the electrode. For example, if the neighbouring ion tracks of $C^{6+}$ ($A/Z$ = 2.00) and $O^{7+}$ ($A/Z$ = 2.29), corresponding to $\Delta(A/Z)$ = 0.29, using 100 mm electric plates will provide track separation at significantly higher ion energies compared to using 50 mm electric plates with the same electric field or 50 mm plates with an electric field of double the strength [110].

The performance of a TPS with different electric plate lengths and the effect on the separation of the different charge states was simulated using PTRACE. These simulations assumed a point source of ions entering the TPS, when in reality the pinhole at the entrance of the TPS will determine a finite track size at the detector, thus the highest energies resolv-

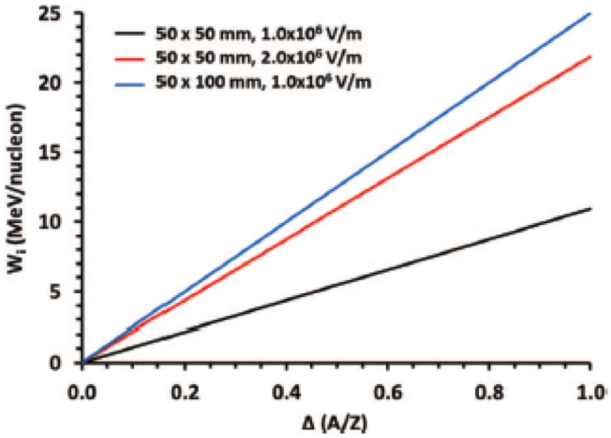


Fig. 3.9 Comparison of the maximum energy of $A/Z$ = 2.0 resolvable for different values of $\Delta(A/Z)$ achieved with 50 x 50 mm plates at 1 x $10^6$ V/m, 50 x50 mm plates at 2 x $10^6$ V/m, and 50 x 100 mm plates at 1 x $10^6$ V/m, assuming $L_{E2}$ = 150 mm [110].

able by the TPS will be generally lower in reality than those predicted by the simulations. The length of the electric plate, $L_{E1}$, was increased, while keeping $B_{peak}$, $L_{B1}$ and $L_{B2}$ constant. There was a significant improvement in the track separation at high energies (around 100 MeV protons and 200 MeV $C^{6+}$) for 150 mm electric plates, as compared to a standard TPS with 50 mm electric plates, shown in Figure 3.10.

A benchmark experiment for the longer electric plates was carried out at the Vulcan Petawatt laser facility of RAL-STFC, UK. A TPS with 150 mm electric plates and a Fuji BAS-TR image plate detector were employed. The laser was focused on target using a $f/3$ OAP, delivering $\sim$ 250 J of energy on target in a pulse duration of 0.75 ps. The 10 nm gold foil target was irradiated with an intensity of 3 x $10^{20}$ $Wcm^{-2}$. The TPS was placed 1.7 m from the laser irradiated target with a 100 $\mu$m pinhole at the front. The applied magnetic and electric fields in this case were $\sim$ 1.0 T and 1.8 x $10^6$ $Vm^{-1}$ respectively. As shown in the experimental data in Figure 3.11, the TPS was able to clearly resolve proton traces, several charge states of carbon and oxygen ions, and gold ions with adjacent charge states ranging from $\sim$ 30 to $\sim$ 50 [110].

The trapezoidal electric plate design was also benchmarked in a recent experiment car-

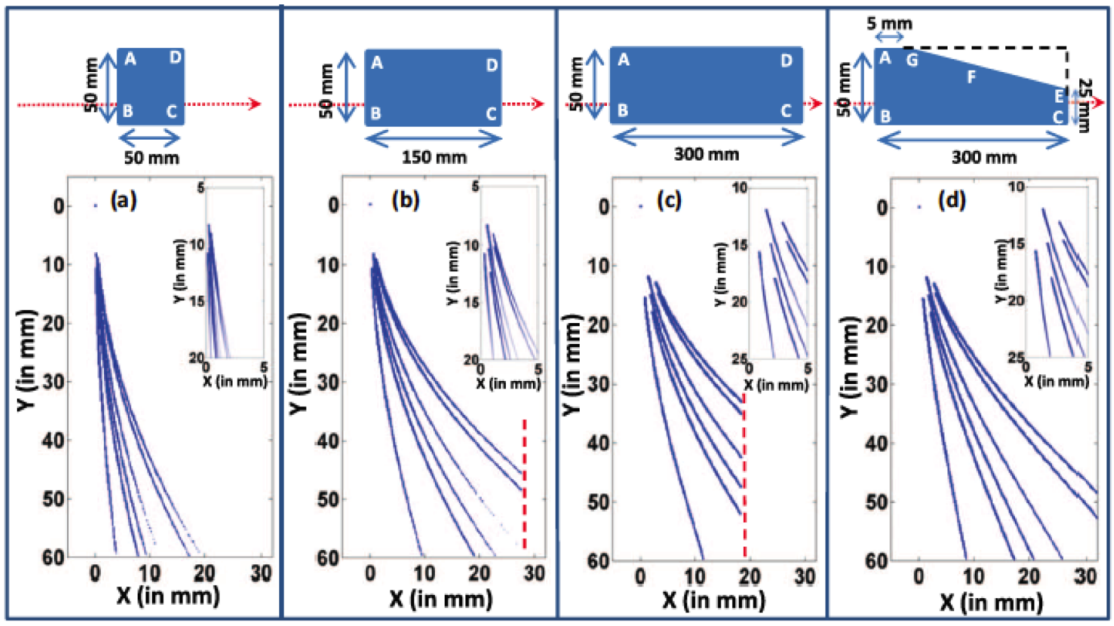


Fig. 3.10 Comparison between the TPS traces of several ion species (from left to right; up to 100 MeV $p^+$, up to 200 MeV $C^{6+}$, $C^{5+}$ and $C^{4+}$ ions, and up to 1000 MeV $Au^{40+}$ and $Au^{45+}$ ions) obtained using the different TPS configurations shown in the schematics. The red arrows show the ion beam direction, with the beam axis 10 mm above the bottom edge of the electric plate. For all simulated configurations $L_{E1} + L_{E2} = 300$ mm, the $B = 1.0$ T magnets were 50 mm in length ($L_{B1}$), the distance between the magnets and electric plates was 5 mm ($D$), the electric field strength $E = 1.8$ x $10^6$ V/m, and the electric plates were 18 mm apart ($d = 9$ mm). The insets show a zoomed in view of the high energy portion of the ion traces. There is improved trace separation in **(b)** as comapred to **(a)**, and even better $A/Z$ resolution and trace separation is obtained in **(c)**. Some clipping of the low energy ions is observed in **(b)** and more seriously in **(c)** as shown by the dotted red line. Trapezoidally shaped electric plates, as shown in **(d)**, can be used in such high resolution spectrometers allowing the lower energy ions to pass over the top of the plate, whilst keeping the same trace separation for the high energy ions as obtained in **(c)** [110].

ried out employing Vulcan Petawatt. The laser was focused onto the 25 $\mu$m aluminium targets in a $\sim$ 6 $\mu$m full width at half maximum spot using a $f/3$ OAP. This delivered a peak intensity in excess of $10^{20}$ Wcm$^{-2}$. The TPS employed in this experiment had 300 mm long trapezoidal electric plates ($L_{E1}$), $B = 0.972$ T 50 mm magnets ($L_{B1}$), the detector was placed 118 mm from the end of the electric plate ($L_{E2}$) and the electric field $E$ was $\sim$ 2.0 x $10^6$ Vm$^{-1}$. The experiment was interested in characterising proton and $C^{(4-6)+}$ ions,

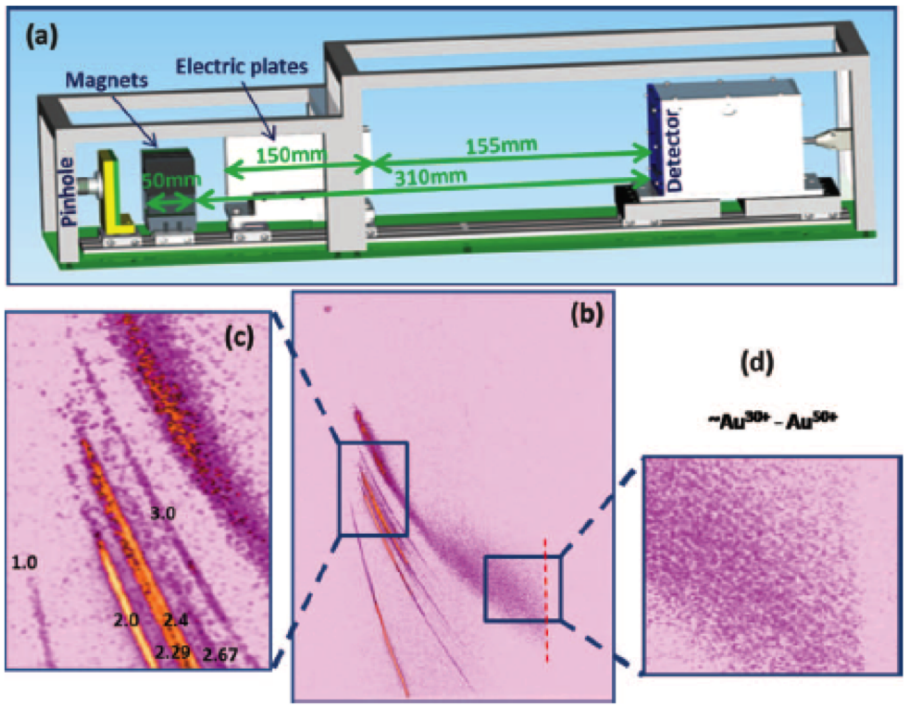


Fig. 3.11 **(a)** 3D schematic view of the TPS employed in the experiment, **(b)** data obtained by the TPS showing traces of different energy and mass-to-charge ratio ions produced by the interaction of the Vulcan laser with a 10 nm gold foil. The low energy ions are clipped by the electric plate as shown by the dotted line, **(c)** a zoomed in view of the enhanced species separation produced by the 150 mm rectangular electric plates, where the numbers represent $A/Z$ values for the ion species, such as 1.0 - $p^+$, 2.0 - $C^{6+}$ and $O^{8+}$, 2.29 - $O^{7+}$, 2.4 - $C^{5+}$, 2.67 - $O^{6+}$, 3 - $C^{4+}$, **(d)** a zoomed in view of the fine charge state separation of Au ions, which are clipped by the longer electric plate [110].

thus the trapezoidal geometry was chosen according to the following equations:

$$L_e^{clip} = \sqrt{\frac{\gamma^2 - 1}{\gamma} \frac{2\Delta mc^2}{qE}} \tag{3.16}$$

$$y_e^{clip} = \frac{qBL_{B1}}{mc^2\sqrt{\gamma^2 - 1}} \left( L_{B1} + D - \frac{L_{B1}}{2} + L_e^{clip} \right) \tag{3.17}$$

where $\gamma$ is the Lorentz factor and (x, y, z) = ($\Delta$, $y_e^{clip}$, $L_e^{clip}$) is the clipping position for a given separation ($\Delta$) between the beam axis and the electrode (a more complete explanation

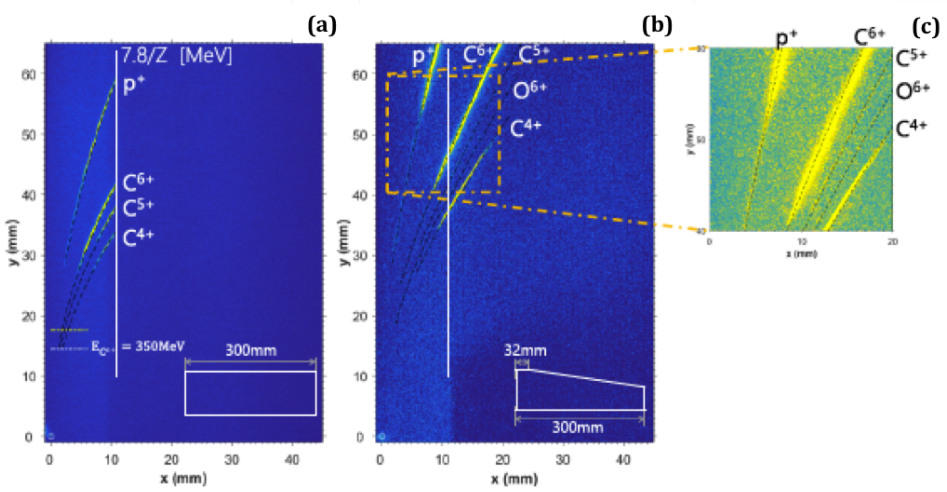


Fig. 3.12 Raw experimental data from the image plate scans employing different electric plate designs, as shown by the inset at the bottom right corner. The white line in **(a)** represents the clipping of the lower energy ion traces, which are not clipped when using the plate geometry shown in **(b)**. **(c)** shows a zoomed in view of the data shown in **(b)**, as marked by the orange square [112].

is available in reference [112]). The experimental results are shown in Figure 3.12, which shows that the longer electric plate was clearly able to resolve all the ion species with the significant clipping of the ion traces combated with the use of the trapezoidal plate.

### 3.3.2 Image Plate Detectors

Image plates (IPs) are widely used in laser plasma experiments for the detection of charged particles and X-rays, with the most commonly used types being BAS-MS and BAS-TR. Image plate detectors were developed by Fuji Photo Film Co. Ltd [117] in the early 1980s. They are passive detectors based on the principle of photoluminescence (PL), where an atom is excited to a higher energy state then returns to a lower state emitting a photon in the process. They are made of phosphors with phosphorescent properties and store energy for long periods of time, before being stimulated by photons of suitable wavelengths and releasing the stored energy as a de-excitation [104, 118]. They have many attractive properties such

as high spatial resolution of up to 10 $\mu$m, a high dynamic range of 4-5 orders of magnitude, insensitivity to electromagnetic noise, a linearity in response (the fluorescence emission is proportional to the radiation dose in the entire range) and they are reusable as the signal can be erased after every use by exposure to an intense visible light source for 10 - 15 minutes [102].

An IP has three main components; a protective layer, a photo-stimulable phosphor layer and a support. The plastic protective layer is normally 0 - 10 $\mu$m thick and is used to preserve the efficency of the phosphor by reducing the intensity of the radiation, with different thicknesses suitable for different applications, and IPs with no protective layer (such as BAS-TR mentioned above) used for low intensity radiation. The phosphor layer is 50 - 180 $\mu$m thick and is comprised of photo-stimuable crystal grains of BaF$X$:$Eu^{2+}$ ($X$ = Cl, Br or I, typically $X = Br_{0.85}I_{0.5}$) [119] of an average density 5.2 $gcm^{-3}$ and 5 $\mu$m size embedded in a urethane resin [104]. The support material of the IP is usually flexible polyester for ease of use in experimental set-ups.

The half-life for spontaneous decay from the metastable state of the phosphor layer is typically a few days, following a much faster decay phase in the first thirty minutes post exposure [102, 103, 111]. The energy stored in the IP is retrieved by stimulating the excited metastable state, up to several hours post exposure, using optical photons in the red part of the visible spectrum. The energy released is referred to as photo-stimulated luminescence (PSL), and is released as UV light.

PSL is formed by duplicate stimulations. When the IP is exposed to ionising radiation, electrons are liberated from the $Eu^{2+}$ ions are promoted into the conduction band of the phosphor. These electrons become trapped in the metastable lattice defects, called F-centres, producing a latent image in the phosphor with a lifetime of several days. These defects are intentionally introduced into the phosphor layer during the manufacturing process. The latent image is retrieved by scanning the IP with a 632.8 nm red read-out laser, which

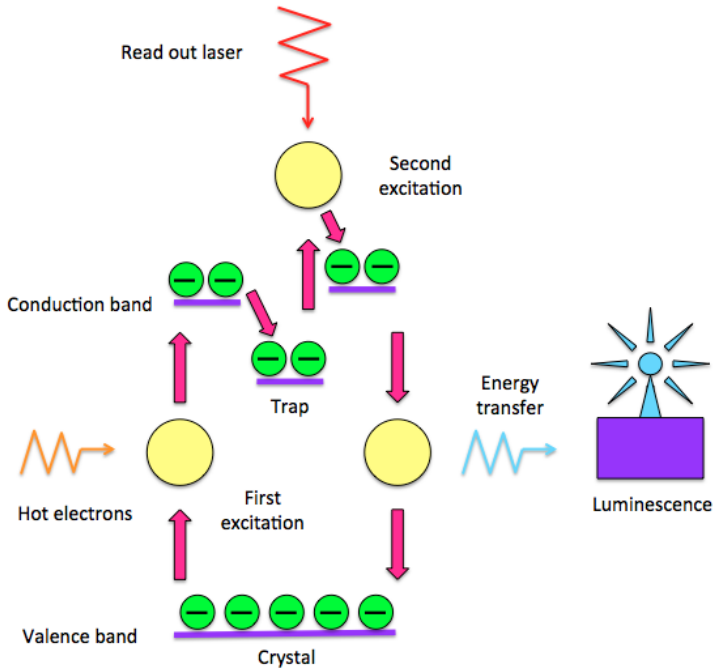


Fig. 3.13 The PSL process. Reproduced from [119].

excites the trapped ions into the conduction band, where they recombine with the $Eu^{3+}$ ions, emitting blue light at 400 nm that is detected with a photomultiplier tube. Some types of photo-stimulable layers with blue dye absorb the 632.8 nm red read-out laser to avoid the reduction of spatial resolution caused by the diffusion of the laser. The intensity of the emitted light is proportional to the incident energy of the particles that initially struck the IP. The laser and photomultiplier tube are housed in a complete reader (Fujifilm FLA-5000) which has a mechanism to scan the laser across the entire plate. The signal is digitised by an analogue to digital converter (ADC) and an algorithm in a 16 bit discrete number, thus the image is stored in a 16 bit format where each pixel represents a scanned position on the IP surface. The stored information in the IP is completely erased by returning the $Eu^{2+}$ ions to the ground state through exposure to a strong white light, allowing the IP to be reused [103, 118, 120, 121]. A schematic of the PSL process is shown in Figure 3.13.

The PSL value stored in each pixel of the readout image can be obtained by converting its

bit value, or quantum level (QL), using the following formula provided by the manufacturer of the scanner unit [117]:

$$PSL = \left(\frac{R}{100}\right)^2 \times \frac{4000}{S} \times 10^{Lx\left(\frac{QL}{2^G-1}-\frac{1}{2}\right)} \tag{3.18}$$

where R is the resolution, L is the latitude or dynamic range, S is the sensitivity and G is the bit depth [104, 111].

Some of the electrons which are trapped in the metastable state spontaneously recombine with the $Eu^{3+}$ ions before they are read-out by the laser, thus the recorded image is faded [103, 119]. The rate at which the image fades varies from very fast in the first tens of minutes post irradiation, to a significantly slower rate over the next few days. The fading rate close to the time of irradiation is dependent on the PSL signal strength at the time of exposure, the duration of the exposure and the type of IP [111]. A fading curve was obtained by Alejo et al. [111] for BAS-TR IPs, and the following empirical formula was inferred from the curve to determine the PSL signal at a reference time point of 30 minutes after exposure when the IP is scanned at time '$t$';

$$PSL_{30} = \left(\frac{30}{t}\right)^{-0.161} PSL(t) \tag{3.19}$$

The IPs used in the experiments described in this thesis were BAS-TR (Fuji Photo Film Co. Ltd.), which do not have the protective layer covering the phosphor active layer, thus allowing the detection of very low energy particles, making them the most sensitive IP existing on the market [102].

### 3.3.3 Radiochromic Films

GafChromic radiochromic films (RCF) have been used extensively for dosimetry of ionising radiation in medical physics and more recently for the characterisation of protons beams

from laser foil interactions. These films are self developing, consisting of an active monolayer which polymerises upon exposure to ionising radiation to form a darker dye. The dose versus the optical density response of RCF is quasilinear over several orders of magnitude in dose, is independent of the dose rate (Li *et al.* exposed films to X-rays, $\gamma$-rays and a 3.8 MeV electron beam over an absorbed dose rate range of 0.8 to 5 x $10^8$ $Gys^{-1}$, with the films exhibiting equivalent responses [122]), low dependence on the energy of the ionising particles and near water equivalence [100, 123, 124]. The films offer a superior spatial resolution compared to any other digital dosimetric 2D detector array (more than $10^4$ dots per inch (dpi) or less than 2.54 $\mu$m [106]), with the ability to detect steep dose gradients attractive for intensity-modulated radiation therapy (IMRT) with both photons and protons. The dose rate independent response makes RCF ideal for the dose determination in cell irradiation experiments employing laser driven ions, however the positioning of the samples and the RCF must be carefully considered [125]. Many types of RCF are available such as MD-V3, HD-V2, EBT-2 and EBT-3, each suited to a different purpose [126]. The films used in the cell irradiation experiments described in this thesis were EBT-3 normal and customised films designed by Ashland, International Speciality Products, Wayne, NJ, USA.

Care must be taken to reduce uncertainties associated with film dosimerty including film batch and scan orientation consistency, post exposure time, scanner warm-up characteristics and lateral film position on the scanner [101, 124]. Accurate film dosimetry guidelines have been published many times in literature, most notably by the American Association of Physicists in Medicine [127].

#### EBT-3 Normal and Customised Films

Gafchromic EBT (External Beam Therapy) films were designed as a substitute for silver halide radiography films in IMRT quality assurance systems [128]. Normal EBT-3 films are yellow tinted and comprise a 28 $\mu$m active layer sandwiched between two 125 $\mu$m

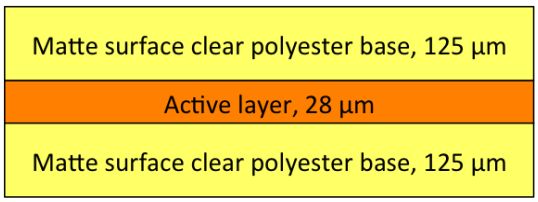


Fig. 3.14 The structure of EBT-3 dosimetry film. The film has 28 $\mu$m active layer sandwiched between two 125 $\mu$m matte-polyester substrates. The active layer contains the active component, a marker dye, stabilisers and other components which give the film its near energy-independent response [129].

matte surface clear polyester substrates, as shown in Figure 3.14. The symmetrical design prevents probable errors in measurement of optical density and also prohibits fringe artefact formation [123, 128]. Customised EBT-3 films have one of the protective layers removed. EBT-3 is particularly suited to for high energy photons, with a dynamic dose range of 0.1 to 20 Gy, but an optimum dose range of 0.2 to 10 Gy [129].

The active layer of the RCF is composed of polycrsytalline diacetylene suspended in a synthetic or natural polymer, the full chemical name of which is pentacosa-10,12-dyinoic acid (PCDA). The lithium salt of PCDA, LiPCDA, is used in EBT-3 films, which has more hair like crystals than PDCA. The addition of the lithium salt dopant provides the film with a greater low energy sensitivity [130]. When exposed to ionising radiation, the active layer undergoes polymerisation via a free-radical mechanism forming polydiacetylene chains. These chains are blue in colour and and provide the change in colour and optical density of the active layer. The number of chains formed is related to the dose deposited in the active layer, and thus the change in the optical density [130, 131]. The optical density is the reduction in the intensity of light that can be transmitted through the film and is defined as follows [118];

$$OD = log_{10}\left(\frac{I_0}{I}\right) \tag{3.20}$$

where $I_0$ is the maximum light intensity without the film and $I$ is the light intensity transmitted through the exposed film. The absorption spectrum typically has two peaks in the visible

region at 583 and 635 nm for EBT-3 films, so highest sensitivity and contrast during digitization is achieved using red light [131]. Transmission densitometers, spectrophotometers or film scanners can be used to digitise the RCFs, although attention must be paid to the time at which the films are scanned, as nearly complete dyeing occurs within milliseconds but increased dyeing can occur for the next 24 hours [106]. The pixel value for each particular colour channel is used for $I$ in equation 3.20.

The films used in the experiments described in this thesis were scanned with an Epson Perfection V750 Pro calibrated flat-bed transmission scanner. The scanner settings used were RGB 48 bit with resolution 300 dots per inch (dpi). To achieve accurate signal to dose conversion, the EBT-3 customised and normal films were calibrated for protons and X-rays. The calibrations were incorporated into a dose conversion Macro for ImageJ written by Domenico Doria for protons and carbon ions, and adapted by the author for X-rays. This Macro directly converts the raw signal from the scanned RCF image into dose. It takes each colour channel separately and converts it from 16 bit colour to dose, and recombines the three channels to produce a dose converted image. The dose is measured by selecting the appropriate region of the image relating to the ion energy of interest using ImageJ.

### 3.3.4 Ion Detection

In reality, numerous ion detection methods are used simultaneously with custom analysis packages to provide the best view of ion species and their properties produced in high power laser experiments. For example, images plates used in conjunction with TPSs were leveraged as part of a recent experiment employing the petawatt arm of the Vulcan laser system at the Rutherford Appleton laboratory, investigating the scaling of ion energy in a hybrid TNSA-RPA regime. The laser, focused by a f/3 off axis parabolic mirror, delivered 147 - 172 J at intensities of 2.2 - 9.7x$10^{19}$ Wcm$^{-2}$ to a variety of target materials (Ag, Al, Au, Cu, Formvar and composite targets) and thickness (10-3000 $\mu$m) in 1.0 - 5.2 ps pulses.

Three TPSs with BAS-TR image plates, TP-3, TP0 and TP3 were placed at -5.66, -0.59 and 9.24 degrees respectively from the laser axis. The image plates were analysed using a specially designed MATLAB GUI called TPspec.

TPspec works by reading in PSL converted, background subtracted images scanned from the Image plates placed at the exit of the TPS. The zero point of the image is manually selected, and the required parameters of the TP including the field positions and widths, solid angle, and the position of the image plate relative to the start of the magnet are read from a configuration file. The atomic mass M and the charge Z of the desired species to be traced are entered and the code generates a trace line on the image, according to the values of the electric and magnetic fields chosen. The equation set used to calculate the magnetic, $S_B$, and electric, $S_E$ field deflections are shown by Equations 3.9 and 3.10 below;

$$S_B = r_L - \sqrt{r_L^2 - L_{B1}^2} + \frac{L_{B1}L_{B2}}{\sqrt{r_L^2 - L_{B1}^2}} \tag{3.21}$$

$$S_E = \frac{qEL_{E1}}{mv_0^2}\left(\frac{L_{E1}}{2} + L_{E2}\right)\frac{r_L^2}{\sqrt{r_L^2 - L_{B1}^2}} \tag{3.22}$$

where $r_L = mv_0/qB$ is the Larmour radius, $L_{B1}$, $L_{B2}$, $L_{E1}$ and $L_{E2}$ correspond to the distances shown in Figure 3.7, $m$ is the mass (in kg) and $q$ is the charge (in C) of the species being traced, $v_0$ is the initial velocity of the ion, and $E$ and $B$ are the electric and magnetic field strengths respectively. Both the rotation of the image and the field strengths can be modified to exactly match the generated trace line to the experimental data.

Different species are traced by changing the values of M and Z, thus enabling the identification of all the M/Z ratios present. The data is obtained by selecting a region enclosing the traced species, subtracting a background region of the same size, and then the signal and the energy spectrum are calculated. To select the region, two points are chosen; one at

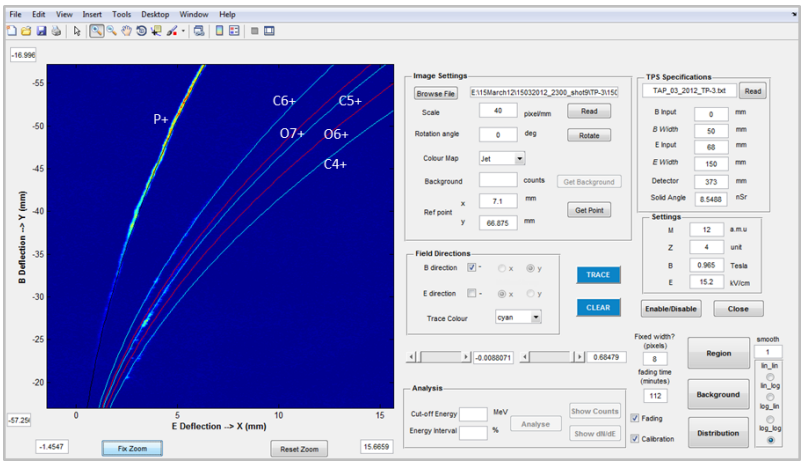


Fig. 3.15 MATLAB GUI TPspec with an example of an image plate showing traced proton, carbon and oxygen tracks.

the high energy end and the other at the low energy end of the trace line. The code stores all the values of the $y$ co-ordinates between these two points, which corresponds to the deflection owing to the magnetic field, calculates the energy of the particle that produced that deflection and uses these values to calculate the corresponding $x$ co-ordinates, or electric field deflection. An analogous method is used to obtain the background region. The signal and thus the energy per nucleon of the desired species is calculated by summing the signal from the region surrounding the trace line and subtracting the summed signal from the background region. The distribution can be viewed immediately on linear or logarithmic axes and exported to Excel for more detailed analysis.

Options are available to calibrate the data according to the species traced and to correct the signal level for fading. The calibration function determines the energy of the entire ion species, as well as calculating the energy per nucleon, and the fading function calculates the signal that would have been present on the image plate directly after the shot was taken according to how many minutes after the shot time the image plate was scanned.

Figures 3.16, 3.17 and 3.18 shows example proton, carbon and gold ion spectra obtained using the TPspec code for three different laser shots, each on 10 nm Au targets, irradiated

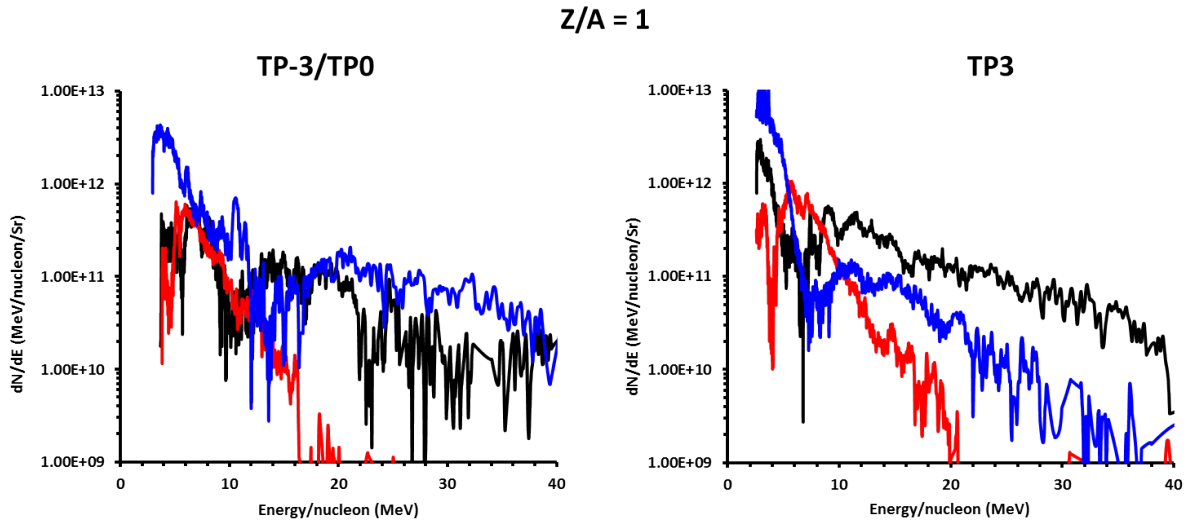


Fig. 3.16 Proton spectra obtained from three shots on 10 nm Au targets of [energy on target (J), pulse duration (ps)] of [171.54, 5.2] shown in black, [150.93, 2.3] shown in red and [147.36, 1.0] shown in blue.

with laser pulses with intensities of $2.2\text{x}10^{19}$, $4.3\text{x}10^{19}$ and $9.7\text{x}10^{19}$ $\text{Wcm}^{-2}$ and pulse durations of 5.2, 2.3 and 1.0 picoseconds respectively.

Here narrow band features which could be attributed to RPA can be clearly seen in the proton (Z/A = 1), carbon (Z/A = 0.5) and gold (Z/A = 0.228) spectra, with the spectral peaks being well separated from the lower energy component. The protons and carbon ions which have been accelerated have originated from the hydrocarbon contaminants present on the surface of the gold target. The peaks in the ion spectra appear to be ordered with the proton peak at a slightly higher energy than the carbon peak, $\sim$ 3 - 4 MeV/nucleon.

The highest energy peak for protons was calculated to be 20.7 $\pm$ 7.2 MeV/nucleon, for $C^{6+}$ it was 12.5 $\pm$ 5.3 MeV/nucleon, and for $Au^{45+}$ it was 7.6 $\pm$ 2.2 MeV/nucleon. These energies were all obtained in the same shot which is shown in blue in Figures 3.16, 3.17 and 3.18.

In order to assess the possible influence of radiation pressure effects on the spectral profiles obtained, a previously developed simple theoretical model was used, which takes

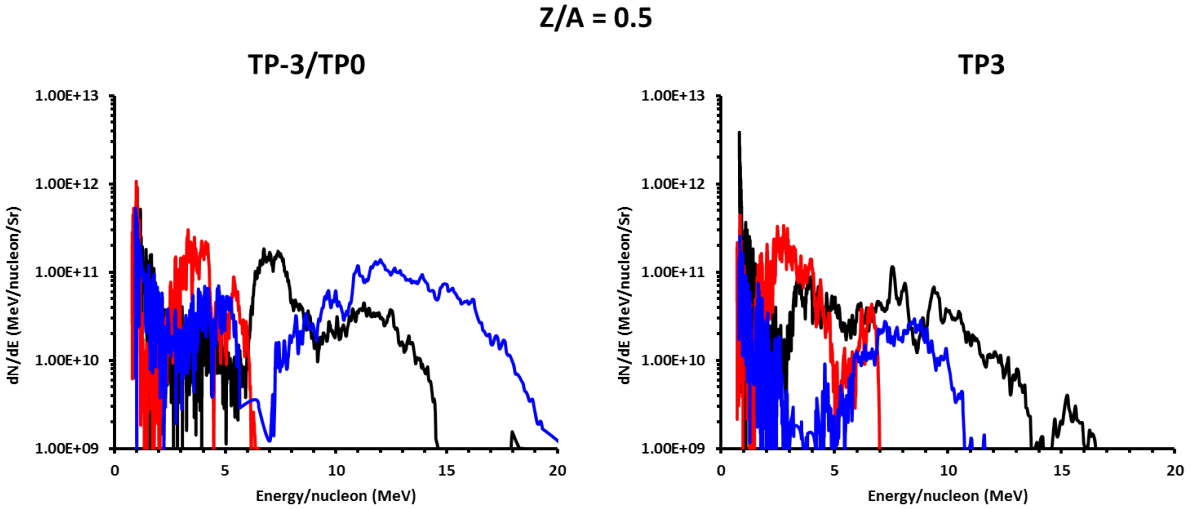


Fig. 3.17 $C^{6+}$ spectra obtained from three shots on 10 nm Au targets of [energy on target (J), pulse duration (ps)] of [171.54, 5.2] shown in black, [150.93, 2.3] shown in red and [147.36, 1.0] shown in blue.

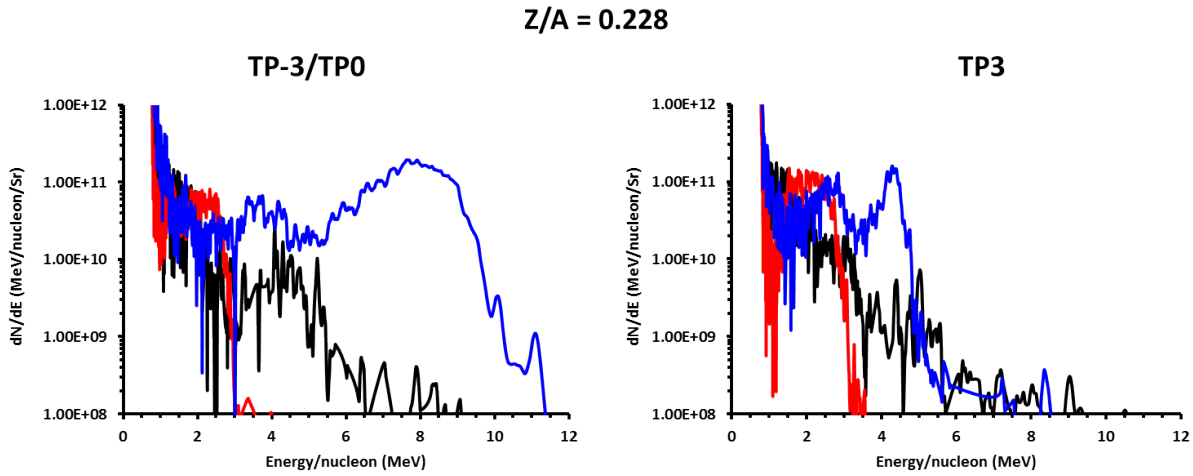


Fig. 3.18 $Au^{45+}$ spectra obtained from three shots on 10 nm Au targets of [energy on target (J), pulse duration (ps)] of [171.54, 5.2] shown in black, [150.93, 2.3] shown in red and [147.36, 1.0] sown in blue.

into account the hole-boring and light-sail regimes of the RPA mechanism [46]. For thin targets (sub-micron) and high intensities, the time required for hole-boring to saturate is much less than the laser pulse duration, which is approximately equal to the time scale required for light-sail, thus light-sail will dominate over hole-boring and will have higher efficiency. In such a limit it can be estimated that the peak energy of the ion will scale as $\varepsilon^{\alpha}$, with $\alpha = 2$ for $\varepsilon \ll 1$ and $\alpha = 1$ for $\varepsilon \gg 1$ in the ultra-relativistic case, where $\varepsilon$ is the dimensionless fluence parameter and is approximately equal to $a_0^2\tau_p/\chi$ [46].

The dimensionless fluence parameter $a_0^2\tau_p/\chi$ was calculated for each laser shot, where;

$$a_0 = 0.85\sqrt{I_0\lambda^2/10^{18}Wcm^{-2}} \tag{3.23}$$

$$\tau_p = ct_p/\lambda \tag{3.24}$$

$$\chi = \rho' l/\lambda \tag{3.25}$$

$$\rho' = \rho/m_p n_c \tag{3.26}$$

where $I_0$ is the peak laser intensity (in $\mathrm{Wcm^{-2}}$), $\lambda$ is the laser wavelength (1.054 $\mu$m), $t_p$ is the laser pulse duration (in ps), $c$ is the speed of light (300 $\mu\mathrm{m\ ps^{-1}}$), $l$ is the target thickness (0.01 $\mu$m in this case), $\rho$ is the target density (19.32 $\mathrm{gcm^{-3}}$ for Au), $m_p$ is the mass of a proton ($1.27\mathrm{x}10^{-24}$ g) and $n_c$ is the critical electron density ($1\mathrm{x}10^{21}$ $\mathrm{cm^{-3}}$).

By assuming the switch-on time for the light-sail phase is the time at which the compressed ion front reaches the target rear surface as a result of the hole-boring phase, we have a simple rigid model where the degree of ionisation of the target ions and the number of different ion species present in the compressed layer are irrelevant. Hence the contaminant

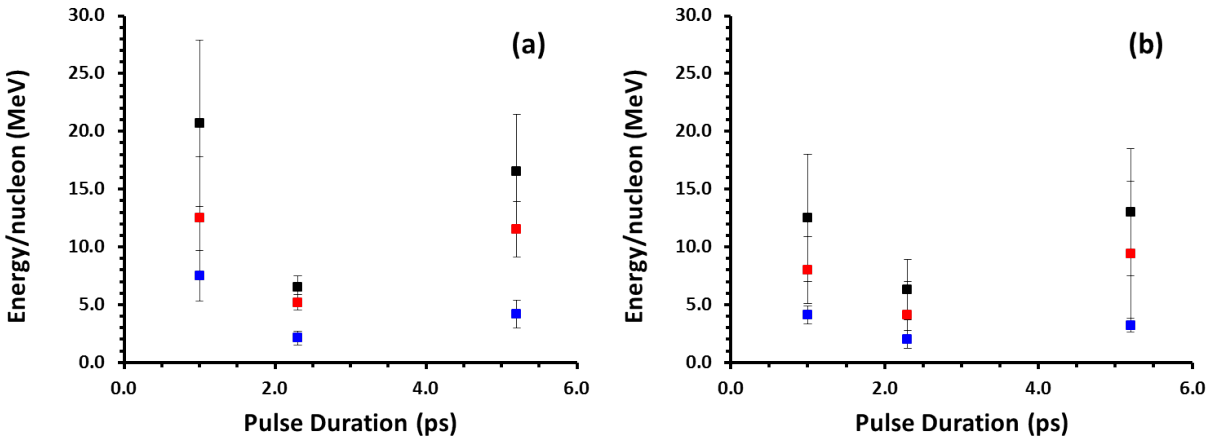


Fig. 3.19 Peak ion energies plotted against pulse duration for the three shots summarised in Table 3.1 for TP-3/TP0 in **(a)** and TP3 in **(b)**.

layer on the target, which is typically a few nm thick and has a significantly lower density than the target material, can be ignored without any loss of generality.

| Shot | $t_p$ (ps) | Energy (J) | Intensity (Wcm$^{-2}$) | Fluence (Jcm$^{-1}$) | $a_0^2\tau_p/\chi$ |
|---|---|---|---|---|---|
| 1 | 5.2 | 171.54 | 2.1748x10$^{19}$ | 1.26x10$^{9}$ | 235.38 |
| 2 | 2.3 | 150.93 | 4.3261x10$^{19}$ | 1.11x10$^{9}$ | 207.1 |
| 3 | 1.0 | 147.36 | 9.7147x10$^{19}$ | 1.08x10$^{9}$ | 202.2 |

Table 3.1 Summary of shot details.

The three shots which have been considered all have the same target thickness and material (10nm Au), roughly the same energy delivered to the target, but different pulse durations. The details of these three shots are summarised in Table 3.1 above. The laser focal spot size remained constant for all three of these shots at 1.36x10$^{-7}$ cm$^2$, and the fluence is defined as the pulse energy per unit surface [49].

Figure 3.19 shows a plot of the peak ion energies against pulse duration, and as the ion energies remain almost constant for the 1.0 and 5.2 ps pulses, this could be an indication of the favourable dependence on fluence rather than intensity as described earlier. However, as the 2.0 ps pulse does not produce a similar energy, this is not conclusive and all shots may

have been subject to fluctuations.

For the non-relativistic case, the energy scaled as $(a_0^2\tau_p/\chi)^2$ as expected, and the hole-boring phase terminated well before the peak of the laser pulse with the non-linear reflectivity remaining at unity for the duration of the laser pulse. Therefore the results of this experiment suggested that the ion energy could be enhanced by increasing the fluence of the laser and/or reducing the target areal density.

# Chapter 4

# Radiation Therapy

The clinical concept of radiation therapy is to deliver a high dose of radiation to tumours to kill all cancerous cells, whilst minimising the dose to normal tissue to avoid acute and late side effects. Radiation therapy is received by approximately 60% of cancer patients in the USA, either alone or in combination with other therapies, and is usually delivered to the tumour by electron linear accelerators [132]. The radiation reacts with the water inside the cells to generate reactive oxygen species (ROS) which cause damage to the DNA. Apoptosis, or cell death, will be induced in the cells that contain large amounts of damaged DNA. The supply of oxygen affects the potency of ionising radiation, with more double strand breaks occurring in cells irradiated in the presence of oxygen [132]. In the presence of oxygen, the induced damage is also more likely to be permanent.

The advantages of radiation therapy over other treatments such as chemotherapy or surgery include better cosmesis, the loco-regional treatment of cancer without direct removal of organs or tissues, thus organs may be preserved, and the treatment prescribed is less restricted by pre-existing medical conditions. However, it is almost impossible to avoid some damage to normal tissues, though repair and recovery of said tissue is possible, multiple daily treatments over several weeks may be required, especially for curative treatments and there is also the psychological drawback of not actually "removing" the cancer.

The dose of radiation that can be used on a patient is limited by the damage induced in normal tissues. The adverse effects on normal tissues can be minimised by focusing multiple radiation beams from different angles onto the cancer and by the use of fractionation. Typically the daily dose given to a patient is 2 Gy, which in total is appreciably greater than those that have been shown to cause cancer, hence the overall DNA damage will be sufficient to kill the cancer cells rather than just generate changes that can be repaired within the tumour [133].

## 4.1 Interaction of Radiation with Matter

An understanding of the interactions of ionizing radiation with matter is essential when discussing radiation therapy. Ever since Wilhelm Conrad Röntgen discovered X-rays in 1895, it has been known that radiation interacts in many different ways with matter. Radiation therapy depends upon the absorption of radiation by biological tissues, and the biological effects following the interaction represent the effort of the biological tissue to deal with this absorbed energy. Five important generalisations which should be remembered when discussing these effects are as follows [134]:

1. the interaction of radiation with cells is a matter of chance, it may or may not happen, and damage may or may not be produced,

2. the initial deposition of energy is very rapid – approximately $10^{-17}$ s,

3. the energy is deposited randomly within the cell,

4. the damage produced in the cells by ionizing radiation is non-unique and cannot be distinguished from damage produced by other traumas suffered by the cell,

5. the changes which occur biologically only occur after a period of time, the length of which depends on the initial dose of radiation received.

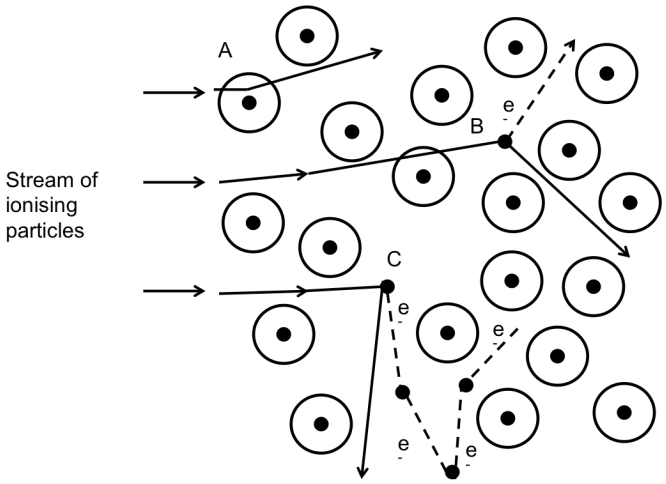


Fig. 4.1 A simplified model of the interaction of radiation with matter. Interaction A causes excitation, B causes ionisation, and C causes multiple ionisations. Each ioisation frees an electron from the atom to which it was bound. Reproduced from [134].

A simplified model of radiation-matter interactions is to consider the radiation as a stream of fast moving particles, whether that be protons, photons or other charged or uncharged particles, and the matter as an array of atomic nuclei each with their own electron shell system. As the fast moving particles try to penetrate the array of atoms, they will invariably collide with the atoms, sometimes transferring the energy of excitation during the collision, which is quickly dissipated as heat [135]. These types of collision are discussed in more detail in Section 4.1.1. Occasionally ionisation of the atoms occurs, where the interaction is so violent that one of the bound electrons in the outermost shell is knocked out and becomes free. This electron may itself have enough energy to cause further ionisations, and a cluster of ions may be formed in the medium. The amount of energy required for ionisation to occur is 34 eV (average energy required to produce an ion pair in tissue [136]), an amount invariably possessed by both a quantum of X-ray photons and all charged particles of interest to radiobiology.

With regard to the attenuation and range of the different particles in the target medium, the mass and charge of the particle are important factors. As the bombarding particle will be

moving through a highly charged region, an interaction is much more likely to to take place if the particle itself is charged and will therefore come under the influence of the strong electric fields associated with the nucleus and electrons of the target material. Since X-ray photons have no charge and have zero rest mass, they are very difficult to attenuate, unlike protons which have a larger mass and are charged, therefore are more easily attenuated. Charged particles, such as protons, eventually become trapped in the high electric field around the nucleus and have a finite range. X-ray photons on the other hand are stopped by random processes and are attenuated exponentially, thus do not have a finite range [135].

### 4.1.1 Photon Radiation

The absorption of photon radiation is a statistical process that can be described by an exponential function:

$$I = I_0 e^{-\mu \rho d} \tag{4.1}$$

where $I_0$ is the initial intensity, $I$ is the remaining intensity after penetration through a layer of thickness $d$ and density $\rho$, and $\mu$ is the mass absorption coefficient in $\mathrm{cm}^2\mathrm{g}^{-1}$. The photons interact with the atoms of the penetrated material via four distinct effects:

1. elastic scattering
2. the photoelectric effect
3. the Compton effect
4. pair production

The photon interacts with the electron shell system of the atom in elastic scattering, the photoelectric and Compton effects, and with the atomic nucleus in the pair production effect [137].

### Elastic Scattering

When photons pass very close to atoms in the target material, they may cause the electrons in the target atom to take up vibrational energy. The electron will vibrate at a specific frequency which corresponds to the incoming photon as this is a resonant process. The electron quickly re-radiates this energy, as the this is an unstable state, with the radiation being emitted in all directions with the same frequency as the incoming photon. This process scatters and attenuates the photon energy, but does not absorb it.

This interaction is dominant when the majority of the electrons behave as bound electrons, which occurs when the binding energy of the electrons is high, i.e. when the scattering material has a high atomic number, and when the bombarding photons have have relatively low quantum energy [135].

The probability of elastic scattering is expressed through identifying the mass attenuation coefficient particular to this process, $\varepsilon/\rho$, as is numerically expressed as a cross section area. The process is more likely to occur if the cross section area is high, and increases with increasing atomic number of the scattering material,

$$\varepsilon/\rho \propto Z^2 \tag{4.2}$$

but decreases with increasing radiation quantum energy [135].

$$\varepsilon/\rho \propto \frac{1}{hf} \tag{4.3}$$

### The Photoelectric Effect

The photoelectric effect normally occurs when the photon reacts with the innermost electrons of the atom and is thus totally absorbed. The liberated electrons are ejected from the atomic system of the atom, creating vacancies in the shell system, followed by the emission

of photons of lower energy. If the binding energy of the electron is $E_x$ and the photon energy is $E_\gamma$, the kinetic energy of the ejected atom is $E_\gamma - E_x$, therefore $E_\gamma$ must be greater than $E_x$ for this interaction to take place. This criteria gives rise to absorption edges in the spectra.

Although the energy is most often released in the form of an emitted photon, it can also be transferred to another electron, which is in turn ejected from the atom. This second ejected electron is called an Auger electron. The kinetic energy of this electron corresponds to the energy difference between the initial electronic transition into the vacancy and the ionisation for the electron shell from which the Auger electron was ejected. The energy of the Auger electrons range from a few to several hundred eV, so their range in tissue is short, thus their energy is deposited in the immediate vicinity of the decay site, and the photoelectric effect results in the total absorption of the initial photon. The resultant high local energy density can equal or even exceed that along the track of an $\alpha$-particle with corresponding radiobiological damage [135].

The photoelectric effect is dominant for photons below 100 keV. In heavier atoms there is a larger number of electrons with which the photon can interact, thus the cross section is dependent on a fairly high power of the atomic number $Z$ of the atom [137]:

$$\sigma_{PE} \propto Z^5 \alpha^4 \left( \frac{m_e c^2}{E_\gamma} \right)^{3.5} \tag{4.4}$$

where $\alpha = e^2/(4\pi\varepsilon_0 \hbar c)$ is the fine structure constant, $\varepsilon_0$ is the dielectric function, $e$ the elementary charge, $c$ the velocity of light and $\hbar$ is Planck's constant. $E_\gamma$ is in units of MeV. The electrons which have been liberated by the interaction move through the solid material, losing energy by colliding with other atoms, raising the temperature of the material until they are captured in the outer state of another atom.

The strong $Z$ dependence of photoelectric absorption is the basis of diagnostic radiology [138], where the degree of absorption at any point in the body is determined by the atomic number and the density of the material at that point. The continuous X-ray spectra which

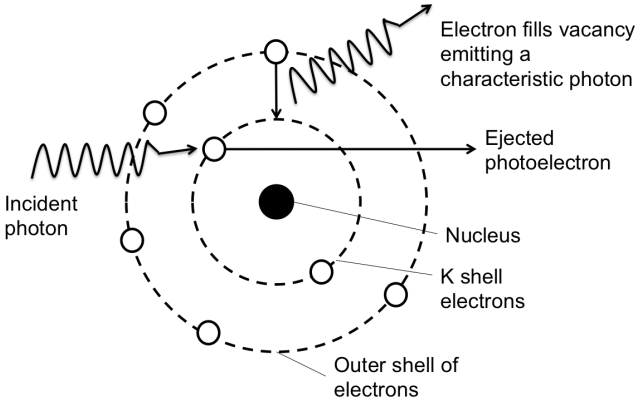


Fig. 4.2 Schematic representation of the photoelectric effect, reproduced from [135].

are favoured for diagnostic imaging, contain wide ranges of photon energies, and the strong energy dependence of photoelectric absorption ensures the absorption cross-section also extends over a wide range, allowing detail in lightly and strongly absorbing anatomical features to be imaged effectively.

### The Compton Effect

Discovered by Arthur Holly Compton in 1927, this is a scattering effect of photons on loosely bound electrons, where the incoming photon changes its original direction of motion, transferring some of its energy to the electron in the process. The energy of the loosely bound electron is much smaller than that of the incoming photon, and can be considered as quasi-free during this process. The interaction of the electron and the incoming photon complies with the laws of conservation of momentum and energy.

From the conservation of momentum:

$$p_e \sin\phi = \frac{E'}{c} \sin\theta \tag{4.5}$$

$$\frac{E}{c} = p_e \cos\phi + \frac{E'}{c} \cos\theta \tag{4.6}$$

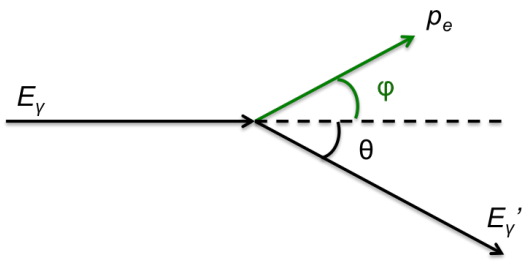


Fig. 4.3 Illustration of the Compton effect, reproduced from [138].

For the conservation of energy:

$$U^2 = p_e^2c^2 + m_e^2c^4 \tag{4.7}$$

Hence,

$$\left(E_\gamma - E'_\gamma + m_ec^2\right)^2 = p_e^2c^2 + m_e^2c^4 \tag{4.8}$$

Using equations 4.5 and 4.6, and the trigonometric identity $\sin^2\phi + \cos^2\phi = 1$:

$$\sin^2\phi = \left(\frac{E'_\gamma}{p_ec}\sin\theta\right)^2 \tag{4.9}$$

$$\cos^2\phi = \left(\frac{E_\gamma}{p_ec} - \frac{E'_\gamma}{p_ec}\cos\theta\right)^2 \tag{4.10}$$

$$p_e^2c^2 = \left(E'_\gamma\sin\theta\right)^2 + \left(E_\gamma - E'_\gamma\cos\theta\right)^2 \tag{4.11}$$

From equation 4.8,

$$p_e^2c^2 = \left(E_\gamma - E'_\gamma + m_ec^2\right)^2 - m_e^2c^4 \tag{4.12}$$

$$\left(E'_\gamma \sin\theta\right)^2 + \left(E_\gamma - E'_\gamma \cos\theta\right)^2 = \left(E_\gamma - E'_\gamma + m_e c^2\right)^2 - m_e^2 c^4 \tag{4.13}$$

$$m_e c^2 \left(E_\gamma - E'_\gamma\right) = E_\gamma E'_\gamma (1 - \cos\theta) \tag{4.14}$$

$$\frac{1}{E'_\gamma} - \frac{1}{E_\gamma} = \frac{1}{m_e c^2} (1 - \cos\theta) \tag{4.15}$$

The photon is therefore scattered with a change of energy, which is a function of the scattering angle. Equation 4.15 can be written in terms of wavelength as $E = hc/\lambda$.

$$\lambda' - \lambda = \frac{h}{m_e c} (1 - \cos\theta) \tag{4.16}$$

Here $h/m_0 c$ is known as the Compton wavelength, and is equal to 2.426 x $10^{-12}$ m. Photons with wavelength much greater than the Compton wavelength (corresponding to $E_\gamma \ll$ 511 keV) suffer a relatively small fractional change in photon energy, while photons with a wavelength much shorter (corresponding to an energy $E_\gamma \gg$ 511 keV) have an increment added which causes the scattered radiation to approach a constant wavelength, irrespective of the primary wavelength [138].

Compton scattering is an incoherent process in which all the electrons act independently. The cross section is given per electron, thus the cross section per atom is proportional to the atomic number Z over a wide range of photon energies:

$$\sigma_C = Z\sigma_C(e) \tag{4.17}$$

The wide range of energies produces a continuous photon spectrum which starts with a sharp energy, called the Compton edge, and continues to lower energies [137].

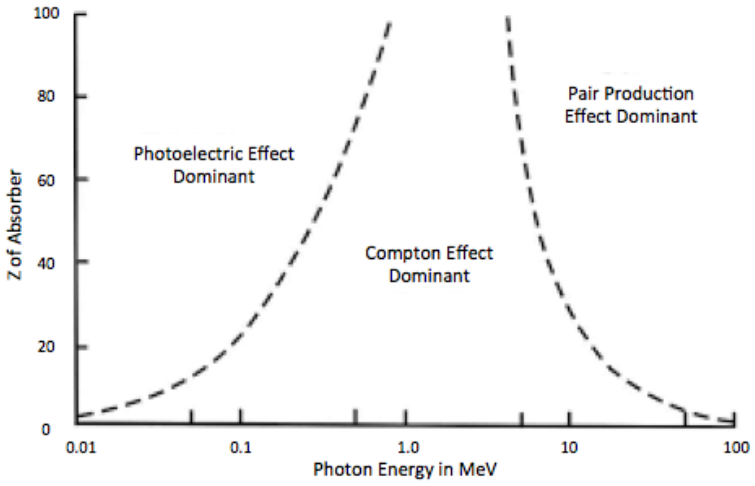


Fig. 4.4 Relative importance of photoelectric absorption, Compton scattering and pair production reproduced from [138].

### Pair Production

The Photoelectric effect and Compton scattering both depend upon the quantum behaviour of the photon. The third process of pair production occurs when photon energy exceeds $2m_ec^2$ (1.022 MeV). When the photon is in close proximity to atomic nucleus, the electromagnetic field of the photon interacts with the Coulomb field of the nucleus, causing the creation of an electron-positron pair. It is necessary for two particles to be emitted in order to conserve charge, thus no process of this nature can occur below the threshold energy.

Using equation 4.7 and conservation of momentum, the total momentum, $p_T$ of the two charged particles can be calculated as follows:

$$U_-^2 = p_-^2c^2 + m_e^2c^4 \qquad \text{and} \qquad U_+^2 = p_+^2c^2 + m_e^2c^4 \tag{4.18}$$

$$p_- = \frac{1}{c}\left(U_-^2 - m_e^2c^4\right)^{\frac{1}{2}} \qquad \text{and} \qquad p_+ = \frac{1}{c}\left(U_+^2 - m_e^2c^4\right)^{\frac{1}{2}} \tag{4.19}$$

$$p_T = \frac{1}{c}\left\{\left(U_-^2 - m_e^2c^4\right)^{\frac{1}{2}} + \left(U_+^2 - m_e^2c^4\right)^{\frac{1}{2}}\right\} \tag{4.20}$$

This is the value of the total momentum in the limiting case, in which both particles are propagated in the same direction from the point of production. From inspection we can see that this combined maximum momentum is always less than the momentum of the initial photon, $p_\gamma$, which is:

$$\frac{1}{c}\left(U_- + U_+\right) \tag{4.21}$$

In order for the momentum to be conserved there must be an additional body present, which can be supplied by a nucleus, and thus the interaction takes place via its Coulomb field [138].

The remaining electrons in the partially ionised atom screen the nuclear charge, thus the cross section is dependent on the state of ionisation of the atom. The general form of the cross section is given by:

$$\sigma_{Pa} \propto 4\alpha r_e^2 Z^2 \tag{4.22}$$

where $\alpha$ is again the fine structure constant and $r_e = e^2/\left(m_e c^2\right)$ is the classical electron radius. This process becomes more probable as the energy of the photon increases as the difference between $p_\gamma$ and $p_T$ becomes progressively less. The momentum can be divided between the electron and positron in any proportion, but in the most probable events the momentum is divided equally, maximising $p_T$ and thus minimising $p_\gamma$. Pair production is important at high photon energies and becomes even more important at high atomic numbers.

The relative importance of the three processes discussed in illustrated in Figure 4.4.

### 4.1.2 Swift Charged Particles

In general the charged particles interact with the atoms of the matter which they penetrate. The interactions take place simultaneously between the charged particle and the electron shell system and atomic nucleus of the target atom. Interactions involving the electron shell system are termed energy loss, and interactions with the nucleus are termed nuclear energy loss.

#### Heavy Charged Particles

The swift particle carries a transient field which is felt by both the target nuclei and the electrons of the target atom [137]. As the ion passes the target atom, momentum is transferred which gives more energy to the electrons, because of their much smaller mass, rather than the heavier nucleus. In general, electronic energy loss is the main process by which energy is lost.

The stopping power of the medium is the rate at which energy is lost per unit path length. This process of energy loss is statistical as the amount of energy transferred in each collision varies. A classical and quantum mechanical calculation of the stopping power in the energy range of swift charged particles relevant for medical applications results in the following Bethe-Bloch formula:

$$\frac{-dE}{dx} = \left(\frac{ze^2}{4\pi\varepsilon_0}\right)^2 \left(\frac{4\pi Z\rho N_A}{Am_e v^2}\right) \left\{ ln\frac{2m_e v^2}{\left\langle E_B^{(e)} \right\rangle} - ln\left(1-\beta^2\right) - \beta^2 \right\} \tag{4.23}$$

where $z$ is the actual charge state of the ion, $Z$, $A$, and $\rho$ are the atomic mass number, the atomic number and the density of the stopping material, $N_A$ is Avogadro's number, $v = \beta c$ is the relativistic ion velocity, and $m_e$ is the mass of the electron. $\left\langle E_B^{(e)} \right\rangle$ is an averaged ionisation energy for the material.

The energy dependence can be written as a function of the ion energy using an exponent

$k$:

$$\frac{dE}{dx} = \frac{const.}{E^k} \tag{4.24}$$

if all the constants are combined.

The dominant term in equation 4.23 is proportional to $1/v^2$, with a smaller contribution coming from the logarithmic term. Equation 4.24 is an empirical approach which is reliable if $k \approx 0.8$ for practical calculations.

Using simple integration the range of particles in matter can be calculated from equation 4.24:

$$R = \int dx = \int \frac{dE}{dE/dx} \propto E^{1+k} \tag{4.25}$$

From equation 4.23 it can be seen that the stopping power will rise as the energy of the particle decreases, thus the number of ions produced per unit path length (the ionisation density) increases until the end of the particle range is reached.

The dependence of the stopping power on the ion velocity, 4.23 can be rewritten as:

$$\frac{dE}{dx} \propto z^2 f(v) \tag{4.26}$$

which shows the dependence of the actual charge of the particle $z$, allowing the range of the particle to be expressed as a function of the ion velocity $f(v)$, which is useful for estimating the range of a charged particle in matter:

$$R = \int_E^0 \frac{dE}{(dE/dx)} \propto \frac{m_e}{z^2} F(v) \tag{4.27}$$

Equation 4.23 also contains the dependence on the density of the stopping medium,

which for a fixed charge is:

$$\frac{1}{\rho}\frac{dE}{dx} \propto \frac{Z}{A} ln\left(\frac{2m_e v^2}{\left\langle E_B^{(e)}\right\rangle}\right) \tag{4.28}$$

with $\left\langle E_B^{(e)}\right\rangle$ as the averaged ionisation energy. These are all statistical processes for which the average values are known [137].

### Electrons and Positrons

When passing through matter, light particles such as electrons and positrons suffer collisional energy loss $-dE/dx|_{coll}$. However, they suffer an additional loss of energy owing to their small mass. This energy is lost through the emission of electromagnetic radiation, termed $-dE/dx|_{rad}$. This effect arises from a charge, such as the electron charge, being scattered in the electric field of another charge, mainly that of the atomic nucleus [137]. Energy lost in this way is known as bremsstrahlung radiation. In the case of the electron, it is radiation arising from the acceleration of the electron as it's path deviates from the straight-line path by electrical attraction in the nucleus's field. In the case of the positron, it is the radiation produced form the deceleration of the positron through electrical repulsion.

Below 10 MeV, the contribution of the radiative energy loss is relatively small compared to the other processes. Even at energies of 50 keV, these very light particles travel at velocities approaching the velocity of light, therefore equation 4.23 must be modified, and the energy loss and range of the particles have to be calculated on the basis of special relativity.

Collisional interactions, such as the Coulomb interaction, are only efficient for a very short time when the particles are travelling at high velocities. Even though the quantity $-dE/dx|_{coll}$ is much smaller, the particles can undergo many collisions, thus the range is much larger than that calculated by simply integrating $dE/dx$. However, electrons colliding with other electrons lose a much higher proportion of their energy, thus the range of

electrons is much less well defined than for heavier particles. Furthermore, if the incoming electron transfers almost all its energy to another electron, the penetrating electron may not be the same as the original electron. The movement of these electrons causes the temperature of the material to increase.

As long as the positrons are moving quickly, they behave much as the electrons do. However, at the end of their range they normally form a hydrogen like atom called positronium (electron-positron bound state), which finally annihilates into $\gamma$-quanta [137]. The sum of the energies corresponds to twice the mass of the electron, $2m_e c^2 = 1.022$ MeV.

## 4.2 Radiation Effects on Human Tissue

### 4.2.1 Radiation Damage

DNA (deoxyribonucleic acid) is the main target for the biological effects of radiation. Consequently, it is damage to DNA that leads to all observed macroscopic biological effects. The DNA molecule is the most important molecule with respect to the function and reproduction of a cell. DNA is a coiled double-helical polymer comprised of deoxyribose-sugar molecules linked to one of the four phosphate base groups; adenine, guanine, cytosine and thymine [137]. Two of the bases, thymine and cytosine, are single-ring groups called pyrimidines, the other two, adenine and guanine, are double ring groups called purines [139]. In this double helix, the two bases meet and associate in the middle of the double helix to stabilise the molecule. Only certain pairs of bases can associate in this fashion: adenine must pair with thymine, and guanine must pair with cytosine. This means that by describing one strand of the DNA molecule you have also defined the other strand, and the sequence of the bases specifies the genetic code. The human body uses one strand of DNA to make a new copy by matching a complementary set of new bases with the existing strand as the template [140].

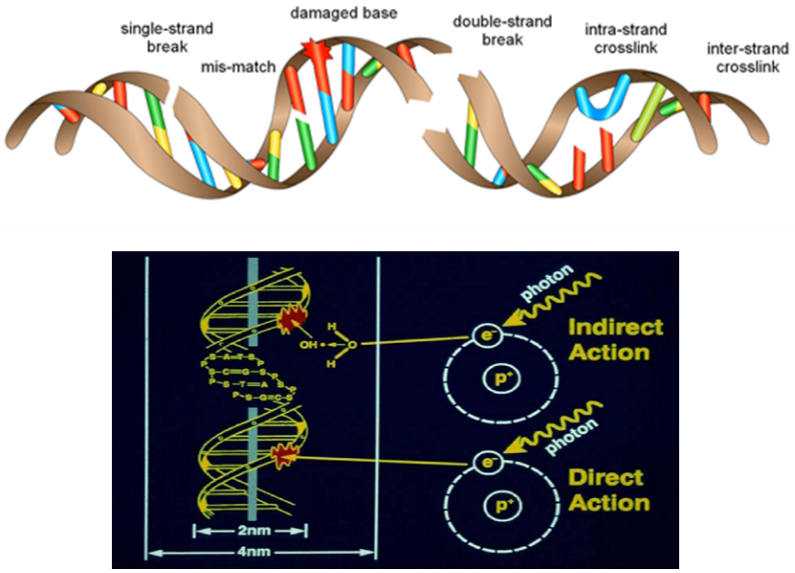


Fig. 4.5 The different types of DNA damage [141] and the direct and indirect effects caused by ionising radiation [142].

Ionising radiation is radiation which carries enough energy to force electrons out of atoms. When ionising radiation enters the body, there is a probability that it may be transmitted without transferring any of its energy, however, those particles that do interact can cause the ionisation of atoms along the path. Some ionised atoms harmlessly recombine with their electrons, but the ionisation also has the potential to break a chemical bond. The freed electron can go on to ionise further atoms, potentially causing further chemical damage. Those ionisations that do result in immediate chemical harm are referred to as the direct effect. Ionising radiation primarily affects water, as water makes up a large fraction of the cells volume. When water is ionised, it can form many reactive chemical species [132], called free radicals, which last only for a short time ($10^{-9}$ - $10^{-6}$ seconds). However, during this short time they are able to break chemical bonds in other nearby molecules. This secondary ionisation of other molecules by reactive water is called the indirect effect, and is hypothesised to be the dominant mechanism by which ionising radiation harms cells [140] (see Figure 4.5). Directly ionising radiation accounts for 30-40% of DNA damage

and indirectly ionising radiation accounts for 60-70% of damage [143].

Ionising radiation contains energies much greater than those in chemical bonds, thus the latter can be broken by the radiation. Ionising radiation can cause roughly four basic injuries to DNA; damage to the bases without breakage of the backbone, cross-links formed between the DNA and itself or another molecule and single (SSB) and double (DSB) strand breaks in DNA resulting in chromosome damage involving mainly deletions and rearrangements [140]. The first two defects can be healed by DNA repair enzymes, so it is not clear if these cause lasting genetic damage.

**Base Damage** - The sequence of bases within DNA is what stores and transmits the genetic information, thus any alteration in the DNA base sequence through loss or damage of the bases can be of major consequence to the cell. Any damage or loss of bases is considered a mutation, irregardless of the severity of any consequences [134].

**Crosslinking** - Radiation can produce covalent crosslinks between two regions of the same DNA strand, termed intrastrand crosslinks, or between two complementary DNA strands or completely different DNA strands, termed interstrand crosslinks. The DNA molecules can also be linked to a protein molecule with a DNA-protein crosslink. The significance of these types of DNA lesions in cell killing is unclear, but they may be of importance if they are not properly repaired by the cell [134].

**Single-Strand Breaks** - A SSB involves the cleavage of a bond along the backbone of one strand of the double helix. Since the other strand is left intact, it is possible to reconstruct the original sequence perfectly, using repair enzymes that match the unharmed strand base-for-base. The repair time proceeds rapidly, with a half-life of several minutes, so SSBs are relatively innocuous with little or no long-term consequences to the cell. If two SSBs occur on opposite sides of the DNA strand, they are still treated as individual damages and repaired separately as long as they are far enough apart (more than a few base pairs).

**Double-Strand Breaks** - DSBs occur when chemical bonds are cleaved along both

backbones, so that the entire DNA molecule has been split in two [140]. This destroys the pairing needed to complete the sequence of bases, and the broken DNA ends are vulnerable to further physical and chemical assault resulting in the loss or damage of bases and the formation of abnormal DNA structures [144]. All these events can result in the loss of genetic information. Even if repair enzymes heal the break, the strands may be improperly joined, or the joined ends may suffer lasting damage. Should this occur, additional layers of the body's DNA surveillance system exist to find such errors and either prevents the cell from dividing or triggers cell death. Thus, this is the most detrimental form of DNA damage caused by ionising radiation. The yield of DSBs is approximately 0.04 times that of SSBs, as two breaks in the backbone on either side of the DNA molecule must occur within one or two helical turns, and they are induced linearly with dose, indicating they are formed by single tracks of ionising radiation [139].

The energy from ionising radiation is not deposited uniformly in the medium through which it is traversing, but is located along the tracks of the charged particles set in motion. There are three arbitrary groups into which these events can be divided depending on the event size: spurs, blobs and short tracks. A spur contains up to 100 eV of energy and involves on average three ion pairs [139]. 95% of the energy deposition events involving X- and $\gamma$-rays are spurs, which have a diameter of approximately 4 nm, twice that of the DNA double helix. Blobs contain about 12 ion pairs with an energy range of 100-500 eV, and have a diameter of approximately 7nm. These are much less frequent for X- and $\gamma$-rays. Since blobs and spurs have similar dimensions to the DNA double helix, multiple radical attacks occur if they overlap the DNA helix, producing a wide variety of lesions including base damage and DSBs. This phenomenon is called a locally multiply damaged site, coined by John Ward [139]. This multiple damage could extend out to 20 base pairs from the damage site because of the diffusion of the free radical species produced. In the case of densely ionising radiation, a greater proportion of blobs is produced, therefore the damage produced

is qualitatively different from that of sparsely ionising radiation and is much more difficult for the cell to repair [139].

### 4.2.2 Reactive Oxygen Species

The free radicals derived from oxygen, known as reactive oxygen species (ROS), represent the most important radical species generated in biological systems [145–147]. A free radical is defined as a molecule or molecular fragment which contains one or more unpaired electron in its atomic or molecular orbit, rendering it chemically unstable [145]. The chemical stability of an atom or molecule is owed to it having an even number of paired electrons that are paired in spin. Free radicals have an uneven number of electrons that are not paired in spin, a state which confers a high level of reactivity [134]. Under normal circumstances ROS are produced specifically by the cell to serve essential biological functions or as a by-product of metabolic processes such as mitochondrial electron transport [133]. As discussed in Section 4.2.1, ionising radiation can damage the DNA directly by causing ioisation of the atoms comprising the DNA, or indirectly by interaction with water molecules, generating dangerous ROS as intermediaries. These reactive oxygen species may go on to react with other critical sites such as the DNA or other biomolecules, causing damage to the cell. Since approximately 80% of the cell is made up of water [134, 148], the probability of radiation damage occurring through the indirect effect following the ionisation of water molecules is much higher than for damage occurring through direct ionisations of the important biological targets [134].

The generation of ROS through the interaction of ionising radition with water molecules, is known as radiolysis. In the first "physical" stage, the radiation striking the water molecule causes the molecule to lose an electron and become extremely reactive [147–149]. This begins the second and third "physiochemical" and "non-homgeneous chemistry" stages in which a three step chain reaction converts the water to oxygen. The products of these

chain reactions are distributed in a highly non-homogeneous track structure, with the various chemically reactive species diffusing and reacting with each other and the surrounding environment until all intra-track reactions are complete [148]. Finally there is a "biological" stage in which the cells respond to the damage resulting from the products formed in the preceding stages.

The radiation will only interact with a single water molecule at a time, thus it cannot split directly into the diatomic gasses $H_2$ and $O_2$, but instead radiolysis results in the sequential generation of three dangerous reactive oxygen species, with an electron being lost at each step [149]. In sequence these ROS are the hydroxyl radical ($^{-}$OH), hydrogen peroxide ($H_2O_2$), and the superoxide radical ($O_2^-$). This process is very fast, happening in $\sim 10^{-8}$ s, with the products, apart from hydrogen peroxide which is relatively stable, disappearing in less than $10^{-3}$ s [147].

$$\begin{array}{ccccccc} & & \text{Hydroxyl} & & \text{Hydrogen} & & \text{Superoxide} \\ & & \text{radical} & & \text{peroxide} & & \text{radical} \\ H_20 & \xrightarrow{e^-} & \bullet OH & \xrightarrow{e^-} & H_2O_2 & \xrightarrow{e^-} & O_2^-\bullet \xrightarrow{e^-} O_2 \end{array} \tag{4.29}$$

The hydroxyl radical is an extremely reactive molecule which immediately strips electrons from any molecules in its path, propagating a chain reaction by turning that molecule into a free radical itself. However, it is also very short-lived and can only diffuse approximately 4nm before reacting [150]. Neither the hydrogen peroxide nor the superoxide radicals are as reactive as the hydroxyl radical, but hydrogen peroxide is more dangerous to the DNA as its slower reactivity allows the molecule time to travel into the nucleus of the cell where it can react with the DNA molecule [149]. Oxidation by the removal of electrons by free radicals can produce several types of DNA damage including oxidised bases and is one of the main causes of mutation in cells. The presence of iron during the radiolysis process can exacerbate the consequences of hydrogen peroxide production, as hydrogen peroxide

can be reconverted back into the hydroxyl radical by receiving an electron from the iron molecule in the Fenton reaction [145, 146, 148], (equation 4.30).

$$H_2O_2 + Fe^{2+} \longrightarrow OH^- + \bullet OH + Fe^{3+} \tag{4.30}$$

This hydroxyl radical could then go on to attack the DNA again. The superoxide radical also acts as a catalyst for the generation of hydrogen peroxide and the hydroxyl radical in the presence of iron as it helps regenerate the iron in the form required for the afore mentioned Fenton reaction, (equation 4.31).

$$O_2^- \bullet + Fe^{3+} \longrightarrow O_2 + Fe^{2+} \tag{4.31}$$

In biological systems, organic radicals are also formed by hydrogen abstraction initiated by •OH radicals. These radicals then react rapidly with $O_2$ to give peroxyl radicals ($RO_2\bullet$), which are even stronger oxidising agents. These peroxyl radicals can abstract H• from other molecules to form hydroperoxides (ROOH) [148].

ROS produced through water radiolysis are not the only source of ROS induced by ionising radiation. It has been shown that ionising radiation can also increase the intracellular level of ROS several hours after exposure, suggesting that the radiation stimulates ROS production from biological sources [147]. The early biochemical modifications induced by ionising radiation were thought to be responsible for the majority of the effects of ionising radiation in mammalian cells, however oxidative changes my continue to arise for days or months after the initial exposure, presumably because of the continuous generation of ROS. These effects can manifest themselves in the cells and their progeny, and oxidative stress may spread to non-targeted bystander cells through intercellular communication mechanisms [148]. It is clear that secondarily generated ROS have a variety of roles within the cell, including apoptotic signalling, genomic instability and bystander effects, which

ultimately effect the cellular integrity and survival [147].

### 4.2.3 The Cell Cycle

Cell proliferation is a cyclic process involving the reproduction of one parent cell to form two daughter cells, with each daughter cell going on to reproduce two granddaughter cells. All the DNA contained within the parent cell must be replicated and distributed equally to the daughter cells. Between these process of DNA synthesis and mitosis are gaps during which RNA (ribonucleic acid) and protein is made and the cell reorganises itself for the next round of division [133]. There are four phases through which the cell cycles between each division, thus it is known as the cell cycle (shown in Figure 4.6). There is a fifth phase outside the cell cycle where the cells are inactive, but the cells can be induced to re-enter the cell cycle from this phase [149]. The cycle is controlled by proteins known as cyclin-dependent kinases (CDKs).

The cell cycle is a complex series of events in which the cells amplify their synthetic machinary in preparation for DNA synthesis and then reorganise their interphase cromatin into chromosomes prior to mitosis; a process which needs careful regulation [133]. For accurate cell reproduction, three main checkpoints must be traversed in the $G_1$, $G_2$ and M phases. For the cell to transition from the $G_1$ to the S phase, a critical level of regulatory macromolecules must be achieved. At the $G_1$ checkpoint, growth stimuli such as hormones, growth factors and cell contacts act to increase the probability of the cell passing this barrier. This check-point ensures two functions: i) there is adequate machinery for future events; and ii) the accurate transmission of genetic information [133]. The $G_2$ checkpoint ensures the elimination of damaged cells which may have escaped the $G_1$ checkpoint or which have not accurately replicated their DNA. The spindle assembly M checkpoint monitors accurate chromosome alignment and retraction into the two daughter cells [133].

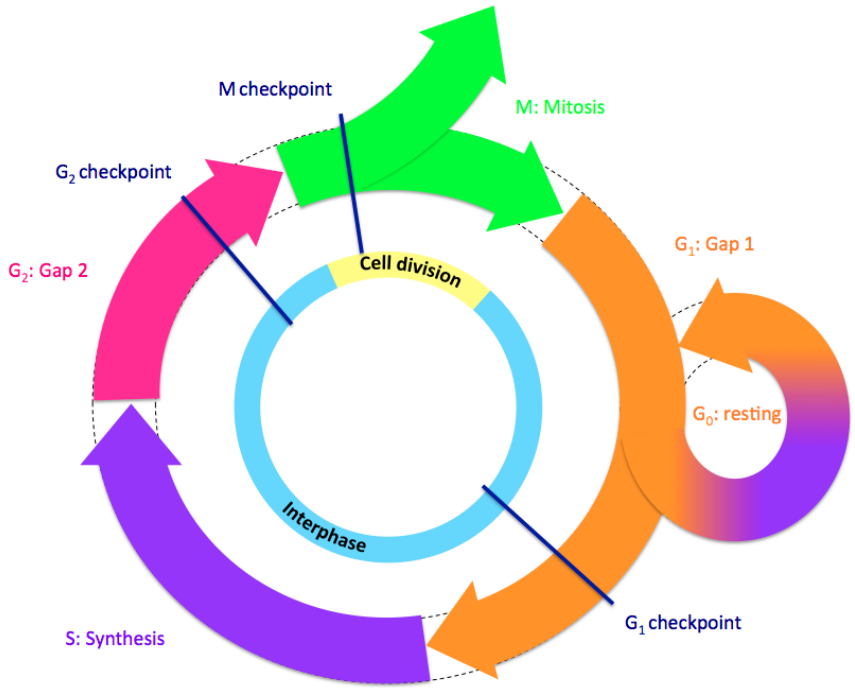


Fig. 4.6 The cell cycle and the cell cycle checkpoints. The average length of the cell cycle is 16 hours: 15 hours in the interphase and 1 hour in the mitosis phase.

### Phases of the Cell Cycle

**$G_0$: resting phase** - In this phase the cells are quiescent and inactive. Cells spend much of their lives in this phase not dividing or preparing to divide, but carrying out their day-to-day functions [151]. This phase can last from a few hours to several years depending on the cell type, and this is where most cells in an adult reside. Mitogens or growth factors can induce the cells in the $G_0$ phase to re-enter the cell cycle and pass a control point called the $G_1$ restriction point [149] which occurs just before the $G_1$ checkpoint.

**$G_1$: the first gap phase** - In this phase the RNA and proteins are made for dividing. This is the most variable phase in the cell cycle, with the length of this phase being the major determinant in the length of the full cycle. It is this phase in which the future commitment of the cell to divide, differentiate or die is made and is the focal point for many important regulatory signals. The cell cycle will be affected if these signals are altered. The cell

receives information that determines if and when it will go into the next phase, then starts making more proteins in preparation for division. The RNA required to copy DNA is also produced in this phase.

Three protein families are involved in the regulation of the $G_1$ checkpoint, namely cyclins, cyclin-dependent serine/threonine protein kinases (CDKs) and ccylin-dependent kinase inhibitors (CDIs) [133]. The kinases alter the biological functions of regulatory proteins. The second element of $G_1$ regulation involves DNA repair. Damaged DNA is detected by mechanisms involving the repressor protein p53, which blocks cycle progression until the DNA damage is repaired.

**S: the DNA synthesis phase** - In this phase the chromosomes containing the DNA are copied so that both daughter cells will contain the same DNA. Synthesis of the DNA is largely controlled by the build-up of enzymes, regulatory proteins and nucleotide triphosphates at the $G_1$/S boundary. During synthesis, the DNA strands are separated and the bases are exposed, thus they are sensitive to external agents. Once started, synthesis should be completed as quickly as possible to avoid damage to the exposed bases. Given the importance of DNA replication, any defects in synthesis would be lethal to the cell. DNA repair also occurs in the S phase.

**$G_2$: the second gap phase** - More information about if and when to proceed with cell division is gathered during this phase. Several synthetic and reorganisational events occur in this phase. The double compliment of chromatin proteins and DNA formed in the preceding S phase condense and are packaged into sister chromatids. Additional processes to rectify defects such as intertwining chromosomes, damaged DNA that escaped repair and unreplicated DNA are completed in this phase, otherwise these defects may block mitosis in the next phase. These processes are monitored at the $G_2$ checkpoint, probably by different means to the $G_1$ checkpoint but still requiring the cyclin/CDK/CDI system.

**M: mitosis phase** - In this phase the cell divides into two identical daughter cells. Sister

chromatids must be aligned correctly to the opposite poles of the divding cell, with this process being monitored through the spindle assembly M checkpoint. Once again CDKs are required for these events. There are four stages of mitosis: prophase, metaphase, anaphase and telophase. In the prophase, chromosomes appear as a result of condensation, the nuclear membrane breaks down, duplicated centrosomes separate, and the mitotic checkpoint proteins are assembled at the centromeres. In the metaphase, the chromosomes are aligned on the metaphase plate and microtubules assemble to form the mitotic spindle. The microtubule captures both centromere regions of the chromatid pair resulting in the silencing of the checkpoint. The metaphase is completed when the last pair is attached to the spindle. The anaphase is characterised by the spindle pulling apart and separating chromatid pairs. The telophase includes the accumulation of chromosomes at their respective poles, re-forming of the nuclear membrane, chromosome decondensation and cytokinesis which is the separation into separate cells [149].

### The Cyclin-Dependent Kinase System

Activity changes of protein kinases work to regulate the cell cycle. These kinases are activated by cyclins, so are thus termed cyclin-dependent kinases. Another group of regulatory proteins have the opposite effect on the kinases, so are called cyclin-dependent kinase inhibitors. Cyclins were so named because of the cyclical cahnges in their concentrations that occur over a series of cell divisions [149]. The cell cycle checkpoints are regulated by the inteatcions of the cyclins, cyclin-dependent kinases and the cyclin-dependent kinase inhibitors [133].

These three components represent different famiies of molecules which are activated at different phases of the cell cycle. Cyclin D is the first cyclin to be synthesised and remains at a constant level throughout the cell cycle after rising early in $G_1$. This cyclin, together with CDK 4/6, drives progression through the $G_1$ phase, and also plays a role in the $G_1$ to S

transition. The cyclins E, A and B are highest in late $G_1$, $G_2$ and M respectively, with their prescence contributing to the checkpoint regulation in each of those phases [133]. Cyclin A-CDK2 is important for S phase progression, with cyclins A, B-CDK1 directing $G_2$ and the $G_2$ to M phase transition. Each of these cyclins preferentially binds to a particular CDK, with the presence or absence of specific cyclins and CDKs at different periods determining which kinase is active during each period [133]. Inhibitory signals involve the CKI family of proteins, with different signals using different methods to increase CKI activity.

The regulation of CDK activity is crucial for precise cell reproduction. There are four mechanisms by which this CDKs are regulated: their association with cyclins, their association with CKIs, addition of phosphate groups that activate CDK activity, and the addition of phosphate groups which inhibit CDK activity [149].

### Cell Cycle Checkpoints

These checkpoints are a series of biochemical signalling pathways that sense and induce a cellular response to DNA damage [149]. They are important for maintaining the inegrity of the genome as disruption of checkpoint function leads to genomic and chromosomal instability which causes mutations in the cell. The $G_1$ checkpoint ensures that DNA damage is not replicated in the S phase, as it arrests the cell cycle as a response to DNA damage. The $G_2$ checkpoint also arrests the cell cycle in response to damaged or unreplicated DNA to ensure that the S phase is properly completed. The M checkpoint, or spindle assembly checkpoint, responds to misalignment on the mitotic spindle by arresting chromosomal segregation [149].

Retinoblastoma protein (RB) is a key substrate of the cyclin D-CDK 4/6 complex, mentioned earlier, which serves as a molecular link for the $G_1$ checkpoint allowing the cell to transition to the S phase. The activity of the E2F transcription factor family is regulated by RB, and the transcription factor is essential for the expression of genes needed for the S

phase of the cycle. RB does this by physically interfering with the transactivation domain of the E2Fs. The activity of the RB itself is regulated by sequential phosphorylation events by cyclin-CDKs [149].

The $G_2$ checkpoint is there to prevent any cells which have incurred DNA damage in previous phases or not correctly completed the S phase from entering the M phase. DNA damage activates either of two kinases, ATM or ATR [149], which then phosphorylate and activate the checkpoint kinases Chk1 and Chk2, which in turn target the Cdc25 tyrosine phosphatases that regulate CDK activity by removing inhibitory phosphates. The B and C type Cdc25s are important in the $G_2$-M phase transition. The activation of the $G_2$ checkpoint results in the inhibition of Cdc25s by Chk1/2 [149].

The mitotic checkpoint, or spindle assembly checkpoint, is a signalling cascade that ensures correct chromosomal segregation during mitosis and the production of two genetically identical nuclei [149]. This checkpoint plays an important role in preventing the mis-segregation of single chromosomes.

### The Cell Cycle and Radiation

As early as the late 1960s, the effect of the cell's age and phase in the cell cycle on radiation response were being examined [152, 153]. Cells exhibit a different response depending on the phase of the cell cycle they were in at the time of irradiation [152]. Cells are most sensitive to ionising radiation during the $G_2$ and M phases of the cell cycle, less sensitive during the $G_1$ period, and radioresistence rises to a peak during the latter part of DNA synthesis. Conversely, early S phase is the sensitive period for chemical agents and UV light [133]. The idea of synchronising tumor cells in a phase of the cell cycle more sensitive to radiation is recognised as a potential way of enhancing the clinical efficacy of radiotherapy [154–156], however the application is extremely limited. The complete synchronicity of cell populations is difficult to achieve and maintain, and would be cumbersome duing

fractionated therapies [157].

It has been shown that ionising radiation can have the effect of slowing down the progression of the cell through the cell cycle, by inducing delays in the $G_1$, S and $G_2$ phases. Initial studies carried out on HeLa cells (human cervical adenocarcinoma) indicated a transient division delay accompanied by an accumulation of cells in the S phase, with lower doses of radiation producing no S phase delay but a dose dependent lengthening of the $G_2$ phase [158]. Results also indicated that the phase in which the cells were irradaited influenced the extent of the delay produced with cells in $G_1$ being least affected , and cells in S or $G_2$ showing progressively greater delays [153]. Arresting in $G_1$ as a response to irradiation is thought to be the result of signals transmitted by the p53 tumour suppressor protein in response to cellular damage. The level of p53 protein rises 1-2 hours post irradiation and remains at this elevated level for the next 72 hours. The p53 acts as a transcriptional activator causing increased synthesis of regulatory proteins implicated in cell cycle arrest [158]. A delay in the progression through the S phase of the cell cycle is caused by the slowing of the DNA synthesis rate. The response to dose of this effect is biphasic, indicating the radiosensitive (low dose) and radioresistent (high dose) components of the delay [158]. The radioresistent response is caused by the reduction in the rate of DNA chain elongation [159], while the radiosensitive response is due to a decrease in replication initiation [160]. The arrest in the $G_2$ phase is affected by differences in cell cycle progression between radioresistent and radiosensitive cell lines. Results show mammalian cells deficient in $G_2$ arrest are highly sensitive to ionising radiation and do not undergo a $G_2$ delay after exposure to radiation [158]. Studies using caffeine have shown that this drug reduces or abolishes the radiation induced $G_2$ delay and renders cells more sensitive to radiation [161].

The phosphatidyl-inositol kinase-related protein ATM (ataxia telangiectasia mutated) is the most proximal signal transducer initiating cell cycle changes after DNA damage induced by ionizing radiation [157, 162]. Cells with defective ATM and/or lacking in ATM are

extremely sensitive to ionising radiation, highlighting the essential role of ATM in DNA damage and repair [163–165]. Patients with a mutated ATM gene show extreme sensitivity to radiation, and exhibit defective $G_1$, S and $G_2$ arrest after ionising radiation [157].

Division delay, which is a dose-dependent cellular response, is directly related to the position in the cell cycle of the cell [158]. Low doses of radiation affect cells in the most radiosensitive phases of the cell cycle delaying their progression through mitosis for a given period of time. High doses of radition affect all cells and produces a longer mitotic delay [134].

The main response of cells to DNA damaging agents is the activation of the cell cycle checkpoints, which provide a controlled temporary arrest at a specific stage of the cell cycle to correct possible defects [166, 167]. Ionising radiation, as discussed earlier, induces arrests in the $G_1$, S and $G_2$ phases of the cell cycle. The $G_1$ checkpoint prevents the replication of damaged DNA before transition into the S phase, and the $G_2$ checkpoint prevents the segregation of aberrant chromosomes during the M phase [157]. There are two distinct $G_2$/M checkpoints, the first being dose independent, ATM dependent, transient and occuring early after exposure to ionising radiation [168]. This early $G_2$/M block represents the failure of the cell to progress to mitosis, and may be the mechanism by which low-dose hyper-radiosensitivity is converetd to resistence [157]. In contrast the late accumulation in $G_2$/M only becomes measurable after several hours, is dose dependent, ATM independent, and represents the cells that were in an earlier phase of the cell cycle at the time of the radiation exposure [168]. $G_2$/M accumulation after exposure to ionising radiation is enhanced in cells lacking the radiation induced S phase checkpoint and is not affected by the early $G_2$/M checkpoint [157, 168].

Because the cell cycle is strongly affected by radiation, and radiosensitivity depends on cell cycle position and progression, there is some association between apoptosis and radiosensitivity [157].

### 4.2.4 Repair Pathways

The various different types of damage suffered by the cell were discussed in Section 5.2.1. The cell has developed several different specialised pathways which sense, respond to and repair these different types of damage. Different mechanisms are used to repair base damage than those used to repair strand breaks, and different methods are used depending on the stage in the cell cycle.

#### Base Excision Repair

Base excision repair (BER) is, as the name suggests, the pathway through which damaged bases are repaired. This is a generalised repair mechanism which repairs many ionising radiation induced alterations to the bases. The damaged base results in a minor disruption of the DNA structure, with the damaged base and its associated sugar being removed by a two step process. In the first step the base alteration is recognised by a class of enzymes known as the DNA glycosylases, which release the damaged base leaving an abasic site [169]. Secondly, an incision is made at the abasic site by an AP-endonuclease and the remaining sugar is released by a deoxyribo phosphodiesterase. The one base gap that is a result of this process is filled by a DNA polymerase, using the undamaged complementary strand to ensure that the gap is filled with the correct base. The polymerase leaves a nick in the DNA backbone which is sealed by a DNA ligase, thus completing the repair with no loss of genetic information [169]. If more than one nucleotide has to be replaced, a complex polymerase performs the repair synthesis [139]. This form of repair is also used to repair abasic sites. BER is very efficient, although defects in the process may lead to increased mutation rates but not usually increases in cellular radiosensitivity [139].

### Nucleotide Excision Repair

Nucleotide excision repair (NER) removes bulky adducts in the DNA such as pyrimidine dimers [139]. This type of damage interfers with transcription and replication. There are five essential steps in this pathway; 1) the damage has to be recognised, 2) incisions in the DNA that bracket the lesion, approximately 24 to 32 nucleotides in length, 3) the region containing the adduct is removed, 4) repair synthesis to fill the gap, and 5) DNA ligation [139]. There are two subpathways in NER: global genome NER which surveys the helix distortion and transcription-coupled repair identifies damage that interfers with transcription [149]. Sensitivity to ionising radiation is not a result of mutations in nucleotide excision repair genes, however an increased sensitivity to ultraviolet induced DNA damage and ultraviolet light is a consequence. This is a relatively complex and time consuming process, therefore cell proliferation is stopped by a p53 mediated process to allow time for repair. Another protein, TFII, is utilised in this process, which is more usually associated with the synthesis of mRNA, thus the damaged cell can divert other functions to achieve repair [133].

### Single-Strand Break Repair

Single strand breaks are repaired in a manner similar to BER. An exonuclease removes any sugar remnants, along with the phospahte group on the 5' of the sugar [169]. The gap which results is filled by a DNA polymerase using the complimentary strand as a template, and a DNA ligase closes the remaining single-strand nick. As a complimentary strand of DNA is used for this type of repair, this lesion and its repair pose little or no permanent genetic risk.

### Double-Strand Break Repair

The repair of DSBs is difficult or impossible and there is a direct link between unrepaired DSBs and cell death. There are two main repair pathways for DSBs; homologous recombination (HR) and non-homologous end-joining (NHEJ), with single-strand annealing (SSA)

and variable diversity joining recombination (V(D)J) emerging as possible alternative repair pathways for DNA DSBs.

**Homologous Recombination (HR)** - comprises a series of related sub-pathways that use DNA strand invasion and template directed DNA repair synthesis, culminating in error free, but slow, repair [170]. An undamaged strand of DNA is required as a participant in the repair as a template. This type of repair plays a role in the S and $G_2$ phases of the cell cycle, when an undamaged sister chromatid is available to act as the template. The increased activity of this pathway during late S/$G_2$ suggest its primary function is to repair and restore the functionality of replication forks within DNA DSBs [139]. In HR, the unprotected ends of the DNA strand exposed by a DSB provide sites for strand specific exonucleolytic degradation and the generation of protruding single strand ends [169]. The second strand of complimentary DNA is invaded by a protruding end resulting in base pairing between the two strands. This invading strand acts as a primer for DNA synthesis along the complementary strand of the intact molecule. A section of the intact molecule is displaced, called the D-loop, which provides a single-strand region that can pair with the remaining end of the damaged molecule [169]. Synthesis proceeds along the D-loop, where missing information is restored, leaving two single-strand nicks. Holliday junctions [139, 144, 169] form when these nicks are sealed by a polynucleotide ligase. These cross-strand structures can be resolved to form non-crossover and crossover products [169, 170], depending on which sections of each molecule are retained, but all genetic information remains intact as the missing DNA sequences have been replaced. This type of repair accounts for 30-50% of endonuclease induced DSB repair events in dividing mammalian cells [171].

**Non-homologous End-Joining (NHEJ)** - this, the most common DSB repair pathway, involves modifying the two broken ends of the double helix to make them compatible, followed by re-joining without reference to an intact partner. NHEJ can be divided into four steps: 1) end recognition, 2) end processing, 3) fill-in synthesis or end bridging, and 4)

ligation [139]. A few of the phosphate base groups are lost at each end of the DNA break when NHEJ is used, so this is an imperfect non-conservative process from the standpoint of preserving genetic information; it is fast but error prone [144, 171, 172]. Furthermore, without the use of a template it cannot be guaranteed that the two ends being joined were from the same initial break [169]. This is the main pathway for the repair of DSBs when the cell is in the $G_0$, $G_1$ and early S phases of the cell cycle, and continues to repair a minority of breaks in the late S and $G_2$ phases [172]. Hence, when ionising radiation is used for cancer treatment, many DSBs are formed, thus the faster repair method of NHEJ is used, resulting in more errors and cell death.

**Single Strand Annealing (SSA)** - Single-strand annealing is a transitional process between HR and NHEJ, which uses direct repeat sequences for its repair process [173]. As half the human genome consists of repetitive DNA sequences, it is a potentially competitive repair pathway for DNA DSBs [174]. The DNA DSB ends are digested by an exonuclease, until homologous regions are exposed on both ends of the break [139]. The two tails, which are nonhomologous, are removed so that the two exposed ends can be ligated. SSA and HR share parts of the same pathway, but SSA results in the loss of some genetic information because of the degradation of the DNA ends by the exonuclease [139, 171] thus it is know as a nonconservative repair pathway [173, 175].

**Variable Diversity Joining Recombination (V(D)J)** - V(D)J is the process which mediates the development of antibodies as part of the normal immune response. It has been linked to DNA DSB repair, and may provide an intriguing possible link between ionising radiation induced DNA damage, p53 stabilisation and cell cycle control [169]. Three different genetic elements are used to assemble an antibody "gene"; the variable (V), diversity (D) and joining (J) regions [144]. The V, D and J sequences have to be selected form those available and joined to form the final antibody gene [169]. The V(D)J recombination system does this by inducing it's own DSBs and providing for their repair.

Failure to repair even a single DSB can have dire genetic consequences for the cell. Cell division becomes challenging as mitosis relies on the segregation of intact chromosomes, which are not present owing to the physical discontinuity of DSBs. A chromosome deletion can occur if two or more DSBs occur within the same chromosome. If this deleted section is not associated with a centromere, the section will be lost during mitosis, thus depriving the cell of a fraction of its genetic heritage [169]. Inaccurrate repair may result in loss of genetic information or mutations and inappropriate repair may result in harmful genomic rearrangements [144]. As DSBs are signals for cell cycle checkpoints, if even one is unrepaired prior to cell division this may lead to prolonged cell cycle arrest, failure to undergo cell division and cell death [144].

### Cross-Link Repair

The mechanisms used to repair DNA-DNA or DNA-protein cross links are still under investigation. Currently it is thought to be a combination of NER and recombinational repair pathways that are needed to repair cross-links. Chromatins that contain actively transcribed genes are more susceptible to DNA-protein cross-links, and the cross-linked proteins are usually nuclear matrix proteins [139].

### Mismatch Repair

This pathway repairs small insertions, deletions and base-base mismatches that occurred during replication and escaped editing by polymerases. Base-base mismatches which occurred as intermediaries of homologous recombination are also removed [139]. Incorrectly matched base pairs are removed by specific exonucleases called exinucleases that digest the DNA in both directions from the incorrect bases. The gap is then correctly filled by DNA polymerase and ligated by DNA ligase [133]. These main molecular events can be desricbed in the following five steps: 1) the mismatch is recognised by hMSH2/6 and hMSH2/3 pro-

teins, 2) hMLH1/hPMS2 and hMHL1/hPMS1 are recruited, 3) the newly synthesied strand is identified (flagged by the replication machinary), 4) endonucleases and exonuclease remove the nucleotides around and including the mismatch, 5) DNA polymerases resynthesise a newly replicated strand [149]. Any mutations in the mismatch MSH, MLH or PSM families of repair genes lead to microsatellite instability, which are small base insertions or deletions, and cancer [139].

### 4.2.5 LET, RBE and OER

#### Linear Energy Transfer

As different forms of radiation release their energy at different rates, the concept of linear energy transfer (LET) is used to define the energy released per unit path length. It is a measure of the rate at which energy is transferred to the medium and hence the density of the ionisation [135]. The process of energy loss is dominated by electronic collisions and can be described by the Bethe-Bloch formula [176];

$$\frac{dE}{dx} = \frac{4\pi e^4 Z_{eff}^2 ZN}{m_e v^2} ln\left(\frac{2mv^2}{I}\right) + \text{relativistic terms} \tag{4.32}$$

where $dE/dx$ is the energy loss per unit length, $Z$ is the atomic number of the target, $N$ is the electron density of the target, $m_e$ and $e$ are the mass and charge of an electron, $v$ is the velocity of the ion and $Z_{eff}$ is the effective charge of the ion. $Z_{eff}$ can be approximated by the Barkas formula [177];

$$Z_{eff} = Z\left(1 - exp\left(-125\beta Z^{-\frac{2}{3}}\right)\right) \tag{4.33}$$

The dominant parts of the Bethe-Bloch formula are the dependence on $1/v^2$ and $Z_{eff}$, as these determine the amount of energy being deposited along the beam profile. As $1/v^2 \approx 1/E$, a decrease in particle energy will yield an increase in the energy lost.

A given amount of energy released in a short distance does more damage than the same amount released over a longer distance. It is usual to refer to low and high LET radiation, with the latter being more effective at causing DNA damage. It follows that radiation that is easily stopped has high LET, and radiation which is more penetrating has low LET. High LET radiation, such as that produced by $\alpha$-particles and neutrons, generates so much DNA damage that the cell will die, whereas low LET radiation, such as X-rays, is much less cytotoxic. To help explain why high LET radiation is more damaging than low LET radiation let us consider the DNA DSB. DSBs are less likely than SSBs, since two separate chemical events are needed to cause them, but high LET radiation, such as protons, causes a series of closely clustered ionisations that result in a trail of damage. If these ionisations occur approximately 2 nm apart, they coincide roughly with the diameter of the DNA double helix, thus the passage of a single particle has the potential to cause a double strand break. X-rays on the other hand have a much lower LET and the probability of a single track causing a double strand break is very low and in general more than one track is required.

### Radiobiological Effectiveness

The LET is one of several factors influencing the relatie biological effectiveness, RBE, of a particle, with other factors being dose, fractionation, tissue type and biological endpoint [179]. In practice, two different types of radiation, one high LET and the other low LET, can produce the same biological effects if the dose of the high LET radiation is reduced in accordance with the RBE of the particle. The RBE, or relative biological effectiveness, is the ratio of the dose of 250 keV X-rays compared to the dose of the test radiation required

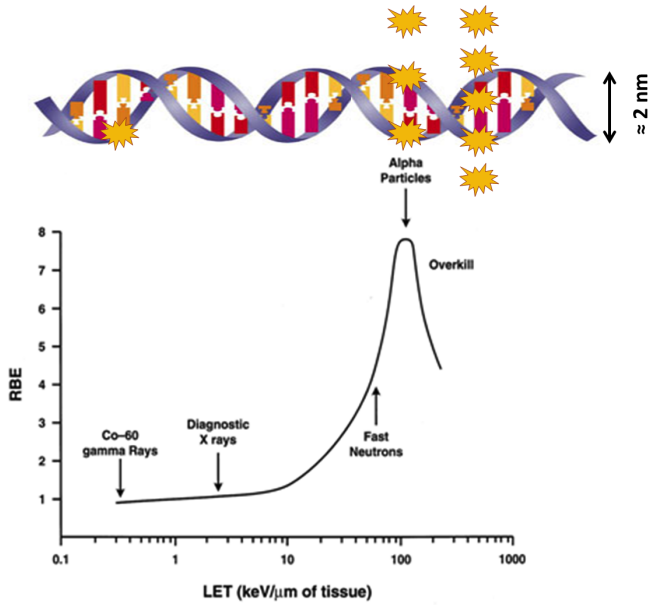


Fig. 4.7 The relationship between LET, RBE and DSBs [139, 178].

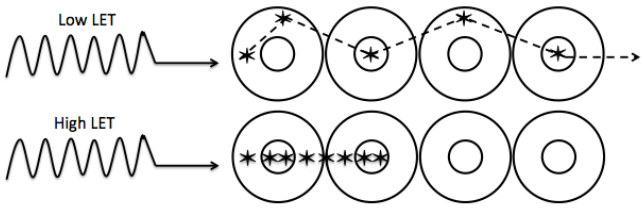


Fig. 4.8 Comparison of the effects of low- and high-LET radiation on a population of cells [134].

to produce the same biological effect;

$$RBE = \frac{\text{dose of 250 keV X-rays}}{\text{dose of test radiation}} \tag{4.34}$$

RBE values are higher for tissues that accumulate and repair large amounts of sub-lethal damage (SSBs for example) and low for those that do not repair sub-lethal damage. The RBE can vary with the dose rate because the slope of the dose response curve for sparsely ionising radiation, such as X- or $\gamma$- rays, varies critically with a changing dose rate. In contrast, the biological response to densely ionising radiation depends little on the rate at

which the radiation is delivered. In the case of sparsely ionising X-rays the probability of a single track causing a DSB is low, thus X-rays have a low RBE. At the other extreme, densely ionising radiation readily produces DSBs, but the energy is wasted, thus the RBE is lower than optimal LET radiation. This effect is known as overkill where the density of energy deposited in the DNA molecule is higher than what is need for its breakage.

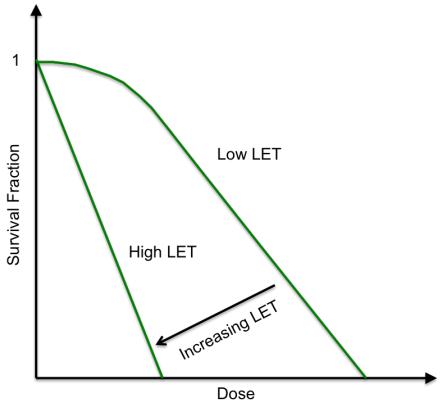


Fig. 4.9 The relationship between LET and the cell survival curve. The width of the shoulder represents the part of the dose which is wasted, thus the higher LET radiation has a greater RBE compared to the lower LET radiation as less of the dose is wasted.

### Oxygen Enhancement Ratio

Oxygen is a sensitising agent which renders cells more susceptible to radiation damage. When irradiating cells with photons or low-LET ions, they demonstrate different survival behaviour depending on the presence or absence of oxygen [180].

Oxygen is a truly universal radiosensitiser as it it enhances the radiation response of all organisms from bacteria to mammalian cells to entire organisms. The oxygen enhancement ratio (OER) is the ratio of radiation dose required for the same biological effect, such as cell survival or the number of DNA DSBs, in the absence (annoxic) versus the presence of

oxygen (oxic) [181]:

$$OER = \frac{D_{anoxic}(E)}{D_{oxic}(E)} \tag{4.35}$$

The OER describes the degree to which the cellular sensitivity to radiation increases or decreases depending on the oxygen concentration of the cellular environment [182]. For mamalian cells the OER is generally given as $\sim$ 2.5-3.5 after high single doses. The effect is most pronounced for low LET radiations and is not as effective for high LET radiations, as the amount of damage induced by high LET radiations is large and unrepairable and the presence of oxygen would not enhance the radiation response to the same extent as low LET radiation. The OER for high LET radiation varies between 1.7 and 1.2 [134].

The OER can also be defined as the ratio between the dose to hypoxic cells (reduced oxygen levels) and aerobic cells (usually in air), with the OER decreasing with increasing oxygen partial pressure in the cell environment. This is usually termed the hypoxia reduction factor (HRF) rather than the OER [183].

The oxygen effect can vary depending upon when the oxygen is delivered to the sample being irradiated. The oxygen effect is most pronounced when the oxygen is administered simultaneously with the radiation, the response is less dramatic when the oxygen is delivered pre- or post-irradiation. This has been attributed to the fact that the oxygen effect involves the reaction of the radiation at a chemical level. The exact mechanism of the reaction is still not fully understood, but the two leading hypotheses are as follows [134]:

1. The oxygen may enhance the formation of free radicals or draw the existing free radicals formed by the radiation interacting with the water content of the cells, into chain reactions producing new highly damaging radical species.

2. The oxygen may block restoration of chemical changes which have occurred as a result of the irradiation thus increasing damage in the cell. These changes would

normally be reversible in the absence of oxygen.

In the oxygen fixation hypothesis the absorption of radiation leads to the production of fast charged particles which produce a number of ion pairs as they pass through the sample. These ion pairs have extremely short life spans of $10^{-10}$ seconds and produce free radicals which have an appreciably longer life span of $10^{-5}$ seconds. These free radicals break chemical bonds, producing chemical changes which initiate a chain of events resulting in the final expression of the biological damage, which depends on the presence or absence of oxygen. If oxygen is present, the radicals (R.) will interact with the DNA. The so produced DNA radical can be reduced by reacting with an SH group, however if $RO_2$ is formed, the chemical change is permanent. This cannot take place in the absence of oxygen, since then many of the ionised target molecules are able to repair themselves and recover the ability to function normally. The oxygen is then said to make permanent or 'fix 'the radiation lesion [139].

Because the oxygen increases the amount of damage to the organism by increased formation of free radicals or fixing the damage, more targets will be lethally affected per given dose of radiation.

The OER is significantly affected by the position of the cells in the cell cycle, when measured for fast-growing proliferating cells in vitro. The OER was measured at $\sim 2.35$ for $G_2$ phase cells, compared to $\sim 2.85$ for S phase, with an intermediate value for $G_1$ phase cells [139].

### 4.2.6 The Role of Hypoxia

Hypoxia is a pathophysiological property that is defined as a stae of depressed oxygen tension [184]. Hypoxia can be present in both tumours and normal tissue, causing the impairment of cellular or organ function once critical levels of oxygen depletion are breached. The increased resistance of hypoxic cells to ionizing radiation is usually believed to be the

primary reason for treatment failure in tumors with oxygen-deficient areas [185]. Under hypoxia, the proliferation rate of tumour cells outstrips the vasculature formation rate leading to the development of oxygen deficient zones within the tumour [186]. Such hypoxic zones have a reduced response to radiotherapy [187, 188] owing to a decrease in ROS that are required to produce enough DNA damage to cause cell death [189, 190]. Radiation induced ROS generation is well reported as one of the main determining factors in cellular damage through the induction of a spectrum of lesions including DNA base damage, SSBs and DSBs [191]. The radicals produced enter into a competition for either oxidation, which makes the damage permanent, or reduction which can restore the DNA to its original form [192].

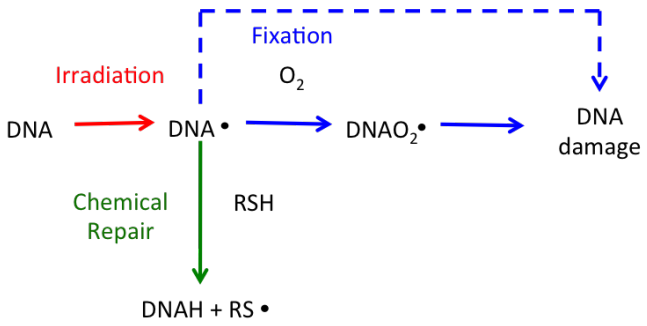


Fig. 4.10 Radicals are either oxidated, fixing the damage, or reduced, restoring the DNA to its original form.

Intra-tumoral hypoxia induction is non-uniform, where a temporary occlusion of a blood vessel produces a region of acute hypoxia which varies within a short time frame. Acute hypoxia is perfusion limited and is defined as a short-term exposure to a reduction in oxygen resulting in oxygen concentrations of less than 3%. Chronic hypoxia is diffusion limited, and is defined as a long-term exposure to a reduction in oxygen resulting in concentrations of less than 0.1%, induced by a consistently depleted oxygen supply as the distance between the cells in the growing tumour and the blood suply increases, slowing reoxygenation [184, 193]. Areas of complete anoxia (0% $O_2$) are present in regions of the tumour more than

150 $\mu$m from the vasculature as this is the diffusion limit of oxygen within tissues [189]. Recurring tumours often have a larger hypoxic area than primary tumours, but a tumour's hypoxic status cannot be determined easily as the presence of hypoxia is independent of size, stage, grade or histology [184]. Intratumoral oxygenation often disperses heterogeneously, therefore the hypoxic content can only be measured accurately through a composite set of complementary measurements.

It has been demonstrated that the sensitising effect of the oxygen concentration can only be observed when oxygen is present during irradiation. When the oxygen concentration is > 3% the full sensitising effect is observed, while at lower concentrations, especially from 1% - 0.1%, a steep decrease in radiosensitivity is measured [194]. However, there is some discrepancy as some researchers report that chronic and acute hypoxia similarly modulate radiosensitivity [195].

Because of the radio-protective effect of hypoxia in tumours, new strategies are required to individualise the treatment and improve the outcome for patients with hypoxic tumours. As the OER decreases with increasing LET, high LET radiation therapy is envisaged as a possible solution, particularly employing carbon ions. This treatment modality combines high RBE with a reduced OER, with a favourable dose depth profile which theoretically can be targeted at the hypoxic tumour [183, 196].

### Defining Tumour Hypoxia

Normoxia is almost universally used to describe the normal oxygen levels in tissue culture flasks, which is approximately 20-21% $O_2$. This is far from accurate for peripheral tissues where the oxygen levels can range from 3.4 to 6.8%. Even lung alveoli have a reduced oxygen level of 14.5% owing to the presence of water vapour and $CO_2$. Measurements of the oxygen levels in normal tissues do show distinct normal ranges, dependent on the tissue type, but normoxia is not the relevant oxygenation range. A more accurate level

of oxygenation to which experimental conditions can be compared is 5% $O_2$ which has recently been termed physoxia. The lower limit of physoxia is approximately 3% $O_2$, with cells of different origins having different oxygen sensitivities. Brain tissue for example is very sensitive to oxygen depletion and can only survive for approximately 3 minutes without adequate oxygenation, whereas vascular smooth muscle can survive for up to 72 hours [197].

| % Oxygen | Hypoxia Definition |
|---|---|
| 5.0 | Physoxia: physiological oxygen level in peripheral tissues with an average of approximately 6% (7.5-4 % depending on the tissue). For experimental studies, 5% is the proposed compromise since this is often used. |
| 2.0 | Physiological hypoxia: the lower level at which normal hypoxic responses are elicited (lower limit $\sim$ 1%, upper limit $\leq$ 5%) |
| 1.0 | Pathological hypoxia: shows persistence of poor oxygenation suggesting disruption to normal homoeostasis. Below this level pathological hypoxia applies. |
| 0.4 | Radiobiological hypoxia: the oxygen level at which the cytotoxic effect of radiation is half maximal. |

Table 4.1 Approximate levels of oxygen corresponding to the different levels of hypoxia [184].

The oxygen level at which tissues respond to maintain their preferred oxygen level is termed physiological hypoxia. These responses are usually physiological such as up-regulation of hypoxia response genes or increasing blood flow. The physiological hypoxia range is generally 2-6% $O_2$ as different tissue types have different hypoxic trigger points, and the response is presumed to be transitory but sufficient to return the tissue to its preferred level of oxygen.

Pathological hypoxia is the point at which homoeostatic mechanism no longer responds effectively to reverse falling oxygen levels. This is usually well below 1.3% $O_2$. In tumours the homoeostatic processes are disrupted for two main reasons:

1. The vasculature is of very poor quality and cannot adequately and reliably provide

oxygen leading to,

2. A sizeable proportion of tumour cells are significantly hypoxia tolerant as they do not die in this environment

The second reason may be attributed in part to the switch to glycolysis for the supply of energy. In addition, exposure to prolonged pathological hypoxia will naturally select hypoxia-tolerant tumour cells that are stress resistant and more malignant [184]. This occurs at approximately 1% $O_2$.

### Hypoxia Inducible Factor

Hypoxia Inducible Factor 1 (HIF-1) is a basic-loop-helix-loop motif heterodimeric transcription factor, comprised of an oxygen regulated $\alpha$ subunit and a constitutively expressed $\beta$ subunit (also called aryl hydrocarbon receptor nuclear translocator, or ANRT) [198–200], that is activated in mammalian cells under hypoxic conditions. The $\alpha$ subunit (HIF-1$\alpha$, -2$\alpha$ or -3$\alpha$) is sensitive to oxygen tension and dominates the transcriptional activity. Under hypoxic conditions the rate of HIF-1$\alpha$ turnover is inhibited, resulting in an increased rate of the protein accumulation [201]. It potentiates a variety of biochemical processes that are aimed at alleviating the effects of hypoxia, and is constantly expressed and degraded by oxidation dependent oxidation, therefore its degradation is slowed at low oxygen pressure with elevated protein levels found in many hypoxic tumours [184].

The HIF pathway is a major mediator of the biological effects in tissue after exposure to hypoxia. Under normal oxygen conditions, the $\alpha$ subunits rapidly degraded by hydroxylation by $Fe^{2+}$ dependent prolyl hydroxylases (PHD) in the oxygen dependent degradation domain at proline residues 402 and 564 in human HIF-1$\alpha$ [200, 202, 203], interaction with the von Hippel-Lindau protein (pVHL) E3 ubiquitin ligase complex and proteasomal degradation [184, 204]. The PHDs require molecular oxygen; under hypoxia they lose activity and no longer degrade HIF-1$\alpha$ [205]. This confers a sensitivity to hypoxia, under which

the HIF-1$\alpha$ is stabilised and initiates a multistep pathway of activation that includes rapid accumulation of HIF-1$\alpha$ and its translocation inside the nucleus [206]. Inside the nucleus the HIF-1$\alpha$ heterodimerizes with HIF-1$\beta$ (ANRT), recruits transcriptional coactivators and binds to hypoxia response elements (HREs) in the regulatory regions of many target genes [207]. Under normal oxygen conditions, HIF-1$\alpha$ is usually unsatble and virtually undetectable [202].

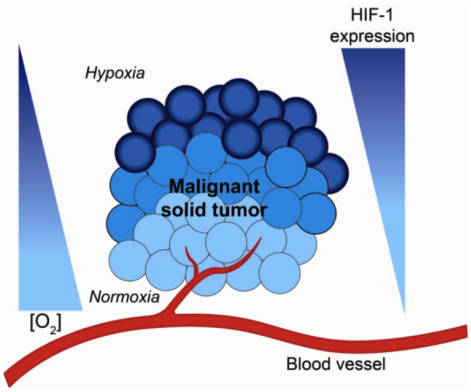


Fig. 4.11 The spatial relationship between a blood vessel and a solid tumour in the context of HIF-1 and $O_2$ concentrations. In normoxic conditions of 5%, within 70 $\mu$m of the blood vessel, the HIF-1 is rapidly degraded or has a very low level of expression. Hypoxic regions exist at distances greater than 100 $\mu$m from the blood vessel, where the HIF-1 expression is increased and $O_2$ concentration is decreased [208].

Hypoxia can be physically induced in samples by exposing them to a hypoxic gas mixture (95% $N_2$, 5% $CO_2$) in hypoxic incubators, workstations or chambers. The activity of PHDs and the subsequent stabilisation of HIF-1$\alpha$ can be affected by chemical agents such as desferrioxamine and flavonoids [202]. A number of transition metals have also been identified as hypoxia mimetic agents including desferrioxamine, nickel chloride and cobalt chloride. It has been reported that specific prolyl hydroxylases have an iron binding centre critical for enzymatic activities. Iron chelators can remove this iron from the enzyme, replacing it with cobalt, inactivating the hydroxylation activity in the process. Cobalt chloride can also induce HIF-1$\alpha$ expression by binding to the PAS domain resulting in the blockage of HIF-1$\alpha$ pVHL binding and therby HIF-1$\alpha$ stability [204, 209]. Cobalt chloride ($CoCl_2$)

has been used by many investigators as a hypoxia mimetic agent in cell culture [209–211], however this compound may possess some unknown effects in addition to the induction of Hypoxia-Inducible Factor 1 (HIF-1). The question of whether the effects produced by chemical hypoxia mimetics regarding cell survival and proliferation are identical to those when there is reduced oxygen is of considerable biological relevance, given the diverse actions that many of these chemical agents can exert on biological samples [211]. The actions of cobalt chloride may be mediated by signalling pathways not necessarily shared by a 'true' hypoxic response and may cause oxygen independent biological effects [206].

## 4.3 Hadron-Therapy

Hadron-therapy is the radiation therapy technique which employs protons, neutrons or carbon ions to irradiate cancer tumours. Owing to the advantageous energy deposition properties of ions compared with the more commonly used X-rays, at least 1% and possibly as many as 12% of patients currently treated with X-rays would be better treated with protons [5]. The range of a proton or ion is fixed by its energy, which avoids irradiation of healthy tissues at the rear-side of the tumour, while the well localised maximum of the energy loss, known as the Bragg peak (shown in Figure 4.12), in the matter leads to the substantial increase in the irradiation dose in the vicinity of the stopping point [52]. There is also a reduction in the irradiation of healthy tissue in close proximity to the tumour, as the proton or ion scattering on the atomic electrons is weak. The radiation induced cancer risk for children in particular is reduced, as much less energy is deposited in the body by ion therapy when compared with conventional X-ray based therapy [5]. The proton energy window of therapeutic interest ranges between 60 and 250 MeV [8], depending on the location of the tumour. The required energy for carbon ions extends beyond 350 MeV/nucleon [52, 212].

Ion beam therapy has been used at numerous clinical facilities and has proven to be

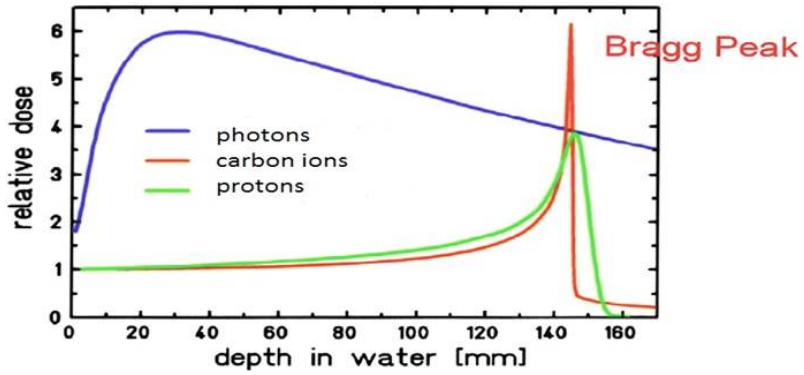


Fig. 4.12 Advantageous energy deposition of ions and protons compared with X-ray photons [213].

both effective and advantageous in a number of tumours. An example study was carried out by Yock et al. [214], where they compared traditional photon therapy with proton radiotherapy to assess late complications, acute side effects and survival rates in paediatric medullablastoma, the most common malignant brain tumour in children. This was a non-randomised, open label (each participant knew how they were being treated), single centre, phase 2 (investigating the safety and ethics of the treatment) trial of fifty-nine 3 - 21 year olds, who had all received surgery prior to the proton therapy being administered within 35 days post surgery to the head and spine [214]. All patients received chemotherapy as part of their treatment as well. Complications which can arise from treating medullablastoma with photon or proton therapy, include cognitive impairment and hearing loss. In this study 16% of the children had serious hearing loss five years after proton beam therapy, which compares favourably with standard radiotherapy, where about 25% have serious hearing loss five years after treatment [215]. Cognitive impairment was also slightly less, with 1.5 intelligence points (IQ) lost per year compared to 1.9 in studies of standard radiotherapy. The overall survival was 83% at 5 years, which was reported to be similar to standard radiotherapy [215]. The main limitation of this study was that it was not a randomised controlled trial directly comparing the two forms of radiotherapy, but this would have been unethical. Grutters *et al.* [216] provide a comparison between radiotherapy with photons, protons

and carbon ions in the treatment of non-small-cell lung cancer (NSCLC) after performing a meta-analysis of observational studies. They carried out a systematic review to find eligible studies on conventional radiotherapy, proton therapy, carbon ion therapy, stereotactic radiotherapy and concurrent chemo-radiation. They obtained pooled estimates of 2 and 5 year disease specific and overall survival, and the occurrence of severe adverse events for each treatment modality, through a random effects meta-analysis, with the pooled estimates corrected for effect modifiers [216]. Meta-analysis is used to synthesise quantitative information from related studies to produce results which summarise a whole body of research [217]. The meta-analysis can either be fixed or random effect. Fixed effect assumes all studies are estimating the same treatment effect, whereas random effects allow for differences in the treatment effect from study to study [217]. Their results showed that corrected pooled estimates for 2 year overall survival in stage I inoperable NSCLC ranged from 53% for conventional radiotherapy to 74% for carbon ion therapy [216]. The 5 year overall survival for conventional radiotherapy was 20%, statistically significantly lower than for stereotactic radiotherapy (42%), proton therapy (40%) and carbon ion therapy (42%) [216]. The authors warrant caution owing to the limited number of patients and limited length of follow up of the particle studies. The overall findings of this analysis was that the survival rates for particle therapy were higher than those for conventional radiotherapy, but similar to stereotactic radiotherapy in stage I inoperable NSCLC. Particle therapy may be more beneficial in stage III NSCLC especially in reducing adverse events [216].

Ion beam facilities mainly employ protons from synchrotron, cyclotron or linear accelerators. Cyclotrons provide higher dose rates than synchrotrons owing to their fast cycling and larger beam current characteristics, but more advanced accelerator designs such as the non-scaling fixed-field alternating gradient (NS-FFAG) [218] and dielectric wall accelerators could provide even higher dose rates. Protons are currently the most widespread form of ion therapy, however, there has been a move towards carbon ions in recent years, as they

have a higher radiobiological effectiveness (explained in Section 4.4.2) making them an effective treatment for radioresistant and hypoxic tumours [219]. Normally, in the absence of oxygen (hypoxia) there is approximately three times less damage formed.

Conventionally, large magnetic steering systems called Gantries have to be employed to enable multi-directional irradiation of a lying patient. These Gantries weigh up to 100 tons for proton systems and 500 tons for carbon ion systems [220], making them very costly to build, and not many hospitals can accommodate the large accelerators required. A potential solution is to use laser-driven accelerators for cancer therapy [6, 221], as they could considerably reduce the size and cost of accelerators for medical applications. The creation of specialised, relatively small medical laser proton accelerators would reduce the size of the accelerator gantry set-up to approximately 2 - 3 m and a few tons, compared to conventional systems which are approximately 6-8 m in diameter, 10-12 m in length and weigh 100 tons or more [6].

## 4.4 Laser-Driven Ion Sources for Hadron-Therapy

There is a wide range of ways in which high quality laser-produced proton beams could be used for medical accelerators. Bulanov [6] suggested an all optical system in which the ion beam was accelerated in the treatment room itself, and thus the issues of beam transport and delivery were minimised. A laser would irradiate the target at the entrance to the treatment room, which would require the conventional Gantry system to be redesigned, as there would be no need for the beam transportation channels, central accelerator or the larger part of the Gantry magnetic system, thus substantially reducing the cost. Antici [222] suggests that laser-produced beams could be used as high quality injectors in a standard radio-frequency based particle accelerator, as this hybrid proton accelerator would benefit from both the excellent properties of the laser based source and the flexibility, reliability and know-how of beam handling as provided by the RF based accelerator structures.

There are significant obstacles which have to be overcome before laser-driven ion beams meet therapeutic specifications, in terms of maximum energy, energy spectrum, repetition rate and general reliability to the levels required by medical standards. A raw beam is an extremely dangerous tool which must be shaped and controlled before it can be used for radiation therapy. The most basic of all requirements is the range of the beam, which should be 25 to 30 cm in tissue, equating to energies of 200-225 MeV for protons and 400-430 MeV/amu for carbon ions [212]. This energy has to be available at the entry point of the patient; therefore higher energies will be required from the accelerator if the beam has to pass through materials for spreading or shaping. Treatment times must be kept to a maximum of a few minutes, owing to immobilisation issues and patient comfort, but also because current RF technologies deliver their dose in this timescale, and a treatment that would take longer than the current modality is unattractive and uncompetitive. The vast majority of patients who receive radiation therapy will be treated in the supine position, as this is both comfortable, improving immobilisation, and coincides with the position in which the diagnostic scans are taken. Accurate treatment plans can only be developed if there is a precise knowledge of the target, organs and other body structures, and it is imperative that the patient is treated in the same position in which the diagnostic scans were taken. For the greatest flexibility, optimum beam delivery is attained when the therapy beam can be aimed at the supine patient from any angle in the vertical plane, whilst retaining the freedom to rotate the patient about the vertical axis. This will allow full access to all the normal entry angles, but also all the oblique ports, often invoked to avoid critical structures [212]. This is a major attraction of laser-driven ion sources, as there is the possibility of bringing the laser into the treatment room and redirecting it with mirrors.

At present the parameters of ion beams achievable are still far from what is required, and extensive and long-term research is needed to ascertain if and how these laser-driven ion beams will become a competitive option [52]. Currently there are several major projects

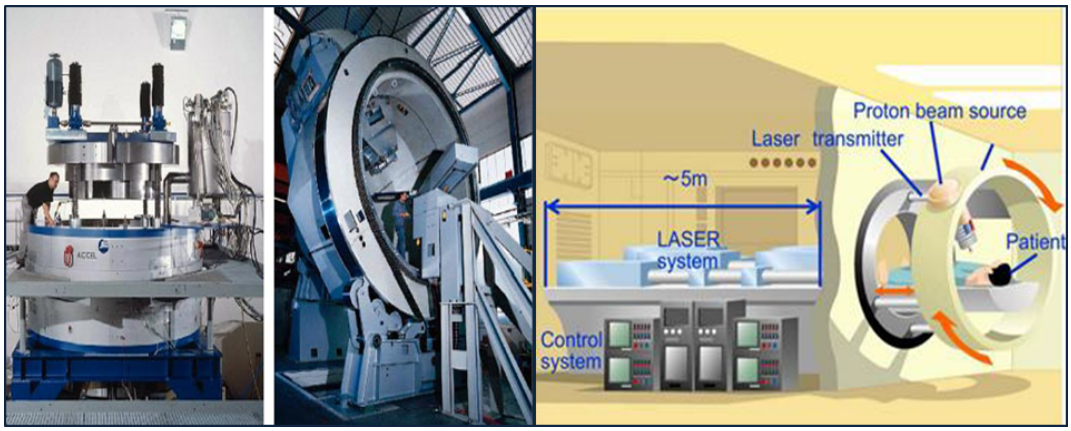


Fig. 4.13 A conventional cyclotron based system [223] on the left compared to a conceptual laser accelerated proton therapy instrument [224] on the right.

worldwide which are exploring the potential of laser-driven ion sources for biomedical applications such as those of Auer [225], Bin [17], Borghesi [226], Doria [227], Hanton [10], Fourkal [228] and Zeil [229]. Others have started to design the possible delivery systems for this treatment, including target chambers and shielding [230], particle energy selection and beam collimation systems [18, 231].

| | Conventional Accelerator | Laser-Driven Accelerator |
|---|---|---|
| Size | large | small |
| Cost | expensive | relatively inexpensive |
| Energy | up to 250 MeV | several tens of MeV (at present) |
| Gantry | large (100-500 tons) | small (1-10 tons) |
| Dose deposition time | 100 ms | ns-ps range |
| Dose rate | $\sim 30$ Gys$^{-1}$ | $> 10^9$ Gys$^{-1}$ |
| Mode | continuous | pulsed |
| Particles produced | singly | bunched |

Table 4.2 Comparison between a conventional particle accelerator and a laser-driven accelerator [224].

The most important thing to keep in mind is that laser-driven ion beam therapy will not become successful just with the arrival of a 200-250 MeV proton source, the hardware and software needed to effectively convert the raw accelerator beam into a suitable therapeutic

radiation beam is also a major factor. The beam delivery systems available at present require well defined energy, very narrow energy spread and tightly focused ion beams, which are currently not producible by laser-driven systems, although Zeil *et al.* [229] appear to have made some progress with table-top systems. Other problems include verifying scaling laws for proton energy with laser power, improving shot to shot reproducibility, developing techniques for accurate dose control and cut-off and addressing the aspects of quality assurance and patient safety [212]. These are not insurmountable problems, but it will take time before laser-driven sources replace conventional accelerator sources for ion beam therapy.

The goals of current research are to:

- Increase the beam energy
- Increase the efficiency of the laser energy conversion into ions
- Improve and control the spectra to achieve mono-energetic ions
- Improve beam quality, repetition rate, collimation and purity
- Optimise acceleration with table-top lasers with shorter pulse durations

The routes to achieving these goals lie in optimising the TNSA mechanism of acceleration (see Section 2.4.1) and exploring innovative mechanisms such as the RPA mechanism (see Section 2.4.2).

### 4.4.1 Ultra-High Dose Rates

Before the clinical application of laser-driven ions, cell irradiation experiments with laser-driven beams constitute an important preliminary step in demonstrating the maturity of this emerging technology. In addition, the biological effectiveness of ultra-short pulsed beams with nanosecond ion bunches of high charge, compared to quasi-continuous beams from conventional accelerators, can be assessed [17]. The unique characteristics of laser-driven

ion beams as compared with its RF counterpart has meant the development of innovative dosimetric approaches, where a dose of 1-10 Gy is delivered to the cells in short bursts of approximately nanosecond duration. More generally, time-resolved radiobiological studies with sub-nanosecond particle bunches might help to elucidate the ultra-fast processes underlying the biological response of cells to ion irradiation [232].

The first demonstration of the feasibility of cell irradiation using laser-driven protons was carried out by Yogo *et al.* [233]. They showed that there was a distinct formation of $\gamma$-H2AX foci, which are an indicator of DNA DSBs, when in vitro human cancer cells were irradiated with a proton dose of 20 Gy [233]. Kraft *et al.* [234] also carried out in vitro proton irradiations of cells using laser-accelerated pulses and showed that there was dose dependent biological damage. A correlation between increasing the dose from 1.5 to 2.7 to 4.1 Gy and an increase in the number of DNA DSBs was observed, and thus the dose effect of the biological damage to the tumour. The dose was fractionated and the average dose rate was comparable to those used in irradiations with conventional accelerator sources ($\sim$ 0.1 $\text{Gys}^{-1}$) [52].

Bin *et al.* [17] showed that by combining advanced acceleration using nanometre thin targets and beam transport, truly nanosecond quasi-monoenergetic proton bunches could be generated with a table-top laser system, delivering single shot doses to living cells of up to 7 Gy. The biological response of the cells, in terms of initial damage to the DNA was quantified using the $\gamma$-H2AX assay [235] and the preliminary relative biological effectiveness obtained was the same as for conventionally produced proton beams at comparable energies [236].

However, in Wilson *et al.'s* [237] recent review in the British Journal of Radiology, we are reminded that ultra-high dose rates may not necessarily be advantageous owing to adverse consequences arising from local oxygen depletion. Both the yield and variety of free radicals formed when ionising radiation interacts with biological systems are enhanced by

the presence of oxygen, as is the fixation of this damage. Within the Bragg peak of an ion species, there are particle mass and particle charge dependent increases in the local intensity of ionisation on a macroscopic scale (the LET), which in turn results in a higher RBE [237]. Both LET and RBE are reduced by spreading out many Bragg peaks to cover a tumour target, which then includes more low LET parts away from the peak itself. The local clustering of high LET biological damage differs from the biological damage produced by X-rays and electrons, and accounts for the increased RBE as clustered damage is more difficult to repair by cellular enzymatic processes. A further advantage of using charged particles is that the extent of oxygen sensitisation on cellular radiosensitivity is reduced for particles with atomic numbers greater than two, however, this effect is reduced by spreading out the Bragg peak, although even a mild reduction in the oxygen dependency could be advantageous in the case of carbon ions [237]. The design of future laser-based systems should take into account the radiobiological concerns associated with the potential oxygen depletion in hypoxic tumours and should aim to minimise any potential disadvantages associated with ultra-high dose rate effects.

The main difference between conventionally produced particle beams and laser produced particle beams, and the potential differences in their radiobiological effects, arise from the fact that the laser produced beams will be pulsed. While the laser pulses required for the acceleration of high energy particles are in the range of femtoseconds, the particle pulses created will be spread in time during the beam transport and the expected duration of the pulse at the target will be approximately 1 ns. Since the repetition rates of laser accelerators are expected to be rather moderate (tens of Hz in-line with currently available clinical accelerators [238]), one can envisage that during one session each voxel of the planning treatment volume can be targeted at most a few times, if the treatment time is to be kept reasonably short [225]. Thus with one pulse a considerable fraction of the required dose at a target voxel has to be given. Assuming a deposition of $>1$ Gy in 1 ns, this translates to an

ultra-high dose rate of $>10^9$ Gys$^{-1}$.

In a recent publication Fourkal *et al.* [228] discusses the LET of proton clusters. He states that in conventional particle accelerators, the particles are produced in long pulses, with average inter-proton distances larger than those in a laser-plasma interaction scheme[228]. Therefore the radiobiology of such protons will be governed by the interaction of a single proton with the cell. In the laser-plasma interaction scheme, the protons will be emitted as a single bunch of particles, less than 1 ps in duration, with inter-proton distances many orders of magnitude shorter. They will therefore not only interact with the medium they are traversing, but also each other [228], which under certain conditions may lead to an interference effect manifested by the increased energy deposition per unit length.

Fourkal's linear response theory predicts that when the distance between protons in the cluster becomes less than its velocity divided by the characteristic frequency of the collective excitations supported by the medium it is traversing, the cluster's LET starts increasing so that the stopping power of the individual proton in the cluster increases compared to that of a single moving particle. The cluster's LET increase is a consequence of the interaction with the outer-shell electrons of the medium, where each passing projectile of the cluster excites the collective oscillations supported by the medium. If the distance between the projectiles is small enough, the field wakes interfere coherently leading to increased energy loss by the whole cluster.

If all the protons in a cluster are at the same spatial location, i.e. the inter-particle distance is zero, the effective charge of the cluster would be $Ne$, where $N$ is the number of protons in the cluster and $e$ is the elementary charge, thus the stopping power would scale as $S \sim (Ne)^2$. If the protons are separated by a great distance, the stopping power of the cluster will scale as $S \sim Ne^2$. As the ratio between the two stopping powers is $N$, the individual stopping power of a single proton in the cluster will scale from 1 to $N$ depending on how close the particles are to each other. This increase in stopping power is physically explained

by considering the hard and soft inelastic collisions between the proton and the inner- and outer-shell electrons in the medium. In the collisions involving the inner-shell electrons, the individual electron behaviour dominates and the characteristic response frequency of the electrons is much larger than the characteristic frequency of the external field created by two charges (a simplistic view of a cluster). Under this condition, the two external charges are seen as two separate entities and the stopping power of the cluster owing to the interaction with the inner-shell electrons is equal to the sum of the individual stopping powers of the particles. However, the characteristic response frequency of the outer-shell electrons may, under certain resonance conditions, be comparable to the characteristic frequency of the external electric field and the collective aspect of the interaction has to be invoked. In these conditions, the passing projectile will excite a wake of collective electron density fluctuations behind it [228]. The interference between the two wakes will determine the effective stopping power of the cluster. If the two projectiles are in the same spatial location, the two wakes are in the same phase and interfere coherently so that the stopping power of a cluster scales as a square of the number of particles in the cluster. When the particles are far apart, the excited wakes will have random phases and will not interfere with each other, thus the stopping power of the cluster will just be the sum of the stopping powers of the individual particles in it.

An interesting point which Fourkal further discusses is the effect which the increased LET of the proton cluster may have on the RBE. He provides two possible scenarios: the increased LET of the cluster is translated into the increased LET of the individual protons in it and the data for the single proton RBE can be used to determine the biological effectiveness of the cluster; the RBE also depends on the charge of the particles, where the higher the charge the higher the RBE and the cluster could be viewed as a quasi-particle with the effective charge greater than 1 and a RBE value closer to that for heavier ions. Both of these scenarios result in an increase in the RBE of the cluster and the RBE of a spread-out

Bragg peak built out of different energy proton clusters should also be elevated [228], both conclusions that support the use of laser-driven ions for hadron-therapy.

When a laser interacts with a thin foil target, electrons are expelled from the target by the action of the laser's ponderomotive force and the remaining charged substrate expands owing to the Coulomb explosion effect [228]. Assuming 10% of the electrons completely escape the target, which was of initial size 10 $\mu$m, the proton cloud concentration at 1 m away would be approximately 2 x $10^8$ $cm^{-3}$ for protons with a velocity of c/2 [228]. This is much lower than the threshold value of $\sim 10^{11}$ $cm^{-3}$ for the collective effects to be observed. However, at a distance of 10 cm from the target, the proton concentration is 2 x $10^{11}$ $cm^{-3}$, which is above the threshold for collective effects to be observed [228]. This suggests that the point of observation where these collective effects may be detected has to be located no more than 10 cm from the target. This condition means that these collective effects will not be observed during the cellular irradiations employing laser driven ions described in Chapter 6 as the cell plane will be more than 10 cm from the target. To place a sample this close to the target, the sample will have to be placed inside the vacuum, which is not feasible for cell samples as they will not survive. These investigations could be carried out with plasmid DNA which is more resilient.

# Chapter 5

# Biological Tools and Techniques

This chapter describes the biological techniques and equipment employed during the radiobiological experiments performed as part of this thesis, including the design and validation of a portable, compact, beam-line hypoxia chamber compatible with both X-ray irradiations and low energy laser accelerated proton irradiations.

## 5.1 Cell Culture

Tissue culture was first developed in the early 1900s (a frog embryo nerve fibre was outgrown by Harrison in 1907 [239]) as a means of studying the behaviour of cells in response to normal and experimental stress, free of the variations that might arise in the whole organism. Initial methods used fragments of tissues, but as the techniques employed were refined and developed, it became possible to study the behaviour of single cells, thus the name was changed to cell culture [240]. Cell culture refers to the removal of the cells from a host organism and their subsequent growth in a favourable artificial environment composed of nutrient solutions, a suitable substrate to support the growth of the cells, and carefully controlled conditions of temperature, humidity and gaseous atmosphere. The cells may be directly removed from the tissue of the organism and disaggregated by mechanical or enzy-

matic means before they are cultivated, or they can be derived from a cell line or cell strain that is already established [240, 241].

Primary cell culture refers to the stage of the culture process after which the cells have been isolated from the host tissue and proliferated under the appropriate controlled conditions until they have reached confluence, where they occupy all the available space on the substrate. After this point the cells must be sub-cultured or passaged. The passage number of the cells is the number of sub-cultures the cells have undergone. This number should not be allowed to get too high, otherwise the cells will start to undergo genetic drift and other variations. The split ratio used when sub-culturing is dependent on when the cells are required for experiments; for example a 1:2 split should be 70-80% confluent and ready for use within 1 to 2 days, a 1:5 split will be ready in 2 to 4 days and a 1:10 split will be ready in approximately 4 to 6 days. Cells should be sub-cultured when they are approximately 80% confluent (80% of the substrate is covered with cells) and in the log phase of growth. When the cells are fully confluent they stop growing, and it takes them longer to recover when they are reseeded. Cells can be sub-cultured if they are less than 80% confluent, but a lower split ratio should be used to ensure the cell density is high enough for the cells to survive, however if the cells are over confluent they will start to die off and may not be recoverable [241, 242].

A cell line is what a primary culture becomes after the first sub-culture. Cell lines which have been derived from primary cultures are most commonly finite cell lines which have a limited life span, as normal cells can only divide a limited number of times before they lose their ability to proliferate through a genetically determined event known as senescence. Continuous cell lines are formed when finite cell lines become immortal through a process known as transformation, where the finite cell acquires the ability to divide indefinitely [241].

The exact conditions of cell culture vary widely and are dependent on what cell type is

being used and what biological processes are being investigated, although all cell culture must be carried out in aseptic conditions under a laminar flow hood to prevent the contamination of the cell line. Most cells are anchorage dependent and must be cultured on appropriate solid or semi-solid substrates to produce monolayer adherent cultures. Other cells can be grown floating in the culture medium in suspended culture. Most cells are stored in a cell culture incubator at 37°C with a 5% $CO_2$ atmosphere and 95% humidity.

### 5.1.1 AG01522 Cell Line

The cell line used for all the radiobiology experiments carried out for this thesis was the human fibroblast cell line AG01522. This is a male apparently healthy non-fetal tissue skin cell line that is untransformed and exhibits fibroblast-like morphology. The cells were obtained from the Coriell Institute for Medical Research (Camden, New Jersey, USA) from the original culture initiated on the $21^{st}$ of January 1976 from explants of minced foreskin removed ante-mortem one day prior to culturing [243].

These are normal non-cancerous adherent cells, which means they must be attached to a substrate such as a culture flask in order to proliferate, and they grow in a single layer called a cell monolayer as a result of contact inhibition. These properties differ from cancerous cells which display a degree of anchorage independence, meaning they can proliferate in suspended culture, and fail to exhibit any contact inhibition thus overgrow their neighbouring cells and form piles of cells or "foci" on the cell monolayer [133, 149]. Contact inhibition is the stopping of the continued locomotion of the cell in the direction which has brought it into contact with an adjacent cell, such that one cell does not use another as a substratum [244]. This type of anti-social behaviour between the cells is a reflection of the altered interactions between the cell membranes in contact with each other and the substrate on which they are growing [133].

AG01522 cells exhibit fibroblast morphology where the cells are bipolar or multipo-

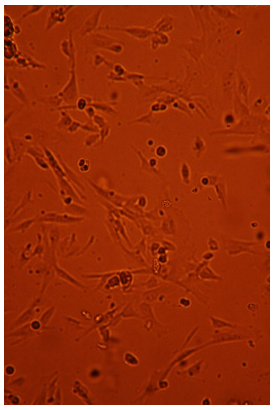

Fig. 5.1 AG01522 human fibroblast cells at 10 x magnification. Image taken a few hours after seeding as the cells are starting to attach and spread out.

lar and grow in a flat extended manner and not the round morphology (lymphoblast-like) adopted by cancerous cells [149, 241]. At confluence AG01522 cells have a cellular cross sectional area estimated between 800 $\mu$m$^2$ [245] and 1370 $\pm$ 50 $\mu$m$^2$ [246], with a nuclear area of 144 $\mu$m$^2$ and nuclear thickness of 1.2 $\mu$m [247].

### 5.1.2 Sub-culture Technique

The AG01522 were cultured in filtered minimum essential medium eagle with alpha modifications (alpha-MEM, Sigma Aldrich) supplemented with 20% FBS (foetal bovine serum) and 5% Pen-Strep (penicillin streptomycin antibiotics). This equates to $\sim$ 100 ml of FBS and 5 ml of 1 x Pen-Strep being added to a standard 500 ml bottle of alpha-MEM. Only one or two bottles of media were prepared at a time to keep the media fresh and the cultures contamination and crystal free. If the media showed signs of crystallisation or contamination, it was discarded and fresh media prepared. The prepared and unprepared media were stored in the fridge or cold room at 5° and warmed to 37° in a water bath before use with the cells.

The cells used were from a stock of cryo preserved passage 9 cells kept in the CCRCB -80° freezer, originally from the Coriell Institute. The cells were thawed by holding the 2 ml

vial in the water bath for approximately 3 minutes to thaw the cell suspension, then adding the suspension drop wise using a Gilson pipette to a 50 ml centrifuge tube containing 10 ml of fresh cell medium. The combined suspension is gently mixed and pipetted to disperse the cells evenly in a single cell suspension, then added to a T25 tissue culture flask (a plastic flask with a cell growth area of 25 $cm^2$ and a vented filter cap). The flask is stored in a standard cell culture incubator with a 95% air, 5% $CO_2$ atmosphere, 95% humidity and a temperature of 37°. After 24 hours, the cell media is removed and replaced with 15 ml of fresh media. The cells are left to grow until they reach 80% confluence, with the media being changed every two days. When the cells reach confluency, the media inside the flask changes colour, and appears turbid when the media becomes infected with bacteria when the culture flask is swirled. If the cells are over confluent it can be difficult to reseed the cells in a uniform density as the cell pellet tends to clump, giving uneven growth in the new culture flask. The cells should either be transferred from the T25 flask into a single T75 flask (a flask with a growth area of 75 $cm^2$), or split into two or three T25 flasks, to allow the cells more space to proliferate. These cells are now in passage 10. The cells should be allowed to multiply and grow in number until you have enough for your experiment, usually around passage 12, and experiments should be carried out with cells of roughly the same passage number (12-14 in the experiments discussed) for the reasons described in Section 5.1 above.

The methods used for seeding the cells on the cell dishes ready for the experiments and reseeding the cells in culture flasks after splitting are predominantly the same, with slight variations in the final steps. The cells are first removed from the incubator and the old media is discarded. The cells are then washed with 10 ml of sterile PBS (Phosphate Buffered Saline) three times to remove any remaining media. This washing step removes any traces of serum, calcium and magnesium that would inhibit the action of the dissociation agent [241]. The PBS is discarded and 10 ml of 0.05% Trypsin EDTA (diluted in PBS) is

added to trypsinise the cells in the T175 culture flask. The flask is placed in the incubator for approximately 3 to 5 minutes for the trypsin to work. The cell flask is gently tapped to help the cells dislodge from the surface. The trypsin in the flask becomes cloudy when the cells have detached, and the flask is checked under the microscope to make sure all the cells are now in suspension. The suspension is neutralised with 10 ml of fresh culture medium, and is gently pipetted against the side of the flask to break up any clumps of cells and to ensure all the cells have been detached into the suspension. The amounts of 0.05% Trypsin EDTA and cell culture medium can be adjusted depending on the size of flask the cells are in; 5 ml and 5 ml should be used for a T75 flask for example, 3 ml and 3 ml for a T25 flask. The suspension is then transferred to a 50 ml centrifuge tube and spun at 1200 rpm for 6 minutes to produce a cell pellet. The supernatant containing the trypsin and media is gently poured off and the cell pellet is re-suspended in 5 ml of fresh media. The media is gently pipetted several times to dislodge the pellet and form a single-cell suspension. This is where the methods start to diverge. At this point the cell suspension can be directly transferred to two or more fresh flasks of the same size, or one larger flask depending on the volume of cells required and the passage number, with 25 ml of fresh media added to the flask (T175, less for smaller flasks). When specific volumes of cells are required for experiments, the cell suspension must be counted to obtain the number of cells per ml. This was done by several different methods: a Z2 Coulter Counter particle and size analyser (Beckman Coulter, High Wycombe, UK); a portable Scepter 2.0 Cell Counter (Merck Millipore, Darmstadt, Germany); and a Hemocytometer. The Coulter Counter and Scepter were used for X-ray experiments carried out in the CCRCB and laser-driven ion experiments carried out in TARANIS, the Scepter was used for experiments carried out at Vulcan, and the Hemocytometer was used for experiments at LULI and the previous work carried out at Gemini.

When using the Coulter Counter, 0.1 ml of the cell suspension is added to a Coulter

counting cup containing 9.9 ml of Isoton solution (Beckman Coulter) to produce a 1:100 solution. A background reading is established using a cup containing 10 ml of Isoton, which must be below 50 before the cell suspension is analysed. The Coulter Counter works by using electrical sensing technology often referred to as the Coulter Principle. This principle is based on measurable changes in the electric resistance produced by the cells suspended in the Isoton solution (which acts as an electrolyte). There is an aperture in the Coulter probe, between two electrodes, which is the sensing zone through which the cells pass. Each cell in the sample will displace its own volume in the electrolyte, with this displaced volume being measured as a voltage pulse, and the pulse height being proportional to the cell volume [248]. The volume of solution drawn through the probe is 0.5 ml and is precisely controlled by a mercury free metering system, allowing both accuracy and speed. Thresholds can be set such that only particles between 5 and 21 $\mu$m are counted. The cup containing the cell sample is then loaded into the Coulter counter, and the number of particles is measured three times. An average number of particles is calculated and this number is multiplied by the dilution factor to determine the number of cells per ml in the original cell suspension. For example if the average count was 1006 in 0.5 ml of the 1:100 solution, the cell number per ml would be calculated as follows:

$$1006 \times 2 \times 100 = 201200 \text{ cells ml}^{-1} \tag{5.1}$$

When using the Scepter, 0.5 to 1 ml of the cell suspension is required for the counting sample, therefore the cell pellet should be re-suspended in 10 ml of media rather than 5 ml so as not to waste a large proportion of the sample. The 0.5 ml sample of the suspension should be added to a 1.5 ml micro-centrifuge tube, which should be gently agitated to keep the suspension single cell before counting. The Scepter is turned on and a sensor tip is attached when prompted, with the electrode sensing panel facing forwards. The plunger on the Scpeter is depressed and the sensor tip submerged in the sample, then the plunger

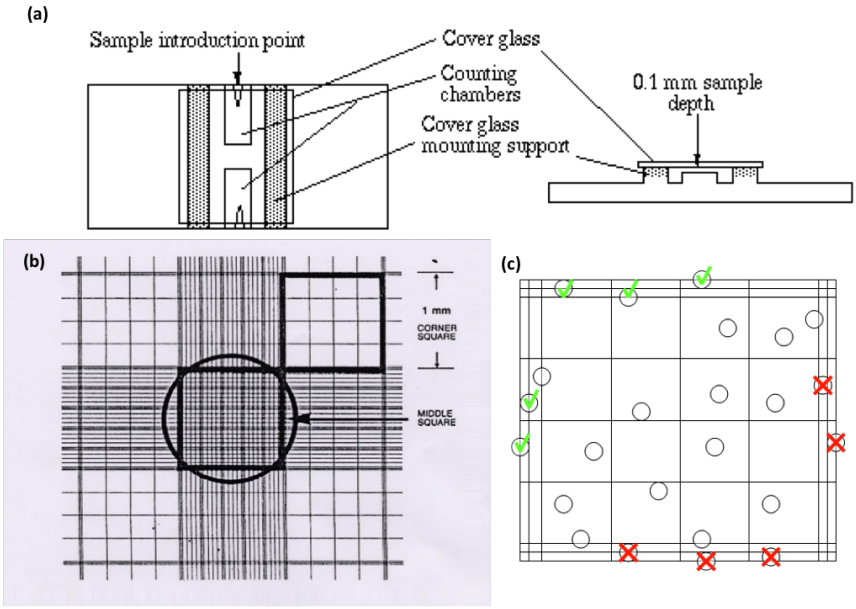


Fig. 5.2 **(a)** Schematic of a Hemocytometer [251]. **(b)** The appearance of the counting grid visualised under the microscope [10]. **(c)** Counting system to ensure accuracy and consistency; cells within the large square and those crossing the edge on two out of the four sides are counted [252].

is released to draw 50 $\mu$l of the suspension into the channel embedded in the sensor. The Sceptor detects each cell passing through the sensor's aperture, calculates the concentration and displays a histogram as a function of cell diameter or volume on its screen [249]. The Scepter also employs the Coulter Principle, where the cells flow into the sensor, increasing the resistance and thus the voltage by Ohm's law (V = IR). Voltage spikes of the same size are bucketed into a histogram, giving you quantitative data on the cell morphology which can be used to evaluate the health of your cells [250]. The concentration displayed on the Scepter is the number of cells per ml of the solution.

When using the Hemocytometer, it is first cleaned with ethanol and the coverslip affixed. 10 $\mu$l of the cell suspension is gently pipetted at the edge of the coverslip and allowed to run under the coverslip by capillary action. The coverslip has a series of lines etched on it producing a 3 by 3 grid of 1 $mm^2$ squares. Each of the corner squares is divided into 16 squares of area 0.0625 $mm^2$, and the centre square is divided into 25 0.04 $mm^2$ squares

which are subdivided into 16 squares themselves [253]. The corner squares should be used for counting the AG01522 cells. The Hemocytometer is visualised under a microscope and the four 1 $mm^2$ corner squares are counted as shown in Figure 5.2. This produces 4 counts which should be averaged, with the cell concentration per ml calculated as follows:

$$\text{avaerage number of cells in a 1 mm}^2\text{ square } \times \text{ dilution factor } \times 10^4 \tag{5.2}$$

The cell counts obtained with the Coulter Counter and the Scepter are both very accurate and are in good agreement with each other for concentrations up to 5 x $10^5$ cells per ml when theoretical and measured cell concentrations are compared. The Hemocytometer is in good agreement up to concentrations of 2.5 x $10^5$ cells per ml. The Coulter counter and the Scepter both use the Coulter method to calculate the number of cells, hence why they are in good agreement, but as the Hemocytometer is a manual method, human error creeps in at higher concentrations, with the concentration usually being over estimated [254].

The original cell suspension can then be diluted accordingly for plating specific cell quantities, or the total number of cells can be obtained to determine the split ratio for re-seeding. The cell suspension is diluted to the desired concentration with fresh cell culture media and transferred to fresh culture flasks for re-seeding or sterile cell dishes for experiments.

### 5.1.3 Mycoplasma Testing

Mycoplasma contamination is one of the most prevalent and serious sources of cell line contamination. Mycoplasma represent a large group of micro-organisms called Mollicutes, characterised by a lack of a rigid cell wall and plasma-like form. They have extremely basic genomes, forcing them to function as parasites in order to meet their energy demands, thus they adhere to other cells and exploit their host cells to survive. These characteristics, coupled with their small size (0.3 - 0.8 $\mu$m), make them invisible to the naked eye and

| Type | Incidence |
|---|---|
| primary cell cultures | 1 % |
| early passage cell cultures | 5 % |
| continuous human or animal cell lines | 15 - 35 % |

Table 5.1 Incidence of Mycoplasma contamination in cell culture [255]

very hard to detect by optical microscopy even at high concentrations (> $10^7$ cfu/ml, colony forming units per ml) [255–257]. Bacterial and Fungal infections are also important in cell culture, but they are not so serious as they are usually obvious and easily detected. Mycoplasma contamination does not cause any visible changes to the growth media such as turbidity or a change in pH, which are commonly associated with bacterial or fungal infections, thus infections can remain undiscovered for several months.

The use of contaminated cells endangers almost all aspects of cell physiology, often leading to the loss of unique cell lines and erroneous results. One of the first signs of an infection is a slowdown in cell profliferation as the cells and Mycoplasma compete for nutrients. Other signs include cell aggregation and poor transfection efficienices. The Mycoplasma grow very slowly, and do not kill the host cell outright but affect variuos cellular parameters. As they cause so many changes, the infected cell line can nearly be considered as a different cell line [258]. This is a real problem as it seriously impacts the reliability, reproducibility and consistency of experimental results, thus Mycoplasma testing is an important quality control measure.

The primary sources of mycoplasma contamination are cross contamination from untested infected cells, contaminated cell culture medium reagents such as serum and trypsin, or direct infection from the researcher [256, 257]. Personnel are the main source of M. orale, M. fermentans, and M. hominis, which account for more than half of all Mycoplasma infections, M. arginni and M. laidlawii originate in FBS, and trypsin is a main source of M. hyorhinis [259]. To effectively prevent Mycoplasma contamination, good aseptic technique

| Species | Frequency | Natural Host |
|---|---|---|
| M. orale | 20 - 40 % | Human |
| M. hyorhinis | 10 - 40 % | Swine |
| M. arginini | 20 - 30 % | Bovine |
| M. fermentans | 10 - 20 % | Human |
| M. hominis | 10 - 20 % | Human |
| M. laidlawii | 5 - 20 % | Bovine |

Table 5.2 Most common species of mycoplasma that cause cotamination [255]

must be used, laboratory accidents should be reduced, the laboratory should be kept clean, and a strict policy of quarantining all incoming cell lines until testing has confirmed they are Mycoplasma free [258]. Once Mycoplasma have been detected, the contaminated cell line should ideally be discarded as the contamination can spread rapidly to other cultures through the dispersion of aerosol droplets. However, if this is not a feasible option, they can be treated with Mycoplasma-eradication products, including Mycoplasma selective antibiotics (the lack of cell wall means Mycoplasma are unaffected by many common antibiotics such as Penicillin and other beta-lactam antibiotics that target the cell wall [260]), which can eliminate the Mycoplasma and restore the cell behaviour within a few days/weeks [256].

There are several different methods of Mycoplasma testing including histological staining, electron microscopy (TEM and SEM), biochemical methods (e.g. enzyme assays and protein analysis), immunological procedures (such as fluorescence staining), DNA fluorochrome staining, microbial culture, RNA hybridization (filter/liquid) and polymerase chain reaction (specific and universal PCR primers) [255]. All cell samples used for the experiments in this thesis were tested for Mycoplasma by the laboratory technician in the CCRCB at regular intervals and found to be Mycoplasma free.

### 5.1.4 Cell Doubling

An experiment was preformed using AG01522 human fibroblast cells to determine the difference in doubling time of cells plated on the Mylar used for all our radiation exposure experiments and normal cell culture slide flasks.

Approximately 100,000 cells were seeded onto 6 cell dishes, each with a 3 $\mu$m Mylar substrate stretched between a stainless steel ring and plate, sealed with an O-ring, and 100,000 cells were also seeded in 6 cell culture slide flasks. These cells were cultured in the same growth medium with the same supplements, and stored on the same shelf of the cell culture incubator at 37°C, 5% $CO_2$ and 95% humidity. Two samples each of those plated on Mylar and slide flasks were left in the incubator for 72 hours, another two for 48 hours and the final two for 24 hours.

After 24 hours, the first two samples of each type were removed from the incubator and trypsinised with 1 ml of 0.01% Trypsin EDTA. The Trypsin was continually pipetted over the cell sample and the dish or flask gently agitated to remove all the cells, checking under the microscope to ensure all cells had detached. The solution was then neutralised with 1 ml of fresh culture media, and the suspension was still continuously agitated to ensure a single cell suspension. A 10 $\mu$l sample of this suspension was then added to a Coulter cup containing 9.9 ml of Isoton solution, and counted twice with the Coulter Cell Counter. The cell concentration per ml, and thus the total number of cells in the 2 ml sample were calculated. This process was repeated with the four 48 hour samples and the four 72 hour samples at the appropriate times. The results are presented in Table 5.3.

The cell doubling time was calculated for the cells grown on Mylar and the cells grown on the slide flasks using the following formula:

$$\text{Doubling time} = \frac{\text{Duration} \times log(2)}{log(\text{Final Concentration}) - log(\text{Initial Concentration})} \tag{5.3}$$

Using this equation, the doubling time for cells grown on Mylar was found to be 13.73

| 24 hours | Mylar Sample 1 | Mylar Sample 2 | 24 hours | Slide Flask Sample 1 | Slide Flask Sample 2 |
|---|---|---|---|---|---|
| Count 1 | 59200 | 55200 | Count 1 | 98800 | 118000 |
| Count 2 | 51200 | 54000 | Count 2 | 109200 | 98800 |
| Average | 54900 | | Average | 106200 | |
| St. Dev. | 3321 | | St. Dev. | 9269 | |
| St. Err. | 1660 | | St. Err. | 4635 | |
| 48 hours | Mylar Sample 3 | Mylar Sample 4 | 48 hours | Slide Flask Sample 3 | Slide Flask Sample 4 |
| Count 1 | 165200 | 199200 | Count 1 | 235600 | 279600 |
| Count 2 | 172000 | 201200 | Count 2 | 219200 | 276400 |
| Average | 184400 | | Average | 252700 | |
| St. Dev. | 18472 | | St. Dev. | 30000 | |
| St. Err. | 9236 | | St. Err. | 15000 | |
| 72 hours | Mylar Sample 5 | Mylar Sample 6 | 72 hours | Slide Flask Sample 5 | Slide Flask Sample 6 |
| Count 1 | 134800 | 210000 | Count 1 | 207600 | 255200 |
| Count 2 | 152800 | 202800 | Count 2 | 210400 | 258800 |
| Average | 175100 | | Average | 233000 | |
| St. Dev. | 36999 | | St. Dev. | 27775 | |
| St. Err. | 18499 | | St. Err. | 13888 | |

Table 5.3 Summary of the number of cells in each 2 ml sample from each of the two counts, average number of cell from the counts, the standard deviation and the standard error of the AG01522 cells grown on 3 $\mu$m Mylar (surface area of 16.63 $\pm$ 0.73 cm$^2$) and cell culture slide flasks (surface area of 9.2 $\pm$ 0.2 cm$^2$), measured 24, 48 and 72 hours after seeding.

$\pm$ 0.66 hours, and the doubling time for cells grown on the slide flasks was 19.19 $\pm$ 1.63 hours. The cell counts at the different data collection times are shown in Figure 5.3.

Unfortunately, the counts obtained show that almost 50% of the original seeded cells were not present on the Mylar 24 hours after seeding. This could be due to errors in the original calculations when plating the cells, however this is unlikely as the same solution was used to plate all the samples and more than 100,000 cells were present in the slide flasks. The cell solution may not have been a single cells suspension, thus more cells were plated on the slide flasks than the Mylar, or more cell clumps were deposited on the Mylar affecting the ability of the cells to attach and proliferate, or there is something present on

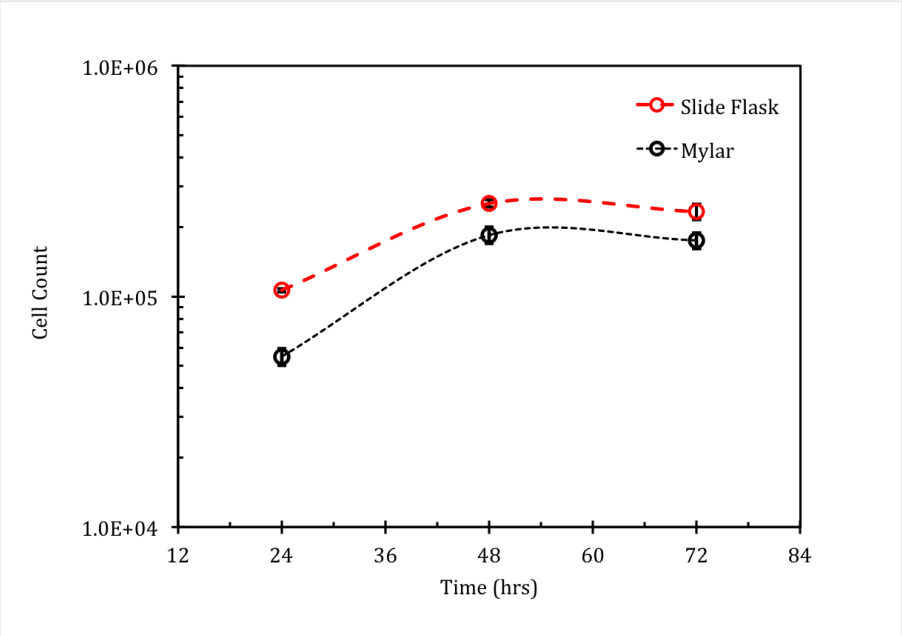


Fig. 5.3 Graph showing the total number of cells in the 2 ml samples 24, 48 and 72 hours after seeding. The samples were counted using a Coulter Counter, with the total cell number calculated using the method described in Section 5.1.2.

the surface of the Mylar which the cells do not like. However, once the cells do attach, they appear to proliferate faster on the Mylar than on the slide flasks.

There could also be problems with using the Coulter Counter to obtain the counts, as the Coulter Counter is most accurate with raw cell counts of between 500 and 5000. The raw cell counts obtained before plating the original samples and after harvesting the samples at the different time points were between 125 and 700, thus some of the counts fall outside this range and may not have been properly detected by the Coulter Counter as the concentration was too low.

All the experiments presented in Chapter 6 were carried out on Mylar, so whatever effect occurred was present for all experiments. Being aware of this issue allowed us to adjust the numbers of cells plated to ensure the values we required would be present on the Mylar. For example we would normally plate 300,000 cells, but we increased this to 400,000 cells to account for some lost cells.

## 5.2 Detection of DNA Damage

A DNA DSB is the only form of critical DNA damage, as it is believed that a single unrepaired DSB is sufficient for the induction of the cell death process [261, 262]. A DSB is a type of DNA damage in which two complementary strands of the double helix are damaged simultaneously in locations close to each other, as described in Section 5.2.1. The factors leading to the formation of DSBs include exogenous factors such as ionising radiation and endogenous factors, which are associated with physiological processes occurring in the cell [263], such as a constant process of oxidative damage by ROS that are produced inside the cell as a result of metabolic processes. It is estimated that in a single cell cycle at least 5000 single stranded DNA breaks can occur as a result of ROS production[261]. Approximately 1% of these DNA breaks are converted into double strand breaks, mainly during DNA replication, while the remaining 99% is repaired. Thus, during the cell cycle in a single nucleus, about 50 so called "endogenous" double strand breaks are formed. Accumulation of unrepaired DNA damage induced by ROS leads to cell ageing and may be responsible for the induction of neoplastic transformation.

In humans, the efficient repair of DNA DSBs is essential for cell survival. Two major pathways have evolved to deal with these lesions, HR and NHEJ as described previously (Section 5.2.4). The mechanism of HR is based on using the genetic information from a corresponding undamaged region present on the second DNA molecule or homologous chromosomes and therefore is active mainly during the S and $G_2$ phases of the cell cycle, while NHEJ is based on a direct ligation of the two ends of damaged DNA molecules and repairs double strand breaks mainly in the $G_1$ phase.

### 5.2.1 $\gamma$−H2AX

It was reported several years ago that in mammalian cells the phosphorylation of the subtype of histone H2A, called H2AX, in the position Ser139 occurs in response to double strand

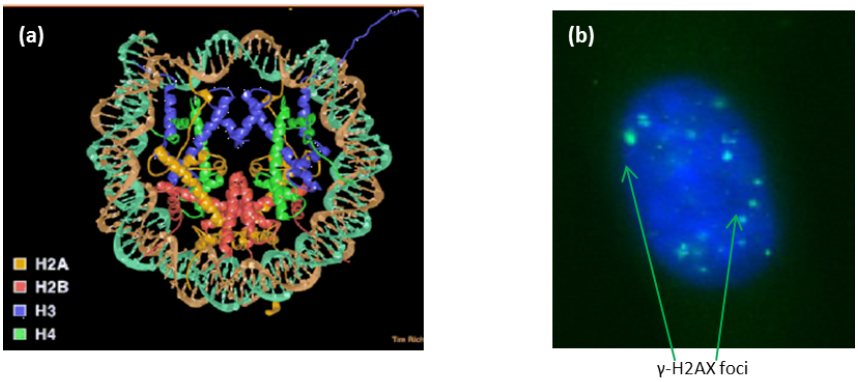


Fig. 5.4 **(a)** Schematic of a chromatin containing histones [266]. **(b)** $\gamma$-H2AX foci [10].

break formation [235, 263] (hundreds to thousands of H2AX are phosphorylated per double strand break [264]). $\gamma$-H2AX induction is one of the earliest events detected in cells following exposure to DNA damaging agents; it appears within minutes and reaches maximum levels after 30 minutes [235]. H2AX represent 2-10% of the H2A subfamily of histone proteins in chromatin and has not been found to be concentrated at a specific region of the DNA, but instead is randomly incorporated into histones throughout the DNA. The phosphorylated form of H2AX is called $\gamma$-H2AX, as it was first observed in cells exposed to $\gamma$-rays [262]. Since then, many researchers have focused on the explanation of the mechanisms which induce phosphorylation of H2AX and its role in DNA damage signaling and repair. H2AX proteins within a few mega-bases of the damage site are involved, but it is unclear how this phosphorylation propagates form the damage site. After DNA repair, $\gamma$-H2AX is dephosphorylated [263], which is useful for the assessment of DNA repair [265].

Histone H2AX is a substrate of several phosphoinositide 3-kinase-related protein kinases (PIKKs), such as ATM, ATR (ATM and Rad3-related), or DNA-dependent protein kinase (DNA-PK) [261, 264]. ATM kinase is considered as a major physiological mediator of H2AX phosphorylation in response to double strand break formation. ATM is activated by its autophosphorylation at Ser1981 position, which leads to dissociation of the inactive ATM dimers into single protein molecules with increased kinase activity. A tri-protein com-

plex called MRN complex recognises DNA damage, recruits ATM to the site of damage and also functions in targeting ATM to initiate phosphorylation of the respective substrates. It is also reported that ATM activation requires prior ATM acetylation, mediated by Tip60 histone acetyltransferase. H2AX can also be phosphorylated by ATR and DNA-dependent protein kinases. ATR phosphorylates H2AX in response to single strand DNA breaks and during replication stress, such as replication fork arrest. DNA-PK mediates phosphorylation of H2AX in cells under hypertonic conditions and during apoptotic DNA fragmentation. However, DNA damage caused by ionising radiation leads to phosphorylation of H2AX that is mediated by all PIKK kinases, ATM, ATR and DNA-PK [261].

Measuring DNA damage has been of interest in the research community because of its predictable nature. Development of an antibody specific to $\gamma$-H2AX made it possible to detect H2AX phosphorylation and thus detection of DNA damage in individual cells. The presence of $\gamma$-H2AX in chromatin can be detected shortly after induction of double strand breaks in the form of discrete nuclear foci produced by large numbers of $\gamma$-H2AX molecules [262]. Since each focus represents a double strand break in a 1:1 manner [264], their frequency reports the incidence of double strand breaks [263]. Compared with alternative methods of DNA damage assessment, the immunocytochemical approach is less cumbersome, more precise, requires only a small sample size and offers much greater sensitivity [235, 261, 262, 264]. The presence of $\gamma$-H2AX containing nuclear foci can be measured by microscopy, flow cytometry and possibly Western blotting of cell/tissue lysates, with normalisation for the total H2AX levels.

$\gamma$-H2AX foci are most commonly detected and quantified by fluorescence, which involves the primary $\gamma$-H2AX antibody described above and fluorescent secondary antibodies. Immunofluorescence requires the use of epifluorescent microscopes, which allow the naked eye to count cells with DNA damage. $\gamma$-H2AX foci are manually counted by eye through the microscope or in images previously captured, it is laborious, time consuming and subject to

human error. It is therefore clear that there is an incentive to develop high throughput foci counting systems for research and routine clinical assay. However, validation of these automated systems unavoidably relies on comparisons with manual counting, but once achieved, enables the extension to the analysis of foci size and intensity [262]. To assess the $\gamma$-H2AX foci, the results of immunofluorescence have been tested against the comet assay. This assay has been deemed quick, simple and reliable, but recently it has been established that the $\gamma$-H2AX assay is 100 times more sensitive to detecting damage levels than the comet assay [264]. Microscopy reveals valuable information inaccessible by other methods, such as differential response in tumour tissues (homogeneous vs. non-homogeneous DNA damage induction) and the extent of DNA damage (separate foci in weakly damaged cells vs. pan-staining in suspected apoptotic cells) [262]. The $\gamma$-H2AX assay can also be exploited to study distinct cell cycle phases and individual cells [265].

The most important clinical application of $\gamma$-H2AX measurements is to follow double strand break levels induced by radio- and chemotherapy as a marker of treatment efficiency and in dose/scheduling estimation, as well as to determine the efficiency of DNA repair to predict possible tumour sensitivity of resistance to DNA damaging anticancer agents.

### 5.2.2 53BP1

Owing to the action of the DNA damage checkpoints, cells generally do not enter the S or M phase before DNA lesions are properly repaired. Cancer cells have often lost some aspects of checkpoint function, therefore they have a greater sensitivity to DNA damaging agents, which in turn provides them with a higher rate of genomic evolution to acquire a growth advantage. The DNA damage checkpoint is a signal transduction cascade that relays information from DNA lesions to components of the cell cycle [267]. In response to DNA damage, the downstream effector checkpoint kinases Chk1 and Chk2 are activated by the ATM-related protein kinases [268], then Chk2 phosphorylates p53, arresting the cell cycle

at the $G_1$/S or $G_2$/M boundary respectively [269]. Yeast genetics have identified the genes that appear to be involved in the early stages of sensing and processing DNA damage and have been classified into three different groups; yeast homologues of ATM-related kinases that are structurally similar to phosphatidylinositol 3 kinase, putative sliding clamp and clamp loader complexes structurally related to PCNA and RFC, and proteins with BRCT domains [267]. The sliding clamp and its loader are required for the phosphorylation of BRCT proteins, and BRCT proteins are required for the phosphorylation and activation of the checkpoint kinases. The carboxyl termini of the BRCT proteins contain a tandem repeat of BRCT domains, each consisting of $\sim 95$ amino acid residues that were first identified in BRCA1. In humans, BRCA1 is thought to function as a counterpart of the BRCT proteins in yeast. Some proteins involved in checkpoint control or repair are relocalised to nuclear foci after DNA damage, including BRCA1 [267].

ATM-dependent phosphorylation of the p53 tumour suppressor is known to mediate cell cycle arrest in response to DNA damage [268]. The gene which encodes p53 is the most frequently mutated gene in all cases of human cancer, with the levels of the p53 protein being activated and stabilised in cells exposed to ionising radiation. One protein which interacts with p53 is 53BP1 [268, 270]. 53BP1 is relocalised to a number of nuclear foci after DNA damage by ionising radiation [269], with DSBs being most effective in inducing this focal phenotype. The focal redistribution of 53BP1 is related to the extent of its phosphorylation [271], which is also induced by DNA damage [268].

The 53BP1 foci colocalise with other damage induced foci such as $\gamma$-H2AX foci to DSB sites [269–271], with their peak number approximately equal to the number of DSBs induced by ionising radiation and their dephosphorylation over time with kinetics that parallel the rate of DNA repair [272]. 53BP1 foci are quantified in an analogous way to $\gamma$-H2AX foci using antibodies specific to 53BP1, a detailed description of which is given in Section 5.3.

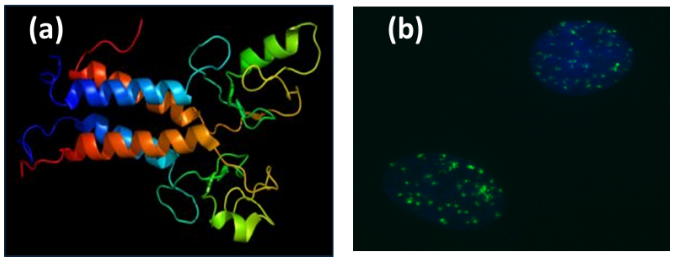


Fig. 5.5 **(a)** Schematic of BRCA1 protein [273], **(b)** 53BP1 foci.

53BP1 concentrates at discrete nuclear foci within 5-15 minutes [272] and the assembly of the foci is not cell cycle stage dependent, in contrast to BRCA1 which shows a focal distribution in the S phase. Ionising radiation induces BRCA1 focal assembly in cells presumed to be in either the G1 or G2 phases of the cell cycle, whereas irradiation induced 53BP1 foci occur in almost all cells except those in mitosis [267].

In a comprehensive study by Paull *et al.* [274], it was shown that the different types of damage-induced foci, including BRCA1, all originate from $\gamma$-H2AX foci at certain stages of the post-irradiation period, with the associations appearing in a sequential order. Kinetically the appearance of 53BP1 foci and 53BP1's hyper-phosphorylation occur slightly later than the appearance of $\gamma$-H2AX foci and H2AX's hyper-phosphorylation, but earlier than other types of damage-induced nuclear foci [267, 272, 274]. This is explained by the fact that 53PB1 needs to be recruited to the foci after DNA damage in contrast to H2AX which is already present at DSBs. More than half of the radiation induced DSBs are rejoined in the order of minutes, with the rest persisting for several hours; 53BP1 may be implicated in the repair and/or checkpoint control associated with the latter [267].

## 5.3 Immunofluorescence

Immunofluorescence is the labelling of antibodies or antigens with fluorescent dyes, a technique often used to visualise the sub-cellular distribution of biomolecules of interest. Tissue

sections or cultures are studied using a fluorescent microscope or confocal microscopy.

The $\gamma$-H2AX and 53BP1 immunofluorescence assays are techniques that use fluorescently labelled antibodies to locate and quantitatively study DNA DSBs in biological samples. The 53BP1 assay was used on the main laser-driven ion radiobiology experiments presented in this thesis, as well as the previous work presented in Section 7.1.1 which was the first time that this particular assay was chosen instead of the $\gamma$-H2AX assay normally used for this type of radiobiology experiment. The majority of the experiments involving X-rays also employed the 53BP1 assay, with the remainder employing the $\gamma$-H2AX assay. This 53BP1 assay was chosen as in testing it had provided better results in terms of clearly discernible foci, and when combined staining of HIF-1$\alpha$ was required the HIF-1$\alpha$ antibodies compatible with 53BP1 staining produced much better staining of the HIF-1$\alpha$ than those compatible with the $\gamma$-H2AX antibodies (antibody compatibility is discussed below).

The immunofluorescence technique is an established and sensitive approach which allows the direct imaging of the location of the double strand breaks [267, 272]. This assay has been optimised for a variety of radiation types in order to monitor qualitative and quantitative changes [11, 272].

Immunofluorescence can also be used to visualise the induction of hypoxia, by similarly labelling HIF-1$\alpha$. This produces more of a pan staining of the cell nucleus rather than discrete foci as seen in DNA DSB staining.

Several different markers can be studied at the same time using the immunofluorescence technique, as long as the primary antibody and the corresponding fluorescent secondary antibody for each marker are raised in different animals. For example, samples which were exposed to a hypoxic gas mixture prior to irradiation we stained for both 53BP1, raised in rabbit, to study DNA DSB damage, and HIF-1$\alpha$, raised in mouse, to study hypoxia induction. These antibodies are also available raised in other animals to allow for different combinations of markers to be studied. For example, the antibodies used for the $\gamma$-H2AX

were raised in mouse and were used in combination with HIF-1$\alpha$ antibodies raised in rabbit. The secondary antibodies used were all raised in goat, with anti binding properties of the species the primary was raised in. For example GAR488, is anti rabbit and is used in conjunction with 53BP1 raised in rabbit.

### 5.3.1 Immunofluorescence Protocol

The main steps of the immunofluorescence protocol are the same for the 53BP1, $\gamma$-H2AX and HIF-1$\alpha$ assays. These steps are fixation, permealisation, blocking, primary and secondary antibody addition, and slide mounting.

#### Fixation

Fixation refers to the killing of the cells whilst maintaining the environment at the point of kill. During this step it is important that the cellular structure remains in its native conformation as far as possible, with the ideal fixation conserving the cellular and sub-cellular architecture whilst providing unblocked antigens for good antibody binding [275]. Once the sample is fixed the rest of the protocol can be carried out without losing the biomarker of interest [276]. There are several different fixatives that can be used, but these can be roughly divided into two groups: organic solvents and chemical crosslinkers. Organic solvents fix the cells through denaturation by removing and replacing the free water in the cells and tissues causing a change in the tertiary structure of the proteins by destabilising the hydrophobic bonding [277]. They also create large holes in the cellular membrane by dissolving lipids [278]. Crosslinkers chemically react with the proteins and other cell and tissue components, becoming bound to them by addition and forming inter- and intra-molecular crosslinks [277]. They create bonds chiefly between lysine residues, keeping the structure of most proteins intact [278]. Both types of fixatives were used throughout the biological investigations presented.

Fixation using an organic solvent (a 1:1 solution of methanol:acetone) was employed on the previous work discussed in this thesis (Section 6.1.1), the radiobiology experiments carried out at LULI (described in Section 6.3) and the experiments carried out at TARANIS (described in Section 6.2).

*Fixation with Methanol:Acetone*

- All the media is removed from the cell samples.
- Each sample is washed twice with 5 ml of PBS.
- All the remaining PBS is removed.
- 5 ml of chilled 1:1 methanol acetone solution is added to each sample, which is stored in the fridge for 10 minutes
- The fixing solution is removed from the samples, which are then washed thrice with 5 ml of PBS.

Fixation using a crosslinker (4% PFA - paraformaldehyde solution[1]obtained from diluting a stock 8% PFA solution in PBS) was employed on the TAP radiobiology experiment (described in Section 6.4) and the comparative X-ray experiments carried out in the CCRCB (Section 6.5).

*Fixation with PFA*

- All the media is removed from the cell samples.
- Each sample is washed twice with 5 ml of chilled PBS.
- All the remaining PBS is removed.
- 2 ml of 4% PFA is added to each sample for 10 to 12 minutes at room temperature.

[1]Paraformaldehye is technically not the correct term to use when referring to this fixative, as paraformaldehyde is a polymerised formaldehyde which cannot be used as a fixative. It is instead a methanol free formaldehyde solution obtained by boiling paraformaldehyde [279], hence why the name paraformaldehyde has stuck.

- The PFA is removed from the samples, which are then washed thrice with 5 ml of PBS.

PFA becomes less effective as a fixative the older it is, so large quantities should not be made. It also has to be carefully disposed by diluting to even lower concentrations in sealed containers, then left for several days before being flushed away.

The first step of washing the cells must be carried out very quickly when dealing with hypoxic samples, as as soon as they are removed from the hypoxia chambers they immediately start to reoxygenate. If too much time is taken to complete this step a true representation of the interaction conditions will not be preserved in the sample. This step was carried out in approximately 30 seconds, thus a small amount of re-oxygenation does occur, but not enough to influence the results.

Fixation is carried out at the specific time points post irradiation which are relevant to the biological marker being studied. Samples which have been fixed are stored in the fridge covered in at least 3 to 5 ml of PBS, until all samples are fixed and ready for the next stage of the process.

### Permeabilisation

Through permeabilisation the cellular structures are made accessible to the antibodies which would otherwise be unable to pass through the lipid membranes of the cell [275]. Fixation with organic solvents can permeabilise the cells to some degree and this step can be skipped, however, fixation with chemical crosslinkers does not and additional treatment with detergents such as Triton X-100 or organic solvents such as methanol is required [276].

Permeabilisation using an organic solvent was employed on the previous work discussed in this thesis (Section 6.1.1), the radiobiology experiments carried out at LULI (described in Section 6.3) and the experiments carried out at TARANIS (described in Section 6.2).

*Permeabilisation with Methanol*

- Any remaining PBS is removed from the samples.
- 2 ml of chilled methanol is added to each sample, which is incubated on ice for 10 minutes.
- The methanol is removed from the samples, which are then washed thrice for 5 minutes with 5 ml of chilled PBS.

Permeabilisation using a detergent solution was employed on the TAP radiobiology experiment (described in Section 6.4) and the comparative X-ray experiments carried out in the CCRCB (Section 6.5).

*Permeabilisation with Triton X-100*

- Any remaining PBS is removed from the samples.
- 2 ml of the permeabilisation buffer of 0.5% Triton X-100 in PBS is added to each sample for 10 minutes at room temperature.
- The buffer is removed from the samples, which are then washed thrice for 5 minutes with 5 ml of PBS.

**Blocking**

Before adding any antibodies to the samples, all epitopes on the tissue sample should be blocked to prevent non-specific binding of the antibodies, which will greatly improve the staining [276, 280]. Normal serums are common blocking reagents as they carry antibodies that bind to reactive sites thus preventing non-specific binding of the secondary antibody, although the serum must be from the same species that the secondary antibody was generated in as opposed to the primary antibody, otherwise the secondary antibody's specificity to the primary antibody will be lost [275, 280].

The samples were blocked with a blocking buffer of 10% Goat Serum, as the secondary antibodies used were all generated in goat, and 0.1% Triton X-100 in PBS. However, the

amount of Triton X-100 was increased to 0.25% when there was significant pan staining of the cell cytoplasm.

- Any remaining PBS is removed from the samples.
- 2 ml of the blocking buffer is added to each sample for 1 to 2 hours , with the samples being stored inside the incubator at 37°C for the duration.
- The blocking buffer is removed from the samples, but there is no need to wash the samples after this step.

**Antibody Addition**

The antibodies used in this step were specific to 53BP1 or $\gamma$-H2AX for DNA DSB detection and HIF-1$\alpha$ for hypoxia induction verification. The antibodies can be mixed to test for more than one protein at a time as long as they originate from different species. The perfect primary antibody will have good affinity and specificity to the protein of interest. The antibody/antibodies are diluted to the desired concentration in the blocking buffer used in the previous step. For the DNA damage antibodies, a concentration of 1:1000 was used, and for HIF-1$\alpha$ 1:500 was used.

*Primary Antibody*

- Add 1 ml per sample of primary antibody/antibodies in blocking buffer, and leave on the rocker at room temperature or place in the incubator for 1 to 2 hours
- Wash samples thrice with 3 ml of washing buffer, then once with 5 ml of PBS

The washing buffer was 0.1% Triton X-100 in PBS. The washing steps help to reduce the background signal produced by unspecific binding of the secondary antibody, by sucking all the antibody solution out of the specimen, so it is important to allow several minutes for this step to ensure the efficient diffusion of the washing buffer into the sample.

The sceondary antibodies fluorescently label the primary antibodies. The secondary antibody/antibodies are diluted in the same concentrations and blocking buffer as the primary antibody/antibodies. Ensure the secondary antibody is anti the species the primary was raised, for example a primary raised in mouse should be used in conjunction with an anti-mouse secondary. The secondary antibodies used were Alexa Fluor GAR488 (goat anti rabbit) and GAM594 (goat anti mouse). The Alexa Fluor conjugated antibodies are excellent bright and stable fluorophores which are cross-absorbed for goods species specificity [276]. It is necessary to carry out all further work in the dark to prevent bleaching of the samples, as the dyes are light sensitive.

*Secondary Antibody*

- Add 1 ml per sample of secondary antibody/antibodies in blocking buffer, and leave on the rocker at room temperature or place in the incubator for 1 hour
- Wash samples twice with 3 ml of washing buffer, then once with 3 ml of PBS
- Remove all remaining solution

**Slide Mounting**

The cell nuclei are stained to allow better orientation of the cell sample during microscopy, but also indicates the cellular status of the sample. Gibco Prolong Gold Antifade Mountant with DAPI (abbreviated to DAPI) was used to stain the cell nuclei and mount the samples on coverslips. Small 2 ml dropper bottles of pre diluted DAPI were the most convenient way of adding the DAPI to the samples. The DAPI is able to enter the nucleus and intercalate into the DNA, even without permeabilisation [275]. The mounting medium helps preserve the sample and raises the refractive index to give good performance with oil objectives, often containing scavengers which soak-up free radicals and reduce photo-bleaching [276].

- Ensure the samples are as dry as possible

- Mark the back of the sample with any relevant information using a permanent marker to determine where to place the coverslip. Seal the markings with clear nail varnish
- Add 2 drops of DAPI to the cell side of each sample, trying to avoid creating any bubbles, and attach a coverslip to each sample
- Remove the excess by gently dabbing the sides of the coverslip with a tissue, and leave to dry for 24 hours in the dark
- Seal the edges of the coverslip with clear nail varnish
- Attach a glass slide to the other side of the sample using a few drops of Superglue, again trying not to create any bubbles
- Cut the sample from the dish when the Superglue is dry
- Store at 4° in the fridge or -20° in the freezer until you wish to study the slide under the microscope

A concise step by step guide for the finalised protocol used in the main laser-irradiation experiments is provided in Appendix B.

## 5.4 Fluorescence Microscopy

After the samples were mounted, images of the cells were obtained using the Carl Zeiss Axiovert 200M fluorescence microscope with CCD acquisition capability and Axiovision Rel 4.8 software package, located in the CCRCB. A x63 magnification oil immersion objective and x40 magnification objective were used to focus the microscope and take several images of each region of interest on each slide. For each region of interest a sufficient number of images were taken to allow the counting and recording in a minimum of 100 cells. The foci were counted using the Cell Counter application in ImageJ (NIH, USA), where the foci are

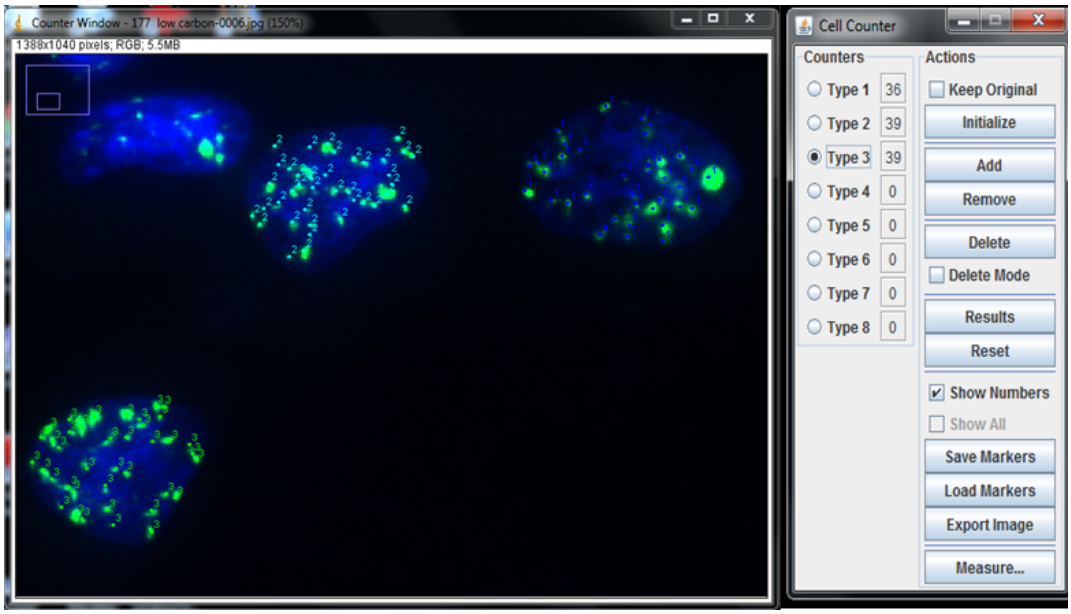


Fig. 5.6 Screen-shot of the ImageJ Cell Counter application used to count the DNA DSB 53BP1 or $\gamma$-H2AX foci in the experimental data.

still recognised manually by the user, but the program records the number, allowing more accurate and efficient data acquisition. Overlapping cells, cells with high background and abnormally sized/shaped cells were ignored; only cells with clearly discernible foci were counted. Fluorescence microscopy for all experimental data presented in this thesis was carried out at the CCRCB.

## 5.5 Hypoxia Chamber

The treatment of hypoxic tumours is challenging even with the most advanced X-ray based therapies, which often leads to the failure of such treatments. Recently ion beam therapy using carbon ions and other high LET particles has been shown to be effective in killing hypoxic tumour cells [13–16]. However, as discussed previously, the very high installation and operational costs currently make ion beam therapy a very expensive treatment option [281] in its current form. In recent years there has been a demonstration of the capability of

high-energy lasers to generate suitable ion beams for cancer therapy [17–19], which could greatly reduce the cost involved in the construction of future facilities [6]. However, the radio-biological effects of these ion beams under hypoxic conditions are largely unexplored, therefore a portable and compact hypoxia chamber was developed. This chamber is suitable for characterising the biological effects of laser accelerated beams under a range of different oxygen concentrations.

To fully understand the relationship between laser accelerated ion induced DNA damage and oxygen dependency it is necessary to have a compact and reliable device capable of maintaining hypoxia for the duration of the radiation exposures and afterwards. Several groups have demonstrated their hypoxia inducing devices, including modular incubator chambers that are filled with low $O_2$ gas (1% $O_2$, 5% $CO_2$, 94% $N_2$) [282], hypoxia cell culture incubators with external high pressure $N_2$ gas supplies [283], hypoxic work stations that offer precise control of oxygen concentration [284], and more recently size variable inflatable hypoxia chambers [54]. All these methods of hypoxia induction work well within the cell culture laboratory, however they are not necessarily compatible with the irradiation procedures and set-ups required for laser accelerated ion beams owing to the complex geometry and designs of the interaction chambers. Also, sample reoxygenation problems arise as soon as cells are removed from the hypoxic environment. The modular and inflatable chambers may be compatible with X-ray irradiations but not with proton or ion irradiations, as the material and size of the chamber may not allow the particles to reach the cellular target within the hypoxia chamber, however, a compact hypoxia chamber compatible with irradiations employing high-energy ions from conventional accelerators has been developed [193, 194].

Nevertheless, a commercially available compact hypoxia chamber for use with laser-driven ion sources is unavailable. Presently the protons and ions produced from the interaction between high-power lasers and thin foils reach the energy of 10 - 20 MeV compared

to 60 MeV produced by conventional accelerators. At 10 - 20 MeV, these ions have a relatively short range and are unable to penetrate existing hypoxia chambers, which led to the design of the following compact and portable hypoxia chamber for laser ion radiobiology applications.

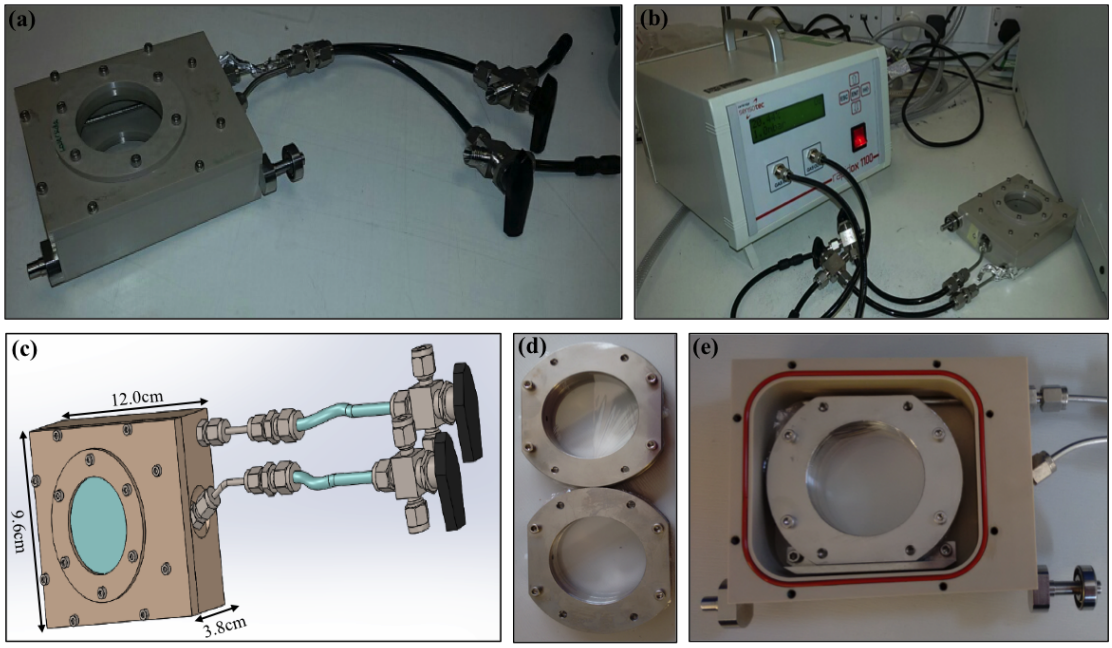


Fig. 5.7 **(a)** The new compact hypoxia chamber. The chamber is small enough that 6 can be stored in a standard 3 shelf incubator. **(b)** Continuous measurement of the $O_2$ concentration inside the hypoxia chamber using a Rapidox 1100Z meter. **(c)** Schematic of the new hypoxia chamber. The chamber is 12.0 by 9.6 by 3.8 cm in size, with the main body constructed from PEEK and the windows from Saran. **(d)** Stainless steel and aluminium cell dish. **(e)** View of the cell dish placement inside the new hypoxia chamber. The cell dish is secured in place by an aluminium bracket.

### 5.5.1 Design

The main body of the new hypoxia chamber, shown in Figure 5.7 (a) and (c), is a 12.0 cm by 9.6 cm, 3.8 cm deep box made of polyetheretherkeytone (PEEK), and the front and back faces of the box have circular apertures 4.7 cm in diameter. The apertures are covered with 12.5 $\mu$m Saran (polyvinylidene chloride, PVDC), (Goodfellow Cambridge Ltd, Hunting-

don, England), attached with 0.4 cm and 0.2 cm thick PEEK rings on the front and back respectively, creating two transparent windows held in place by six screws in each ring. All openings are sealed with silicon O-rings.

Two metal gas ports, one inlet and one outlet, are attached to the right side of the box. These ports are connected to two-way valves by 14 cm lengths of polyurethane tubing. The inlet port extends inside the chamber to the left hand side of the box to ensure the best possible gas flow. These valves can be connected to a 95% $N_2$, 5% $CO_2$ gas supply, (BOC, Linde Group, Munich, Germany) and a Rapidox 1100Z oxygen meter, (Cambridge Sensotec, St. Ives, Cambridgeshire, England), for real time measurements of the oxygen concentration within the hypoxia chamber.

Three different tests were carried out to characterise the new hypoxia chamber, two concerning the physical characterisation and one concerning the biological characterisation.

### 5.5.2 Physical Characterisation

Primarily, the ability of the hypoxia chamber to maintain a hypoxic environment was tested, followed by a study of the variation in the radiation dose inside and outside the chamber.

#### Oxygen Concentration

The empty chambers were connected to a hypoxic gas supply (BOC, 95% $N_2$, 5% $CO_2$) through the inlet port, and the outlet port was connected to the inlet port of a Rapidox 1100Z meter using polyurethane tubing. The outlet port of the Rapidox meter was connected to a small flask of water to check the gas flow rate while filling the chamber. The chambers were gassed until the low oxygen alarm sounded on the Rapidox meter (approximately 15 minutes), which meant the oxygen concentration inside the chamber was between 0.1% and 0.5%. The gas supply was then disconnected and the Rapidox meter attached to the inlet port of the chamber as well as the outlet to allow a continuous measurement of the oxygen

| Time (mins) | $O_2$ (%) | | | Rate of change (%/min) for each time interval | | | Rate of change (%/min) from initial value | | |
|---|---|---|---|---|---|---|---|---|---|
| | A | B | C | A | B | C | A | B | C |
| 1 | 0.49 | 0.27 | 0.02 | - | - | - | - | - | - |
| 5 | 0.51 | 0.28 | 0.03 | 0.0050 | 0.0025 | 0.0025 | 0.0050 | 0.0025 | 0.0025 |
| 10 | 0.52 | 0.28 | 0.04 | 0.0020 | 0.0000 | 0.0020 | 0.0033 | 0.0011 | 0.0025 |
| 15 | 0.53 | 0.29 | 0.06 | 0.0020 | 0.0020 | 0.0040 | 0.0029 | 0.0014 | 0.0029 |
| 20 | 0.55 | 0.30 | 0.07 | 0.0040 | 0.0020 | 0.0020 | 0.0032 | 0.0016 | 0.0026 |
| 25 | 0.56 | 0.31 | 0.08 | 0.0020 | 0.0020 | 0.0020 | 0.0029 | 0.0017 | 0.0025 |
| 30 | 0.57 | 0.32 | 0.09 | 0.0020 | 0.0020 | 0.0020 | 0.0028 | 0.0017 | 0.0024 |
| 60 | 0.65 | 0.39 | 0.16 | 0.0027 | 0.0023 | 0.0023 | 0.0027 | 0.0020 | 0.0024 |
| 120 | 0.85 | 0.47 | 0.26 | 0.0033 | 0.0013 | 0.0017 | 0.0030 | 0.0017 | 0.0020 |
| 360 | 1.59 | 0.85 | 0.66 | 0.0031 | 0.0016 | 0.0017 | 0.0031 | 0.0016 | 0.0018 |
| 1440 | 4.05 | 2.37 | 2.50 | 0.0023 | 0.0014 | 0.0017 | 0.0025 | 0.0015 | 0.0017 |

Table 5.4 Summary of the oxygen concentration measurements for the 3 chambers. The Rapidox 1100Z meter and the hypoxic gas supply were connected to each chamber. The chamber was gassed for approximately 15 minutes, and then the oxygen concentration was measured continuously for the next 24 hrs. The rate of change for every 4 or 5 min interval was calculated, as was the rate of change from the starting value of 0.49%, 0.27% and 0.02% for chambers A, B and C respectively.

concentration inside the chamber for the next 24hrs. This was repeated for the 3 chambers, the results are shown in Figures 5.8 (a) and (b), and summarised in Table 5.4.

As shown in Figure 5.8 (a), each of the 3 hypoxia chambers tested was able to maintain a physoxic environment ($< 5\%$ $O_2$) for the full 24 hr test period. Chamber A maintained pathological hypoxia ($< 1\%$ $O_2$) for 2 hrs, physiological hypoxia ($< 2\%$ $O_2$) for 7 hrs and physoxia for 24 hrs. Chamber B maintained radiobiological hypoxia ($< 0.4\%$ $O_2$) for 1 hr, pathological hypoxia for 7 hrs and acute hypoxia ($< 3\%$ $O_2$) for 24 hrs. Finally Chamber C maintained radiobiological hypoxia for 3 hrs, pathological hypoxia for 8 hrs and acute hypoxia for 24 hrs. This demonstrates that the chambers are able to maintain a hypoxic environment for 24 hrs, allowing the study of radiation induced DNA damage and repair kinetics under fully hypoxic conditions without the need to remove the samples from the chambers.

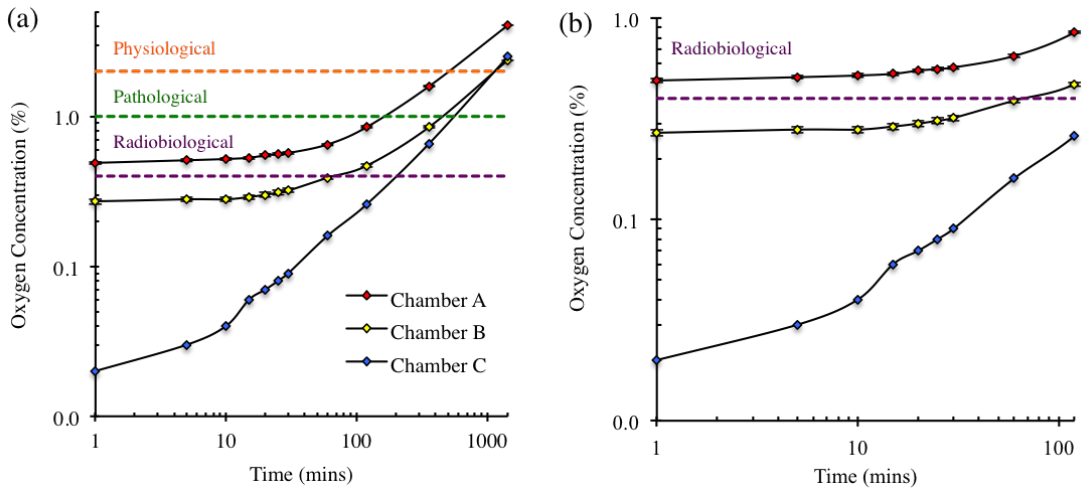


Fig. 5.8 **(a)** Recorded $O_2$ concentration inside 3 of the hypoxia chambers compared with the accepted levels of physiological ($< 2.0\%$ $O_2$), pathological ($< 1.0\%$ $O_2$) and radiobiological hypoxia ($< 0.4\%$ $O_2$) [197]. All 3 chambers maintained a physoxic ($< 5\%$ $O_2$) [197] environment for the full 24 hr test period. **(b)** Zoomed in view of the first 2 hrs.

### Dose

A fully assembled cell dish, complete with a radio chromic film (RCF) mask and normal EBT-3 film [123, 285], was placed inside the hypoxia chamber. The chamber was then placed inside the 225 kVp XRAD225 X-ray cabinet (precision X-ray Inc. Newhaven, CT, USA) located in the Centre for Cancer Research and Cell Biology (CCRCB). The X-ray tube was fitted with a 2 mm copper filter to cut off the low energy part of the spectrum and was operated at 13 mA with a dose rate of 0.591 Gy/min. The hypoxia chambers were irradiated with 0, 0.5, 1, 2, 4 and 8 Gy at a distance of 50 cm from the source. These irradiations were repeated with just the cell dishes and RCF films. The dose was obtained from a set of films alone irradiated with the same range of doses. The results of these irradiations are shown in Figure 5.9.

Dosimetry is one of the most important aspects of radiobiology studies and irradiation conditions significantly impact the physical dose delivered. How the geometry and material of the hypoxia chamber could impact the dose was investigated as shown in Figure 5.9

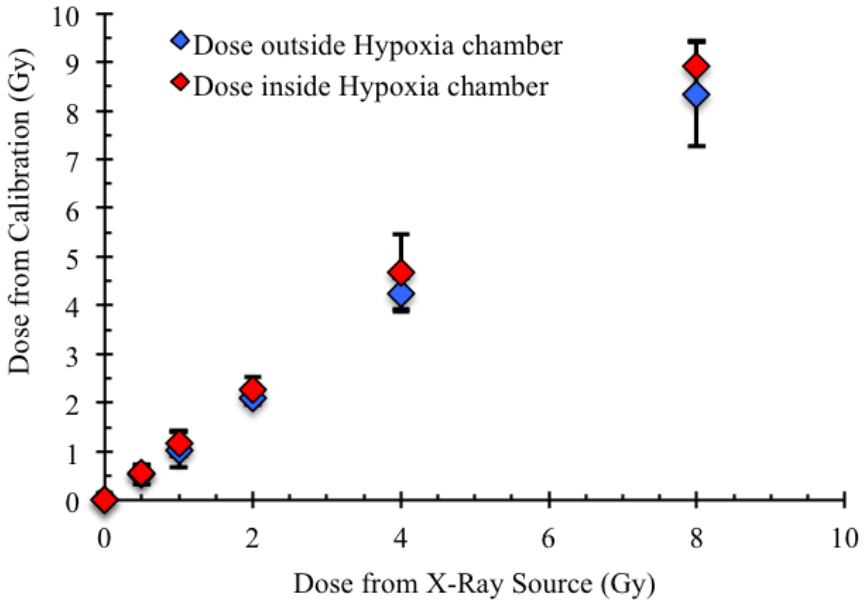


Fig. 5.9 Graph showing the dose of 225kVp X-rays deposited on the EBT-3 normal film mounted underneath the cell dish placed inside the hypoxia chamber (red), and the dose deposited when the dish and film were irradiated outside the hypoxia chamber (blue). The calibration was calculated from a set of EBT-3 films irradiated in the X-ray cabinet without being mounted on the dish, or being inside the hypoxia chamber.

where the dose of 255 kVp X-rays deposited on EBT-3 films, irradiated inside and outside the hypoxia chamber is shown. At low dose values, below 4 Gy, the dose deposited on the films was comparable inside and outside the chamber, but above 4 Gy slight differences in the deposited dose were observed, however the dose was still the same within error. At even higher doses this may not be the case, and the slightly higher dose within the chamber could be attributed to scattering phenomenon inside the chamber. However, we intend to use the chamber primarily with low doses (between 0.5 and 2 Gy) where little or no difference in the dose deposited was observed.

### 5.5.3 Biological Characterisation

The final test was to evaluate the expression of the hypoxia biomarker HIF-1$\alpha$ in the cellular samples placed inside the new hypoxia chambers compatible with X-ray and low energy laser accelerated proton irradiated set-ups.

#### HIF-1$\alpha$

Human skin fibroblast cells (AG01522) were seeded on to 3 $\mu$m mylar mounted on cell dishes (see Figure 5.7 (d)) 24 hrs prior to the irradiations. On the day of the irradiations, the cell dishes were mounted inside the hypoxia chambers. These chambers were then connected in series and kept inside a $CO_2$ incubator, and gassed with a hypoxic gas mixture (BOC, 95% $N_2$, 5% $CO_2$) for the next 4 hrs to ensure that radiobiological hypoxia [197] levels were attained inside the chamber. Irradiations with X-rays were carried out using the aforementioned X-ray machine in the CCRCB, and proton irradiations were carried out employing the petawatt arm of the Vulcan laser facility at the Rutherford Appleton Laboratory, Oxford, UK. The samples were irradiated with 1 Gy of 225 kVp X-rays or $\sim$1 Gy of 15 MeV protons, and fixed with 4% paraformaldehyde (PFA) for 10 - 12 minutes (room temperature) at 0.5 and 24 hrs post-irradiation. Until fixation, the samples were kept inside the sealed hypoxia chambers, maintained at 37 °C in a normal tissue culture incubator.

For staining, the PFA was discarded and the samples were rinsed thrice with PBS (Phosphate Buffered Saline) and later permeabilized with 0.5% Triton X-100 (Sigma Aldrich) in PBS for 10 minutes at room temperature and subsequently blocked in 2 ml of blocking buffer (10% goat serum and 0.25% Triton X-100 in PBS) at 37°C for 2 hours. The samples were then stained for both 53BP1, a biomarker of DNA DSB damage, and HIF-1$\alpha$ to show the induction of hypoxia. Approximately 1 ml of the primary antibodies, 1:1000 53BP1 (Novus Biologicals, Littleton, CO, USA) and 1:500 HIF-1$\alpha$ (Abcam, Cambridge, UK) diluted in the blocking medium was added to the dishes and incubated at 37°C for

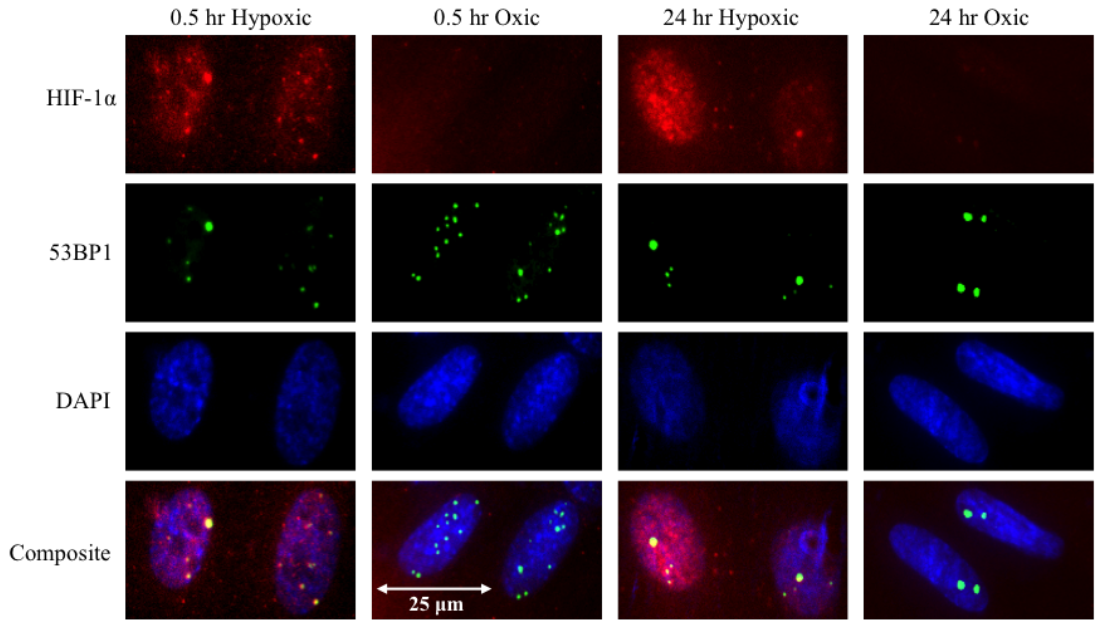


Fig. 5.10 AG01522 human skin fibroblast cells were irradiated with 15 MeV laser accelerated protons employing the petawatt arm of the Vulcan laser facility at the Rutherford Appleton Laboratory, Oxford, UK. The samples were kept inside the hypoxia chambers after the irradiations to maintain the hypoxic environment. The samples were fixed at 0.5 and 24 hrs post irradiation, then stained for HIF-1$\alpha$ to show the induction of hypoxia, 53BP1 to highlight DNA DSB damage and DAPI for detecting the cell nuclei. Images were acquired using the Carl Zeiss Axiovert 200M fluorescence microscope (at 40x magnification) with a CCD camera and the Axiovision Rel 4.8 software package, located in the Centre for Cancer Research and Cell Biology, Queen's University Belfast.

1 hour and later washed three times in PBS containing 0.25% Triton X-100. The cells were later probed with secondary antibodies, goat anti-rabbit-Alexa Fluor 488 conjugated and goat anti-mouse-Alexa Fluor 594 conjugated, (Invitrogen, Life Technologies, Carlsbad, CA, USA) at a dilution of 1:1000 and 1:500 respectively in blocking buffer and incubated for 1 hour at 37°C. The samples were then washed and mounted on coverslips using an ant-fade reagent containing DAPI (Invitrogen, Life Technologies, Carlsbad, CA, USA).

53BP1 foci formation is regarded as one of the hallmarks of DNA DSB damage. We detected 53BP1 foci formation in AG01522 cells irradiated with 15 MeV protons employing the petawatt arm of the Vulcan laser facility, with simultaneous staining of HIF-1$\alpha$,

a hypoxia biomarker, through immuno-fluorescent microscopy as shown in Figure 5.10. Qualitatively, the red channel shows the HIF-1$\alpha$ staining, the green is 53BP1 and the blue is the DAPI contrast staining of the cell nuclei. The images show the nuclear localisation of the 53BP1 foci in the hypoxic and oxic samples. More foci are present at 0.5 hr in the oxic samples compared to the hypoxic, but this is reversed with the 24 hr samples.

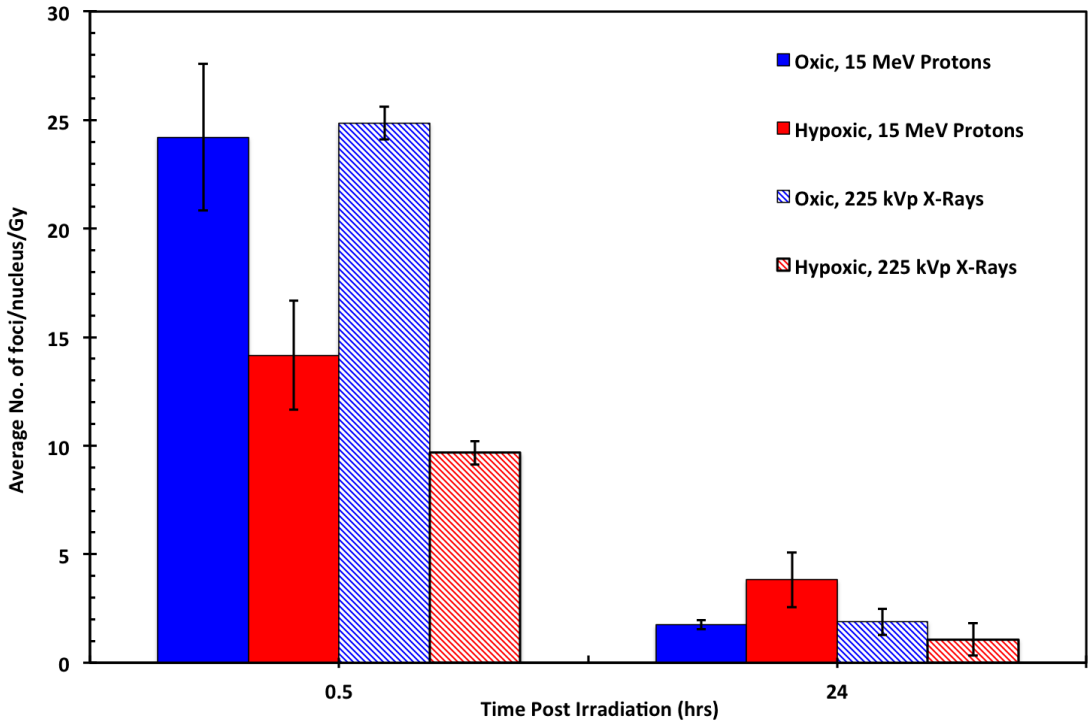


Fig. 5.11 53BP1 foci induction and repair in AG01522 human skin fibroblast cells after exposure to 15 MeV laser accelerated protons and 225 kVp X-rays under oxic and hypoxic conditions. The initial damage is shown at 0.5 hrs and the residual damage is shown at 24 hrs post irradiation.

Figure 5.11 shows the quantification of the initial (0.5 hrs) and residual (24 hrs) 53BP1 foci in AG01522 cells irradiated with 15 MeV protons and 225 kVp X-rays. The average number of 53BP1 foci/nucleus/Gy at 0.5 hrs under oxic conditions was comparable for both protons and X-rays, 24.21 $\pm$ 3.38 and 24.87 $\pm$ 0.76 respectively. There was a slight difference in the number of residual foci present, with 1.74 $\pm$ 0.21 for X-rays and 1.88 $\pm$ 0.60 for protons (control values of 1.81 $\pm$ 0.11 and 1.85 $\pm$ 0.08 for Protons and X-rays

respectively). Similarly, under hypoxic conditions the initial foci values were $14.16 \pm 2.51$ and $9.67 \pm 1.19$, and the residual values were $3.82 \pm 1.26$ and $1.07 \pm 0.09$ at 24 hrs for protons and X-rays respectively (control values of $1.84 \pm 0.12$ and $2.16 \pm 0.07$ for protons and X-rays respectively). The values for the 15 MeV protons have been averaged over four shots each for the 0.5 hr oxic and hypoxic samples and the oxic 24 hr samples, with the hypoxic 24 hr values averaged over three shots. The 0.5 hr oxic and hypoxic and 24 hr oxic values have been averaged over two samples, but the 24 hr hypoxic value is from a single sample. All values have the control value subtracted. This shows that the chambers were compatible with both X-ray and laser-driven ion irradiation conditions.

### 5.5.4 Conclusions

In conclusion, a new compact portable hypoxia chamber has been designed for use with low energy laser-driven ion sources. The chamber has proved capable of maintaining a radiobiologically hypoxic ($<0.4\%$ $O_2$) environment for up to 3 hrs, an acutely hypoxic ($<3\%$ $O_2$) environment for 24 hrs, and there was no dose enhancement inside the chamber compared to outside the chamber at the low doses the chamber will be used with. The chamber was used in conjunction with a 225 kVp X-ray source and 15 MeV laser accelerated protons to induce DNA damage in AG01522 cell samples under oxic and hypoxic conditions. These samples were tested for 53BP1 foci as a marker of DNA DSB damage and HIF-1$\alpha$ as a biomarker of hypoxia induction. Results showed that hypoxia was indeed induced in the cell samples as well as DNA damage, with more initial damage in the oxic samples and more residual damage in the hypoxic samples.

These tests show that the new compact portable hypoxia chamber will be a valuable tool in the study of the biological effects of laser-driven ions under hypoxic conditions.

# Chapter 6

# Biological Effects of Laser-Driven Ions

As described earlier, the amount and complexity of the DNA damage induced determines the biological outcome. While a good indicator of the amount of damage induced is the dose absorbed by the cells, the complexity of the damage is linked to the clustering of DNA lesions. If the spatial distribution of DNA lesions is a critical parameter for all charged particle exposures, using pulsed laser-driven ions sources at their temporal limit has yet to be fully investigated. Several effects related to the ultra-short nature of the deposition have been suggested. There could be an alteration in the production of free radicals owing to oxygen depletion effects [237], there could be a spatio-temporal overlap of independent tracks resulting in collective effects [228] and there could be a lack of interaction between direct and indirect DNA lesions [286] (see Section 5.4.1). These have all been suggested as possible effects to alter the biological response to laser-driven beams. Very little is known about this ultra-fast dose deposition regime and the only way to assess these predications is via experiment. Previous work has not highlighted any deviation from the known cell response to the longer ion bursts used in radiotherapy, however, these investigations have been limited to protons and in most cases to Gy-level doses obtained by accumulating multiple irradiations with an effective dose rate of $\mathrm{Gys}^{-1}$ as in conventional radiation therapies [234, 287].

The use of proton and carbon ions of different energies is fundamental in studying the role of ionisation clusters. The LET is a critical parameter in radiobiology which changes towards the end of the particle path [179] with great concerns for radiation therapy applications as this coincides with the tumour volume. Moreover, the range of secondary electrons is proportional to the energy of the main beam with increasing probability of spatio-temporal overlap of the secondary radiation tracks for high energy beams [11]. This may impact on the qualitative difference in the DNA damage induced along the beam path, i.e. depth in the sample or patient.

Rabdiobiological experiments employing laser driven ions have been carried out for several years and can be grouped into two categories when considering the effects related to the short pulse nature of the beams. The first category is experiments in which the dose was delivered in a number of fractionated consecutive pulsed irradiations, however, while these experiments may be more relevant to modalities of future laser-based treatment, they are less suited to highlighting the collective effects related to the ultra-short nature of the irradiation, as fractionated approach reduces the effective dose rate on the cells to the $Gys^{-1}$ range normally used in radiotherapy. The second category of experiments employ single shot irradiations, such as the Gemini experiment described in the next section. These experiments have been limited to energies of 1 - 5 MeV and on cell pulse durations in the order of ns, which also poses strong limitations to the possibility of observing collective effects. So far, no experiment has highlighted any deviations from the results of experiments carried out with conventional RF beams.

None of the experiments carried out to date have addressed oxygen depletion effects on the biological response as all samples were irradiated in air, thus were well oxygenated. The TARANIS experiment described in section 6.2 was the first to use the newly designed hypoxia chamber described in section 5.5, and the TAP experiment described in section 6.4 was the first investigate the effect of chemically induced hypoxia and a free radical scav-

enging environment. These experiments are a clear step forward from prior studies, investigating for the first time conditions where clear differences from conventional radiotherapy should be observed.

## 6.1 Previous Work

In two previous experiments carried out by the LIBRA consortium on the Gemini laser to investigate ion acceleration, a double plasma mirror configuration was employed. This facilitated the irradiation of ultra-thin low-Z foils with intensities up to $10^{20}$ Wcm$^{-2}$ as the ASE contrast was reduced to $10^{-10}$ below the peak intensity [11]. The very large number of ions produced per shot when ultra-thin foils of amorphous carbon were irradiated (in the order of $10^{12}$-$10^{13}$ MeV$^{-1}$Sr$^{-1}$ for protons and $10^{10}$ MeV$^{-1}$Sr$^{-1}$ for carbon ions) offered a unique platform for cellular irradiation experiments, the first of their kind on the Gemini laser. In a single laser shot a dose corresponding to more than 1000 high-energy protons per cell could be delivered and a carefully designed system allowed ultra-high dose rate delivery at $>10^{9}$ Gys$^{-1}$, thus opening up the possibility to explore the biological effects of ultra-high dose rates and ultra-fast dose deposition.

### 6.1.1 Gemini 2013 - First Carbon Ion Irradiations

The LIBRA consortium pioneered single shot radiobiology utilising laser-driven ions in effective experiments carried out on the TARANIS [96] laser at Queen's University Belfast, where radiosensitive Chinese Hamster fibroblast cells (cell line V79) were irradiated with proton bursts of nanosecond duration in the 1-5 MeV range [10, 227]. The survival rates of the cells observed were in line with published results from conventional sources, which was an encouraging result in view of future therapeutic uses of ultra-short bursts of laser-driven ions. It was during this experiment that the methodology used in the Gemini 2013

experiment was developed, though some modifications had to be made to accommodate the higher energies and different ion species available on Gemini. Although the energies of TARANIS and Gemini are comparable at approximately 10 J, conversion efficiency is much higher on Gemini at greater than 10% compared to 1% on TARANIS. The beam is also much more collimated, 4-5 degrees versus 30-40 degrees at 5 MeV [11] and the proton fluxes are an order of magnitude higher on Gemini compared to TARANIS. This leads to dose rates higher by up to two orders of magnitude at comparable dose, or doses >10 Gy. Of particular interest to the 2013 campaign was the use of carbon ions at high energies and flux, which are simply not available from standard lower intensity interactions from thicker target foils.

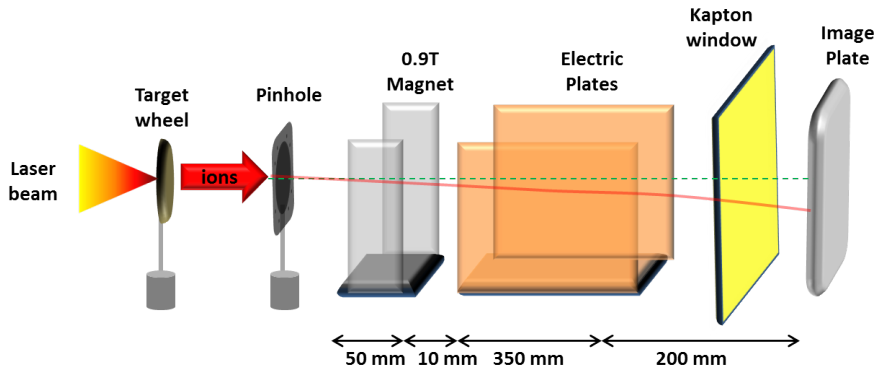


Fig. 6.1 Experimental configuration used to characterise the beam. For the cellular irradiations the 0.9 T magnets were removed.

The main aim of the Gemini experiment was to establish a procedure for cell handling and irradiation compatible with the laser-plasma interaction environment, allowing the investigation of the effects of irradiating AG01522 human fibroblast cells with laser-accelerated proton and carbon ions at ultra-high dose rates. The set-up used also allowed same shot comparisons of high and low LET radiation.

Amorphous carbon and aluminium targets were irradiated at laser incidence of 0° and 35° with linear and circular polarisation. The ion beam was generated by focusing a single

Gemini beam with an f/2 parabola onto the ultra-thin targets at intensities of $\sim 10^{20}$ Wcm$^{-2}$, employing the double plasma mirror configuration as in previous LIBRA campaigns. A maximum cut-off energy of 20 MeV/nucleon for protons and carbon ions was achieved using 25 nm amorphous carbon targets and linear polarisation at 0°. A crucial element of the experimental arrangement was the beam delivery system capable of separating the different charged species whilst maintaining the high flux on the cell plane. This components design was an evolution of the design used for cell irradiations on TARANIS [227, 288], and was also based on the experience gained in developing high dispersion ion spectrometers [110].

The beam was characterised prior to the cellular irradiations using a TPS with micro channel plate detection (0.9 T magnets and a variable magnetic field), high sensitivity RCF (EBT2) stacks and CR39 placed outside the chamber in the cell sample position. The proton spectra were found to be exponential in nature, associated with the TNSA acceleration mechanism, with a proton flux of $\sim$ 2 x $10^{10}$ MeV/nucleon/Sr at 10 MeV, and a maximum cut-off energy of 23 MeV. The spectra of the $C^{6+}$ indicated peak-like structures which could be attributed to the RPA mechanism of acceleration, with a maximum cut-off energy of 13 MeV/nucleon and flux of $\sim$ 8 x $10^9$ MeV/nucleon/Sr at 7 MeV [38]. For the cellular irradiations a 5.5 $\mu$m aluminium filter was placed in front of the cell dish to prevent low energy carbon ions ($\leq$ 3.7 MeV/nucleon) from reaching the samples, as these energies overlapped with the high energy protons (approximately 12 MeV protons).

For the cell irradiations, the dispersed beams were transported to the cell dish, placed outside the experimental chamber, through a Kapton window of 50 $\mu$m thickness, with transverse dimensions of a few centimetres. The cells were placed vertically on a specially designed dish during the exposure, and were quickly removed for processing as required.

The particular aspects that were investigated in the Gemini 2013 experiment were the DNA damage and subsequent cellular response of AG01522 cells exposed to laser-driven proton and carbon ions at ultra-high dose rates, with the one main objective of the charac-

terisation of DNA DSBs. The 53BP1 immunofluorescence technique (discussed in Section 6.3) was used to monitor the formation of DNA DSBs and their subsequent repair as a function of dose and time post irradiation. For a given dose the cells were stained and analysed 0.5 hours, 1 hour, 2 hours, 6 hours and 24 hours post irradiation, which allowed the reconstruction of the dynamics of cell repair after DNA damage. This aspect, as yet unexplored with laser-driven ions prior to this experiment, could be strongly affected by the temporal history of the dose deposition.

10 MeV Protons

| Time (hrs) | Corrected Dose (Gy) | Mean Foci/Nucleus |
|---|---|---|
| 0.5 | 1.53 $\pm$0.12 | 45.5 $\pm$1.7 |
| 1 | 1.00 $\pm$0.08 | 22.1 $\pm$0.8 |
| 2 | 2.07 $\pm$0.05 | 24.7 $\pm$0.8 |
| 6 | 2.31 $\pm$0.08 | 20.53 $\pm$0.07 |
| 24 | 1.68 $\pm$0.17 | 5.1 $\pm$0.3 |

5 MeV/nucleon Carbon Ions

| Time (hrs) | Corrected Dose (Gy) | Mean Foci/Nucleus |
|---|---|---|
| 0.5 | 2.18 $\pm$0.05 | 29.4 $\pm$1.4 |
| 1 | 2.47 $\pm$0.05 | 20.2 $\pm$0.8 |
| 2 | 5.7 $\pm$0.9 | 47.7 $\pm$1.2 |
| 6 | 2.9 $\pm$0.6 | 22.7 $\pm$1.2 |
| 24 | 1.6 $\pm$0.7 | 13.2 $\pm$0.8 |

Table 6.1 Raw experimental data obtained for 10 MeV protons and 5 MeV/nucleon carbon ions [38].

Images of the cells were obtained using the Carl Zeiss Axio Imager.Z2 fluorescence microscope with CCD acquisition capability and MetaSystems Isis software package, located at the Rutherford Appleton Laboratory. A x63 magnification oil immersion objective was used to focus the microscope and take several images of each region of interest on each slide. The number of foci/nucleus across the sample were carefully aligned with the corresponding dose profile and a clear trend in the foci between the proton and carbon ion region was observed in each shot with a dramatic rise in the foci count in the lower energy carbon

ion region close to the Bragg peak [38]. This corresponded to a high deposited dose in the EBT2 film used for dosimetry. The regions of interest were identified as the regions irradiated by 10 MeV protons and 5 MeV/nucleon carbon ions, and the dose was calculated from the corresponding area of the RCF film. The mean number of foci/nucleus was divided by the respective dose to give the mean foci number/nucleus/Gy.

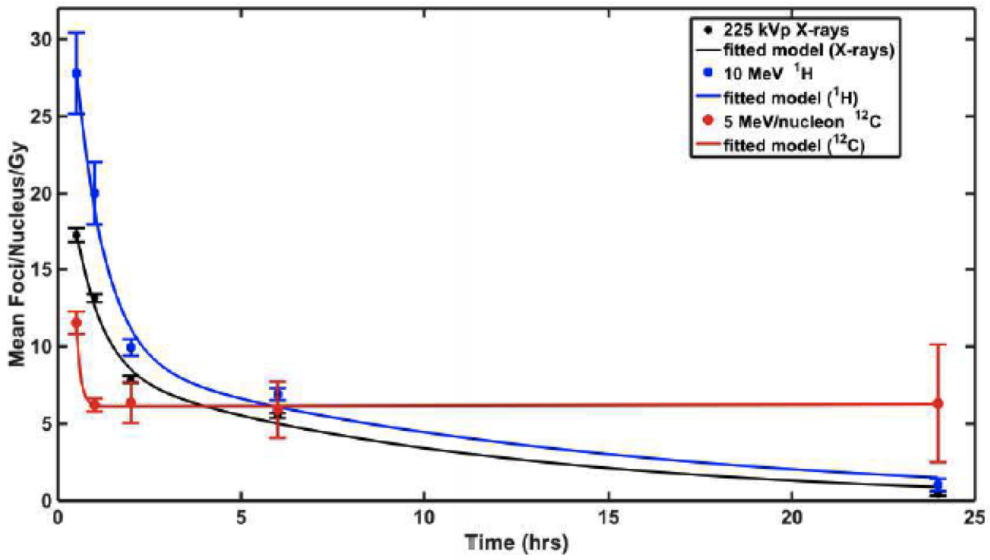


Fig. 6.2 Temporal kinetics of phosphorylated 53BP1 foci in cells exposed to protons, carbon ions and X-rays over a 24 hr period [38].

The 53BP1 foci kinetics were measured over a 24 hr period with initial values of 27.8 $\pm$ 2.6 and 11.5 $\pm$ 0.7 foci/nucleus/Gy at 30 mins post irradiation and 0.5 $\pm$ 0.14 and 6.3 $\pm$ 3.8 at 24 hrs post irradiation for 10 MeV protons and 5 MeV/nucleon carbon ions respectively. The RBE was calculated as 1.6 $\pm$ 0.2 and 13 $\pm$ 9 for protons and carbon ions respectively. The value obtained for protons agrees with that reported in literature and did not appear to show any enhanced biological effectiveness owing to the ultra-high dose rate. Conversely there seems to be a significant enhancement in the biological effectiveness of carbon ions (literature values are between 2.1 and 3.3 [289] compared to 13 $\pm$ 9), however this was attributed to an underestimation of the dose by the RCF even though the expected RBE

value lay within the margin of error.

## 6.2 TARANIS Experiment

This experiment was the first time the newly designed hypoxia chamber would be tested with laser accelerated protons. The chamber had already been tested with X-ray irradiations and had been shown capable of maintaining a pathologically hypoxic environment (< 1% $O_2$). This experiment was used as a proof of principle experiment to develop the cell handling procedure and irradiation methods for use in the TAP experiment described later. The effect of hypoxia on DNA DSB induction and repair was investigated by irradiating the AG01522 normal human fibroblast cell samples inside the specially designed hypoxia chamber and also irradiating oxic samples inside the chamber to create a direct comparison for foci kinetics. The end point staining was $\gamma$-H2AX for DNA DSB induction and HIF-1$\alpha$ for hypoxia induction.

### 6.2.1 Experimental Arrangement

The irradiations were carried out employing the TARANIS laser located in the Centre for Plasma Physics, Queen's University Belfast. The experimental setup of the interaction chamber is shown in Figure 6.3, where the parabola, target mount and magnet beam dispersion system are clearly visible. A 500 $\mu$m slit aperture was placed 55 mm behind the target with the 1.0 T magnets used for dispersing the proton beam a further 9 mm from the slit. The end of the magnet was 165 mm from the 50 $\mu$m Kapton window which was attached across a 70 mm aperture in the sealing flange of the interaction chamber. The hypoxia chamber was positioned 56 mm from the Kapton window on the air side of the flange, as shown in Figure 6.5. The mask shown in Figure 6.5 **(a)** was used to attach the un-coated EBT-3 film to the back of the hypoxia chamber.

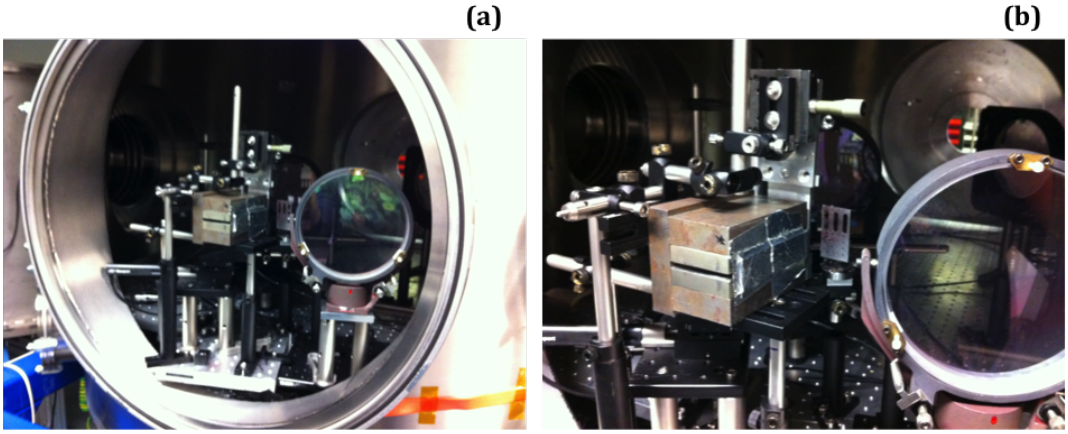


Fig. 6.3 **(a)** The experimental setup of the target chamber in TA2 of the TARANIS laser facility. **(b)** A close up of the magnet and the target mount inside the chamber.

Aluminium and gold targets were used to characterise the beam and irradiate the cells. IPs, RCF and CR39 were used to characterise the beam on the cell plane position. The flux of protons on the cell plane was determined using CR39 and was found to be 2.17 $\pm$ 0.10 x $10^7$ protons per $cm^2$. The positions of certain energies on the cell plane were determined using IPs and aluminium filters of 200 and 325 $\mu$m. Figure 6.4 shows the proton spectra produced by the laser interaction. The sharp cut-off at approximately 24 mm produced by the aluminium filter shows the position of the 6.85 MeV protons, providing an energy fiducial to calibrate the spectrum. The laser energy was approximately 10 J at an angle of incidence of 30 $\pm$ 5°, and the dose rate was approximately $10^9$ $Gys^{-1}$. For the cellular irradiations the majority of the targets were 10 - 12.5 $\mu$m Au.

The original design of the hypoxia chamber was employed for these irradiations, which had 4 gas port inlets, as can be seen in Figure 6.5. After this experiment modifications were made to the design to reduce the size of the chamber as this design would not fit inside the re-entrant pipe that would be used in the TAP experiment described in section 6.4.

The cell samples were placed inside the chambers for all irradiations, with the RCF attached to the outside of the chamber as previous irradiations with the RCF attached to the

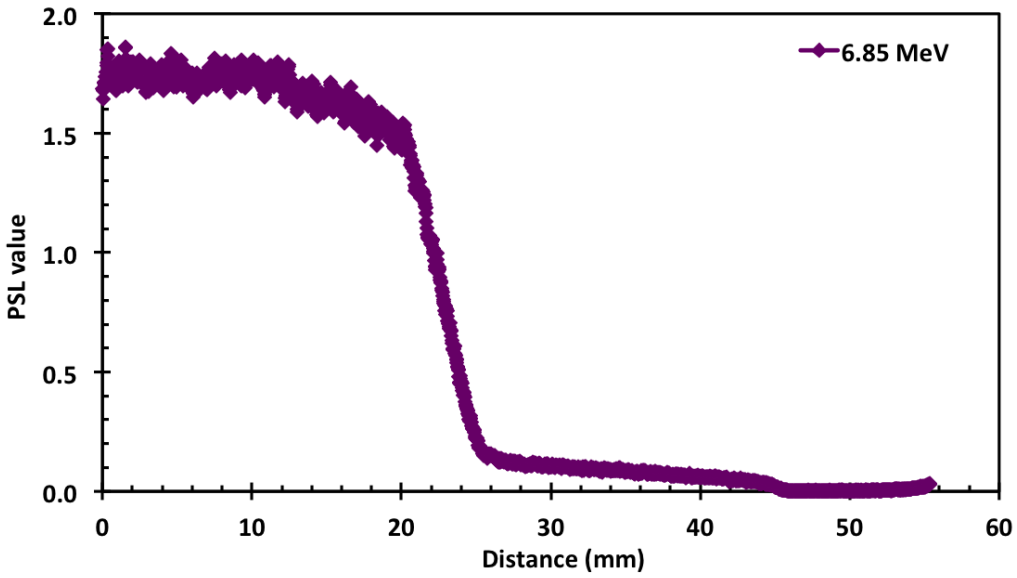


Fig. 6.4 An example of the proton spectra of 6.85 MeV protons on the cell plane. The distance is measured from the straight edge of the reference RCF.

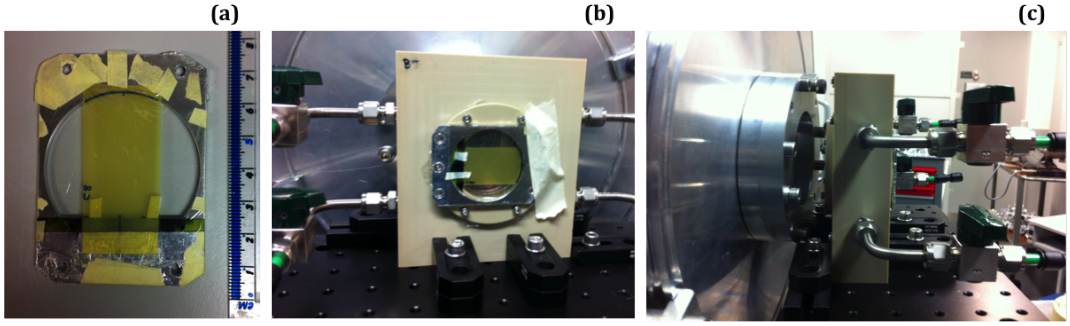


Fig. 6.5 **(a)** The RCF mask used to attach the un-coated EBT-3 film to the back of the hypoxia chamber. The position of the hypoxia chamber during the irradiations form **(b)** the back and **(c)** the side.

back of the dish had resulted in damaged RCF as the cell medium had leaked from the dish destroying the data. The samples were irradiated in a vertical position.

### 6.2.2 Irradiation Setup

For the cellular irradiations, the cells were plated on specially designed cell dishes shown in Figure 6.6 consisting of a stainless steel ring with groves on the front and back surfaces for silicon O-rings, a 3 $\mu$m Mylar surface for plating the cells and two aluminium plates used for securing the Mylar in place. The dishes were assembled with two full layers of Mylar on the front and back surfaces, then one side was trimmed to just below the centre line of the dish. Before plating, the dishes were sterilised for 30 minutes with 225 kVp X-rays using the X-ray cabinet in the CCRCB. The cells were cultured in minimum essential medium eagle supplemented with 20% FBS and 100 $\mu$gml$^{-1}$ of penicillin/streptomycin and seeded at a density of 450,000 cells per dish 24 hours prior to the irradiations. The correct concentration of the cell suspension was calculated using a Coulter Counter as described in section 6.1.2. The samples were kept in normal cell culture incubator with a 5% $CO_2$ 95% air atmosphere, 95% humidity and a 37°C temperature. The cell culture and plating were carried out in the Prise Lab of the CCRCB, then the samples were transported in sealed sterile boxes to the smaller bio-lab on the second floor of the CPP where they were kept in a smaller incubator with the same environment.

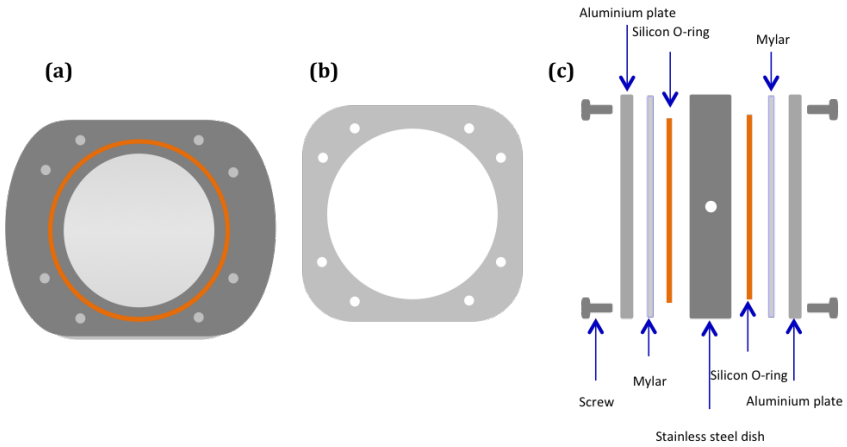


Fig. 6.6 **(a)** Schematic of the stainless steel dish with Mylar attached to the first side with an aluminium plate and O-ring, **(b)** an aluminium plate, **(c)** and how the dish is assembled. The front layer of Mylar is cut to just below the centre line of the dish after it is assembled.

### Oxic Environment

Just prior to the irradiations the samples were removed from the incubator and the media covering the cells was removed and replaced with 1 ml of fresh medium. The samples were secured inside the hypoxia chamber using a plastic bracket, and the lid on the chamber was gently replaced while the gas ports were open to prevent the Saran window from being unnecessarily stretched and damaged. The chamber was transported down to the interaction area in a sterile sealed box, where it was then removed and placed vertically 56 mm from the Kapton window. The RCF was then attached to the back of the chamber. The half layer of Mylar on the front side of the dish allowed the samples to be covered with warmed cell medium for as long as possible before the shot, and they would again be recovered in media as soon as the chamber was laid horizontally. The depth of the Mylar was such that the 1 ml of medium would be held in the bottom half of the dish, outside the irradiation zone thus not attenuating the beam energy. This negated the use of the motorised syringe used for the Gemini experiments described previously, but which would be employed in the LULI experiment described in section 6.3. This method of retaining the cell medium was in preparation for the TAP experiment where the preparation time for each shot would be much longer and the samples would be in danger of drying out if left uncovered for too long.

### Hypoxic Environment

The hypoxic samples were prepared in the same way as the oxic samples, only the cells were plated at least 28 hours prior to irradiation. At least 4 hours prior to irradiation the samples were removed from the incubator and the cell medium was removed and replaced with 1 ml of fresh full serum media. The samples were placed inside the large aluminium hypoxia chambers belonging to the CCRCB as only one of the new chambers was available for testing at this time. Each of these chambers could hold up to six samples. The large hypoxia chamber was tightly sealed with a lid and O-ring while the gas ports were open,

then a hypoxic gas supply of 95% $N_2$ and 5% $CO_2$ was connected to one of the inlet ports of the chamber, with a second piece of polyurethane tubing used to connect an outlet port to a flask of distilled water to monitor the flow rate of the gas. A flow rate of approximately one bubble per second was used to flush all the oxygen from the chamber. The large chamber was gassed for a minimum of 4 hours with the hypoxic gas mixture to remove all the oxygen from the samples and media within the chamber. Just prior to the irradiation the gas was disconnected form the large chamber and one of the samples was removed. the lid was quickly replaced on the large chamber, and the removed sample was quickly mounted inside the new small hypoxia chamber using the plastic bracket (this process was completed in less than a minute). The lid was then tightly sealed on the small chamber while all the inlet and outlet ports were open. the hypoxic gas supply was then connected to the small hypoxia chamber via one of its inlet ports. The other set of inlet and outlet ports were used to connect the small chamber to a Rapidox 1100Z meter to monitor the oxygen concentration inside the chamber. The small chamber was gassed for approximately 10 minutes to ensure there was no oxygen left inside the chamber. After 10 minutes all inlet and outlet ports were closed at the same time to prevent damage to the Saran windows of the chamber, and the gas supply and Rapidox meter were disconnected. The chamber was then transported down to the laser interaction chamber in sterile sealed container and placed vertically as close to the Kapton window as possible. Once the chamber was in position, the RCF holder was used to attach the un-coated EBT-3 film to the back window of the chamber.

After the irradiations the un-coated EBT-3 was removed from the back of the chamber and the chamber was laid horizontally in a sterile sealed box for transportation back to the bio-lab. Both the oxic and hypoxic samples were removed from the chambers and placed inside the incubator until they were required for fixing. The samples were fixed in the bio-lab in CPP, but before starting the staining procedure the samples were transported back to the Prise lab at the CCRCB.

Sham irradiations of control samples were carried out for the oxic and hypoxic irradiation conditions, with the samples being prepared, mounted and transported in exactly the same way as the irradiated samples, the only difference was the samples were not subject to any irradiation. Control samples were also kept inside the incubator.

### 6.2.3 Data Analysis and Results

The samples were removed from the incubator, the cell media was removed, the samples were washed twice with PBS and fixed and five time points of 0.5, 1, 2, 6 and 24 hours post irradiation with an ice cold 1:1 solution of methanol and acetone. At least one shot was required per time point, with the aim to complete at least one complete time point set within the same day to try and limit the differences in the irradiation and incubator conditions across the set. This fact can be used to identify if outlier values within a group of samples fixed at the same time point are just rogue values, or if all samples on that day were affected in the same way. the results presented are averaged over several samples and several days. The samples were then stored in the fridge for 10 minutes before the fixative solution was removed and the samples were washed thrice with PBS. The samples were then kept in the fridge until all the samples were fixed and it was time to commence the staining process. The samples were permeabilised with chilled methanol and incubated on ice for 10 minutes before being washed thrice with chilled methanol for 5 minutes. The samples were then blocked with a buffer of 10% goat serum and 0.1% Triton X-100 in PBS, then the primary antibodies were added at a dilution of 1:1000 for $\gamma$-H2AX and 1:500 for HIF-1$\alpha$ in blocking buffer. $\gamma$-H2AX was chosen for staining as this was a well established protocol, and a new HIF-1$\alpha$ antibody compatible with $\gamma$-H2AX was being trialled. All samples were stained for both bio-markers for comparison of the DNA DSB foci kinetics and hypoxia induction. After incubation with the primary anti-bodies and washing with a washing buffer of 0.1% Triton X-100 in PBS and PBS, the secondary antibodies were added at the same

TARANIS 6.85 MeV Protons

| Time Point (hrs) | Oxic Replicates | Hypoxic Replicates |
|---|---|---|
| Control | 2 | 1 |
| 0.5 | 2 | 1 |
| 1 | 1 | 1 |
| 2 | 1 | 1 |
| 6 | 1 | 1 |
| 24 | 1 | 1 |

Table 6.2 Summary of the TARANIS replicates for each time point and irradiation condition for 6.85 MeV protons. The values represent the number of samples successfully stained with clearly discernible foci.

concentration as the primary antibodies, GAM594 1:1000 (visualised in the red channel) and GAR488 1:500 (visualised in the green channel). The cell nuclei were contrast stained with DAPI during mounting of the samples on glass microscope slides. The back of the Mylar on which the cell monolayer was situated was marked with a vertical line at one side and a curved line at the other edge to indicate the high and low energy ends of the proton spectrum respectively using the mask which attached the RCF to the rear of the hypoxia chamber. The centre of the irradiation zone was also marked. Table 6.2 summarises the number of replicates for each irradiation condition and time point. As can be seen, for most combinations only one sample had clearly discernible foci after the staining process.

Images of the cells were obtained using the Carl Zeiss Axiovert 200M fluorescence microscope with CCD acquisition capability and Axiovision Rel 4.8 software package, located at the Centre for Cancer Research and Cell Biology, QUB. A x 63 magnification oil immersion objective was used to focus the microscope and take several images of the region irradiated by the 6.85 MeV protons indicated by the calibration shots. A sufficient number of images were taken to allow the counting and recording of foci in at least 50-100 cells per shot. The foci were counted using the Cell Counter application in ImageJ, where the foci are recognised manually by the user, with the program recording the number, allowing faster

and easier data acquisition than manually counting the foci through the microscope eyepiece itself. Overlapping cells, cells with a high background and abnormally sized/shaped cells were all ignored; only foci in cells with clearly discernible foci were counted. The images were obtained by lining up the vertical line marked on the Mylar in the centre of the field of view then moving 18.2 mm horizontally towards the curved line marked on the other side of the slide using the motorised stage of the microscope. When the correct position was reached the stage was moved vertically to ascertain the extent of the radiation zone by looking at the number of foci induced in the nuclei. Figure 6.7 shows example images of the oxic and hypoxic samples irradiated with 6.85 MeV protons.

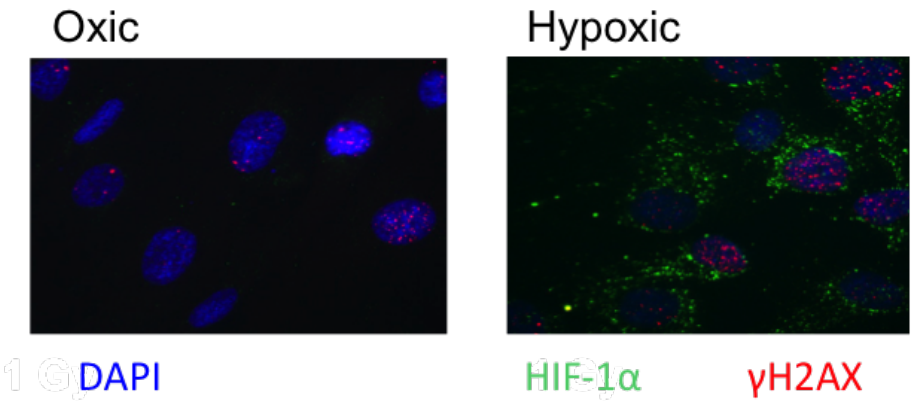


Fig. 6.7 Example foci images obtained for the nuclei irradiated with 6.85 MeV protons. The $\gamma$-H2AX foci have been stained red, the nuclei are contrast stained blue and the hypoxia induction bio-marker HIF-1$\alpha$ has been stained green.

The average number of foci per nucleus was obtained for each time point and is plotted in Figure 6.8. As can be seen from Figure 6.8, there is not a significant difference between the oxic and hypoxic samples, and both data sets have large associated errors related to the actual counts obtained and the position of the energy line on both the RCF and the sample slide. The sample may have moved during the mounting process, thus the images and counts were obtained for a lower energy than that indicated by the mask. The values all originate from one sample per time point and irradiation condition, apart from the 0.5 hr oxic value

which is the average of two samples. All time point values have had the relevant control value of 1.98 $\pm$ 0.78 for oxic samples or 1.75 $\pm$ 0.76 for hypoxic samples subtracted.

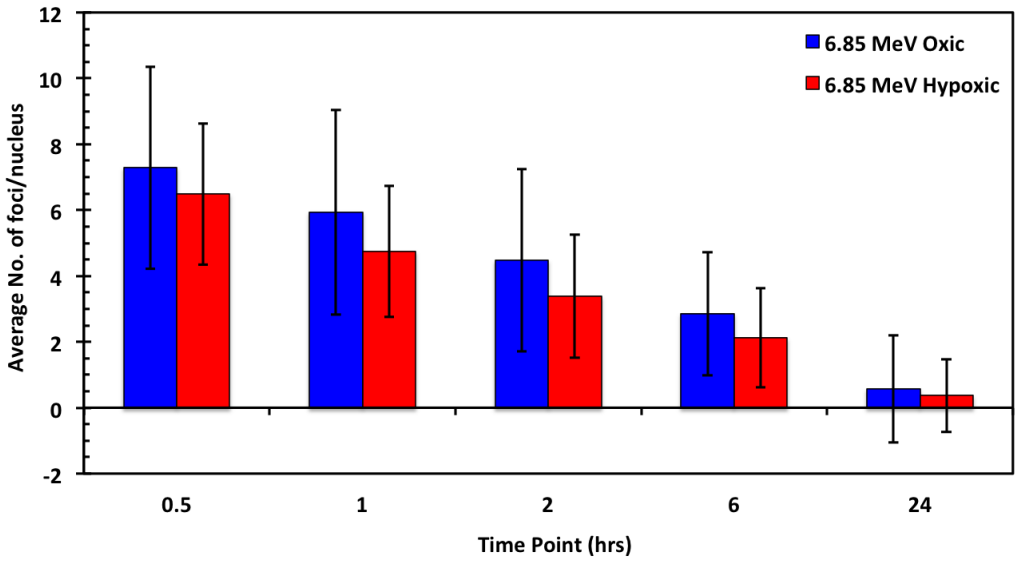


Fig. 6.8 The 53BP1 foci kinetics of laser induced DNA DSBs. The values shown are the average number of foci per nucleus (with the control value of 1.98 $\pm$ 0.78 for oxic and 1.75 $\pm$ 0.76 for hypoxic samples subtracted) as the dose was unobtainable from the RCF as it was below 0.1 Gy for the majority of the shots, hence the low values for the average number of foci per nucleus. These values have the control value subtracted, hence why the value can become negative (for example the 24 hr time point error bars) if the foci count falls below the control value.

The 6.85 MeV proton data sets (LET of 6.3 keV/$\mu$m) do not show a huge difference between the hypoxic and oxic samples, but they do show that a higher percentage of the damage in the hypoxic samples is repaired, and repaired faster, than the damage induced in the oxic samples. This is owing to the absence of oxygen to create free radical species which damage the DNA by indirect actions, and also the lack of oxygen to 'fix' the DNA damage and make it harder or impossible to repair. However not too much can be read into these values as they are much lower than expected and the dose has not been taken into account as will be explained below.

Figure 6.9 shows the percentage of foci remaining at each time point as compared to the

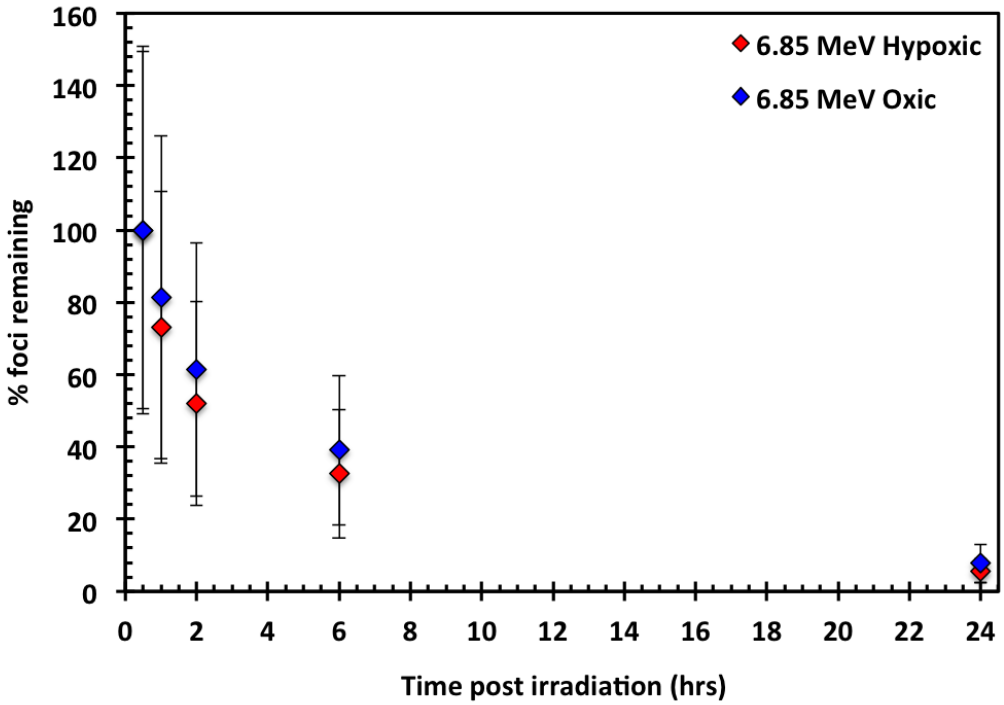


Fig. 6.9 The percent foci remaining at each time point compared to the number of foci present 0.5 hrs post irradiation.

number of foci present 0.5 hrs post irradiation. This figure also shows that more DNA DSBs are repaired and faster for the hypoxic samples, although as before there are large error bars, so in reality the values are the same within error. The relative foci induction, RFI, for oxic versus hypoxic conditions for 6.85 MeV proton irradiations was also calculated for each time point, summarised in Table 6.3, and the average value was found to be $0.77 \pm 0.04$, indicating that more foci were produced in oxic than hypoxic conditions (this was the case at all time points). As can been seen in the table large errors are also involved in these values.

It must be noted that all the samples were removed from the hypoxia chambers directly after the irradiations, even the hypoxic samples, as only one new chamber was available for testing. In hindsight this was seen as a mistake as the samples were able to re-oxygenate as soon as they were removed from the chamber, thus affecting the biological changes that would occur during the subsequent hours before fixation. However, this will prove valuable

| Time Point (hrs) | RFI |
|---|---|
| 0.5 | $0.89 \pm 3.42$ |
| 1 | $0.80 \pm 2.44$ |
| 2 | $0.75 \pm 1.83$ |
| 6 | $0.74 \pm 1.54$ |
| 24 | $0.65 \pm 0.31$ |

Table 6.3 Summary of the RFI for each time point for oxic versus hypoxic irradiation conditions for 6.85 MeV protons.

when comparing the results to the outcomes of future experiments, as it will show that any differences in response arise from the prolonged hypoxic exposure during the repair period rather than the initial hypoxic condition when the samples were irradiated.

The un-coated EBT-3 films were scanned using an Epson Perfection V75 Pro calibrated flat-bed transmission scanner with RGB 48 bit settings and 1200 dpi (dots per inch) resolution. The raw images were then taken into the ImageJ Macro and the dose was obtained from the positions indicated by the calibration shots using aluminium filters. The 6.85 MeV proton line was located 18.2 mm from the vertical line marked on both the EBT-3 film and the Mylar of the cell dish using the RCF mask. Unfortunately approximately two thirds of the shots were irradiated with a dose undetectable by the ImageJ Macro, and the other third were irradiated with doses on average of less than 0.1 Gy, thus when these values were used to calculate the average number of foci per nucleus per Gy the values obtained were vastly over estimated compared to previous results. A contributing factor could have been the placement of the RCF outside the hypoxia chamber rather than directly behind the Mylar with the cell monolayer. At the time of this experiment it was thought the un-coated EBT-3 film would be damaged if it was placed inside the hypoxia chamber and kept inside the incubator for extended periods of time, hence why it was kept behind the rear window on the outside of the hypoxia chamber. In previous cellular irradiations the RCF had been directly attached to the rear of the cell dish, however media from the cell dish had leaked onto the

RCF and damaged the surface thus making it impossible to recover the dose information. To combat this the RCF was wrapped in 0.9 $\mu$m Mylar to protect it, something which was also done in this experiment as a precaution. Later tests proved that the EBT-3 film was capable of surviving for more than 24 hours in the incubator on the back of the cell dish inside a gassed and un-gassed hypoxia chamber, thus this method was adopted for future experiments as it ensured the film was as close as possible to the location of the cell plane for a more accurate dose measurement. The EBT-3 film was still wrapped in the 0.9 $\mu$m Mylar to protect against leakage of cell media.

Even though the physical results obtained for these cellular irradiations did not provide a large or good quality data set they were useful for establishing the procedures that would be used for the TAP experiment. Modifications to the design of the hypoxia chamber could be made to prepare it for use in the TAP experiment discussed in section 6.4. The positioning of the RCF could also be adjusted to provide a more accurate recording of the dose received by the cell plane. Despite the problems, it was established that the new compact hypoxia chamber was compatible with a laser plasma interaction environment and was able to induce hypoxia in the samples inside the chamber.

## 6.3 LULI Experiment

The unique capabilities of the pico2000 laser system in terms of high proton flux and high energies available have been employed to carry out single shot investigations of the cellular response to proton irradiation, through ultra- fast proton dose deposition in normal human cell models. This involved cell preparation and handling on-site at the LULI facility at Laser Lab Europe, and subsequent analysis of data at Queen's University Belfast.

The main aim of this experiment was the characterisation of DNA double strand breaks (DSB) by means of the 53BP1 immunofluorescence assay. The DNA DSB formation and repair in AG01522 normal human fibroblast cells was monitored as a function of dose and

time post irradiation. For given time points of 0.5, 1, 2, 6 and 24 hours post irradiation the samples were fixed, stained and analysed allowing the reconstruction of the dynamics of cell repair following irradiation by laser-accelerated protons.

### 6.3.1 Experimental Arrangement

The biological samples were irradiated with a multi-MeV proton beam generated by the interaction of a high intensity laser pulse with a metal foil. The targets were 5-100 nm gold foils, as high Z targets produce spatially uniform proton beams, ensuring uniform irradiation of the sample. In order to expose the samples to protons within a selected narrow energy range, a beam transport and delivery system was installed inside the interaction chamber, which was capable of separating protons possessing different energies and also maintained a high flux on the cell plane. The system consisted of a modular assembly of static magnets, with a slit entrance aperture, that angularly dispersed the particles according to their energy. As only protons were desired to irradiate the samples, metal filters of suitable thicknesses were placed just in front of the sample to suppress the unwanted heavier ions, while the X-rays were suppressed using suitable lead shielding in the chamber.

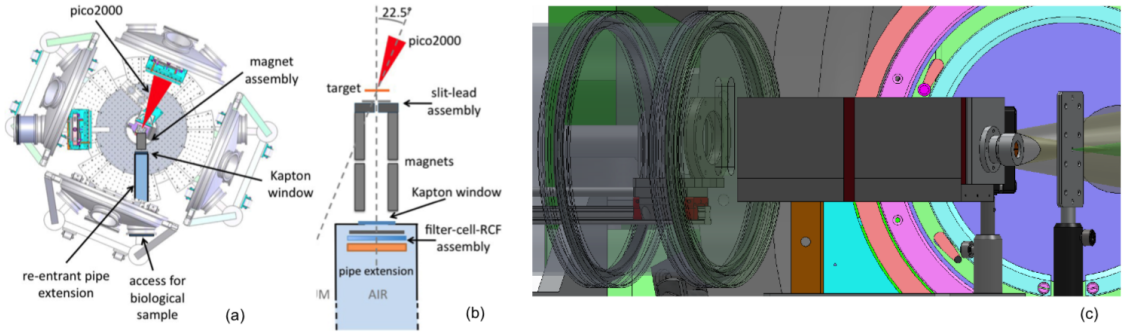


Fig. 6.10 **(a)** Target chamber arrangement, showing the re-entrant tube and magnet assembly. **(b)** Aerial and **(c)** lateral detail of the target arrangement, beam transport delivery system and the position of the biological sample within the re-entrant tube.

The AG01522 cells were grown on 3$\mu$m Mylar in a specifically designed stainless steel

and aluminium dish. A uniform layer of approximately 500,000 cells covering the whole dish allowed single shot exposures of spatially separated cells to several different proton energies and doses. The dish was placed vertically outside the target chamber behind a 50 $\mu$m Kapton window. The use of the Kapton window prevented substantial energy loss in the ion beam prior to irradiating the cells whilst still maintaining a proper sealing of the vacuum chamber. The cell dishes were equipped with an automated syringe system to remove and add the cell media before and after the shot respectively, to preserve the integrity of the cells. Normal and customised EBT2 radiochromic film was placed directly behind the Mylar on which the cells were grown, in order to monitor the dose deposited on a shot to shot basis. This was done by employing a specially designed mask (Figure 6.11) that ensured the film was placed in the same position for each shot, allowing accurate identification of the particle energy at given positions which was then correlated with the position of the DNA damage. Monte Carlo simulations showed that the cells were placed in the tail of the Bragg curve far from the Bragg peak, ensuring a uniform energy deposition across the cell layer and permitting a a precise characterisation of the dose delivered to the biological sample based on the analysis of the dosimetric films.

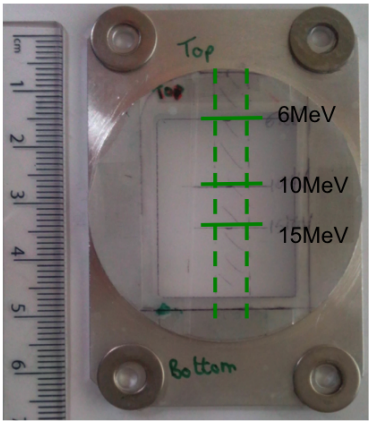


Fig. 6.11 Mask used to attach the RCF with the positions of the 6 MeV, 10 MeV and 15 MeV protons marked.

The experiment was carried out in target area 1 of the LULI2000 laser facility employ-

ing the pico2000 beam-line at it's standard operational parameters of 80 J in 1 ps at $1\omega$. The beam was focused on to the foil targets at angle of incidence of approximately 22.5° using the f = 800 mm, f/4 off axis parabola permanently installed inside the Milka target chamber. The experimental setup is shown in Figure 6.10, with the beam transport and delivery system being shown in more detail in Figure 6.10 (b) and (c). The targets were located at the normal target chamber centre on the permanent motorised target stage, and the beam delivery system was installed inside the chamber along the target normal axis with the system entrance slit approximately 5 cm from the target. The re-entrant tube was required to allow the biological sample to be placed as close to the beam delivery system as possible, reducing the overall distance from the target, thus maximising the irradiation dose on the cells.

### 6.3.2 Irradiation Setup

The biological samples were prepared and stored in the Laboratory of Optics and Biosciences, Ecole Polytechnique-INSERM-CNRS (LOB). All the components of the cell sample dishes were cleaned with water and sterilised under the laminar flow hood using 70% ethanol and PBS. This was not the preferred method of sterilisation as previous investigations had been unable to seed and grow cell cultures on the Mylar after preparing the dishes in this way, however there was no access to an X-ray cabinet at this facility, the preferred sterilisation method, thus this approach was adopted. The dishes were then assembled by stretching 3 $\mu$m Mylar across a stainless steel ring and sealing with an aluminium plate and silicon o-ring. The assembled dishes were again washed with 70% ethanol and PBS under the laminar flow hood. When space permitted the sterile assembled dishes were stored in the laminar flow cabinet until required, otherwise there were placed in sterile petri dishes, wrapped in sterilised aluminium foil and placed in a dedicated drawer until required. These dishes were only unwrapped under the hood and were left under the UV light for at least an

hour prior to seeding samples.

The cell samples were transported to the LULI facility by commercial air transportation in two T175 tissue culture flasks completely filled with 800 ml of reduced serum cell culture medium (10% FBS and 100 $\mu$gml$^{-1}$ penicillin/streptomycin). The flasks were sealed with parafilm, wrapped in bubble wrap, and sealed inside an insulating polystyrene box. One of the flasks leaked during transportation, thus it was discarded owing to possible contamination issues. A replacement flask was sent by air mail. On arrival the low serum media was immediately discarded, the cells were washed once with sterile PBS and 25 ml of full serum media (20% FBS instead of 10% FBS) was added to the flask. The cells were left for at least 24 hours before they were split from one T175 into four T75 flasks. Using smaller flasks allowed the cells to grow faster and some flasks could be kept undisturbed when seeding for the experiments to ensure an adequate cell stock while waiting for the replacement cells.

The AG01522 cells were cultured in filtered Minimum Essential Medium Eagle with alpha modification supplemented with 20% FBS (foetal bovine serum) and 100 $\mu$gml$^{-1}$ penicillin/streptomycin and stored in T75 and T175 tissue culture flasks in a tissue culture incubator with a 5% $CO_2$ and 37°C atmosphere. The cells were trypsinised with 10 ml of 0.05% Trypsin EDTA which was neutralised with 10 ml of culture medium. Approximately 10 $\mu$l of the suspension was pipetted onto a haemocytometer and the cell number calculated. The cell suspension was diluted accordingly with culture medium in order to seed approximately 500,000 cells on each sterile cell dish. Seeding was carried out 24-48 hours prior to irradiation to allow the cells sufficient time to attach to the surface of the Mylar. Any excess cell suspension was reseeded to keep a stock of cells growing.

**Oxic Environment**

Immediately before irradiation, the dishes were removed from the incubator and a second layer of Mylar was stretched over the open side of the stainless steel ring and secured and

sealed with a second aluminium plate and O-ring. The dish was connected to a syringe filled with full serum cell culture medium, part of a remotely operated pump system, by polyurethane tubing and appropriate plastic connectors to allow for a tight seal. The pump system consisted of the syringe, tubing and connectors which would then be placed in a specially designed motorised bed which allowed a push/pull mechanism controlled by a remotely operated motor. The cavity between the two layers of Mylar was slowly filled with medium, so as not to dislodge the attached cells. The dish was then carefully transported from the LOB, in a box containing a flask of warm water to maintain the temperature of the cells at 37°C, to the target area where the RCF was attached using the mask (Figure 6.11). The dish was mounted vertically on a sliding rail in the re-entrant tube and the syringe was placed on a motorised bed. The whole assembly was pushed inside the re-entrant tube along the rail. The syringe remotely removed the medium from the cells approximately 2 minutes prior to the laser shot at a flow rate of 0.22 $mls^{-1}$, where the cells were irradiated with protons produced from the interaction of the laser with the target. Removing the medium reduced the loss of energy owing to transmission through the liquid, whilst the flow rate was chosen to maintain the integrity of the cell dish. The syringe was then used to recover the irradiated cells with medium so they could be transported back to the LOB. The second layer of Mylar and the excess medium were removed from the cell dishes, and the dishes were placed back inside their petri dishes in the incubator until they were required to be fixed.

The irradiations were carried out in an oxic environment where the cells were not treated with any chemicals or gassed prior to, during or post irradiation. The facilities required for hypoxia experiments were not available at LULI. Sham irradiations of control samples were also carried out, with the samples being prepared, mounted and transported in exactly the same way as the irradiated samples, the only difference was the samples were not subject to any irradiation. Control samples were also kept inside the incubator.

The same syringe system employed had already been tested during the 2013 experiment carried out employing the Gemini laser. This system was required for these irradiations as the safety checks, preparation including the cell dish positioning and shot time required a significant amount of time at LULI compared to the time required at TARANIS (up to 10 minutes compared to 2 minutes). If there are any delays in the chain of events leading up to the shot, the cells would be subject to large amounts of stress as they would start to dry out and cool down too much. The syringe system allows the cells to be covered in the warmed cell medium until 30 seconds before the shot, then recovered immediately after the shot, thus reducing the stress to and maintaining the health of the cells. If the cells become too stressed, biological changes may be a result of this stress rather than damage inflicted by the laser accelerated protons.

### 6.3.3 Data Analysis and Results

The irradiated cell samples were washed twice with PBS before being fixed with an ice cold 1:1 solution of acetone and methanol for 20 minutes, at five specific time points of 0.5, 1, 2, 6 and 24 hours post irradiation. At least one shot was required per time point, with the aim to complete at least one complete time point set within the same day to try and limit the differences in the irradiation and incubator conditions across the set. This fact can be used to identify if outlier values within a group of samples fixed at the same time point are just rogue values, or if all samples on that day were affected in the same way. The results presented are averaged over several samples and several days. The cells were permeabilised with chilled methanol and incubated for 10 minutes on ice, after which the methanol was poured off and the cells were washed 3 times for 5 minutes with chilled PBS. The PBS was then discarded and 2 ml of blocking buffer (10% goat serum, 0.1% Triton X-100 in PBS) was added per dish to block non-specific binding and the dishes were incubated at 37°C for 1 hour, after which the dishes were drained. Next approximately 1 ml of the primary

LULI Oxic, Protons

| Time Point (hrs) | 10 MeV Replicates | 13 MeV Replicates | 15 MeV Replicates |
|---|---|---|---|
| Control | 2 | 2 | 2 |
| 0.5 | 2 | 2 | 2 |
| 1 | 3 | 2 | 1 |
| 2 | 3 | 3 | 1 |
| 6 | 3 | 3 | 2 |
| 24 | 2 | 2 | 1 |

Table 6.4 Summary of the LULI replicates for each time point and proton energy for the irradiations under oxic conditions. The values represent the number of samples successfully stained with clearly discernible foci.

antibody, 1:1000 anti 53BP1 in blocking buffer, was added to each dish at room temperature for 1 hour. 53BP1 was chosen to visualise the DNA DSBs this time as the staining from the TARANIS experiment using $\gamma$-H2AX did not prove satisfactory. The dishes were then washed thrice with washing buffer (0.1% Triton X-100 in PBS), and once with PBS. The dishes were drained and approximately 1 ml of the secondary antibody, 1:1000 GAR488 in blocking buffer, was added to each of the dishes. The secondary antibody was left on the dishes for 1 hour and from this point the samples had to be kept in the dark, as light would bleach the data from the cells. The samples were washed twice with washing buffer then once with PBS, then all the remaining solution was removed.

The samples were mounted on glass slides by depositing two drops of Gibco ProlLong Gold Antifade Mountant with DAPI (DAPI) onto the cell side of the Mylar and gently lowering a cover-slip over the irradiated zone indicated by the RCF mask. Excess DAPI was removed by gently pressing with a tissue and the samples were left to dry for 24 hours in the dark. A glass slide was attached to the reverse side of the Mylar using super glue, left to dry, and a scalpel was used to cut around the glass slide to remove the sample from the dish. The glass slide was marked to show the positions of where 6 MeV, 10 MeV and 15 MeV protons should have irradiated the cells using a template produced from simulations

and RCF data. Excess Mylar was cut away from around the cover slip and the edges were sealed with clear nail varnish. The samples were stored at -20°C while on-site at the LOB and on their return to Queen's University Belfast. During transport they were kept as close to -20°C as possible by packing the samples in slide boxes inside insulated polystyrene boxes with ice blocks. Table 6.4 summarises the number of replicates for each proton energy and time point. As can be seen from the table, for 10 MeV and 13 MeV there are at least two or three samples for each time point which had clearly discernible foci after the staining procedure, but for 15 MeV there was only one sample for the 1 hr, 2 hr and 6 hr time points.

After the samples were mounted, images of the cells were obtained using the Carl Zeiss Axiovert 200M fluorescence microscope with CCD acquisition capability and Axiovision Rel 4.8 software package, located at the Centre for Cancer Research and Cell Biology, QUB. A x 63 magnification oil immersion objective and x 40 magnification objective were used to focus the microscope and take several images of each region of interest on each slide. For each region of interest a sufficient number of images were taken, to allow the counting and recording of foci in at least 50-100 cells. The foci were counted using the Cell Counter application in ImageJ, where the foci are still recognised manually by the user, but the program records the number, allowing faster and easier data acquisition. Overlapping cells, cells with a high background and abnormally sized/shaped cells were ignored; only cells with clearly discernible foci were counted. An even more efficient approach for counting the foci would be to use an automated cell analysis program, however as the cells are plated on 3 $\mu$m Mylar which is no longer taut when the samples are removed from the dishes, the cells are no longer resting on a completely flat surface. This causes variation in the focal length required to visualise the cells on the microscope, including variations within the same cell where a portion of the nucleus will be in focus and the other portion out of focus. Manual adjustment of the focus may be more time consuming, but allowed a higher accuracy in the count in this instance.

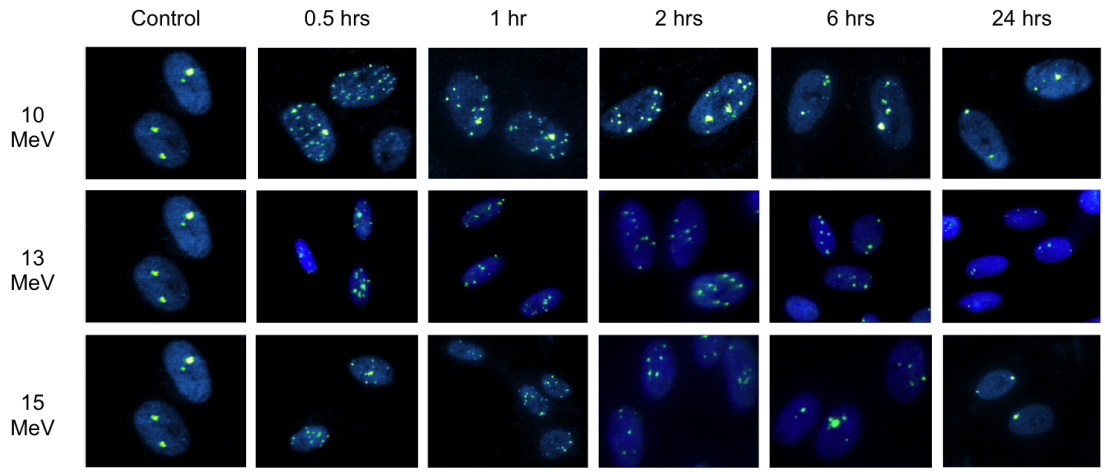


Fig. 6.12 Example images of the 53BP1 foci taken at the positions irradiated by 10 MeV, 13 MeV and 15 MeV protons as indicated by the positions on the RCF mask, at the five different time points of 0.5, 1, 2, 6 and 24 hrs post irradiation and the control.

Figure 6.12 shows example images of the stained cells taken with the Axiovert 200M fluorescence microscope. The foci are clearly visible and well defined. The images were taken along three specific lines, as indicated by the RCF mask, at the positions irradiated by 10 MeV, 13 MeV and 15 MeV protons. Although the 6 MeV line was indicated on the mask, the microscope was unable to focus on this line, so an alternative line at 13 MeV was chosen instead, measured by focusing on the 15 MeV line and moving the microscope stage 2557.5 $\mu$m towards the 10 MeV line. A vertical scan along the 10 MeV line was performed for the first 0.5 hr sample, where an image was taken every 170 $\mu$m using the x 63 objective starting just outside one edge of the radiation zone and finishing just outside the other edge of the radiation zone. The average number of foci per nucleus for each of these images was determined and plotted as a function of distance across the sample. The dose for the shot was obtained from the normal EBT-3 film located behind the cell dish using the ImageJ Macro discussed in Section 3.3.3, and was also plotted as a function of distance across the sample. As can be seen in Figure 6.13, this showed that the average number of foci per nucleus and the dose were relatively uniform across the centre of the radiation zone, but fell

away towards the edges, thus subsequent images for analysis were taken within a central region of the slide (approximately 4 mm). The dose from the customised EBT-3 film was not aligned with the foci number per nucleus as a calibration for this type of film was not available at the time of analysis. The films were scanned with an Epson Perfection V75 pro calibrated flat-bed transmission scanner with setting of RGB 48 bit and a resolution of 300 dpi.

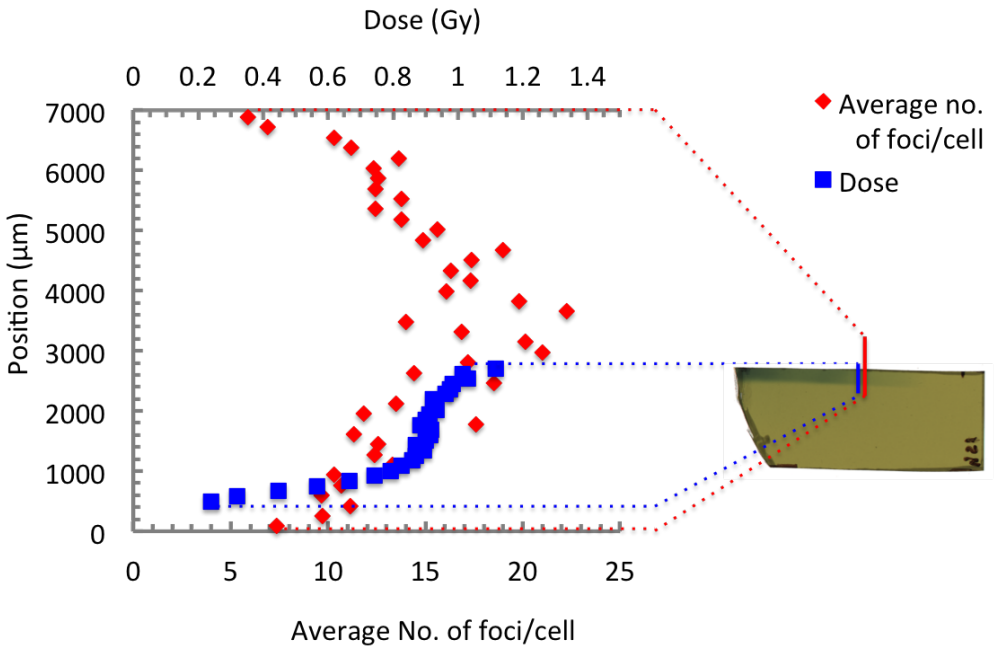


Fig. 6.13 Average number of foci per nucleus aligned with the dose across the normal EBT-3 RCF along the 10 MeV proton line for the first 0.5 hr sample.

Figure 6.13 was used to extract a dose response for the particular shot used to identify the region for foci counting. A dose response is a simple x-y graph relating the magnitude of a stressor, in this case the dose of proton irradiation, to the response of the receptor, in this case the number of DNA DSB foci induced in AG01522 normal human fibroblast cells. The dose response relationship describes the changing effect on an organism caused by different doses after a certain exposure time, in this case 0.5 hrs. In the figure the average number of foci per cell at a certain position on the sample, is plotted against the dose at

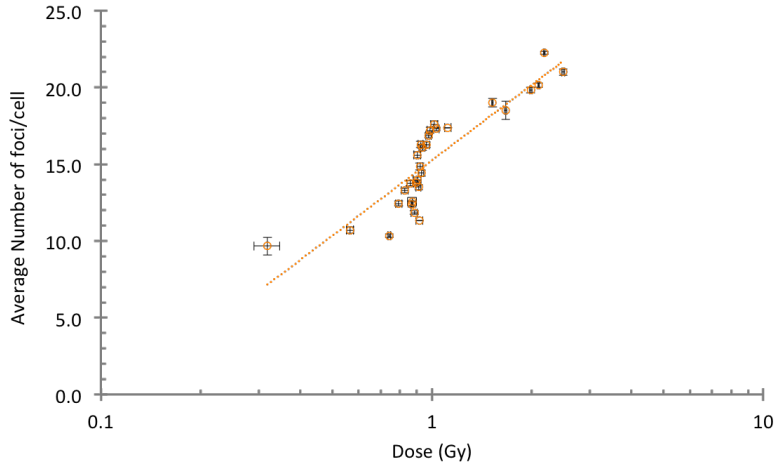


Fig. 6.14 Dose response extracted from Figure 6.13 where the average number of foci per nuclei has been plotted against the dose at that position.

the corresponding position on the RCF behind the sample. The higher the dose obtained from the RCF, the greater the average number of foci per nucleus obtained from the stained sample.

Along each of the specified energy lines, within the central 4 mm zone, an image was taken every 170 $\mu$m using the x 63 objective or 256 $\mu$m using the x 40 objective. The microscope was centred on each of the lines, with the field of view being 226 $\mu$m or 344 $\mu$m across for the x 63 or x 40 objective respectively. The mean number of foci counted for a minimum of 50 cells and a maximum of 200 cells per slide was recorded for each energy line on every slide. The dose for each shot at the position of each energy line was then obtained from the normal EBT-3, and the average number of foci per nucleus per Gy was calculated for each time point. Figure 6.15 shows the average number of foci per nucleus per Gy at each time point for the regions of the sample irradiated with 10 MeV, 13 MeV and 15 MeV protons, and Figure 6.16 shows the percent of foci remaining at each time point compared to the average number visible 0.5 hrs post irradiation. All values are averaged over two to three shots for the 10 MeV, 13 MeV and 15 MeV positions apart from the 1 hr, 2 hr and 24 hr time points for the 15 MeV line which are just one sample each. All values

have the control value of 1.81 $\pm$ 0.05 subtracted,

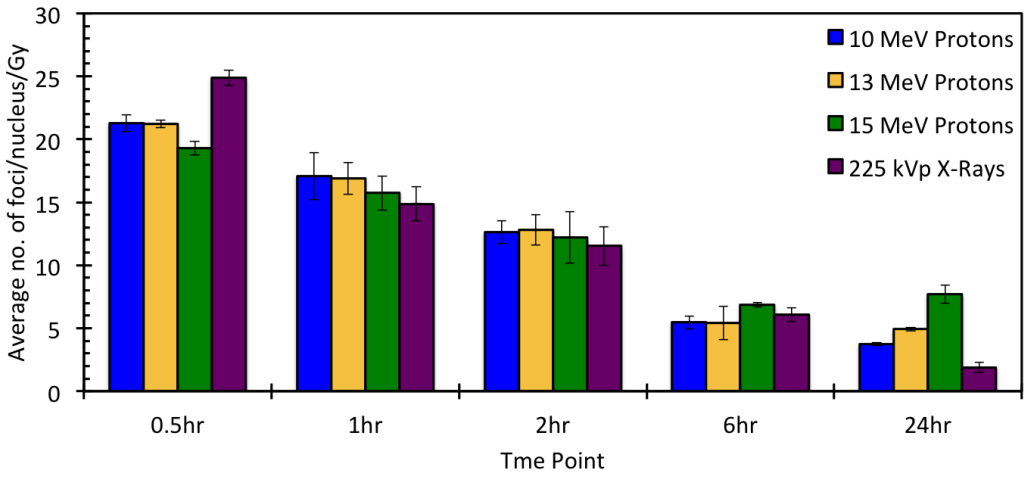


Fig. 6.15 Kinetics of DNA DSB damage and repair visualised through 53BP1 immunostaining and displayed as the average number of foci per nucleus per Gy with respect to time post irradiation.

Figure 6.15 has some promising features in the form of a peak in the number of DSBs, followed by a period of recovery. The 53BP1 foci are dephosphorylated over time with kinetics which parallel the rate of DSB repair. The kinetics, which are measured as a mean number of foci per nucleus per Gy over time (shown in Figure 6.15 and as a percent of foci remaining compared to the number of foci visible 0.5 hrs post irradiation shown in Figure 6.16), represent the fast and slow components of DNA repair. The fast component is apparent from the measured time points of 0.5 to 2 hrs post irradiation, with the slow component extending from 2 to 24 hrs post irradiation. The fast component represents the repair of simple DSBs and the slow component represents the repair of more complex DSBs. The three different proton energies of 10 MeV, 13 MeV and 15 MeV all have similar LET values of 4.6 keV/$\mu$m, 3.7 keV/$\mu$m and 3.3 keV/$\mu$m respectively, hence why they show approximately the same trend and values for the average number of foci per nucleus per Gy for each time point. The slight discrepancies in the values may be owing to over- or

under-estimation of the number of foci for these time points, a slight error in the position of the lines on the glass slides of each sample or an error in the position of where the dose was obtained from the EBT-3.

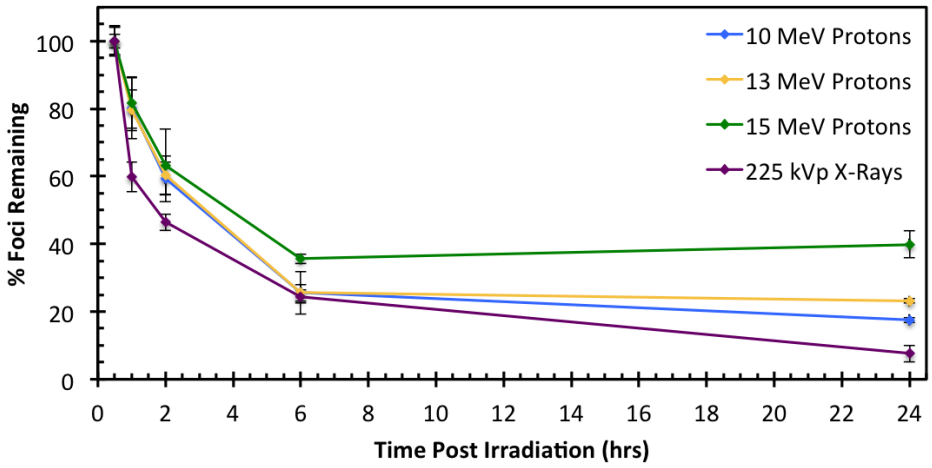


Fig. 6.16 Percent foci remaining at the different time points with respect to the average number of foci 0.5 hrs post irradiation.

Figure 6.16 shows a similar situation with most of the data sets following approximately the same trend. The 10 MeV and 13 MeV proton data sets are closely matched for the longer time points of 6 and 24 hrs, whereas the 13 MeV and 15 MeV proton data sets are more closely matched at the 1 and 2 hr time points (the same can be seen in Figure 6.15).

Figure 6.17 shows the relative foci induction for each of the five time points investigated. The relative foci induction (RFI) is measured as the ratio of the average number of foci induced by the proton irradiations ($F_{Protons}$) of 10 MeV, 13 MeV and 15 MeV compared to the average number of foci per nucleus induced by 225 kVp X-rays ($F_{X-rays}$).

$$RFI = \frac{F_{Protons}}{F_{X-rays}} \tag{6.1}$$

This is an analogous measure to the RBE, which is more commonly used for cell survival

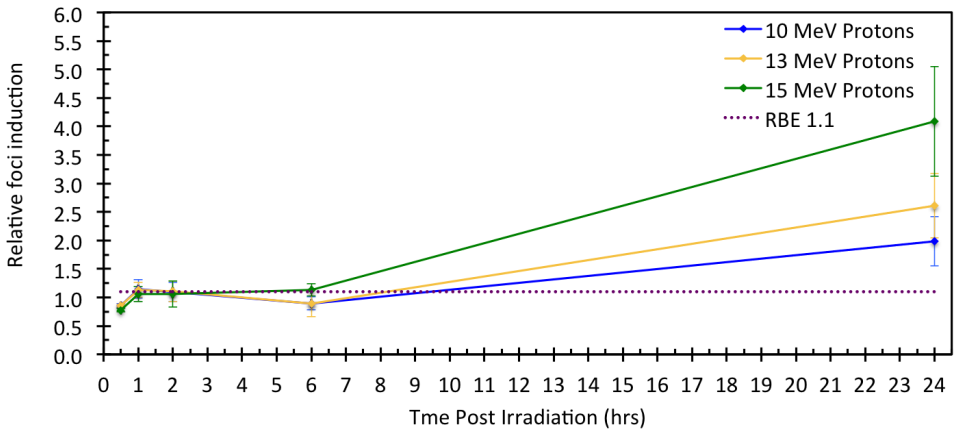


Fig. 6.17 The relative foci induction measured as the ratio of the average number of foci per nucleus per Gy induced by the proton irradiations (10 MeV, 13 MeV and 15 MeV) compared to the average number of foci per nucleus per Gy induced by 225 kVp X-rays for each time point.

studies such as clonogenic assays. The RFI was calculated individually for each time point and plotted along with the generally accepted RBE of 1.1 for proton irradiations, as shown in Figure 6.17. The average RFI for each proton energy was calculated to be $1.20 \pm 0.18$, $1.32 \pm 0.29$ and $1.62 \pm 0.55$ for 10 MeV, 13 MeV and 15 MeV protons respectively, all of which are higher than the generally accepted value of 1.1, but this value falls within the margin of error. The RFI appears to be much higher at 24 hrs for all the discussed proton energies, but especially for 15 MeV protons. The dose calculated from the EBT-3 normal films at the 15 MeV position was very low, the effect of which is amplified by division when calculating the average foci per nucleus per Gy and thus the RFI. Figure 6.18 shows the shot to shot dose variation calculated from the normal EBT-3 films at the three different energy positions.

The average dose across all shots for the 10 MeV proton line was $1.19 \pm 0.30$, for the 13 MeV line it was $0.73 \pm 0.24$ and for the 15 MeV line it was $0.45 \pm 0.22$. The experimental

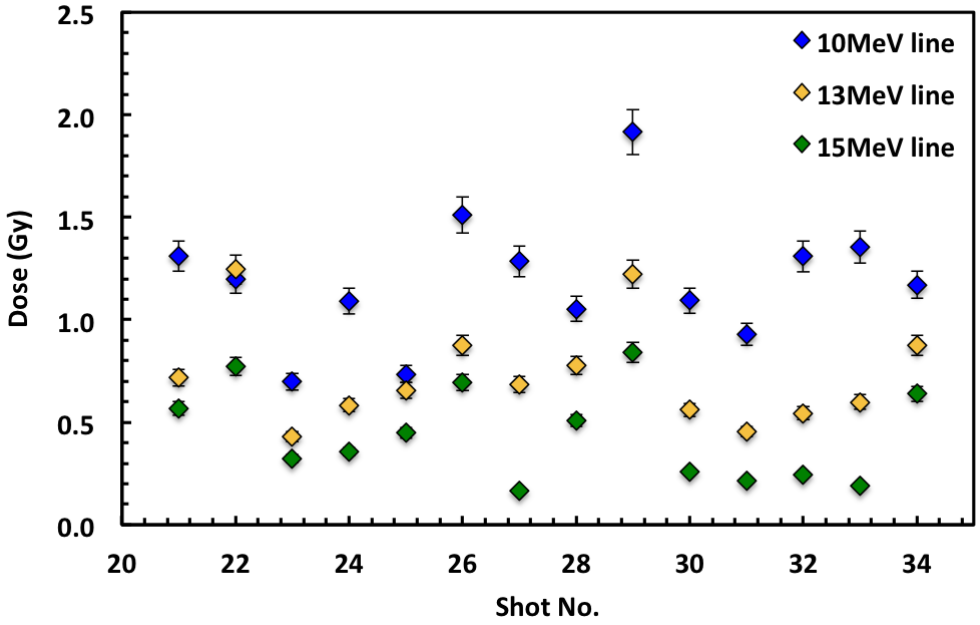


Fig. 6.18 Shot to shot dose variation for all shots calculated from the positions for each energy line indicated from the RCF mask.

| Proton Energy (MeV) | Average Dose (Gy) | Max Dose (Gy) | Min Dose (Gy) |
|---|---|---|---|
| 10 | 1.19 ±0.30 | 1.92 ±0.11 | 0.70 ±0.04 |
| 13 | 0.73 ±0.24 | 1.25 ±0.07 | 0.43 ±0.03 |
| 15 | 0.45 ±0.22 | 0.84 ±0.05 | 0.17 ±0.01 |

Table 6.5 The average dose calculated across all shots for each proton energy line, the maximum dose obtained for each line and the minimum dose obtained for each line.

aim was to obtain dose values around 1 Gy, which was achieved for the 10 MeV and almost achieved for the 13 MeV, but the dose values for the 15 MeV line were much lower at approximately half a Gy. This could also be a contributing factor in the large RFI value obtained at 24 hrs, as an error in a small dose value used for division can dramatically increase the error in the average number of foci per nucleus per Gy and subsequently the RFI.

Figure 6.15, Figure 6.16 and Figure 6.17 show data obtained from comparison X-ray irradiations carried out at the Centre for Cancer Research and Cell Biology at Queen's Uni-

versity Belfast (CCRCB). These irradiations will be described in section 6.5.

## 6.4 TAP 2015 Experiment

Tumour hypoxia represents one of the most important challenges in current radiotherapy. Hadrontherapy employing protons and high LET charged particles has gained momentum worldwide as an effective modality for tumour therapy, including success in inducing cell death in cancer cells under hypoxia as reported by several investigations. Significant advances in laser technologies have led to the prospect of using laser accelerated ions, emitted in ultra-short bursts, as a future cost saving alternative to conventional accelerators. For laser accelerated ions the dose rates which are likely to be achieved may impact on the oxygen dependency of the radiation response. An understanding and characterisation of the radiobiological effects at the ultra-high dose rates delivered by these short ion pulses on human cells under hypoxic conditions is important for the development and further advancement of this technology towards clinical applications.

Previously we have shown the effectiveness of laser accelerated protons and carbon ions (as described in the previous work in sections 6.1.1, 6.2 and 6.3) in the induction of DNA double strand breaks in human cells (AG01522). The Gemini and TARANIS campaigns highlighted limitations in terms of the dose available in a single shot, and a need to relax the energy selection and pulse duration, as both both experiments had similar on target laser energy, which is the main parameter for determining the flux of accelerated protons and consequently the dose. The Vulcan petawatt laser provides up to 100 times more energy on target and a commensurately higher number of protons per shot in a spectrum extending to 40 - 50 MeV, providing ample opportunity to overcome these limitations. Here we aim to demonstrate for the first time laser accelerated proton induced DSBs in human cells under physically induced hypoxia, chemically induced hypoxia and a free radical scavenging environment.

What we want to know is do laser accelerated protons deposited at ultra-high dose rates produce different biological effects under oxic, physically hypoxic, chemically hypoxic and free radical scavenged conditions, as compared to X-rays and conventionally accelerated protons? This was performed using the new compact hypoxia chamber designed specifically for this experiment and tested previously employing the TARANIS laser at Queen's University Belfast. The irradiations were carried out employing the petawatt arm of the Vulcan Nd:glass laser system at the Rutherford Appleton Laboratory, with the cell culture being performed on-site in a dedicated bio-lab, and subsequent analysis carried out in the CCRCB.

### 6.4.1 Experimental Arrangement

The experimental setup incorporates the key requirement of minimizing the distance between the cell sample and the laser target, thus keeping the duration of the selected burst of ions as short as possible. A tilted insertion tube was employed, allowing the cells to be placed approximately 30 cm from the laser interaction point whilst keeping the cell samples outside of the vacuum. The proton beam used for irradiations was generated by focusing the Vulcan beam onto 25 $\mu$m aluminium targets, at intensities above $10^{20}$ Wcm$^{-2}$ and native contrast. The protons will be accelerated by the Target Normal Sheath Accleration (TNSA) mechanism. A 1.0 T was used in conjunction with a collimator and pinhole to disperse and spatially select a proton beam in the order of MeV per mm on the cell plane. The pinhole and collimator were both on axis with the target and the cel sample. The protons will traverse a flange mounted 50 $\mu$m Mylar window before reaching the cell plane, as employed in the Gemini, TARANIS and LULI experiments. A slide rail was mounted inside the insertion tube and an extended handle was used to slide the hypoxia chamber into the tube. The chamber was attached using a special motorised mount attached to the hypoxia chamber and bolted to the slide rail. The chamber was positioned inside the tube with sub mm precision.

In contrast to the previous campaigns employing the Gemini, TARANIS and LULI facilities, the large proton flux available on Vulcan allowed for a much narrower energy selection, reflected in a shorter pulse of protons reaching the cells. Dose rates of $10^9$ - $10^{10}$ $Gys^{-1}$ were achieved in ion pulses of $\sim$ 40 ps and a delivered energy of $\sim$ 600 J [290].

The number of tracks overlapping in space and time is a key parameter for the onset of collective effects, which can bes estimated from the number of protons falling within the section of an ionization track in $\sim$ 1 ps, which is the typical timescale for the completion of pre-thermal physiochemical and physical process in the track such as the formation free radicals. Significant spatio-temporal overlap was obtained for proton energies above 15 MeV even for doses of a fraction of less than 1 Gy, arising from the combination of the short burst duration and the larger sectional area of the ionization tracks obtained for faster protons, which generates more energetic secondary electrons. These conditions were not achievable for energies below 10 MeV. Higher doses to the cell plane were achieved by enlarging the entrance slit to the magnet, which commensurately increases the pulse duration and $\Delta$E, but leaves the dose rate and the track overlap substantially unchanged as all parameters scale linearly. Further control of the dose was achieved by varying the laser intensity on the target to decrease the dose whilst leaving the pulse duration, E and $\Delta$E unchanged [290].

The cell samples had to be shielded from other ionising radiations, as shown by the shielding layout in Figure 6.19. Lead block shielding at the back of the pinhole and around the 50 $\mu$m Mylar window was used to stop the energetic electrons and the bremsstrahlung they produce. The thin 25 $\mu$m Al targets will help reduce the high energy X-rays and gammas from the interaction region. The electrons that did enter the magnet the slit will be deflected out to a beam dump through an aperture on the side of the magnet. Monte Carlo simulations showed that the dose delivered to the cells via protons was at least two orders of magnitude higher than the dose delivered by other radiation sources [290]. The effect of any

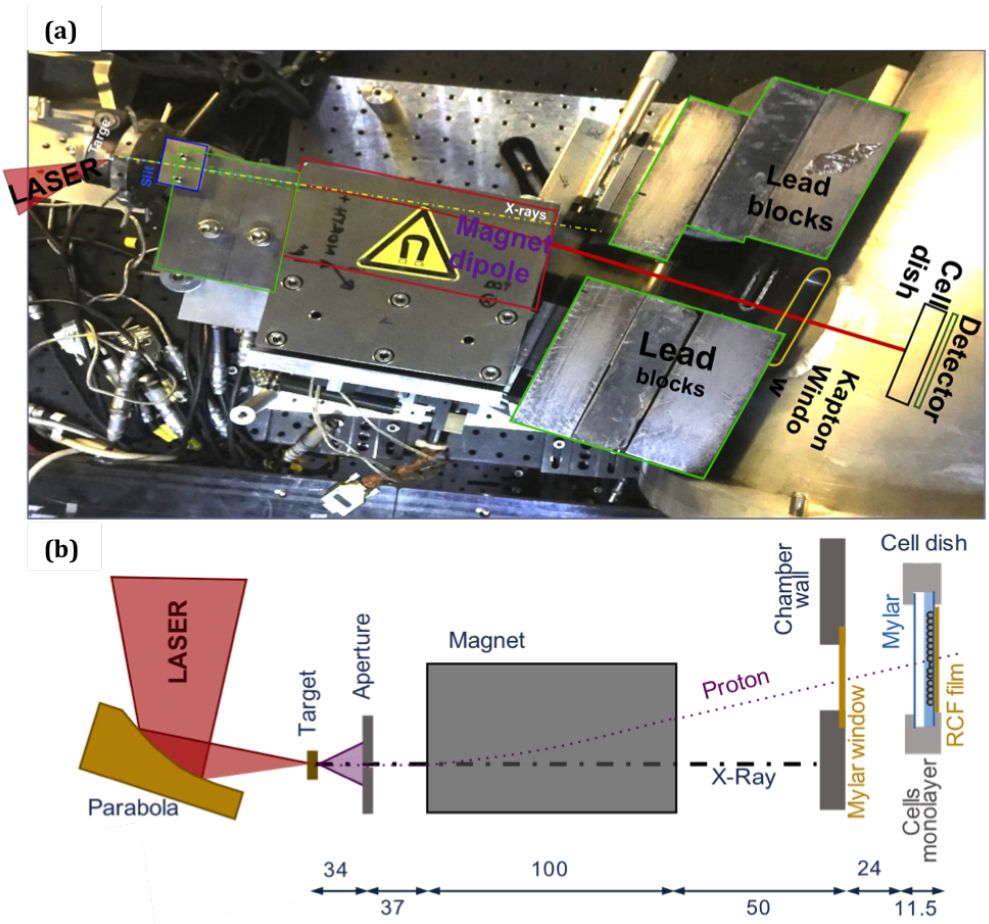


Fig. 6.19 **(a)** The experimental arrangement used for the TAP experiment showing the different elements of the beam delivery system and shielding. **(b)** A schematic of the experimental arrangement.

isotropic background radiation on the cells was monitored by observing the dose delivered to regions of the cell dish not directly exposed to the protons (the regions above and below the irradiated stripe) and served as a control. For these irradiations the 15 MeV portion of the proton spectrum was centred on the cell dish.

The setup used allowed controllable dose, energy spread and pulse duration at proton energies in the range of 5 to 30 MeV. Normal human fibroblast cell line AG01522 was used to allow direct comparisons with both previous proton and X-ray experiments as well as existing data from proton beams from conventional accelerators. The 53BP1 and HIF-1$\alpha$

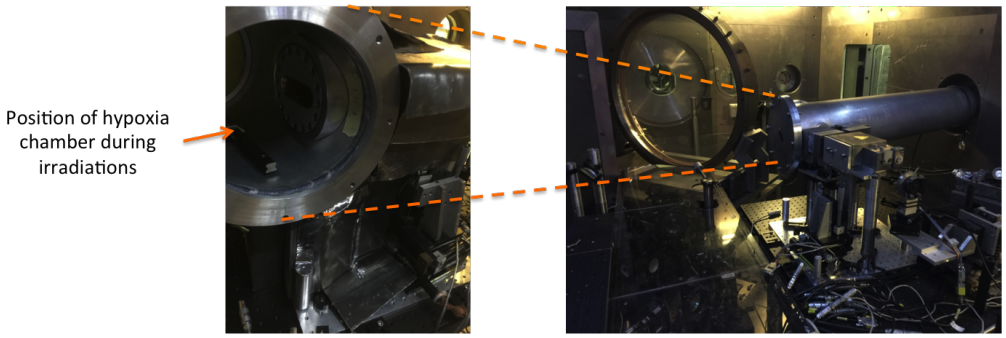


Fig. 6.20 The rail used to position the hypoxia chamber inside the insertion pipe, and the position of the pipe inside the interaction chamber. The front window of the hypoxia chamber is aligned with the flange mounted Kapton window.

immunofluorescence assays allowed the assessment of any deviations form the expected cellular response to proton irradiations. In the presence of an energy dispersed proton dose, this assay allows the collection of information over a range of energies on a single shot basis, and will allow the reconstruction of the temporal dynamics of cell repair.

### 6.4.2 Irradiation Setup

The passage 9 AG01522 normal human fibroblast cells were transported to the Rutherford Appleton Laboratory by commercial air travel in one T75 flask containing 800 ml of reduced serum media (10% FBS 100 $\mu$gml$^{-1}$ penicillin streptomycin in minimum essential medium eagle with alpha modifications). On arrival the reduced serum media was discarded and replaced with full serum media (20% FBS) and after 1 week the T75 was split in a 1:3 ratio to T175 flasks to increase the cell number. Two vials of passage 12 cells from the previous Gemini experiment which had been stored in the liquid nitrogen freezer in the Research Complex at Harwell, were also retrieved, thawed and seeded into 6 T75 flasks as the cell numbers were not increasing as quickly as expected. The cells were stored in a normal tissue culture incubator with a 95% air 5% $CO_2$ atmosphere, 95% humidity and a temperature of 37°C.

For the irradiations the samples were plated on customised stainless steel dishes, a picture of which is shown in Figure 6.22 and a schematic representation in Figure 6.6. These dishes were assembled with a 3 $\mu$m Mylar substrate on which to grow the cells, secured by silicon O-rings and aluminium plates. A second layer of Mylar is added to the front of the dish which is trimmed to just below the level of the irradiation zone, approximately a third of the way up the dish. The dishes were placed inside clean petri dishes and transported to the X-ray machine in the Public Health England building on the Harwell Campus for sterilisation. Six dishes at a time were sterilised inside the petri dishes with the lids on for 45 mins, with 225 KVp X-rays with the copper filter removed from the cabinet operated at 13.3 mA, receiving a dose of more than 1000 Gy. The dishes were then transported back to the bio-lab in a sealed box cleaned with 70% ethanol and placed inside the laminar flow hood until they were required. Every morning the UV light was turned on for approximately 2 hours. The hypoxia chambers were also cleaned inside and out with 70% ethanol before and after every shot to reduce the possibility of contaminating the samples and the sterile environment inside the laminar hood.

The irradiations were carried out under four different conditions: oxic, physical hypoxia, chemical hypoxia and a free radical scavenging environment.

### Oxic Environment

The irradiations of the oxic samples were carried out in a 21% $O_2$ environment. The samples were seeded 24 hours prior to the irradiations on the sterile cell dishes at a density of 450,000 cells per dish. The concentration of the cell suspension was determined using a Sceptre counter as described in section 6.1.2. Just prior to the irradiations the existing media on the cell dish was removed and replaced with 1 ml of fresh full serum media. The customised EBT-3 film was wrapped in 0.9 $\mu$m Mylar and attached to the underside of the cell dish using the mask shown in Figure 6.22. The sample was then secured inside the chamber

using an aluminium bracket and the lid was sealed while the two gas ports were open inside the laminar flow hood, preventing damage to the delicate Saran window of the chamber. The gas ports were then sealed and the chamber was transported to the laser interaction area for irradiation. The samples were irradiated in a vertical position with the front layer of Mylar allowing the 1 ml of media to be caught in the bottom third of the dish during the irradiations. This was below the irradiated portion of the dish. After irradiation the samples were transported back to the bio-lab where the customised EBT-3 film was removed from the back of the dish, and the samples were stored in the normal cell culture incubator until they were required for fixation.

**Hypoxic Environment**

These irradiations were carried out in a 0 to 0.1 % $O_2$ environment induced by physically removing the oxygen from the sample through gassing the hypoxia chamber. The compact hypoxia chamber was specially deigned for laser-driven irradiations. The hypoxic samples were seeded at least 28 hours prior to the time of the irradiation on the sterile dishes at a density of 450,000 cells per dish. The concentration of the cell suspension was calculated using a Sceptre counter. The samples were kept a normal cell culture incubator for 24 hours, then they were removed and 1 ml of full serum media was added to each dish to replace the discarded media. The customised 0.9 $\mu$m Mylar wrapped EBT-3 film was attached to the back of the dish using the RCF mask and the dish was secured inside the chamber. The lid was sealed tightly while the gas ports were open, then the chamber was taken from the laminar flow hood to the normal incubator which had a gas inlet port at the back. Now all six hypoxia chambers were connected in series to the hypoxic gas supply of 95% $N_2$ and 5% $CO_2$. The first chamber in the series (the one closest to the gas supply) was used as the 24 hour sample, with the last chamber being used as the 0.5 hour sample. The final chamber was also connected to a flask of sterile water to monitor the flow rate of the gas supply. A

flow rate of $\sim 2$ bubbles per second was used to gas the chambers to ensure the small amount of media on the cells did not dry out over the 4 hour gassing period. After a minimum of 4 hours gassing, the final chamber in the chain was removed by closing the valves at the same time to seal the chamber, then restoring the gas flow to the other chambers. The chamber was transported to the laser interaction area where it was placed on the sliding rail inside the insertion tube. After irradiation the chamber was taken back to the bio-lab where the sample was removed from the chamber as quickly as possible and placed inside the hypoxic incubator which had a 1% $O_2$ environment, 37°C and 95% humidity. The RCF was removed from the back of the sample for processing.

**Cobalt Chloride Environment**

For these irradiations hypoxia was induced chemically by the addition on the hypoxia mimetic agent $CoCl_2$ prior, during and post irradiation. The cell samples for these irradiations were seeded 48 hours prior to the irradiation time with full serum media and kept in the normal cell culture incubator. A 25 mMol stock $CoCl_2$ solution was prepared by dissolving 0.237 g of $CoCl_2$ in 40 ml of pure distilled water then filtered using a sterile syringe filter. After 24 hours the samples were removed from the incubator and 3 ml of fresh full serum media was added to each sample along with 18 $\mu$l of the stock $CoCl_2$ solution to give a final concentration of 150 $\mu$Mol. The samples were returned to the incubator for a further 24 hours to allow the $CoCl_2$ time to remove all the oxygen from the sample. After 24 hours the samples were removed from the incubator, the customised EBT-3 protected with 0.9 $\mu$m Mylar was attached to the back of the sample with the RCF mask. The dishes were secured in the hypoxia chamber and the old media was replaced with 1 ml of fresh reduced serum media and 6 $\mu$l of the $CoCl_2$ solution. The lid was secured on the hypoxia chamber while the gas ports were open to protect the Saran windows, then the valves were closed and the chamber transported to the interaction area. After the irradiations the chamber was taken

back to the bio-lab and the samples were removed from the chamber in the laminar flow hood, the RCF was removed and fresh full serum media with the correct concentration of $CoCl_2$ solution was added to the samples. The samples were stored in the normal incubator until they were required for fixation.

**Dimethyl Sulfoxide Environment**

For these irradiations dimethyl sulfoxide, or DMSO, was used as a free radical scavenger. The use of this scavenger pre, during an post irradiation would allow the quantification of the effects of direct ionisation caused by the ions and secondary electrons relative to the indirect DNA lesions induced by radical species. These samples were seeded on the sterile 3 $\mu$m Mylar at least 28 hours prior to the irradiation time. Several 50 ml tubes of stock 0.5 % DMSO solution were made by adding 250 $\mu$l of DMSO to 50 ml of reduced serum cell media. After 24 hours of incubation in the normal cell culture incubator the samples were removed and the full cell media on the dishes was removed and replaced with 3 ml of fresh DMSO supplemented incomplete media. The samples were incubated for a further 2 - 4 hours with these media. Just before the irradiations the customised EBT-3 wrapped in 0.9 $\mu$m Mylar was attached to the back of the dish and he excess media was removed to leave 1 ml of supplemented media on the dishes. The samples were then secured in the chamber using the aluminium bracket, the lid was sealed while the ports were open, then the valves were closed while transporting the chamber to reduce contamination. After the samples were irradiated in a vertical position in the laser interaction area, the samples were taken back to the bio-lab and removed from the chamber under the laminar flow hood. The media was removed and 3 ml of fresh DMSO supplemented reduced serum media was added to each sample. They were stored in the normal cell culture incubator until the samples were required for fixing.

For all irradiation environments the samples were placed inside the hypoxia chamber,

secured by an aluminium bracket. The hypoxia chamber was placed inside a dedicated container and transported from the bio-lab to the interaction area where the chamber was transferred to a portable heat box. The chamber was stored here until it was required for the irradiations. The heat box was used to maintain the chamber at 37°C. The chamber was attached to the sliding rail inside the entrance pipe using a specially designed motorised mount which was connected to a power supply. The motor action was tested before pushing the chamber to the end of the rail inside the pipe using an extended arm. The laser area was searched and sealed before requesting a shot from the laser. The hypoxia chamber was kept in the horizontal position until the shot had been approved as this process could take several minutes. Once the shot had been approved the external motor control was use to raise the chamber into a vertical position as shown in Figure 6.21 **(b)**. As soon as the laser had been fired the chamber was returned to the horizontal position to allow the media to recover the cells and prevent any unnecessary stress to the cells or the sample drying out. The chamber was then transported back to the bio-lab where the oxic, $CoCl_2$ and DMSO samples were removed from the chamber and placed in the normal incubator, and the hypoxic samples were either kept inside the hypoxia chamber and re-connected to the gas supply or removed and placed in the hypoxic incubator with a 1% $O_2$ atmosphere until they were required for fixing.

The hypoxia chamber was positioned at the entrance of the Bragg peak of the proton track, which allowed precise dose measurement using customised EBT-3 film attached directly behind the cell monolayer of all the samples. At the cell plane, the 15 MeV portion of the proton spectra was centred on the cell dish.

Sham irradiations of control samples were carried out for each of the four irradiation conditions, with the samples being prepared, mounted and transported in exactly the same way as the irradiated samples, the only difference was the samples were not subject to any irradiation. Control samples were also kept inside both incubators.

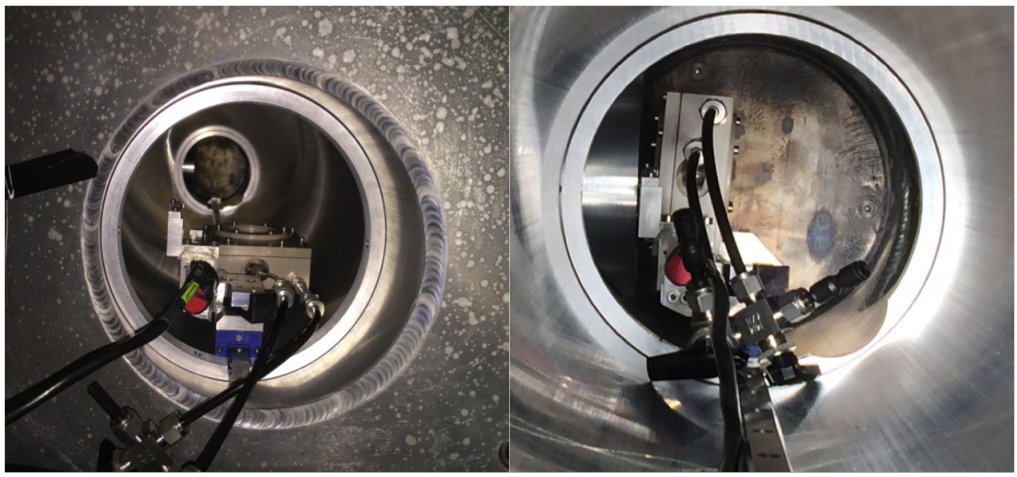

(a) (b)

Fig. 6.21 **(a)** The position of the hypoxia chamber before and after the irradiations and **(b)** during irradiations.

### 6.4.3 Data Analysis and Results

The samples were fixed at five specific times post irradiation: 0.5, 1, 2, 6 and 24 hours post irradiation. The same laser shot cannot be used for multiple time points as once the sample is fixed, the cells have been killed in situ at that specific time. One shot was required per time point, with the aim to complete at least one complete set of all six time points within the same day to try and keep the irradiation and incubator conditions as consistent as possible across the set. This fact can also be used to identify if outlier values within a group of samples fixed at the same time point are just rouge values, or if all samples on that day were affected in the same way. The results presented are averaged over several samples over several days.

The media was removed from the samples they were washed twice with PBS before being fixed with 2 ml of 4% PFA for 10 to 12 minutes at room temperature. 4% PFA was used instead of methanol as this had proved too harsh in testing, affecting the staining of the bio-markers. When fixing the hypoxic, $CoCl_2$ and DMSO samples, this had to carried out very quickly to prevent any change in the conditions present in the cell dish as compared to

the irradiation and incubation conditions. The samples were then washed three times with PBS and stored in the fridge covered in PBS to prevent them drying out before commencing the staining procedure. The samples were stained in batches of 12 to 24 samples at a time. For the immunofluorescence, the cells were stained in their original position; therefore a uniform cell layer covering the region of interest provided a large set of data on the cell response to different irradiation conditions and parameters.

The samples were permeabilised with 0.5% Triton X-100 in PBS for 10 minutes at room temperature, before washing with PBS three times 0.5% Triton X-100 in PBS was used instead of a 1:1 solution of acetone and methanol as this had proved too harsh in testing, affecting the quality of the bio-marker staining. After permeabilisation non-specific binding was blocked with a buffer of 10% goat serum and 0.25% Triton X-100 in PBS for 2 hours at 37°C. After blocking the primary antibodies were added to the samples. The first complete set of each irradiation type were stained for DNA damage and hypoxia induction using 53BP1 at 1:1000 and HIF-1 at 1:500 in blocking buffer respectively. 53BP1 was chosen instead of $\gamma$-H2AX, as the corresponding new HIF1-$\alpha$ antibody for 53BP1 produced much better results in testing for the staining of the hypoxia response. Subsequently only $CoCl_2$ and hypoxic samples were stained with HIF-1$\alpha$ to conserve the antibody. The primary antibody was left on the samples for 2 hours at 37°C to enhance the quality of the staining. From this point the samples were kept in the dark to prevent the data being bleached from the samples. After 2 hours the primary antibody was removed and the samples were washed three times with a 0.1% Triton X-100 in PBS washing buffer and once with PBS. The secondary antibodies of GAR488 (visualised in the green channel of the microscope) at 1:1000 and GAM594 (visualised in the red channel of the microscope) at 1:500 in blocking buffer were used for 53BP1 and HIF-1$\alpha$ respectively. These antibodies were left on the dish for 1 hour at 37°C. The secondary antibodies were then removed and the samples were washed twice with washing buffer and once with PBS.

TAP 15 MeV Protons

| Time Point (hrs) | Oxic Replicates | Hypoxic Replicates | DMSO Replicates | $CoCl_2$ Replicates |
|---|---|---|---|---|
| Control | 3 | 5 | 3 | 3 |
| 0.5 | 4 | 4 | 3 | 3 |
| 1 | 2 | 3 | 3 | 2 |
| 2 | 5 | 4 | 1 | 3 |
| 6 | 3 | 4 | 2 | 3 |
| 24 | 4 | 3 | 2 | 3 |

Table 6.6 Summary of the TAP replicates for each time point and irradiation environment for 15 MeV protons. The values represent the number of samples successfully stained with clearly discernible foci.

At this stage all excess liquid was removed from the dish either by pipette or vigorously shaking the dish. The sample was then turned over and the RCF mask was used to mark the position of the 15 MeV proton line on the back of the Mylar. An L and an H were also marked on the Mylar to indicate the low and high ends of the proton spectra. The mask was created by making a cut wide enough for a 0.7 mm permanent marker in a 125 $\mu$m Mylar substrate at the position of the 15 MeV proton line as indicated by calibration shots and simulations. The slit was 11.5 mm from the straight edge of the centre cut out of the RCF holder and 14 mm from the straight edge of the RCF, which was towards the lower end of the proton spectrum. The mask is shown in Figure 6.22. The marks on the back of the Mylar were sealed with clear nail varnish to protect them from the Superglue which was used to mount the samples on glass slides. Two drops of DAPI were added to the centre of each dish and the dish was gently agitated to evenly distribute the solution. The mask was again used to correctly position the cover-slip over the cells, and the samples were left overnight, or longer if required, to dry. The next day the edges of the cover-slip were sealed with clear nail varnish. If any additional marks were required on the Mylar, they were added and sealed with clear nail varnish. A glass slide was then attached to the back of the sample using a few drops of Superglue, ensuring it was centred on the cover-slip. They were left

to dry, then all the samples were cut from this dishes, the glass slides marked with the shot details and they were stored at -20° both at RAL and the CCRCB where they were scored. Table **??** summarises the number of replicates for each irradiation environment and time point. All time point and environment combinations had two to five replicates with clearly discernible foci after the staining process, apart from the DMSO 2 hr combination which only had one replicate.

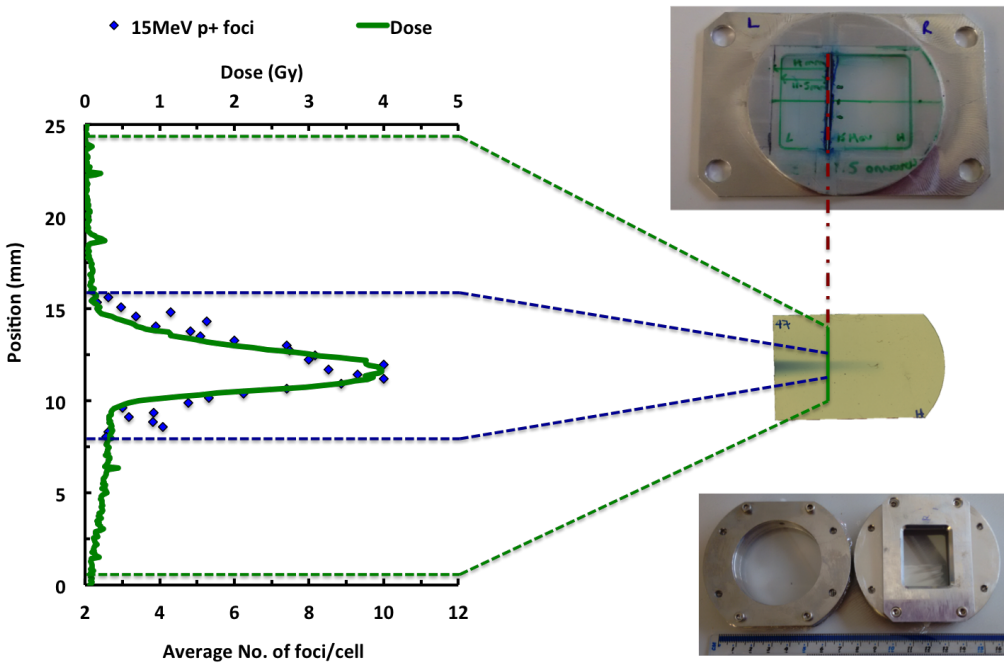


Fig. 6.22 The average number of foci per nucleus across one cell sample aligned with the dose from the customised EBT-3. Both measurements are taken from the position of the 15 MeV proton line as indicated by the RCF mask, which is attached to the cell dish as shown.

After the samples were mounted and transported back to the CCRCB, images of the samples were obtained using the Carl Zeiss Axiovert 200M fluorescence microscope with CCD acquisition capability and Axiovision Rel 4.8 software package. A x 40 magnification objective was used to focus the microscope and take an image every 260 $\mu$m along the 15 MeV line marked on the slide. This provided a full profile of the cell's response with respect to ion energy and dose across the width of the irradiation zone. The foci were

counted using the Cell Counter application in ImageJ. Only cells with clearly discernible foci, not overlapped by other cells, were counted towards the foci number. Example images of the oxic and hypoxic samples are shown in Figure 6.23. The average number of foci per nucleus was calculated for each image and plotted as a function of distance across the sample. This was aligned with the dose across the sample as obtained from the EBT-3 film placed behind the cell monolayer, as shown in Figure 6.22.

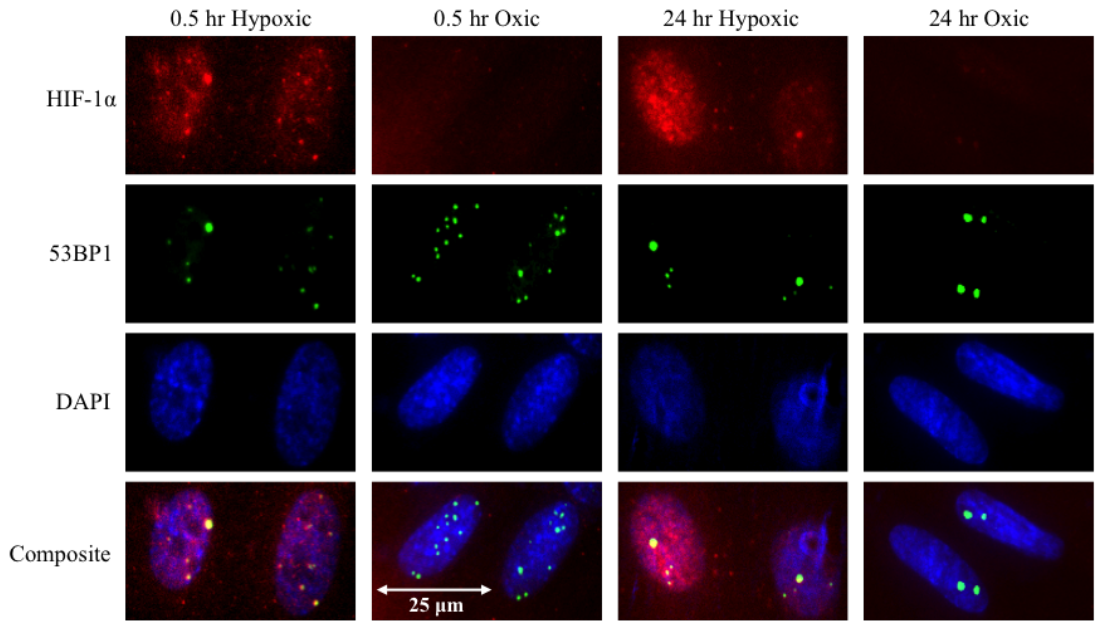


Fig. 6.23 AG01522 human skin fibroblast cells were irradiated with 15 MeV laser accelerated protons employing the petawatt arm of the Vulcan laser facility. The samples were kept inside the hypoxia chambers after the irradiations to maintain the hypoxic environment. The samples were fixed at 0.5 and 24 hrs post irradiation, then stained for HIF-1$\alpha$ to show the induction of hypoxia, 53BP1 to highlight DNA DSB damage and DAPI for detecting the cell nuclei.

Reference dosimetry was performed at a selected position in the spectrum, using strips of customised EBT-3 placed horizontally behind the cell dish inside the hypoxia chamber with no cells present. This absolute reference, together with the transmitted dose and ion transport simulations allowed the dose deposition in the cell to be reconstructed [288]. The cells were located in the entrance of the Bragg peak of the proton spectra ion, to allow

a reasonably accurate measurement of the dose profile from the customised EBT-3 film placed directly behind the cells. The EBT-3 films were scanned with an Epson Perfection V75 pro calibrated flat-bed transmission scanner with resolution of 300 dpi and RGB 48 bit. The dose was obtained from the ImageJ Macro discussed in Section 3.3.3 using the red channel as it is most sensitive at the energies and doses obtained in this experiment. An example of the dose map produced from this Macro is shown in Figure 6.24.

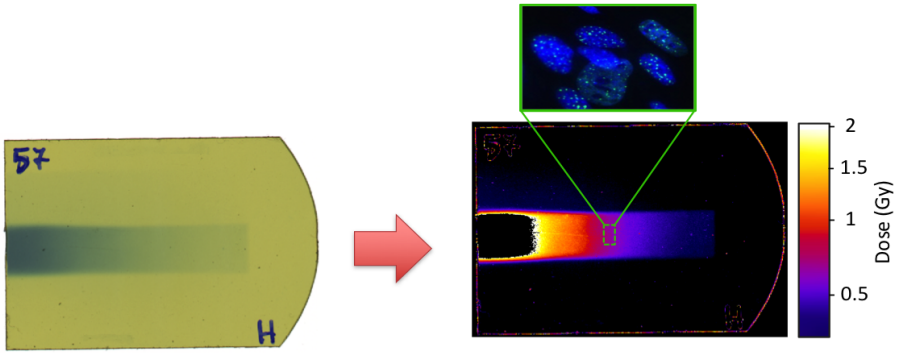


Fig. 6.24 The raw scanned image of the RCF which is converted to a dose map using an ImageJ Macro. The position of the 15 MeV proton line and an example image of the foci is shown.

The average number of foci per nucleus and the dose for each shot were used to calculate the average number of foci per cell per Gy, as shown by the left had plot of Figures 6.25, 6.26, 6.27 and 6.28 for the oxic, physical hypoxia, chemical hypoxia and free radical scavenging environment respectively. The right had plot of each of these Figures shows the percent foci remaining at each time point compared to the average number of foci per nucleus per Gy present at 0.5 hours post irradiation. The values are averaged over several shots, two to five in all cases apart from the value for the 2 hr DMSO 15 MeV proton and the hypoxic 6 hr and 24 hr X-ray time points which are obtained from only one shot each. All the averaged values have the relevant control value (averaged over two to five samples) of $1.85 \pm 0.11$, $1.84 \pm 0.12$, $1.89 \pm 0.18$ and $1.81 \pm 0.09$ for the oxic, hypoxic, DMSO and

$CoCl_2$ 15 MeV proton values, and 1.81 ± 0.11, 2.16 ± 0.08, 1.96 ± 0.05 and 2.72 ± 0.04 for the oxic, hypoxic, DMSO and $CoCl_2$ 225 kVp X-ray values respectively.

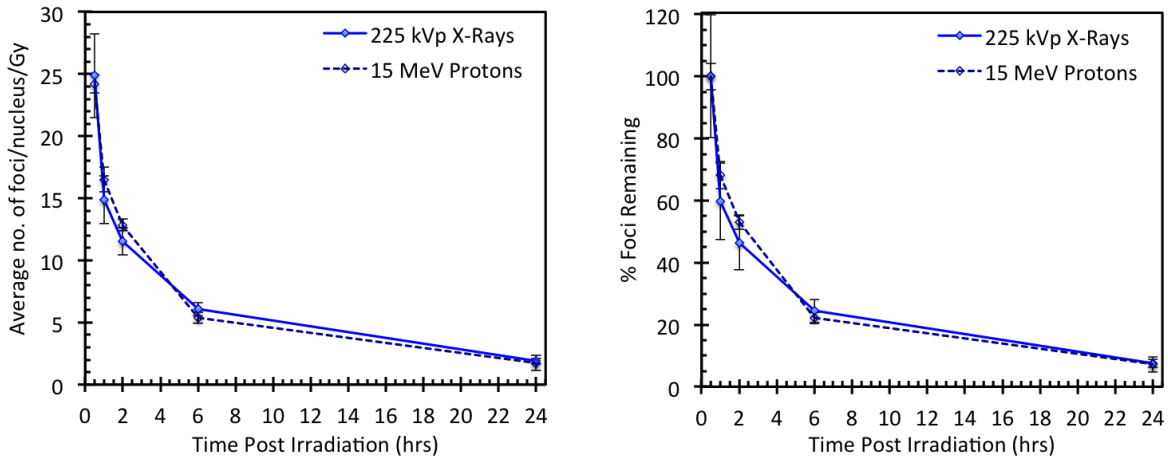


Fig. 6.25 Kinetics of DNA DSB damage and repair visualised through 53BP1 immunostaining for oxic irradiation conditions, displayed as the average number of foci per nucleus per Gy with respect to time post irradiation.

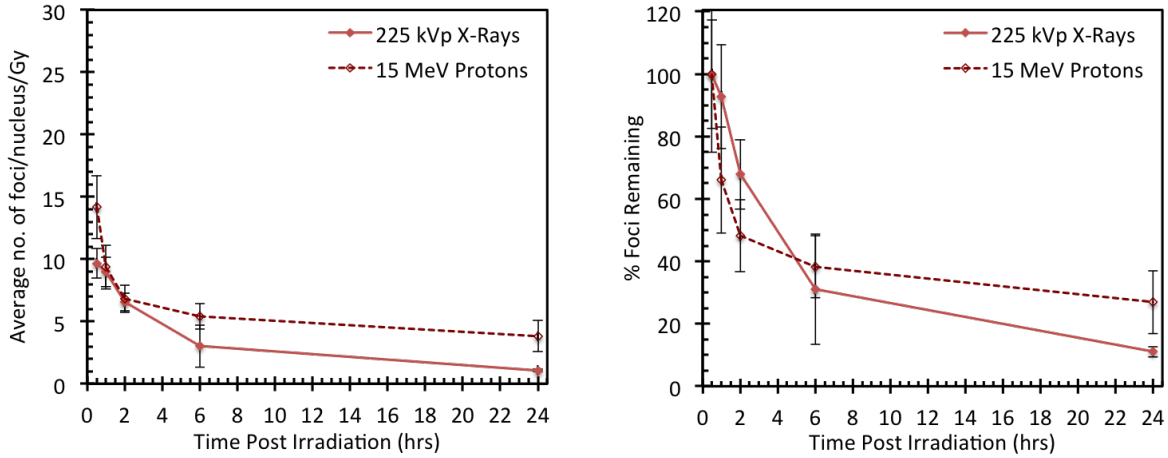


Fig. 6.26 Kinetics of DNA DSB damage and repair visualised through 53BP1 immunostaining for physically hypoxic irradiation conditions, displayed as the average number of foci per nucleus per Gy with respect to time post irradiation.

Figures 6.25, 6.26, 6.27 and 6.28 all show promising features in the form of a peak in the number of DSBs followed by a period of recovery. The 53BP1 foci are dephosphorylated over time with kinetics which parallel the rate at which the DSBs are repaired. The kinetics

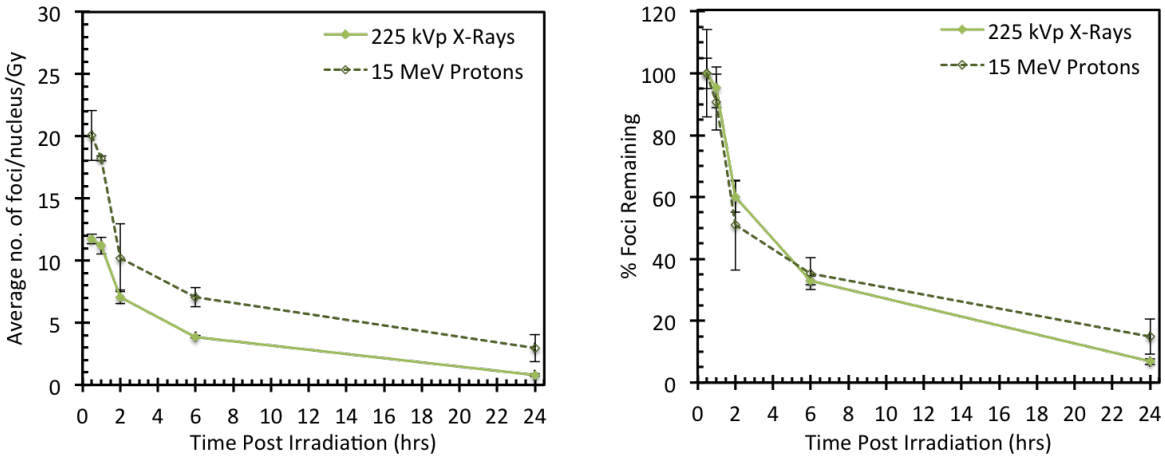


Fig. 6.27 Kinetics of DNA DSB damage and repair visualised through 53BP1 immunostaining for chemically hypoxic irradiation conditions, displayed as the average number of foci per nucleus per Gy with respect to time post irradiation.

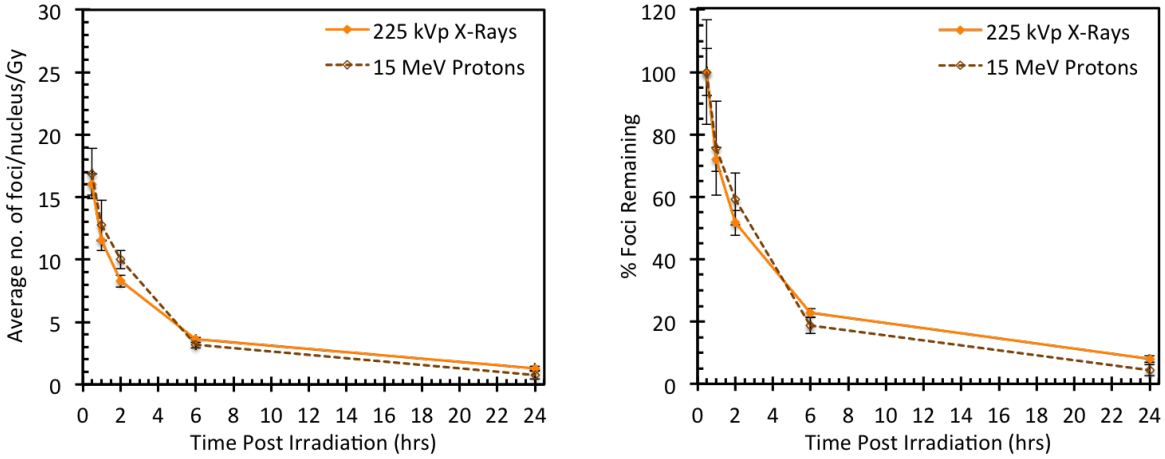


Fig. 6.28 Kinetics of DNA DSB damage and repair visualised through 53BP1 immunostaining for free radical scavenging irradiation conditions, displayed as the average number of foci per nucleus per Gy with respect to time post irradiation.

which are measured as a mean number of foci per nucleus per Gy over time ( shown as the average number of foci per cell per Gy on the left had plot of Figures 6.25, 6.26, 6.27 and 6.28 and as the percent foci remaining compared to 0.5 hours post irradiation on the right hand plot) represent the fast and slow components of the DNA repair. The fast component is apparent from the measured time points of 0.5 to 2 hours post irradiation with the slow

component extending from 2 to 24 hours post irradiation. The fast component of the kinetics represent the repair of the simple DSBs by non-homologous end-joining (NHEJ), and the slow component represents the repair of complex DSBs by homologous recombination (HR). The error bars on the data are produced by combining the error in the manual foci count itself, the dose obtained from the EBT-3 film, the subtracted background count and the subtracted background dose. The error in the average number of foci per nucleus per Gy $\delta F_G$ is given as:

$$\delta F_G = \sqrt{\left(\frac{\sqrt{\delta F^2 + \delta F_C^2}}{F - F_C}\right)^2 + \left(\frac{\sqrt{\delta D^2 + \delta D_B^2}}{D - D_B}\right)^2} \times F_G \tag{6.2}$$

where $F$ is the average number of foci per nucleus $\pm\ \delta F$, $F_C$ is the control average number of foci per nucleus $\pm\ \delta F_C$, $D$ is the dose $\pm\ \delta D$ and $D_B$ is the background dose $\pm\ \delta D_B$. An analogous expression is obtained for the error $\delta F_{\%}$ in the percent foci remaining:

$$\delta F_{\%} = \sqrt{\left(\frac{\delta F_{GT}}{F_{GT}}\right)^2 + \left(\frac{\delta F_{G0.5}}{F_{G0.5}}\right)^2} \times F_{\%} \tag{6.3}$$

where $F_{GT} \pm \delta F_{GT}$ is the average number of foci per nucleus per Gy at the time point of interest and $F_{G0.5} \pm \delta F_{G0.5}$ is the average number of foci per cell per Gy at 0.5 hours post irradiation.

The relative foci induction, RFI, was investigated for each of the irradiation conditions across all the time points. The RFI is the ratio of the average number of foci induced per Gy for the 15 MeV protons compared to the average number of foci induced per Gy by 225 kVp X-rays. This is an analogous measure to the relative biological effectiveness (RBE), which is more commonly used for cell survival studies. The RFI values for each irradiation condition were calculated for each time point and plotted along with the generally accepted RBE value of 1.1 for proton irradiations in Figure 6.29, and are summarised in Table 6.7.

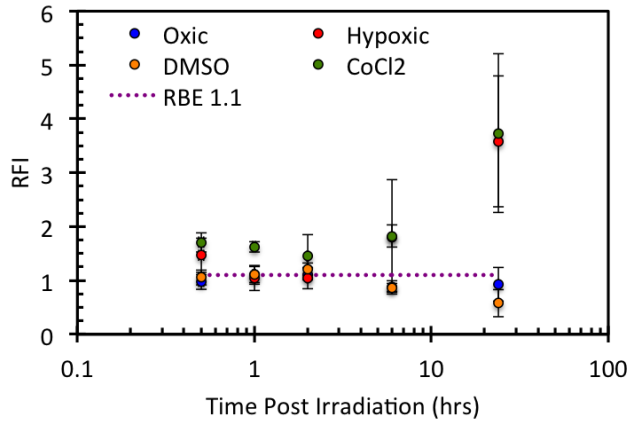


Fig. 6.29 The relative foci induction for each of the irradiation conditions across all time points.

The oxygen enhancement ratio, OER, or perhaps more correctly the hypoxia reduction factor, HRF, was calculated for the physically and chemically induced hypoxic samples compared to the oxic samples for both the 15 MeV protons and the 225 kVp X-rays. The OER is the ratio of the radiation dose required for the same biological effect in the absence versus the presence of oxygen, and the HRF is the same ratio in reduced oxygen conditions compared to oxic conditions. As the hypoxic samples were kept in a hypoxic incubator at 1% $O_2$ the term HFR applies here. The values are summarised in Table 6.7.

| | 15 MeV protons | | 225 kVp X-rays |
|---|---|---|---|
| | RFI | HRF | HRF |
| Oxic | 1.00 ±0.09 | - | - |
| Hypoxic | 1.78 ±0.94 | 1.36 ±0.55 | 1.95 ±0.33 |
| $CoCl_2$ | 2.07 ±0.84 | 0.94 ±0.26 | 1.78 ±0.31 |
| DMSO | 0.96 ±0.22 | - | - |

Table 6.7 Summarised RFI and HRF values for the four different irradiation conditions for 15 MeV protons and 225 kVp X-rays.

For the oxic samples the 15 MeV protons and the 225 kVp X-rays exhibit almost identical foci kinetics. The protons induced marginally fewer foci at 0.5 and 6 hours post irradia-

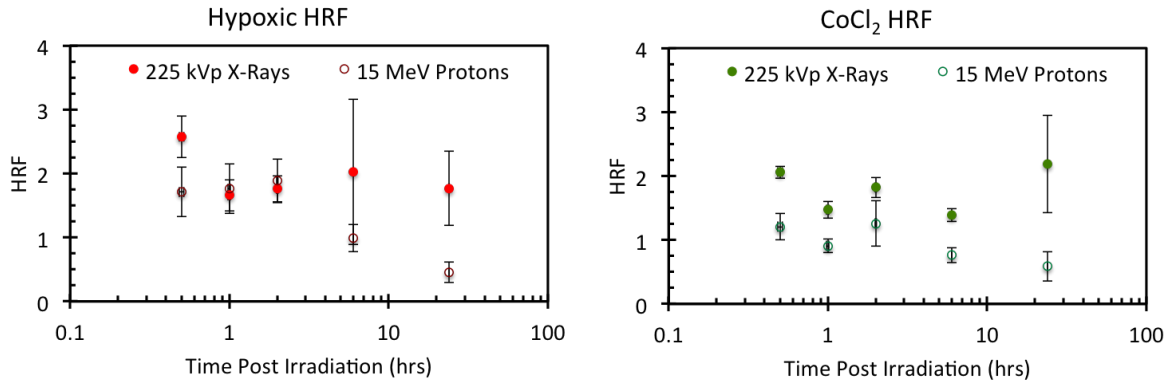


Fig. 6.30 HRF calculated for both 15 MeV protons and 225 kVp X-rays for the physically hypoxic samples and the chemically hypoxic ($CoCl_2$) samples for all time points. The average values were $1.36 \pm 0.55$ and $1.95 \pm 0.33$ for the proton and X-ray hypoxic samples respectively, and $0.94 \pm 0.26$ and $1.78 \pm 0.31$ for the proton and X-ray $CoCl_2$ samples respectively.

tion, but marginally more at 1 and 2 hours post irradiation (Figure 6.25 left hand side). The protons have a marginally slower response in the fast component of repair than the X-rays (Figure 6.25 right hand side). The RFI was calculated as $1.00 \pm 0.09$, with all time points being approximately the same value as shown in Figure 6.29, meaning that the cells have approximately the same response to the proton and X-ray irradiations.

For the hypoxic samples, more initial damage is inflicted on the cells shown by a higher number of foci at the 0.5 hour time point compared to X-rays, at 1 and 2 hours the foci number is approximately equal for both radiation types, and at 6 and 24 hours there are more residual foci for the protons as shown by Figure 6.26. The rate of repair is initially much faster for the damage inflicted by the protons, but after 2 hours the rate slows down significantly as shown by Figure 6.26. The RFI was calculated as $1.78 \pm 0.94$. The value was close to 1.1 for the 0.5 to 6 hour time points, then the value shoots up to approximately 3.5 at the 24 hour time point (see Figure 6.29). The HRF for the protons was $1.36 \pm 0.55$, and it was $1.95 \pm 0.33$ for the X-rays. The HRF was significantly lower for protons at 24 hours post irradiation as shown in Figure 6.30. This shows that irradiations performed with

X-rays are more sensitive to changes in the oxygen concentration. In the hypoxic conditions the protons were more lethal than the X-rays to the cell samples.

Analogous to the hypoxic samples, more damage was inflicted on the cells by the protons for the $CoCl_2$ samples at all time points as shown in Figure 6.27. There also many more residual foci at 24 hours post irradiation for the proton irradiated samples. Initially the rate of repair of this damage is faster for the proton irradiated samples, but after two hours the rate slows down. The RFI was calculated to be $2.07 \pm 0.84$, with the four initial time points with values around 1.5, but an increase to $\sim 3.5$ at 24 hours post irradiation (see Figure 6.29). The HRF was calculated as $0.94 \pm 0.26$ for the proton irradiations and $1.78 \pm 0.31$ fr the X-ray irradiations. This value decreased with time post irradiation for the proton irradiated samples as shown in Figure 6.30. Again this shows the samples irradiated by the protons are less affected by the presence or reduction of oxygen in the environment. Overall the 15 MeV protons appeared again to be more lethal than the X-rays.

The results for the DMSO irradiations were analogous to the oxic irradiations in that the protons and X-rays produced approximately the same response. there were marginally more foci at 0.5, 1 and 2 hours post irradiation in the proton irradiated samples, but marginally more foci in the X-ray irradiated samples at 6 and 24 hours post irradiation (Figure 6.28). Initially the repair of the damage was faster for the proton induced damage as shown in Figure 6.28. The RFI was calculated to be $0.96 \pm 0.22$, with the values being approximately 1.1 for all time points apart from 24 hours post irradiation where the value drops to $\sim 0.5$ (Figure 6.30). Again the samples have approximately the same response for the X-ray and proton irradiations.

The shot to shot dose variation at the position of the 15 MeV line is shown in Figure 6.31 along with the target dose of 1 Gy. The average dose across all shots for 15 MeV protons was $1.27 \pm 0.58$ Gy. The experimental aim was to have a reproducible dose of 1 Gy, which was true on average within error, however there was a large spread of values as indicated

by Figure 6.31, with a maximum and minimum value of 2.35 ± 0.01 and 0.16 ± 0.04 as recorded in Table 6.8.

| 15 MeV protons | |
|---|---|
| Average Dose (Gy) | 1.27 ±0.58 |
| Max Dose (Gy) | 2.35 ±0.01 |
| Min Dose (Gy) | 0.16 ±0.04 |

Table 6.8 The average dose calculated across all shots, the maximum dose obtained and the minimum dose obtained for the 15 MeV proton line.

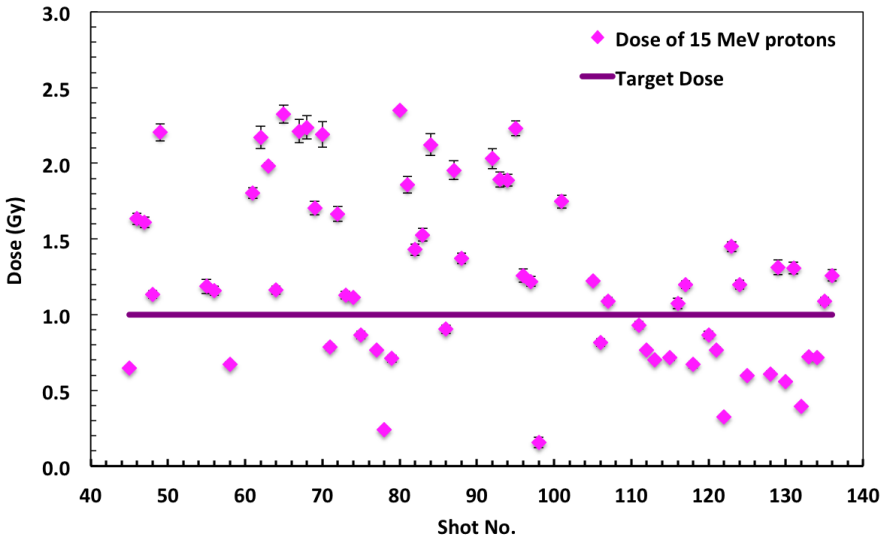


Fig. 6.31 Shot to shot dose variation across all shots for the 15 MeV proton energy line.

The data used for calculating the RFI and HRF for X-rays was obtained in a set of comparative X-ray experiments which are described in the next Section.

## 6.5 Comparative X-ray Experiments

Comparison experiments were carried out employing the 225 kVp XRAD225 X-ray cabinet located in the Centre for Cancer Research and Cell Biology, Queen's University Belfast.

X-rays are the gold standard for current cancer therapy, thus any future treatment modality must be compared to the already existing treatments available. Irradiations in the four different environments of hypoxic, oxic, $CoCl_2$ and DMSO using the same dishes and hypoxia chambers as employed by the previous three experiments were carried out. The results obtained from these irradiations were used to calculate the RFI for the proton energies used in each of the previous experiments, and the results were also used for visual comparisons of the foci induced and the average number of foci per nucleus per Gy.

Sterilisation of the cell dishes was performed using the X-ray cabinets located in both the CCRCB and the Public Health England Building on the Harwell Campus. Dosimetry experiments using normal and customised EBT-3 were also carried out at the CCRCB to create a calibration for updating the ImageJ Macro used for obtaining the dose from the scanned films.

### 6.5.1 Experimental Arrangement

For cell dish sterilisations, the fully assembled cell dishes were placed in petri dishes cleaned with 70% ethanol before being transported to the X-ray machine in a sealed container. The lids of the petri dishes were removed and the dishes were placed on the shelf in the X-ray cabinet at a distance of 50 cm from the source. The X-ray machine was operated at 13.3 mA and 225 kVp for 30 mins. The 2 mm copper filter in front of the source was removed to allow as high a dose as possible to reach the dishes. Once the 30 mins were up, the lids of the petri dishes were replaced (using sterilised gloved hands) and the dishes were placed in the same sealed container as before once it had been cleaned with 70% ethanol. The dishes were then transported back to the laminar flow hood and kept there under UV light until they were required for seeding cells. When at the Rutherford Appleton Laboratory, a similar X-ray cabinet in the Public Health England (PHE) building on the Harwell Campus was used for sterilisation. Again, the copper filter was removed and the dishes were sterilised for 45

mins with 225 kVp X-rays. A longer sterilisation time was used as the dishes were stacked inside the PHE cabinet as a larger number of dishes were required at a faster turn around rate for the TAP experiment. A dosimeter on the PHE cabinet confirmed the dishes were receiving a dose of > 1000 Gy, which was more than adequate for sterilisation.

### 6.5.2 Irradiation Setup

For the dosimetry experiments, normal and customised EBT-3 films were exposed to known doses of X-rays (0, 0.5, 1, 2, 4 and 8 Gy) by themselves, attached to the cell dishes using the RCF mask from the TAP experiment and attached to the dish with the mask and placed inside the hypoxia chamber, to ascertain if there was any increase or decrease in the dose received by the sample owing to scatter from the dish or chamber. The films were scanned with an Epson Perfection V75 Pro calibrated flat-bed transmission scanner with RGB 48 bit and 300 dpi settings.

Cellular irradiations were only carried out using the CCRCB X-ray cabinet. The X-ray cabinet was fitted with the 2 mm Copper filter to cut off the low energy part of the X-ray spectrum and the delivery was controlled with an ISOVOLT Titan E. The cabinet was operated at 13.3 mA and 225 kVp. The samples were irradiated at a source to sample distance of 50 cm for 1 minute and 42 seconds at a dose rate of 0.591 Gy/min, equating to a dose of 1 Gy. For these irradiations the medium was not removed from the dishes as the samples were being irradiated in a horizontal position and the X-rays would not be affected by the small layer of cell culture medium on the cells.

#### Oxic Environment

One set of samples were irradiated inside the hypoxia chambers, but with no gassing or chemical additions before, during or post irradiations. These samples were plated on 3 $\mu$m Mylar on the specially designed cell dishes 24 hours prior to the irradiations. A second

half layer of Mylar was added to the second side of the dish, as for the TAP experiment. Before the samples were placed inside the chamber, the cell culture media was removed and replaced with 1 ml of fresh complete un-supplemented media. The samples were secured inside the chamber with the aluminium bracket, and the gas ports were left open to allow the air to circulate. After the irradiations the samples were removed from the chambers, the second half layer of Mylar was removed and the samples were placed in the normal cell culture incubator until they were required for fixation. The 0.5, 1 and 2 hour samples were left with the media they were irradiated in, but the media was topped up with fresh medium on the 6 and 24 hour samples before they were placed in the incubator.

**Hypoxic Environment**

The hypoxic samples were irradiated inside the hypoxia chambers after being gassed for 4 hours with a hypoxic gas mixture of 5% $CO_2$ and 95% $N_2$. The cells were plated on the 3 $\mu$m Mylar sterile dishes at least 28 hours prior to irradiation. This allowed the cells to attach and grow for 24 hours before commencing the gassing. The cell dishes were placed inside the hypoxia chamber which was tightly sealed, then connected to the gas supply for 4 hours. This time of 4 hours is widely accepted as being sufficient to remove all the oxygen from the cell samples. The oxygen concentration of the gas within the chamber was monitored using a Rapidox 1100Z meter, however the concentration inside the cells and cell media could not be monitored during the gassing or irradiations. The chambers were, however, verified for inducing cellular hypoxia as described in section 6.5.3. After the 4 hours of gassing the chamber valves were sealed and the chamber was placed in the X-ray cabinet. After the irradiation the chamber was placed inside a normal incubator. The shorter time point samples of 0.5 to 2 hours were not reconnected to the gas supply as the chambers could maintain pathological for up to 5.5 hours on average, however the 6 and 24 hour samples were reconnected to the supply to maintain pathological hypoxia. The longer time point

samples were monitored to ensure the samples did not dry out from the gas flow. The gas was passed through a flask of sterile water before reaching the samples to try and reduce the drying effect, however if the medium level appeared to be becoming too low, the gas was then turned off.

The samples were kept in a hypoxic environment as different biological effects would occur as soon as the samples started to reoxygenate.

### Cobalt Chloride Environment

For the $CoCl_2$ irradiations, the samples were seeded on the 3 $\mu$m Mylar dishes 48 hours prior to the irradiations. A stock 25 mMol $CoCl_2$ solution was created by dissolving 0.237 g of $CoCl_2$ in 40 ml of pure distilled water then filtered using a sterile syringe filter. After 24 hours, the media was removed from the samples and 3 ml of fresh complete medium was added to each dish, then 18 $\mu$l of the stock $CoCl_2$ was added to the dishes for a final concentration of 150 $\mu$Mol. The samples were incubated for a further 24 hours with this media. Just before irradiation, the complete $CoCl_2$ medium was removed from the samples and 1 ml of fresh incomplete medium (10% FBS, 100 $\mu$gml$^{-1}$ penicillin/streptomycin) was added to the dish along with 6 $\mu$l of the stock $CoCl_2$ solution. After irradiation the medium was changed for fresh $CoCl_2$ supplemented medium.

The samples were irradiated inside the hypoxia chambers to provide directly comparable irradiation conditions to those of the oxic, hypoxic and DMSO samples, but once the irradiations were complete, the samples were removed from the chambers and stored in the normal tissue culture incubator until they were required for fixing.

### Dimethyl Sulfoxide Environment

For the DMSO irradiations, the samples were seeded on the 3 $\mu$m Mylar dishes at least 28 hours prior to the irradiations. Several 50 ml tubes of stock 0.5% DMSO solution were

created by adding 250 $\mu$l of DMSO to 50 ml of incomplete cell culture medium (10% FBS, 100 $\mu$gml$^{-1}$ penicillin/streptomycin). After 24 hours, the normal cell media was removed from the samples and 3 ml of fresh DMSO supplemented incomplete medium was added to each sample. From this point DMSO supplemented media had to be used on the samples to maintain the radical scavenging environment, otherwise scavengers could be re-introduced into the cell media and affect the biological response. The samples were incubated for a further 2-4 hours with this media. Just before irradiation, the excess medium was removed from the samples leaving 1 ml of the DMSO supplemented medium on the cell sample. After irradiation the medium was changed for 3 ml of fresh DMSO supplemented medium on all samples.

The samples were irradiated inside the hypoxia chambers to provide directly comparable irradiation conditions to those of the oxic, hypoxic and $CoCl_2$ samples, but once the irradiations were complete, the samples were removed from the chambers and stored in the normal tissue culture incubator until they were required for fixing. Sham irradiations of control samples were carried out for each of the four irradiation conditions, with the samples being prepared, mounted and transported in exactly the same way as the irradiated samples, only they were not subject to any irradiation. Control samples were also kept inside the incubator.

### 6.5.3 Data Analysis and Results

The samples were stained and mounted as described in Section 5.3.1. The hypoxic and $CoCl_2$ samples were stained for both the hypoxia induction marker HIF-1$\alpha$ and the DNA DSB marker 53BP1. The oxic and DMSO samples were stained only for the DNA DSB marker 53BP1. The 53BP1 assay was chosen for the superior staining it had produced in conjunction with HIF-1$\alpha$, as compared to HIF-1$\alpha$ and $\gamma$-H2AX. It was also the assay used for the proton irradiations carried out on employing LULI and TAP, so would provide the

CCRCB 225 kVp X-rays

| Time Point (hrs) | Oxic Replicates | Hypoxic Replicates | DMSO Replicates | $CoCl_2$ Replicates |
|---|---|---|---|---|
| Control | 3 | 2 | 2 | 2 |
| 0.5 | 2 | 2 | 2 | 2 |
| 1 | 2 | 2 | 2 | 2 |
| 2 | 2 | 2 | 2 | 2 |
| 6 | 2 | 1 | 2 | 2 |
| 24 | 2 | 1 | 2 | 2 |

Table 6.9 Summary of the CCRCB replicates for each time point and irradiation environment for 225 kVp X-rays. The values represent the number of samples successfully stained with clearly discernible foci.

best comparison. The fluorescence microscopy was performed on the Carl Zeiss Axiovert 200M fluorescence microscope with CCD acquisition capabilities and Axiovision Rel. 4.6 software in the CCRCB. A x 63 magnification oil immersion objective was used to quantify the 53BP1 foci induced by the X-rays and to visualise the hypoxia induction through the nuclear staining of HIF-1$\alpha$. As for the other experimental slides, a minimum of 50 and a maximum of 150 cells were counted for each time point. As an approximately uniform dose of 1 Gy was received by the entire cell monolayer, images could be taken and cells counted at any position of the cell dish for each of the time points, unlike the proton irradiations where the images had to be taken along a specific line chosen at the position of the 15 MeV protons. The position of this line could not be altered to accommodate dose fluctuations between shots, as the proton energy would no longer be consistent for all the shots to provide a proper comparison. Table 6.9 summarises the number of replicates for each irradiation environment and time point. All time point and environment combinations had at least two replicates with clearly discernible foci after the staining process, apart from the hypoxic 6 hr and 24 hr combinations which only had one replicate each.

Owing to the nature of X-ray induced foci, it was possible to count the foci directly through the eyepiece of the microscope, with the images being taken as a reference. How-

ever the same counting constraints relating to overlapping cells, cells with high background and cells in the S phase of the cell cycle were implemented.

The results of the X-ray experiments have been presented on the graphs in the previous sections, and were used to calculate the RFI for the different energies of the protons used in the previous sections.

The results of the dosimetry experiments were used to modify the ImageJ Macro to include calibrations for X-rays. The pixel values of the images were obtained from ImageJ for each of the RGB channels and plotted against dose in Excel. A six order polynomial expression was fitted to the data then transferred to the ImageJ Macro. The Macro was then used to determine the dose received by each of the films irradiated in each channel, with particular interest in the red channel as it is most sensitive to low doses. The results were used to test if there was any reduction or increase in the dose received inside the hypoxia chamber compared to outside the chamber. The results showed that there was no reduction or increase in the dose received by the sample, and were described in detail in section 6.5.2.

## 6.6 Discussion of Results

We report for the first time measurement of the DNA damage with laser accelerated pulsed protons at ultra-high dose rates ($10^9$ - $10^{10}$ $Gys^{-1}$) under physically and chemically hypoxic and free radical scavenging conditions employing the TARANIS, LULI and Vulcan lasers at QUB, Laser Lab Europe and the CLF respectively. The TARANIS experiment served as a proof of principle experiment to establish the cell handling techniques required for the LULI and TAP experiments as well as benchmarking the new compact hypoxia chamber designed at QUB. The results from the laser irradiations have been compared to X-ray results and show some promising features, and have also been compared to foci kinetic results from conventionally accelerated protons.

Slight adaptations and improvements were made to the immunofluorescence protocol

during the course of the investigations. The adaptations arose form poor staining results such as very weak staining of HIF-1$\alpha$ and $\gamma$-H2AX in the TARANIS experiment, to pan staining of the sample arising from too harsh a fixative and permeabiliastion buffer in some LULI samples. The protocol was then adapted to use the 53BP1 antibody and the corresponding HIF-1$\alpha$ antibody as these had produced better staining results in testing, with the primary antibodies being left on the sample for 2 hours rather than one to increase the uptake of the antibody and strengthen the staining. A 4% solution of PFA was used instead of a 1:1 solution of methanol and acetone to fix the samples and a permeabilisation buffer of 0.5% Triton X-100 in PBS instead of methanol was use to help reduce the pan staining that occurred in some samples. The finalised version of this protocol which was used on the TAP experiment is provided in Appendix B.

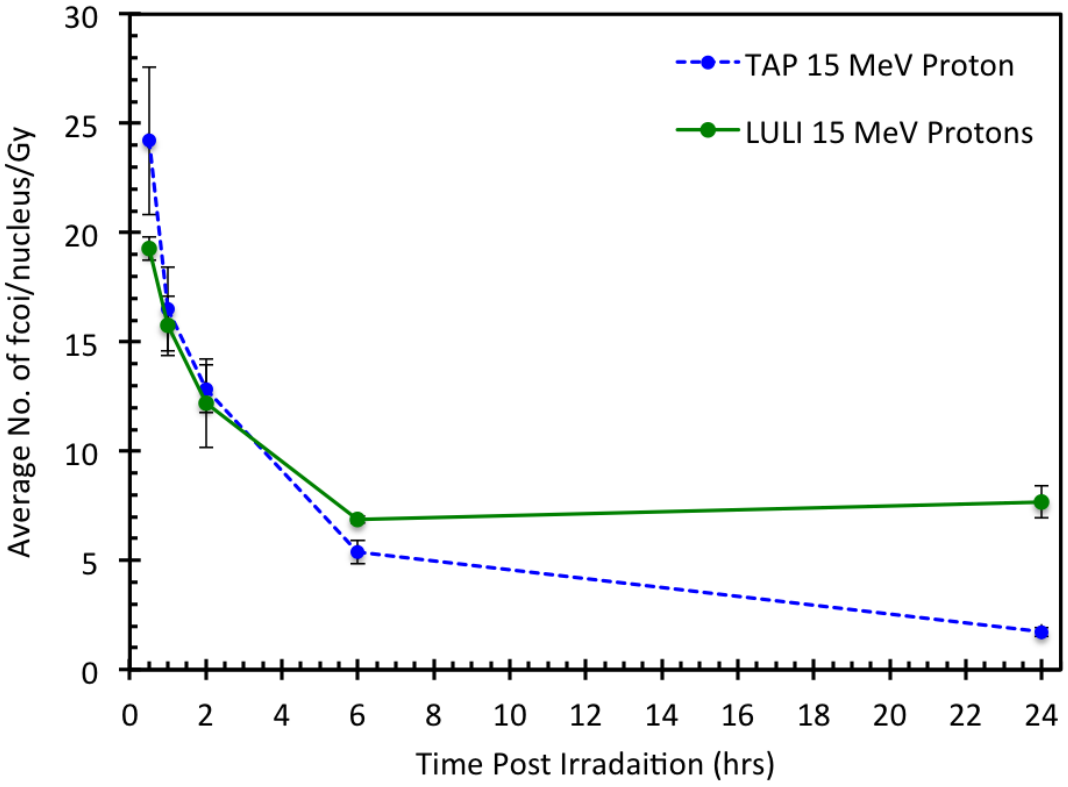


Fig. 6.32 Comparison of the 15 MeV proton DNA DSB kinetic profiles for the TAP and LULI experiments.

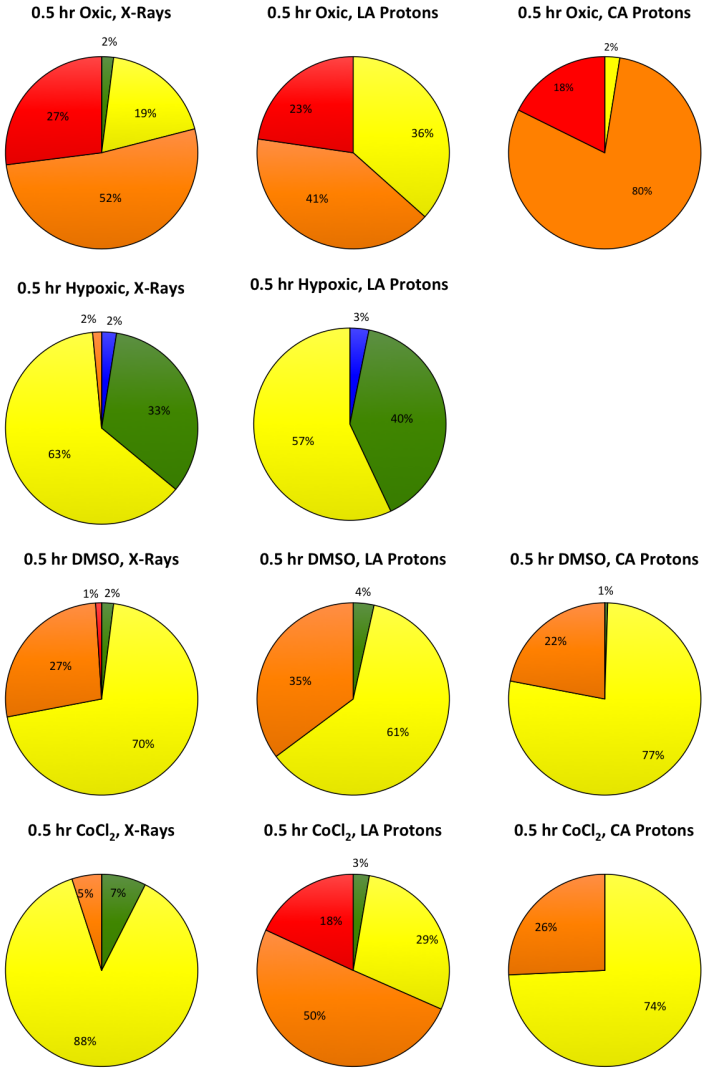


Fig. 6.33 The percentage of cells with 0 - 5 (blue), 6 - 10 (green), 11 - 20 (yellow), 21 - 30 (orange) and > 30 (red) foci per nucleus per Gy at 0.5 hours post irradiation for the four different irradiation environments. The percentages for 225 kVp X-rays from the CCRCB, 15 MeV laser accelerated protons (LA protons, 3.3 keV/$\mu$m) from TAP and conventionally accelerated protons from the 62 MeV beam at Istituto Nazionale di Fisica Nucleare-Laboratori Nazionali del Sud (INFN-LNS), Catania, Italy (CA protons, 1.2 keV/$\mu$m low LET at the entrance of the Bragg peak) are shown. At Catania it was not possible to perform hypoxic experiments using gassed samples at the time of the experiment.

Figure 6.32 shows the response of AGO1522 human fibroblast cells irradiated with 15 MeV protons at both the LULI laser facility and at TAP. Marginally more initial foci were

evident in the TAP samples, with similar numbers at 1, 2 and 6 hours post irradiation. At 24 hours post irradiation there is a difference in the shape of the curves as more residual foci are present in the LULI samples. These differences are most likely a result of the relatively low dose on the cell plane at the 15 MeV position during the LULI experiment and the fact there were three replicates at the TAP experiment and only one for LULI at the 24 hr time point, but there is reasonable agreement between the results. The individual values for each time point of the average number of foci per nucleus for 15 MeV protons at LULI and TAP are summarised in Table 6.10.

| Time Post Irradiation (hrs) | LULI 15 MeV protons | TAP 15 MeV protons |
|---|---|---|
| 0.5 | 19.29 $\pm$0.54 | 24.21 $\pm$3.38 |
| 1 | 15.74 $\pm$1.36 | 16.50 $\pm$1.91 |
| 2 | 12.20 $\pm$2.04 | 12.85 $\pm$1.09 |
| 6 | 6.86 $\pm$0.18 | 5.37 $\pm$0.54 |
| 24 | 7.70 $\pm$0.74 | 1.74 $\pm$0.21 |

Table 6.10 The average number of foci per nucleus for each time point for 15 MeV proton irradiations at LULI and TAP. These values have had the control value of 1.87 $\pm$ 0.05 and 1.85 $\pm$ 0.08 for LULI and TAP respectively, subtracted.

Figures 6.33 and 6.34 show the percentage of nuclei with 0 - 5, 6 - 10, 11 - 20, 21 - 30 and > 30 foci per nucleus, in blue, green, yellow, orange and red respectively, for the TAP samples irradiated with 15 MeV protons and the samples irradiated with 225 kVp X-rays. Comparative data from irradiations carried out at the Istituto Nazionale di Fisica Nucleare-Laboratori Nazionali del Sud (INFN-LNS), Catania, Italy employing their conventionally accelerated 62 MeV proton beamline are also included. There is a pie chart for each irradiation condition at 0.5 hrs and 24 hrs post irradiation. For the oxic samples, all nuclei have at least 11 or 6 foci per Gy for both the conventionally and laser accelerated proton samples and the X-ray samples respectively, and all nuclei have 10 foci or less at 24 hrs post irradiation, although more nuclei have a greater number of foci for the X-ray samples. For the hypoxic samples, all the nuclei have 20 or fewer foci per Gy at 0.5 hrs post irradiation

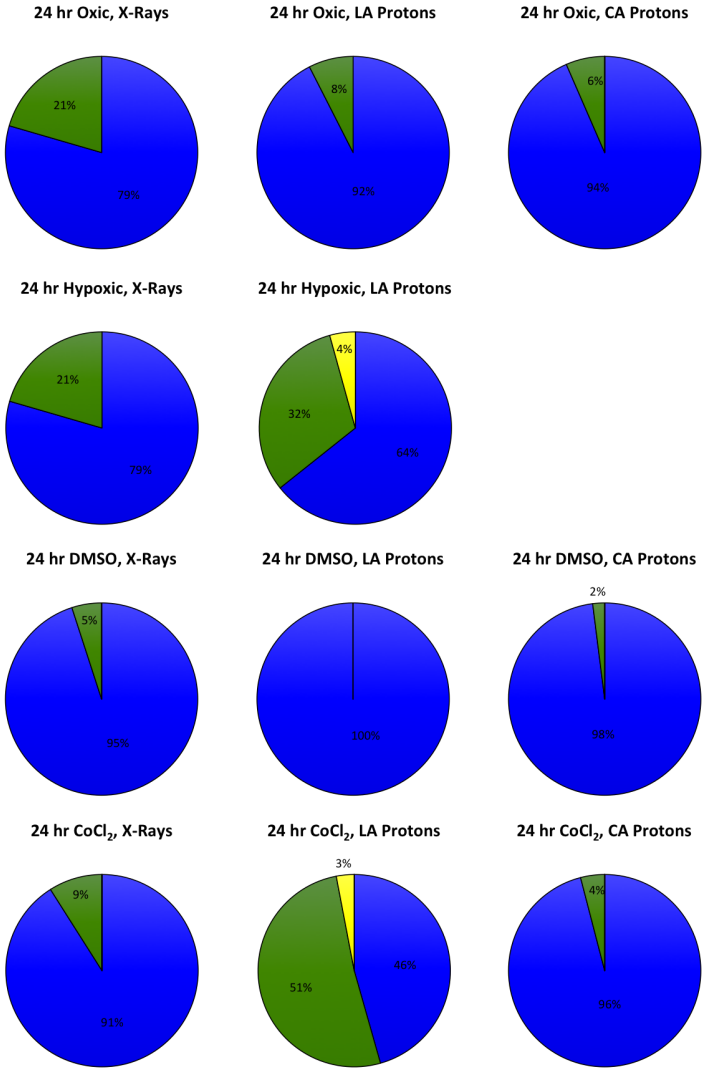


Fig. 6.34 The percentage of cells with 0 - 5 (blue), 6 - 10 (green), 11 - 20 (yellow), 21 - 30 (orange) and > 30 (red) foci per nucleus per Gy at 24 hours post irradiation for the four different irradiation environments. The percentages for 225 kVp X-rays from the CCRCB, 15 MeV laser accelerated protons (LA protons, 3.3 keV/$\mu$m) from TAP and conventionally accelerated protons from the 62 MeV beam at the Istituto Nazionale di Fisica Nucleare-Laboratori Nazionali del Sud (INFN-LNS), Catania, Italy (CA protons, 1.2 keV/$\mu$m low LET at the entrance of the Bragg peak) are shown. At Catania it was not possible to perform hypoxic experiments using gassed samples at the time of the experiment.

for protons although 10 % of the X-ray samples have between 21 and 30 foci. At 24 hrs the X-ray samples have between 0 and 10 foci per nucleus per Gy, whereas some of the pro-

ton irradiated nuclei have up to 20 foci per Gy. The facilities required for gaseous hypoxic irradiations were not available at Catania when the experiment was performed, hence there are no comparative pie charts for the hypoxic samples. For the DMSO samples, at 0.5 hrs post irradiation all nuclei have between 6 and 30 foci per Gy, apart from 1% of the X-ray samples which have > 30 foci per Gy. At 24 hrs post irradiation, all laser proton irradiated samples have 0 to 5 foci per nucleus per Gy, as do the X-ray and conventional proton irradiated samples, apart from 5% and 2% of nuclei respectively which have 6 to 10 foci per nucleus per Gy. Finally, for the $CoCl_2$ samples, 18% of the laser proton irradiated nuclei have > 30 foci per Gy, all other nuclei, including the X-ray and conventional proton samples, have between 6 and 30 foci per Gy at 0.5 hrs post irradiation. At 24 hrs post irradiation, 3% of the proton irradiated samples have 11 to 20 foci per nucleus per Gy, with the rest having 10 or less, including the X-ray and conventional proton samples. These results again confirm the similarity between the X-ray and laser accelerated proton responses in oxic and free radical scavenging conditions, but the differences in physically and chemically hypoxic conditions. The data from Catania also shows similar responses for laser accelerated and conventionally accelerated protons in oxic and free radical scavenging conditions, however more of a difference is seen with the chemically hypoxic samples. More laser accelerated proton irradiated samples have greater percentages of nuclei with a larger number of foci at 0.5 and 24 hrs post irradiation, implying more and more complex damage is induced by the laser accelerated protons than the conventionally accelerated protons.

Figures 6.35 and 6.36 show the same data but with error bars to show the inherent error in the measurements. Again data for the 15 MeV laser accelerated protons from TAP are compared to X-ray irradiated samples from the CCRCB and conventionally accelerated laser irradiated samples form the 62 MeV beamline at the Istituto Nazionale di Fisica Nucleare-Laboratori Nazionali del Sud (INFN-LNS), Catania, Italy.

Figure 6.37 shows a comparison between oxic and hypoxic (physical and chemical) irra-

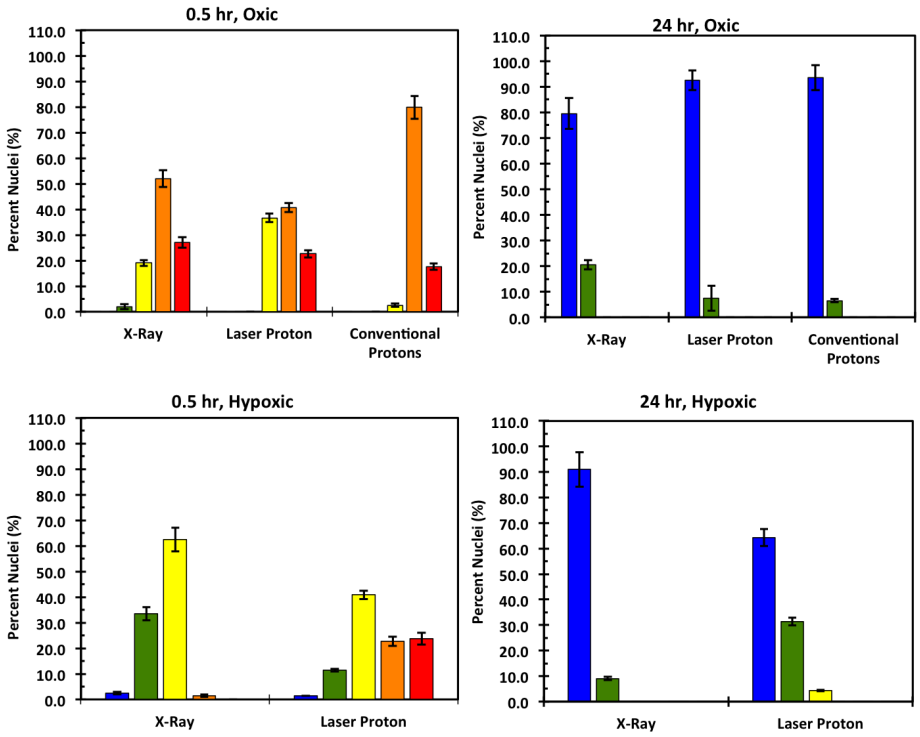


Fig. 6.35 The percentage of cells with 0 - 5 (blue), 6 - 10 (green), 11 - 20 (yellow), 21 - 30 (orange) and > 30 (red) foci per nucleus per Gy at 0.5 and 24 hours post irradiation for the Oxic and Hypoxic irradiation environments. Values are shown for 225 kVp X-rays, 15 MeV laser accelerated protons from TAP (3.3 keV/$\mu$m) and low LET conventionally accelerated protons from the 62 MeV Catania beamline (1.2 keV/$\mu$m at the entrance of the Bragg peak).

diations by 15 MeV protons at TAP, 225 kVp X-ray irradiations in oxic and hypoxic (physical and chemical) conditions at the CCRCB, and 15 MeV oxic proton irradiations carried out at Clatterbridge Cancer Centre, UK. The proton beam generated at the Clatterbridge Cancer Centre is accelerated using a cyclotron.

At the 0.5 hr time point, the largest number of initial foci are induced in the Clatterbridge samples with 27.07 $\pm$ 1.2, followed by the X-ray samples with 24.87 $\pm$ 0.76, and then the TAP samples with 24.21 $\pm$ 3.38 for the oxic conditions. At 24 hrs post irradiation this situation is mirrored with 2.21 $\pm$ 1.1, 1.88 $\pm$ 0.16 and 1.74 $\pm$ 0.21 for the Clatterbridge, X-ray and TAP samples respectively. For the samples irradiated after gaseously inducing

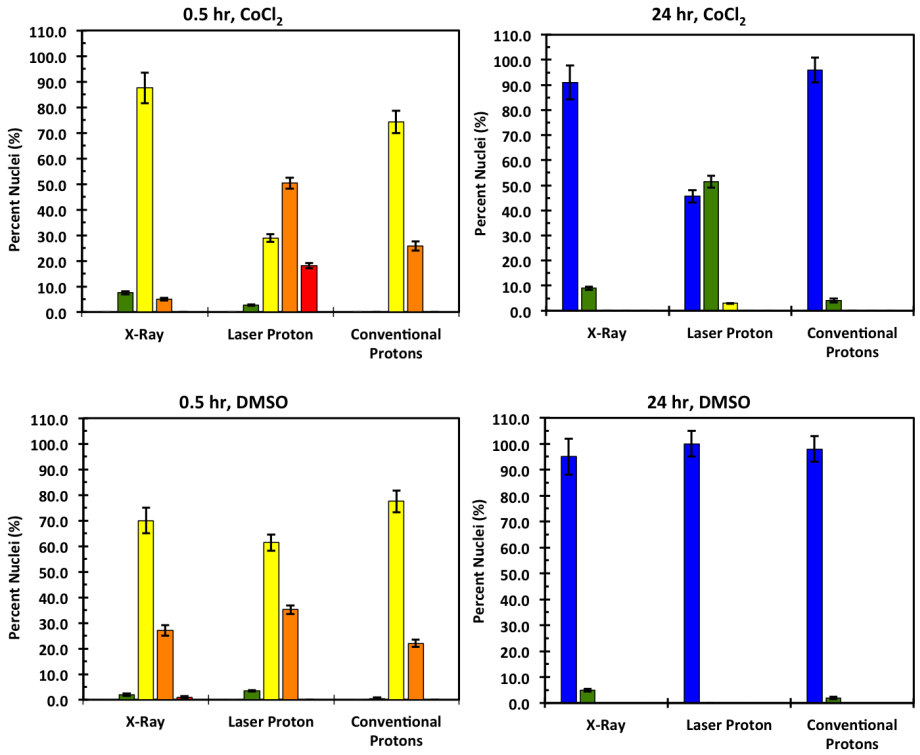


Fig. 6.36 The percentage of cells with 0 - 5 (blue), 6 - 10 (green), 11 - 20 (yellow), 21 - 30 (orange) and > 30 (red) foci per nucleus per Gy at 0.5 and 24 hours post irradiation for the $CoCl_2$ and DMSO irradiation environments. Values are shown for 225 kVp X-rays, 15 MeV laser accelerated protons from TAP (3.3 keV/$\mu$m) and low LET conventionally accelerated protons from the 62 MeV Catania beamline (1.2 keV/$\mu$m at the entrance of the Bragg peak).

hypoxia, the laser accelerated proton irradiated samples had 14.16 $\pm$ 2.51 foci per nuclei per Gy, while the X-ray samples had 9.67 $\pm$ 1.19. Again at 24 hrs post irradiation, the TAP samples had more residual foci with 3.82 $\pm$ 1.26 compared to 1.07 $\pm$ 0.09 for the X-ray samples. A similar situation is true for the samples treated with the hypoxia mimetic agent $CoCl_2$, where the TAP samples have 20.02 $\pm$ 2.00 and 2.97 $\pm$ 1.10 at 0.5 and 24 hrs post irradiation respectively, and the X-ray samples have 11.75 $\pm$ 0.41 and 0.80 $\pm$ 0.11 at 0.5 and 24 hrs respectively. This demonstrates that laser accelerated protons produce a comparative result to conventionally accelerated protons and X-rays under oxic conditions, and for chemically and physically induced hypoxia, laser accelerated protons produce more

initial and residual damage than X-ray irradiations.

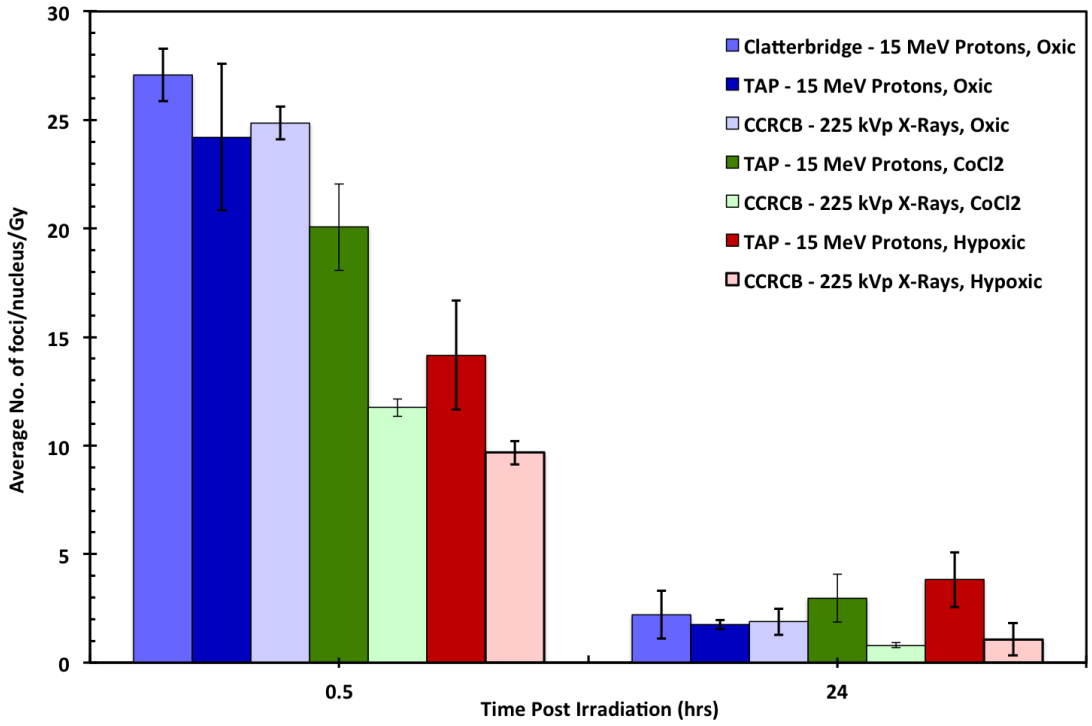


Fig. 6.37 Comparison of the 15 MeV proton DNA DSB kinetic profiles for the TAP and LULI experiments.

Another significant point which can be raised is that the effect of hypoxia observed in the TARANIS and TAP experiments are very different. In the TARANIS experiment the response of the cells to irradiations under oxic and hypoxic conditions produced the same results within error. The number of DNA DSBs induced in oxic conditions at 0.5 hrs post irradiation was marginally higher than for the hypoxic samples, and at 24 hrs the oxic samples still had marginally more foci present. Conversely, for the TAP experiment there was a significant difference in the number of foci at 0.5 hrs post irradiation for the oxic and hypoxic samples (both physically and chemically induced hypoxia). The rates at which the foci were repaired also differed, and at 24 hrs post irradiation there were more residual foci present in the physically and chemically induced hypoxic samples than the oxic samples. The main difference between these experimental approaches was that in the

case of the TARANIS experiment, only one hypoxia chamber was available, thus once the samples were irradiated they were stored inside a normal cell culture incubator and not under hypoxia, thus they were allowed to fully reoxygenate during the 24 hr period of DNA DSB kinetic study. In the TAP experiment, there were six new hypoxia chambers and a dedicated hypoxic incubator, thus once the samples were irradiated they could be kept in hypoxic conditions either inside the small hypoxia chamber or the hypoxic incubator for the full 24 hr DNA DSB kinetic study period, with only minimal reoxygenation during transfer between the chamber and the incubator and during the washing step before fixation. This shows that effects observed in the TAP samples are a result of this continual hypoxic environment during the DNA DS repair process, rather than the initial hypoxia at the time of irradiation.

Other experiments carried out by different research groups may explain some of the results obtained, although it should be noted that different irradiation qualities and cell lines were employed in these experiments. These are discussed below.

Tinganelli *et al* [194] studied the effect of acute hypoxia and radiation quality on cell survival. They employed CHO, Chinese Hamster Ovary, cells and RAT-1 prostate cancer cells. They developed their own compact hypoxia chamber, consisting of a PEEK box with an irradiation window of 1 mm corresponding to a water equivalent thickness 1.23 mm, a transparent PMMA top cover and chamfer at the bottom of the chamber allow control over the sample position. The cells were grown on sample rings made from polyvinyl-chloride and a 25 $\mu$m gas permeable foil. The chamber was gassed for 2 hours with different gas mixtures: 95% $N_2$ and 5% $CO_2$ for anoxic samples and 94.5% $N_2$, 5% $CO_2$ and 0.5% $O_2$ for hypoxic samples. The normoxic samples were kept in 21% $O_2$. All exposures were performed through the irradiation window of the chamber. X-ray irradiations were carried out employing an Isovolt DSI X-ray machine operated at 250 kVp and 16 mA with a 7 mm beryllium, 1 mm aluminium and 1 mm copper filtering at a dose rate of 2 Gy/min. The GSI

synchrotron (SIS) was employed for C-ion and N-ion irradiations and the Heidelberg Ion Therapy (HIT) accelerator was used for O-ion irradiations. A Spread Out Bragg Peak of 1 cm was used for all ion exposures. The LET values were dose-average: 100 and 150 keV/m for C-ions, 140 keV/m for O-ions, and 160 keV/m for N-ions [194]. The OER and RBE were determined from clonogenic assays. They found the OER decreased with increasing LET, and the RBE of CHO cells reached a plateau above 100 keV$\mu$m$_{-1}$ for normoxic conditions but increased under anoxia. The HRF obtained for the TAP 15 MeV proton irradiations compared to the X-ray irradiations (summarised in Table 6.7), an analogous measurement to the OER used for hypoxic exposures, also shows decreasing HRF for increasing LET as the HRF of the hypoxic 15 MeV protons is $1.36 \pm 0.55$ compared to $1.95 \pm 0.33$ for X-rays, and for the $CoCl_2$ samples these figures are $0.94 \pm 0.26$ and $1.78 \pm 0.31$ for the proton and X-ray irradiations respectively.

Raschke *et al* [291] used A549 human lung cancer cells to investigate whether ultra-short laser accelerated proton pulses have similar DNA damaging effectiveness and their immediate nitroxidative stress compared to conventional proton beams. The laser accelerated protons (LAP) were generated using the 200 TW ARCTURUS laser system at the University of Düsseldorf in the single shot mode focused on titanium foil targets. Dose rates of $10^8$ Gys$^{-1}$ were employed. The cell samples were grown on cover-slips and exposed to $2.1 \pm 0.25$ MeV protons with an average LET of 23 keV$\mu$m$_{-1}$. Distinct doses of between 0.25 and 2 Gy were created by accumulative application of several laser shots at 3 s intervals, (a minimum of eight shots) with a known dose per shot. The samples were irradiated on enclosed ring shaped sample holders sealed on one side with 1.5 $\mu$m Mylar and on the other with a glass slide on which the cells were grown. The conventionally accelerated protons (CAP) were generated by a Van de Graaff accelerator at PTB Braunschweig. The primary proton beam was scattered by a 0.5 $\mu$m gold foil in the center of the scattering chamber. A dose rate of 0.01 Gys$^{-1}$ was employed. The same sample dish was used as that for the LAP. The

initial beam energy was 1.54 MeV, producing an energy spectrum with a peak of 0.4 MeV, a width of 0.13 MeV (FWHM) and an LET of 45 keV$\mu$m$_{-1}$. A second higher energy of 1.7 MeV was utilised with a peak around 0.7 MeV, width of 0.11 MeV (FWHM), resulting in an average LET of 32 keV$\mu$m$_{-1}$. Their comparison X-ray irradiations were carried out employing a 320 kV Isovolt 320HS cathode generator at the University of Duisberg-Essen Medical School, using a voltage of 320 kV with a 1.65 mm aluminium filter, delivering a photon energy of approximately 90 keV. For the 0.2 to 2 Gy irradiations, no difference in the DNA DSB foci kinetics measured by the $\gamma$-H2AX and 53BP1 immunofluorescence assays were observed between the LAP, CAP and X-ray samples. For 0.64 to 1 Gy irradiations the time course of decay of the foci was similar for all irradiation types. At 1 hour post irradiation all samples regardless of irradiation type exhibited 19 - 27 foci, and at 12 - 16 hours post irradiation 2 - 4 foci, which was similar to the control value. The RBE for CAP was 1.8 $\pm$ 0.8 and for LAP it was found to be 1.4 $\pm$ 1.0. The mode of irradiation does not seem to affect the response in the energy range employed here, similar to the results obtained from the oxic irradiations at TAP, LULI, Clatterbridge and the CCRCB as described earlier.

Ionising radiation, as well as producing free radicals, induces delayed response involving enhanced nitroxidative stress, which is thought to contribute to late and non-targeted effects. The half life of the primary radicals produced is in the ns range. The LAP are delivered at a dose rate of $10^8$ Gys$^{-1}$, whereas the CAP are delivered at around 0.01 Gys$^{-1}$, about 11 orders of magnitude lower than the lifetime of the primary radicals. Consequently, LAP could possibly have a different radical generating potential and characteristics than CAP, despite having a similar DNA damaging potential. The X-ray irradiations had a 5 fold lower nitroxidative stress and the LAP had a 2 - 3 fold lower nitroxidative stress than CAP.

The salient finding of this experiment was that laser accelerated beams have a similar DNA damage potential as conventional beams but produce less immediate nitroxidative stress, which provides a distinctive therapeutic potential.

Kumareswaran *et al* [292] studied the effect of chronic hypoxia on DNA DSB repair, and the compromising effect it has on genetic stability. The human fibroblast cell line GMO5757 was employed. The anoxic samples were exposed to 0% $O_2$, the hypoxic samples to 0.2% $O_2$ and the oxic samples to 21% $O_2$ for 16 hours prior to the irradiations using an Invivo2 400 chamber. To induce the exogenous DNA damage, the samples were irradiated using a $^{137}$Cs irradiator from MDS Nordion. The samples were then gassed post irradiation for 0.5, 4 or 24 hours at 37$^\circ$ and assayed for residual DNA damage.

The $\gamma$-H2AX and 53BP1 assays were employed to quantify the residual foci in the hypoxic sample 24 hrs post irradiation. DNA repair under continued hypoxia lead to a decreased repair of G1 associated DNA DSBs resulting in chromosomal instability. Aberrant DNA DSB repair under hypoxia is a potential factor in hypoxia mediated genetic instability. The decrease in repair of foci was attributed to a defective NHEL pathway for hypoxic cells, which then leads to the hypoxic samples acquiring increased numbers of residual DNA DSBs under continued hypoxia. The OER obtained for hypoxic samples was 1.81 $\pm$ 0.31 and 2.02 $\pm$ 0.13 for anoxic samples, which is consistent with the range of 1.6 to 2.6 for normal human fibroblasts [292]. The $\gamma$-H2AX induction was $O_2$ dependent with the induced foci number decreasing significantly under hypoxia and anoxia. The number of $\gamma$-H2AX foci in oxic samples fell to background levels after 24 hours, but although the hypoxic and anoxic samples had reduced initial number of foci, the number was elevated at 24 hours compared to the oxic samples. The rate at which the foci were lost fell from 1.11 $\pm$ 0.37 foci per hour for the oxic samples to 0.11 $\pm$ 0.09 foci per hour for the hypoxic samples. The same initial decrease in foci numbers for hypoxic compared to oxic samples was also observed for 53BP1 foci, and the hypoxic samples also retained increased residual foci numbers at 24 hours post irradiation. This is similar to the results obtained for the physically induced hypoxic samples and the $CoCl_2$ samples from the TAP experiment which were kept in reduced oxygen conditions post irradiation, where there are fewer initial

foci but more residual foci compared to the oxic samples, however they exhibit more initial and residual foci compared to the hypoxic and $CoCl_2$ X-ray samples. This is also supported by the TARANIS results which did not exhibit this effect in the hypoxic samples at 24 hrs. These samples had not been kept in hypoxic conditions post irradiation, thus this repair pathway would not have been affected. Therefore the DNA repair is compromised under continual hypoxic exposure leading to increased retention of $\gamma$-H2AX and 53BP1 foci. Kumareswaran showed this effect to be specific to the induction and repair of DNA damage and not a non-specific effect of hypoxia.

# Chapter 7

# Conclusions and Future Directions

## 7.1 Conclusions

This was the first time radiobiological experiments had been carried out on both the LULI and TAP beamlines. Reported for the first time are measurements of DNA DSB damage with pulsed protons at ultra-high dose rates of $10^9$ to $10^{10}$ $Gys^{-1}$ under physical and chemical hypoxia and free radical scavenging conditions. These results were compared with conventionally accelerated protons and standard X-ray irradiations. A close similarity was observed between the foci kinetics of laser and cyclotron accelerated protons under normoxic and free radical scavenging conditions, however differences were observed in the cellular response under physical and chemical hypoxia. No significant difference was observed in the initial damage inflicted, however at 24 hours post irradiation there was an increase in the residual damage in the laser accelerated samples compared to the X-ray samples and the cyclotron accelerated samples, indicating the efficiency of ultra-high dose rate exposures in damage induction under radioresistant conditions. This enhanced number of residual foci could be a result of a deficient NHEJ repair pathway for hypoxic cells which leads to an increase in the number of retained foci 24 hours post irradiation if the samples are kept in continual hypoxia, as suggested by Kumareswaran [292]. The HRF of the laser accelerated

protons was lower than that for X-rays which is agreement with the findings of Tinganelli [194]. As with Raschke [291], it was found that there was a similar DNA damage potential for laser accelerated protons, conventionally accelerated protons and X-rays. The RFI for 15 MeV protons versus 225 kVp X-rays for oxic, hypoxic, $CoCl_2$ and DMSO samples was found to be $1.00 \pm 0.09$, $1.78 \pm 0.94$, $2.07 \pm 0.84$ and $0.96 \pm 0.22$ for the TAP experiment and $1.20 \pm 0.18$, $1.32 \pm 0.29$ and $1.62 \pm 0.55$ for the 10, 13 and 15 MeV LULI proton irradiations respectively. The HRF for the 15 MeV protons at TAP was calculated to be 1.36 $\pm$ 0.55 for the hypoxic samples and $0.94 \pm 0.26$ for the $CoCl_2$ samples, with the respective values of $1.95 \pm 0.33$ and $1.78 \pm 0.31$ for the X-ray irradiations.

Fourkal's theory of the linear response described in Section 4.4.1, predicted that when the distance between protons in a cluster becomes less than its velocity divided by the characteristic frequency of the collective excitations supported by the medium it is traversing, the cluster's LET starts increasing so that the stopping power of the individual proton in the cluster increases compared to a single moving particle. Unfortunately the collective effects predicted by this theory were not observed during the laser proton irradiations of AG01522 normal human fibroblast cells as the samples were placed beyond the distance at which the effect can be observed. The conditions required to observe these effects are only observable within cm distances of the target, which would require the samples to be placed inside the vacuum which they would not survive. It was planned to observe these effects using plasmid DNA instead.

Owing to time constraints and unforeseen circumstances, other planned investigations into cell survival and the effect of laser accelerated protons on plasmid DNA at cm distances (the distance at which Fourkal's [228] linear response theory becomes observable) from the target were not possible. Two shots for clonogenic assays were attempted, but abandoned as the laser flux was too low and the cells were not the best quality at the end of the run. Two shots were also carried out with plasmid DNA, as plasmid DNA is more resilient than

AGO1522 cells and could be placed at cm distances from the target in a cell dish sealed with 1 cm thick aluminium plates to investigate the overlapping of the ion tracks in space and time, as these conditions were only possible at cm distances from the target. These samples have been kept for future reference in the CCRCB.

### 7.1.1 Thesis Aims

The main aims of this thesis were set out in Section 1.2. These were to:

- Demonstrate laser accelerated proton induced DNA DSB under physically induced hypoxia, chemically induced hypoxia and free radical scavenging environments for the first time

The results reported here are the first time laser accelerated protons have been used to induce DNA DSB damage under physically induced hypoxia, chemically induced hypoxia and a free radical scavenging environment in AG01522 normal human fibroblast cells. These results have been compared to data from X-ray irradiations under the same conditions as a comparison, with similar results for laser accelerated protons and X-ray irradiated samples in free radical scavenging conditions, and favourable results for laser accelerated protons under physical and chemical hypoxia, which is encouraging with the view to using laser accelerated protons sources for hypoxic tumour treatment in the future.

- Develop and characterise a new compact hypoxia chamber for use with laser driven sources

To study the radiobiological effects of laser driven ion beams under hypoxic conditions, a new compact hypoxia chamber was designed for low energy laser ion radiobiology applications. The chamber is suitable for characterising the biological effects of laser accelerated beams under a range of different oxygen concentrations. The chamber design was characterised physically and biologically. It proved capable of maintaining a radiobiologically

hypoxic environment (<0.4% $O_2$) for up to 3 hours and an acutely hypoxic environment (< 3% $O_2$) for 24 hours, with no dose enhancement inside the chamber compared to outside the chamber. This chamber was then implemented during the TARANIS, TAP and CCRCB experiments, with results showing that hypoxia was indeed induced in the cell samples as well as DNA damage. This chamber will be a valuable tool in the study of the biological effects of laser-driven ions under hypoxia.

- Develop the cell handling procedure and irradiation methods associated with the new hypoxia chamber

The new chamber was implemented in the TARANIS experiment as a proof of principle to develop the cell handling and procedure and irradiation methods associated with this new chamber. It was previously thought that EBT-3 normal film would not be able to survive on the inside of the hypoxia chamber next to the cell dish for extended periods of time, but it was discovered this was not the case during this experiment. It was also discovered the original design of the hypoxia chamber would not be compatible with the insertion pipe used for the TAP experiment so the design was adjusted accordingly. This experiment was also only carried out with one chamber, thus the samples were allowed to reoxygenate between irradiation an fixation, something which was seen initially as a mistake, but in the end proved as a useful comparison for the effects produced. Issues with staining were also highlighted during this experiment, such as the poor staining produced by $\gamma$-H2AX and the corresponding HIF-1$\alpha$ antibody, thus 53BP1 was used in future experiments. By the time the chamber was implemented on the TAP experiment, a clear technique had been developed for the cell handling and irradiation, thanks to the initial TARANIS experiment.

- Repeat laser accelerated proton experiments in an oxic environment for comparison

Previously, the effectiveness of laser accelerated protons and carbon ions in inducing DNA DSBs in AG01522 normal human fibroblast cells has already been shown, as described in

Section 6.1.1. It was possible to replicate these results in both the LULI and TAP campaigns where the RFI for the 10 MeV, 13 MeV and 15 MeV protons at LULI were found to be 1.20 $\pm$ 0.18, 1.32 $\pm$ 0.29 and 1.62 $\pm$ 0.55, and 1.00 $\pm$ 0.09 for the 15 MeV protons at TAP compared to 225 kVp X-rays. These results are a step closer to showing the potential stability of this mode of radiation delivery as a possible alternative to conventionally accelerated protons.

When compared to conventionally accelerated proton data such as that from Clatterbridge Cancer Centre and INFN-LNS Catania, the average number of foci per cell per Gy and the proportion of nuclei with certain numbers of foci both compare favourably.

- Discover if there are different biological effects produced under the four irradiation environments as compared to X-ray and conventionally accelerated proton irradiations where data exists

A close similarity was observed between the foci kinetics of laser and conventionally accelerated protons under normoxic and free radical scavenging conditions, however there were observed differences under physical and chemical hypoxia in the cellular response. At 24 hours post irradiation there was an increase in the residual damage in the laser accelerated samples compared to the conventionally accelerated samples and the X-ray samples. This indicates the efficiency of ultra-high dose rate exposures in damage induction under chemically and physically induced hypoxia. The RFI for the oxic, hypoxic, $CoCl_2$ and DMSO samples were 1.00 $\pm$ 0.09, 1.78 $\pm$ 0.94, 2.07 $\pm$ 0.84 and 0.96 $\pm$ 0.22 respectively, and the HRF was 1.36 $\pm$ 0.55 and 0.94 $\pm$ 0.26 for the hypoxic and $CoCl_2$ proton samples, compared to 1.95 $\pm$ 0.33 and 1.78 $\pm$ 0.31 for the x-ray samples. This indicates the presence of oxygen has less effect on the laser accelerated samples than the X-ray samples. This is promising in terms of the potential for laser driven ions to be used as an effective treatment for hypoxic tumours.

The effect of hypoxia observed in the TARANIS and TAP experiments was very different. In the TARANIS experiment the response of the cells to irradiations under oxic and hypoxic conditions produced the same result within error. For the TAP experiment there was a significant difference in the number of foci present at 0.5 hrs and 24 hrs post irradiation. At 24 hrs there were more residual foci present in the laser irradiated hypoxic samples as compared to the X-ray irradiated samples. The main difference between these experimental approaches was that in the TAP experiment the samples were not kept in a hypoxic environment after they were irradiated, whereas the TAP samples were kept in a hypoxic environment right up until fixation. This shows that the effects observed in the TAP samples are a result of this prolonged hypoxic environment during the DNA DSB repair process, rather than the initial hypoxia at the time of irradiation.

- Develop a robust immunofluorescence protocol

At the start of the work in this thesis there was a standard immunofluorescence protocol which had been used on previous radiobiological experiments such as those described in Section 6.1.1. During the course of the three experiments described in Sections 6.2, 6.3 and 6.4 slight adaptations were made to this protocol to produce a robust protocol which delivers excellent staining results in the form of clearly discernible 53BP1 DNA DSB foci and bright staining of the HIF-1$\alpha$ hypoxia bio-marker. A copy of this enhanced protocol is included in Appendix B. This protocol can be used with confidence on future experiments.

## 7.2 Future Work

Future work will be directed towards optimisation of higher energies and development of more robust cell based assays for screening the effectiveness of laser accelerated protons in cancer pre-clinical models. Below is a brief description of the techniques that will be used on future experiments;

### 7.2.1 Dose and LET Dependent Cell Survival Studies

The next radiobiology experiment will be carried out at LULI and will attempt to replicate the results presented here. The DNA damage results gathered at the experiment will also be correlated to cell survival, which is the golden standard assay for radiobiology and represents the basis for radiation therapy treatment planning. The Laserlab Europe's LULI2000 laser would allow these studies to be carried out at significantly higher dose rates and doses than in previous experiments. Employing the CLF's Vulcan or Gemini laser would also allow the effects on cell survival of single pulses of carbon ions to be investigated for the first time, allowing the relevance of high-LET doses delivered in nanosecond time-scales to be addressed. Clonogenic assays performed under the same four irradiation conditions as those used at the TAP experiment would allow correlation of these results to cell survival and a calculation of the RBE rather than the RFI.

### 7.2.2 Plasmid DNA Studies

The conditions required to produce collective non-linear effects, predicted to take place when there is spatio-temporal overlap of the tracks formed by single particles in the irradiated biological sample, are dependent on beam density and duration and the energy and LET of the particles in the beam. During the TAP experiment these conditions were only produced within cm distances of the target. To investigate these effects, plasmid DNA will need to be used rather than cell samples as the cell samples would not survive the incredibly high doses this close to the target. Plasmid DNA samples do not need to be in air, so can be irradiated in sealed aluminium cell dishes inside the interaction chamber.

The overlap of tracks leads to modifications in the effective LET of a dense beam of ions, compared to the LET of a single particle, resulting in a different biological response to the radiation, which can be quantifiably measured by the RBE.

# Glossary

**ADC** - Analogue to digital converter. 66

**AG01522** - A human non-cancerous skin fibroblast cell line from the Coriell Institute for Medical Research. 9, 40

**ANRT** - Aryl hydrocarbon receptor nuclear translocator, the alternative name for the $\beta$ subunit of HIF-1. 122

**AR** - Anti-reflection. viii, 46

**ASE** - Amplification of spontaneous emission. 44, 45, 47, 49, 54

**Astra** - The high-power, ultra-short pulse, high repetition rate Ti:sapphire laser located at the Rutherford Appleton Laboratory, Didcot, Oxford, UK. 7, 8, 9, 40, 45, 47, 53, 54

**ATM** - Ataxia telangiectasia mutated. 105, 106, 107

**ATR** - ATM and Rad3-related. 105

**BER** - Base excision repair. 108, 109

**CCRCB** - Centre for Cancer Research and Cell Biology, Queen's University Belfast. 7, 8

**CDI** - Cyclin-dependent kinase inhibitors. 102

**CDK** - Cyclin-dependent kinase. 100, 102, 103, 104, 105

**CPA** - Chirped pulse amplification. viii, 40, 42, 43, 44, 45, 48, 50, 51

**DNA** - Deoxyribonucleic acid. xii, xiii, 7, 9, 79, 93, 95, 96, 97, 98, 99, 100, 101, 102, 104, 105, 106, 107, 108, 109, 110, 111, 112, 114, 116, 118, 119, 131

**DSB** - Double strand break. xii, 7, 9, 95, 96, 109, 110, 111, 114, 115, 116, 118, 131

**EBT** - External beam therapy. xi, 68, 69, 70, 71

**Gemini** - An extension of the Astra system (2 beams) located at the Rutherford Appleton Laboratory, Didcot, Oxford, UK. ix, 6, 7, 8, 9, 40, 45, 47, 54, 53, 54

**HeLa** - a human cervical adenocarcinoma cell line originating from Henrietta Lacks. 106

**HIF** - Hypoxia inducible factor. xiii, 122, 123

**HIF-1** - Hypoxia inducible factor 1 which is comprised of $\alpha$ and $\beta$ subunits. 122

**HR** - Homologous recombination, a form cellular repair. 109, 110, 111

**HRE** - Hypoxia response elements. 122

**HRF** - Hypoxia reduction factor. 117

**IMRT** - Intensity modulated radiation therapy. 68, 69

**IP** - Image plate. 6, 65, 66, 68

**LET** - Linear energy transfer. xii, 113, 114, 115, 116, 117, 120, 131, 133, 134

**LPCR** - Laser pulse contrast ratio. 44, 45

**LULI** - Laboratoire d'Utilisation des Lasers Intenses, Palaiseau, Paris, France. ix, 6, 7, 8, 9, 40, 47, 50, 51

**NER** - Nucleotide excision repair. 108, 112

**NHEJ** - Nonhomologous end joining, a form of cellular repair. 109, 110, 111

**OAP** - Off-axis parabola. 49, 54, 62

**OER** - Oxygen enhancement ratio. 116, 117, 118, 120

**OPCPA** - Optical parametric chirped pulse amplification. 43, 48

**PHD** - Prolyl hydroxylases. 122, 123

**PHE** - Public Health England, Harwell Campus. 233

**PL** - Photoluminescence. 65

**PM** - Plasma mirror. 45, 46, 47

**PSL** - Photo-stimulated luminescence. xi, 66, 67, 68

**PTRACE** - a 3D particle tracing code written by Angelo Schiavi [20]. ix, 8, 58, 59, 61

**pVHL** - Von Hippel-Lindau protein. 122, 123

**QL** - Quantum level. 67

**RA** - Regenerative amplifier. 51, 52

**RB** - Retinoblastoma protein. 104

**RBE** - Relative biological effectiveness. xii, 114, 115, 116, 120, 131, 134

**RCF** - Radiochromic film. 6, 9, 68, 70, 71

**RFI** - Relative foci induction. 207

**RNA** - Ribonucleic acid. 100, 101

**ROS** - Reactive oxygen species. 79, 97, 98, 99, 118

**SSA** - Single strand annealing. 109, 111

**SSB** - Single strand break. 95, 114, 115, 118

**TA1** - Target area 1 of the TARANIS laser system at Queen's University Belfast. 53

**TA2** - Target area 2 of the TARANIS laser system at Queen's University Belfast. 53

**TAP** - Target Area Petawatt of the Vulcan laser system at Rutherford Appleton Laboratory, Didcot, Oxford, UK. 47, 49

**TARANIS** - Terawatt Apparatus for Relativistic And Non-linear Interdisciplinary Science. The laser apparatus located at the Centre for Plasma Physics, Queen's University Belfast.. ix, 6, 7, 8, 9, 40, 47, 51, 52

**TAW** - Target Area West of the Vulcan laser system at Rutherford Appleton Laboratory, Didcot, Oxford, UK. 47

**TPS** - Thomson Parabola Spectrometer. ix, x, 6, 55, 56, 57, 58, 60, 61, 62, 61, 62, 61

**V(D)J** - Variable diversity joining recombination. 109, 111

**Vulcan** - The petawatt laser facility located at Rutherford Appleton Laboratory, Didcot, Oxford, UK. ix, x, 6, 7, 8, 9, 40, 47, 48, 49, 62, 61

# References

[1] M. Borghesi, A. Mackinnon, D. Campbell, D. Hicks, S. Kar, P. Patel, D. Price, L. Romagnani, A. Schiavi, and O. Willi, "Multi-MeV Proton Source Investigations in Ul-

traintense Laser-Foil Interactions," *Physical Review Letters*, vol. 92, p. 055003, Feb 2004.

[2] L. Robson, P. T. Simpson, R. J. Clarke, K. W. D. Ledingham, F. Lindau, O. Lundh, T. McCanny, P. Mora, D. Neely, C.-G. Wahlström, M. Zepf, and P. McKenna, "Scaling of proton acceleration driven by petawatt-laser–plasma interactions," *Nature Physics*, vol. 3, pp. 58–62, Dec 2006.

[3] V. Malka, J. Faure, Y. A. Gauduel, E. Lefebvre, A. Rousse, and K. m. T. Phuoc, "Principles and applications of compact laser – plasma accelerators," *Nature Physics*, vol. 4, no. June, 2008.

[4] M. Borghesi, a. Bigongiari, S. Kar, a. Macchi, L. Romagnani, P. Audebert, J. Fuchs, T. Toncian, O. Willi, S. V. Bulanov, a. J. Mackinnon, and J. C. Gauthier, "Laser-driven proton acceleration: source optimization and radiographic applications," *Plasma Physics and Controlled Fusion*, vol. 50, p. 124040, Dec 2008.

[5] K. W. D. Ledingham, W. Galster, and R. Sauerbrey, "Laser-driven proton oncology–a unique new cancer therapy?," *The British Journal of Radiology*, vol. 80, pp. 855–8, Nov 2007.

[6] S. V. Bulanov and V. S. Khoroshkov, "Feasibility of using laser ion accelerators in proton therapy," *Plasma Physics Reports*, vol. 28, pp. 453–456, May 2002.

[7] T. Ohno, "Particle radiotherapy with carbon ion beams.," *The EPMA Journal*, vol. 4, pp. 1–7, Jan 2013.

[8] M. Borghesi, J. Fuchs, S. V. Bulanov, A. J. Mackinnon, P. K. Patel, and M. Roth, "Fast ion generation by high-intensity laser irradiation of solid targets and applications," *Fusion Science and Technology*, vol. 49, 2006.

[9] F. Wagner, O. Deppert, C. Brabetz, P. Fiala, A. Kleinschmidt, P. Poth, V. A. Schanz, A. Tebartz, B. Zielbauer, M. Roth, T. Stöhlker, and V. Bagnoud, "Maximum Proton Energy above 85 MeV from the Relativistic Interaction of Laser Pulses with Micrometer Thick CH2 Targets," *Physical Review Letters*, vol. 116, no. 205002, 2016.

[10] F. Hanton, D. Doria, K. F. Kakolee, S. Kar, S. K. Litt, F. Fiorini, H. Ahmed, S. Green, J. C. G. Jeynes, J. Kavanagh, D. Kirby, K. J. Kirkby, C. L. Lewis, M. J. Merchant, G. Nersisyan, R. Prasad, K. M. Prise, G. Schettino, M. Zepf, and M. Borghesi, "Radiobiology at ultra-high dose rates employing laser-driven ions," in *Laser Acceleration of Electrons, Protons, and Ions II; and Medical Applications of Laser-Generated Beams of Particles II; and Harnessing Relativistic Plasma Waves III*, (Prague, Czech Republic), SPIE, 2013.

[11] D. Doria, L. Romagnani, K. M. Prise, G. Schettino, and M. Borghesi, "Biological effects of ion irradiation at ultrahigh dose rates," tech. rep., 2013.

[12] B.-J. Hong, J. Kim, H. Jeong, S. Bok, Y.-E. Kim, and G.-O. Ahn, "Tumor hypoxia and reoxygenation: the yin and yang for radiotherapy," *Radiation Oncology*, vol. 34, no. 4, 2016.

[13] A. Wambersie, J. Hendry, J. Gueulette, R. Gahbauer, R. Pötter, and V. Grégoire, "Radiobiological rationale and patient selection for high-LET radiation in cancer therapy," *Radiotherapy and Oncology*, vol. 73, no. Suppl 2, pp. S1–14, 2004.

[14] M. Durante and J. S. Loeffler, "Charged particles in radiation oncology.," *Nature Reviews Clinical Oncology*, vol. 7, pp. 37–43, Jan 2010.

[15] L. Antonovic, A. Brahme, Y. Furusawa, and I. Toma-Dasu, "Radiobiological description of the LET dependence of the cell survival of oxic and anoxic cells irradiated by carbon ions," *Journal of Radiation Research*, vol. 54, no. 1, pp. 18–26, 2013.

[16] K. D. Held, H. Kawamura, T. Kaminuma, A. E. S. Paz, Y. Yoshida, Q. Liu, H. Willers, and A. Takahasi, "Effects of Charged Particles on Human Tumor Cells," *Frontiers in Oncology*, vol. 6, no. 23, pp. 1–19, 2016.

[17] J. Bin, K. Allinger, W. Assmann, G. Dollinger, G. a. Drexler, A. a. Friedl, D. Habs, P. Hilz, R. Hoerlein, N. Humble, S. Karsch, K. Khrennikov, D. Kiefer, F. Krausz, W. Ma, D. Michalski, M. Molls, S. Raith, S. Reinhardt, B. Roper, T. E. Schmid, T. Tajima, J. Wenz, O. Zlobinskaya, J. Schreiber, and J. J. Wilkens, "A laser-driven nanosecond proton source for radiobiological studies," *Applied Physics Letters*, vol. 101, no. 24, p. 243701, 2012.

[18] M. Nishiuchi, H. Sakaki, T. Hori, P. R. Bolton, K. Ogura, A. Sagisaka, A. Yogo, M. Mori, S. Orimo, A. S. Pirozhkov, I. Daito, H. Kiriyama, H. Okada, S. Kanazawa, S. Kondo, T. Shimomura, M. Tanoue, Y. Nakai, H. Sasao, D. Wakai, H. Daido, K. Kondo, E. Agency, H. Souda, H. Tongu, A. Noda, Y. Iseki, T. Nagafuchi, K. Maeda, K. Hanawa, T. Yoshiyuki, and T. Shirai, "Laser-driven Proton Accelerator for Medical Application," in *IPAC'10*, (Kyoto, Japan), pp. 88–90, 2010.

[19] K. Zeil, M. Baumann, E. Beyreuther, T. Burris-Mog, T. E. Cowan, W. Enghardt, L. Karsch, S. D. Kraft, L. Laschinsky, J. Metzkes, D. Naumburger, M. Oppelt, C. Richter, R. Sauerbrey, M. Schürer, U. Schramm, and J. Pawelke, "Dose-controlled irradiation of cancer cells with laser-accelerated proton pulses," *Applied Physics B*, vol. 110, pp. 437–444, Nov 2013.

[20] A. M. M. Schiavi, *Study of Laser Produced Plasmas by X-Ray and Proton Radiography*. PhD thesis, Imperial College of Science, Technology and Medicine London, 2003.

[21] L. V. Keldysh, "Ionization in the Field of a Strong Electromagnetic Wave," *Soviet Physics JETP*, vol. 20, no. 5, pp. 1307–1314, 1965.

[22] G. S. Voronov and N. B. Delone, "Many-photon ionization of the xenon atom by ruby laser radiation," *Soviet Physics JETP*, vol. 23, no. 1, pp. 55–58, 1966.

[23] P. Gibbon, *Short Pulse Laser Interactions with Matter: An Introduction*. London: Imperial College Press, 1st ed., 2005.

[24] W. L. Kruer, *Frontiers in Physics: The Physics of Laser Plasma Intractions*. Boulder: Westview Press, 1st ed., 2003.

[25] M. Cerchez, *Ultrashort laser pulse interaction with overdense plasmas*. PhD thesis, Heinrich-Heine Universität Düsseldorf, 2008.

[26] H. Ahmed, *Optimisation of Laser Driven Proton Beams and Their Applications to Plasma Radiography*. PhD thesis, Queen's University Belfast, 2013.

[27] A. Macchi, S. Veghini, T. V. Liseykina, and F. Pegoraro, "Radiation pressure acceleration of ultrathin foils," *New Journal of Physics*, vol. 12, p. 045013, Apr 2010.

[28] Heinrich Heine University Düsseldorf, "Absorption processes , ponderomotive force , thermal transport , magnetic field generation," 2016.

[29] Z.-M. Sheng, W. Su-Ming, Y. Lu-Le, W. Wei-Min, Y.-Q. Cui, M. Chen, and J. Zhang, "Absorption of ultrashort intense lasers in laser – solid interactions," *Chinese Physics B*, vol. 24, no. 1, pp. 1–14, 2015.

[30] S. V. Nazarenko, A. C. Newel, and A. M. Rubenchik, "Resonant absorption of short pulses," *Physics Letters A*, vol. 197, pp. 159–163, 1995.

[31] A. L. Meadowcroft and R. D. Edwards, "High-Energy Bremsstrahlung Diagnostics to Characterize Hot-Electron Production in Short-Pulse Laser-Plasma Experiments," *IEEE Transactions on Plasma Science*, vol. 40, no. 8, pp. 1992–2001, 2012.

[32] P. Kumar and V. K. Tripathi, "Vacuum electron heating by surface plasma wave," *Applied Physics Letters*, vol. 99, no. 021502, pp. 1–5, 2011.

[33] M. K. Grimes, Y.-S. Lee, and M. C. Downer, "Vacuum Heating vs. Resonance Absorption in the Solid to Plasma Transition of fs-Laser-Irradiated Iron and Aluminium," in *Ultrafast Phenomena XI: Proceedings of the 11th International Conference, Garmisch-Partenkirchen, Germany, July 12–17, 1998*, pp. 398–400, Berlin, Heidelberg: Springer Berlin Heidelberg, 1998.

[34] T. Liseykina, P. Mulser, and M. Murakami, "Collisionless absorption, hot electron generation, and energy scaling in intense laser-target interaction," *Physics of Plasmas*, pp. 1–12, 2014.

[35] I. Y. Dodin and N. J. Fisch, "Correction to the Alfvén-Lawson criterion for relativistic electron beams," *Physics of Plasmas*, vol. 13, no. 103104, pp. 1–7, 2006.

[36] T. Y. W. Ma, *Electron Generation and Transport in Intense Relativistic Laser-Plasma Interactions Relevant to Fast Ignition ICF*. Phd thesis, University of California, San Diego, 2010.

[37] A. P. L. Robinson, D. J. Strozzi, J. R. Davies, L. Gremillet, J. J. Honrubia, T. Johzaki, R. J. Kingham, M. Sherlock, and A. A. Solodov, "Theory of Fast Electron Transport for Fast Ignition," *Nuclear Fusion*, vol. 54, no. 5, pp. 1–78, 2014.

[38] F. Hanton, *Laser Ion Acceleration from Ultrathin Foils and Application to Radiobiology*. PhD thesis, Queen's University Belfast, 2015.

[39] M. Hegelich, S. Karsch, G. Pretzler, D. Habs, K. Witte, W. Guenther, M. Allen, a. Blazevic, J. Fuchs, J. Gauthier, M. Geissel, P. Audebert, T. Cowan, and M. Roth, "MeV Ion Jets from Short-Pulse-Laser Interaction with Thin Foils," *Physical Review Letters*, vol. 89, p. 085002, Aug 2002.

[40] K. Harres, M. Schollmeier, E. Brambrink, P. Audebert, A. Blazević, K. Flippo, D. C. Gautier, M. Geissel, B. M. Hegelich, F. Nürnberg, J. Schreiber, H. Wahl, and M. Roth, "Development and calibration of a Thomson parabola with microchannel plate for the detection of laser-accelerated MeV ions.," *Review of Scientific Instruments*, vol. 79, p. 093306, Sep 2008.

[41] E. Brambrink, J. Schreiber, T. Schlegel, P. Audebert, J. Cobble, J. Fuchs, M. Hegelich, and M. Roth, "Transverse Characteristics of Short-Pulse Laser-Produced Ion Beams: A Study of the Acceleration Dynamics," *Physical Review Letters*, vol. 96, p. 154801, Apr 2006.

[42] R. A. Snavely, M. H. Key, S. P. Hatchett, T. E. Cowan, M. Roth, T. W. Phillips, M. A. Stoyer, E. A. Henry, T. C. Sangster, M. S. Singh, S. C. Wilks, A. MacKinnon, A. Offenberger, D. M. Pennington, K. Yasuike, a. B. Langdon, B. F. Lasinski, J. Johnson, M. D. Perry, and E. M. Campbell, "Intense high-energy proton beams from Petawatt-laser irradiation of solids.," *Physical review letters*, vol. 85, pp. 2945–8, Oct 2000.

[43] S. Steinke, P. Hilz, M. Schnürer, G. Priebe, J. Bränzel, F. Abicht, D. Kiefer, C. Kreuzer, T. Ostermayr, J. Schreiber, a. Andreev, T. Yu, a. Pukhov, and W. Sandner, "Stable laser-ion acceleration in the light sail regime," *Physical Review Special Topics - Accelerators and Beams*, vol. 16, p. 011303, Jan 2013.

[44] E. Clark, K. Krushelnick, M. Zepf, F. Beg, M. Tatarakis, a. Machacek, M. Santala, I. Watts, P. Norreys, and A. Dangor, "Energetic heavy-Ion and proton generation from ultraintense laser-plasma interactions with solids," *Physical review letters*, vol. 85, pp. 1654–7, Aug 2000.

[45] D. Gwynne, "Biological Effects of Laser-Driven Ions at Ultra-high Dose Rates," tech. rep., 2013.

[46] S. Kar, K. Kakolee, B. Qiao, a. Macchi, M. Cerchez, D. Doria, M. Geissler, P. McKenna, D. Neely, J. Osterholz, R. Prasad, K. Quinn, B. Ramakrishna, G. Sarri, O. Willi, X. Yuan, M. Zepf, and M. Borghesi, "Ion Acceleration in Multispecies Targets Driven by Intense Laser Radiation Pressure," *Physical Review Letters*, vol. 109, p. 185006, Nov 2012.

[47] K. F. Kakolee, S. Kar, D. Doria, B. Qiao, M. Geissler, B. Ramakrishna, G. Sarri, K. Quinn, M. Zepf, and M. Borghesi, "Scaling of ion spectral peaks in a hybrid RPA-TNSA regime," *Central Laser Facility Annual Report 2010-2011*, no. RAL-TR-2011-025, 2011.

[48] M. Borghesi, "Radiation pressure acceleration of ions from thin foils irradiated by high intensity pulses," in *Superstrong Fields in Plasmas, Varenna 4-8th October 2010*, Presentation for Superstrong Fields in Plasmas, Varenna 4-8th October 2010, 2010.

[49] A. Macchi and C. Benedetti, "Ion acceleration by radiation pressure in thin and thick targets," *Nuclear Instruments and Methods in Physics Research A*, no. 1, 2010.

[50] C. Scullion, *Investigations of ion acceleration from solid targets driven by ultrashort laser pulses*. PhD thesis, Queen's University Belfast, 2017.

[51] K. Naughton, *Characterization and optimization of laser-driven ion acceleration*. PhD thesis, Queen's University Belfast, 2017.

[52] A. Macchi, M. Borghesi, and M. Passoni, "Ion acceleration by superintense laser-plasma interaction," *Reviews of Modern Physics*, vol. 85, pp. 751–793, May 2013.

[53] G. Schaumann, M. Schollmeier, G. Rodriguez-Prieto, A. Blazevic, E. Brambrink, M. Geissel, S. Korostiy, P. Pirzadeh, M. Roth, F. Rosmej, A. Faenov, T. Pikuz, K. Tsigutkin, Y. Maron, N. Tahir, and D. Hoffmann, "High energy heavy ion jets emerging from laser plasma generated by long pulse laser beams from the NHELIX laser system at GSI," *Laser and Particle Beams*, vol. 23, pp. 503–512, 2005.

[54] R. Wang, F. Jin, and H. Zhong, "A novel experimental hypoxia chamber for cell culture," *American Journal of Cancer Research*, vol. 4, no. 1, pp. 53–60, 2014.

[55] G. M. Petrov, C. McGuffey, A. G. R. Thomas, K. Krushelnick, and F. N. Beg, "Generation of heavy ion beams using femtosecond laser pulses in the target normal sheath acceleration and radiation pressure acceleration regimes," *Physics of Plasmas*, vol. 23, no. 063108, 2016.

[56] K. W. D. Ledingham, P. McKenna, T. McCanny, S. Shimizu, J. M. Yang, L. Robson, J. J Zweit, M. Gillies, J. Bailey, G. N. Chimon, R. J. Clarke, D. Neely, P. A. Norreys, J. L. Collier, R. P. Singhal, M. S. Wei, S. P. D. Mangles, P. Nilson, K. Krushelnick, and M. Zepf, "K W D Ledingham, P McKenna, T McCanny, S Shimizu, J M Yang, L Robson, J Zweit, J M Gillies, J Bailey, G N Chimon," *Journal of Physics D: Applied Physics*, vol. 37, no. 16, 2004.

[57] J. Fuchs, P. Antici, E. D'Humières, E. Lefebvre, M. Borghesi, E. Brambrink, C. a. Cecchetti, M. Kaluza, V. Malka, M. Manclossi, S. Meyroneinc, P. Mora, J. Schreiber, T. Toncian, H. Pépin, and P. Audebert, "Laser-driven proton scaling laws and new paths towards energy increase," *Nature Physics*, vol. 2, pp. 48–54, Dec 2005.

[58] B. Qiao, S. Kar, M. Geissler, P. Gibbon, M. Zepf, and M. Borghesi, "Dominance of Radiation Pressure in Ion Acceleration with Linearly Polarized Pulses at Intensities of 10^{21}Wcm^{-2}," *Physical Review Letters*, vol. 108, p. 115002, Mar 2012.

[59] J. Schreiber, "Ion Acceleration driven by High-Intensity Laser Pulses," vol. 23, no. August, 2006.

[60] T. Esirkepov, M. Borghesi, S. Bulanov, G. Mourou, and T. Tajima, "Highly Efficient Relativistic-Ion Generation in the Laser-Piston Regime," *Physical Review Letters*, vol. 92, p. 175003, Apr 2004.

[61] H. B. Zhuo, Z. L. Chen, W. Yu, Z. M. Sheng, M. Y. Yu, Z. Jin, and R. Kodama, "Quasimonoenergetic Proton Bunch Generation by Dual-Peaked Electrostatic-Field Acceleration in Foils Irradiated by an Intense Linearly Polarized Laser," *Physical Review Letters*, vol. 105, no. 6, pp. 065003–065006, 2010.

[62] A. Henig, S. Steinke, M. Schnürer, T. Sokollik, R. Hörlein, D. Kiefer, D. Jung, J. Schreiber, B. M. Hegelich, X. Q. Yan, J. Meyer-ter Vehn, T. Tajima, P. V. Nickles, W. Sandner, and D. Habs, "Radiation-Pressure Acceleration of Ion Beams Driven by Circularly Polarized Laser Pulses," *Physical Review Letters*, vol. 103, p. 245003, Dec 2009.

[63] B. M. Hegelich, B. J. Albright, J. Cobble, K. Flippo, S. Letzring, M. Paffett, H. Ruhl, J. Schreiber, R. K. Schulze, and J. C. Fernández, "Laser acceleration of quasi-monoenergetic MeV ion beams.," *Nature*, vol. 439, pp. 441–4, Jan 2006.

[64] D. Jung, L. Yin, B. J. Albright, D. C. Gautier, R. Hörlein, D. Kiefer, a. Henig, R. Johnson, S. Letzring, S. Palaniyappan, R. Shah, T. Shimada, X. Q. Yan, K. J. Bowers, T. Tajima, J. C. Fernández, D. Habs, and B. M. Hegelich, "Monoenergetic Ion Beam Generation by Driving Ion Solitary Waves with Circularly Polarized Laser Light," *Physical Review Letters*, vol. 107, p. 115002, Sep 2011.

[65] S. Kar, K. F. Kakolee, B. Qiao, A. MacChi, M. Cerchez, D. Doria, M. Geissler, P. McKenna, D. Neely, J. Osterholz, R. Prasad, K. Quinn, B. Ramakrishna, G. Sarri, O. Willi, X. Y. Yuan, M. Zepf, and M. Borghesi, "Ion acceleration in multispecies targets driven by intense laser radiation pressure," *Physical Review Letters*, vol. 109, no. 18, 2012.

[66] M. Passoni, L. Bertagna, and A. Zani, "Target normal sheath acceleration: theory, comparison with experiments and future perspectives," *New Journal of Physics*, vol. 12, p. 045012, Apr 2010.

[67] K. Zeil, S. D. Kraft, S. Bock, M. Bussmann, T. E. Cowan, T. Kluge, J. Metzkes, T. Richter, R. Sauerbrey, and U. Schramm, "The scaling of proton energies in ultrashort pulse laser plasma acceleration," *New Journal of Physics*, vol. 12, 2010.

[68] D. Wu, B. Qiao, X. T. He, C. McGuffey, and F. N. Beg, "Generation of high-energy monoenergetic heavy ion beams by radiation pressure acceleration of ultra-intense laser pulses," *arXiv preprint arXiv: ...*, pp. 10–14, 2014.

[69] D. Strickland and G. Mourou, "Compression of Amplified Chirped Optical Pulses," *Optics Communications*, vol. 56, no. 3, pp. 219–221, 1985.

[70] M. D. Perry and G. Mourou, "Terawatt to petawatt subpicosecond lasers," *Science*, vol. 264, no. 5161, pp. 917–924, 1994.

[71] J. H. V. Price, A. Malinowski, A. Piper, F. He, W. Belardi, T. M. Monro, M. Ibsen, B. C. Thomsen, Y. Jeong, C. Codemard, M. A. F. Roelens, P. Dupriez, J. K. Sahu, J. Nilsson, and D. J. Richardson, "Advances in high power , short pulse , fiber laser systems and technology," in *SPIE*, pp. 1–9, 2005.

[72] I. Jovanovic, "Chirped-Pulse Amplification: Ultrahigh peak power production from compact short-pulse laser systems," *Optik and Photonik*, vol. 4, pp. 30–33, 2010.

[73] P. Maine, D. Strickland, P. Bado, M. Pessot, and G. Mourou, "Generation of Ultrahigh Peak Power Pulses by Chirped Pulse Amplification," *IEEE Journal of Quantum Electronics*, vol. 24, no. 2, pp. 398–403, 1988.

[74] G. Mourou, "Invited paper The ultrahigh-peak-power laser : present and future," *Applied Physics B*, vol. 65, pp. 205–211, 1997.

[75] G. A. Mourou, T. Tajima, and S. V. Bulanov, "Optics in the relativistic regime," *Reviews of Modern Physics*, vol. 78, 2006.

[76] Y.-H. Chuang, L. Zheng, and D. D. Meyerhofer, "Propagation of Light Pulses in a Chirped-Pulse-Amplification Laser," *IEEE Journal of Quantum Electronics*, vol. 29, no. I, pp. 270–280, 1993.

[77] I. N. Ross, P. Matousek, M. Towrie, A. J. Langley, and J. L. Collier, "The prospects for ultrashort pulse duration and ultrahigh intensity using optical parametric chirped pulse amplifiers," *Optics Communications*, vol. 144, pp. 125–133, 1997.

[78] S. Fourmaux, S. Payeur, S. Buffechoux, P. Lassonde, C. St-Pierre, F. Martin, and J. C. Kieffer, "Pedestal cleaning for high laser pulse contrast ratio with a 100 TW class laser system," *Optics Express*, vol. 19, no. 9, pp. 8486–8497, 2011.

[79] Y.-H. Wang, X. Pan, X.-C. Li, and Z.-Q. Lin, "Optimization of Pulse Temporal Contrast in Optical Parametric Chirped Pulse Amplification," *Chinese Physics Letters*, vol. 26, no. 2, p. 024211, 2009.

[80] B. Dromey, S. Kar, M. Zepf, and P. Foster, "The plasma mirror — A subpicosecond optical switch for ultrahigh power lasers," *Review of Scientific Instruments*, vol. 75, no. 3, pp. 645–649, 2004.

[81] M. J. V. Streeter, P. S. Foster, F. H. Cameron, R. Bickerton, S. Blake, P. Brummit, B. Costello, E. Divall, C. Hooker, P. Holligan, D. R. Neville, P. P. Rajeev, D. Rose, J. Suarez-Merchan, D. Neely, D. C. Carroll, L. Romagnani, and M. Borghesi, "Astra Gemini compact plasma mirror system," *Central Laser Facility Annual Report 2008-2009*, pp. 225–227, 2009.

[82] G. G. Scott, V. Bagnoud, C. Barbetz, R. J. Clarke, J. S. Green, R. Heathcote, H. W. Powell, B. Zielbauer, T. D. Arber, P. McKenna, and D. Neely, "Optimization of plasma mirror re fl ectivity and optical quality using double laser pulses," *New Journal of Physics*, vol. 17, no. 33027, pp. 1–10, 2015.

[83] G. Doumy, F. Quéré, O. Gobert, M. Perdrix, and P. Martin, "Complete characterization of a plasma mirror for the production of high-contrast ultraintense laser pulses," *Physical Review E*, vol. 69, no. 026402, pp. 1–12, 2004.

[84] C. Thaury, F. Quéré, J.-P. Geindre, A. Levy, T. Ceccotti, P. Monot, M. Bougeard, F. Réau, P. D'Oliveira, P. Audebert, R. Marjoribanks, and P. H. Martin, "Plasma mirrors for ultrahigh-intensity optics," *Nature Physics*, vol. 3, pp. 424–429, 2007.

[85] D. C. Carroll, O. Tresca, R. Prasad, L. Romagnani, P. S. Foster, P. Gallegos, S. Ter-Avetisyan, J. S. Green, M. J. V. Streeter, N. Dover, C. A. J. Palmer, C. M. Brenner, F. H. Cameron, K. E. Quinn, J. Schreiber, A. P. L. Robinson, T. Baeva, M. N. Quinn, X. H. Yuan, Z. Najmudin, M. Zepf, D. Neely, M. Borghesi, and P. McKenna, "Carbon ion acceleration from thin foil targets irradiated by ultrahigh-contrast, ultraintense laser pulses," *New Journal of Physics*, vol. 12, no. 045020, pp. 1–15, 2010.

[86] Science and Technology Facilities Council, "Vulcan Laser," 2016.

[87] Science and Technology Facilities Council, "Short pulse laser oscillator," 2016.

[88] C. N. Danson, P. A. Brummitt, R. J. Clarke, J. L. Collier, B. Fell, A. J. Frackiewicz, S. Hawkes, C. Hernandez-Gomez, P. Holligan, M. H. R. Hutchinson, A. K. Kidd, W. J. Lester, I. O. Musgrave, D. Neely, D. R. Neville, P. A. Norreys, D. A. Pepler, C. J. Reason, W. Shaikh, T. Winstone, R. W. W. Wyatt, and B. E. Wyborn, "Vulcan petawatt: Design, operation and interactions at 5x10 20 Wcm2," *Laser and Particle Beams*, vol. 23, no. 1, pp. 87–93, 2005.

[89] C. Danson, P. Brummitt, R. Clarke, J. Collier, B. Fell, A. Frackiewicz, S. Hancock, S. Hawkes, C. Hernandez-Gomez, P. Holligan, M. Hutchinson, A. Kidd, W. Lester, I. Musgrave, D. Neely, D. Neville, P. Norreys, D. Pepler, C. Reason, W. Shaikh, T. Winstone, B. Wyborn, and R. Wyatt, "Vulcan Petawatt — an ultra-high-intensity interaction facility," *Nuclear Fusion*, vol. 44, pp. S239–S246, 2004.

[90] Science and Technology Facilities Council, "Target Area Petawatt (TAP)," 2016.

[91] L'École Polytechnique, "LULI2000," 2016.

[92] L'École Polytechnique, "LULI2000 laser system," 2016.

[93] Laboratoire d'utilisation des lasers intenses - École Polytechnique, "Large-scale scientific infrastructure dedicated to laser-generated plasmas and applications," 2009.

[94] L'École Polytechnique, "LULI2000 experimental areas," 2016.

[95] C. L. S. Lewis, G. Nersisyan, M. Borghesi, D. Doria, B. Dromey, T. Dzelzainis, M. Makita, K. McKeever, D. Riley, S. White, D. Marlow, G. Williams, and M. Zepf, "The TARANIS laser : A multi-terawatt system for laser plasma physics," in *XXVII International Conference on Photonic, Electronic and Atomic Collisions (IPEAC 2011)*, p. 152036, 2012.

[96] T. Dzelzainis, G. Nersisyan, D. Riley, L. Romagnani, H. Ahmed, a. Bigongiari, M. Borghesi, D. Doria, B. Dromey, M. Makita, S. White, S. Kar, D. Marlow, B. Ramakrishna, G. Sarri, M. Zaka-Ul-Islam, M. Zepf, and C. Lewis, "The TARANIS laser: A multi-Terawatt system for laser-plasma investigations," *Laser and Particle Beams*, vol. 28, pp. 451–461, Jul 2010.

[97] Science and Technology Facilities Council, "The Astra Gemini Facility," 2016.

[98] J. Collier, O. Chekhlov, R. Clarke, E. Divall, K. Ertel, B. Fell, P. Foster, J. Govans, S. Hancock, S. Hawkes, P. Holligan, C. Hooker, H. Hutchinson, S. Karsh, A. Langley, W. Lester, W. Martin, D. Neely, P. Norreys, M. Pitts, C. Reason, J. Smith, T. Winstone, R. Wyatt, and B. Wyborn, "The Astra "Gemini" Project," *Central Laser Facility Annual Report 2003-2004*, pp. 182–183, 2004.

[99] Science and Technology Facilities Council, "Laser system - Gemini," 2016.

[100] D. S. Hey, M. H. Key, a. J. Mackinnon, a. G. MacPhee, P. K. Patel, R. R. Freeman, L. D. Van Woerkom, and C. M. Castaneda, "Use of GafChromic film to diagnose laser generated proton beams.," *The Review of scientific instruments*, vol. 79, p. 053501, May 2008.

[101] F. Girard, H. Bouchard, and F. Lacroix, "Reference dosimetry using radiochromic film," *Journal of Applied Clinical Medical Physics*, vol. 13, no. 6, pp. 339–353, 2012.

[102] A. Mančić, J. Fuchs, P. Antici, S. A. Gaillard, and P. Audebert, "Absolute calibration of photostimulable image plate detectors used as ( 0 . 5 – 20 MeV ) high-energy proton detectors," *Review of Scientific Instruments*, vol. 79, no. 073301, pp. 1–6, 2008.

[103] I. J. Paterson, R. J. Clarke, N. C. Woolsey, and G. Gregori, "Image plate response for conditions relevant to laser – plasma interaction experiments," *Measurement Science and Technology*, vol. 19, no. 095301, pp. 1–5, 2008.

[104] D. Doria, S. Kar, H. Ahmed, A. Alejo, J. Fernandez, M. Cerchez, R. J. Gray, F. Hanton, D. A. MacLellan, P. McKenna, Z. Najmudin, D. Neely, L. Romagnani, J. A. Ruiz, G. Sarri, C. Scullion, M. Streeter, M. Swantusch, O. Willi, M. Zepf, and M. Borghesi, "Calibration of BAS-TR image plate response to high energy (3-300 MeV) carbon ions," *Review of Scientific Instruments*, vol. 86, no. 12, pp. 0–6, 2015.

[105] R. Clarke, P. Simpson, S. Kar, J. Green, C. Bellei, D. Carroll, B. Dromey, S. Kneip, K. Markey, P. McKenna, W. Murphy, S. Nagel, L. Willingale, and M. Zepf, "Nuclear activation as a high dynamic range diagnostic of laser–plasma interactions," *Nuclear Instruments and Methods in Physics Research Section A: Accelerators, Spectrometers, Detectors and Associated Equipment*, vol. 585, pp. 117–120, Feb 2008.

[106] F. Nürnberg, M. Schollmeier, E. Brambrink, a. Blazević, D. C. Carroll, K. Flippo, D. C. Gautier, M. Geissel, K. Harres, B. M. Hegelich, O. Lundh, K. Markey, P. McKenna, D. Neely, J. Schreiber, and M. Roth, "Radiochromic film imaging spectroscopy of laser-accelerated proton beams.," *The Review of scientific instruments*, vol. 80, p. 033301, Mar 2009.

[107] R. L. Fleischer, P. B. Price, and R. M. Walker, "Ion Explosion Spike Mechanism for Formation of Charged - Particle Tracks in Solids Published by the AIP Publishing Articles you may be interested in Charged - particle thermonuclear reactions Chemical Etching of Charged - Particle Tracks in Solids Observa," *Journal of Applied Physics*, vol. 36, no. 11, pp. 3645–3652, 1965.

[108] S. Kar, M. Borghesi, L. Romagnani, S. Takahashi, A. Zayats, V. Malka, S. Fritzler, and A. Schiavi, "Analysis of latent tracks for MeV protons in CR-39 Analysis of latent tracks for MeV protons in CR-39," *Journal of Applied Physics*, vol. 101, no. 044510, pp. 044510–(1–5), 2007.

[109] A. Kashefian Naieni, F. Bahrami, N. Yasrebi, and B. Rashidian, "Design and study of an enhanced Faraday cup detector," *Vacuum*, vol. 83, pp. 1095–1099, May 2009.

[110] D. Gwynne, S. Kar, D. Doria, H. Ahmed, M. Cerchez, J. Fernandez, R. J. Gray, J. S. Green, F. Hanton, D. A. Maclellan, P. McKenna, Z. Najmudin, D. Neely, J. A. Ruiz, A. Schiavi, M. Streeter, M. Swantusch, O. Willi, M. Zepf, and M. Borghesi, "Modified Thomson spectrometer design for high energy, multi-species ion sources," *Review of Scientific Instruments*, vol. 85, p. 033304, Mar 2014.

[111] A. Alejo, S. Kar, H. Ahmed, A. G. Krygier, D. Doria, R. Clarke, J. Fernandez, R. R. Freeman, J. Fuchs, A. Green, J. S. Green, D. Jung, A. Kleinschmidt, C. L. S. Lewis, J. T. Morrison, Z. Najmudin, H. Nakamura, G. Nersisyan, P. Norreys, M. Notley, M. Oliver, M. Roth, J. a. Ruiz, L. Vassura, M. Zepf, and M. Borghesi, "Characterisation of deuterium spectra from laser driven multi-species sources by employing differentially filtered image plate detectors in Thomson spectrometers.," *The Review of Scientific Instruments*, vol. 85, p. 93303, Sep 2014.

[112] A. Alejo, S. Kar, A. Tebartz, H. Ahmed, S. Astbury, D. C. Carroll, J. Ding, D. Doria, A. Higginson, P. Mckenna, N. Neumann, G. G. Scott, F. Wagner, M. Roth, and M. Borghesi, "High resolution Thomson Parabola Spectrometer for full spectral capture of multi- species ion beams.," *Review of Scientific Instruments*, vol. 87, no. 083304, p. 083304, 2016.

[113] A. Alejo, D. Gwynne, D. Doria, H. Ahmed, D. C. Carroll, R. J. Clarke, D. Neely, G. G. Scott, M. Borghesi, and S. Kar, "Recent developments in the Thomson Parabola Spectrometer diagnostic for laser-driven multi-species ion sources," in *Journal of Instrumentation: 4th International Conference Frontiers in Diagnostics Technologies*, (Frascati, Rome, Italy), pp. 1–13, IOP Publishing, 2016.

[114] M. J. Rhee, R. F. Schneider, and D. J. Weidman, "Simple time-resolving Thomson spectrometer," *Review of Scientific Instruments*, vol. 58, no. 2, p. 240, 1987.

[115] W. Mroz, P. Norek, a. Prokopiuk, P. Parys, M. Pfeifer, L. Laska, M. P. Stockli, D. Fry, and K. Kasuya, "Method of processing ion energy distributions using a Thomson parabola ion spectrograph with a microchannelplate image converter camera," *Review of Scientific Instruments*, vol. 71, no. 3, p. 1417, 2000.

[116] D. Carroll, P. Brummitt, D. Neely, F. Lindau, O. Lundh, C.-G. Wahlström, and P. McKenna, "A modified Thomson parabola spectrometer for high resolution multi-MeV ion measurements—Application to laser-driven ion acceleration," *Nuclear Instruments and Methods in Physics Research Section A: Accelerators, Spectrometers, Detectors and Associated Equipment*, vol. 620, pp. 23–27, Aug 2010.

[117] Fujifilm, "Fujifilm Global: Value from Innovation," 2016.

[118] P. R. Bolton, M. Borghesi, C. Brenner, D. C. Carroll, C. D. Martinis, F. Fiorini, A. Flacco, V. Floquet, J. Fuchs, P. Gallegos, D. Giove, J. S. Green, S. Green, B. Jones, D. Kirby, P. Mckenna, D. Neely, F. Nuesslin, R. Prasad, S. Reinhardt, M. Roth, U. Schramm, G. G. Scott, S. Ter-Avetisyan, M. Tolley, G. Turchetti, and J. J. Wilkens, "Physica Medica Instrumentation for diagnostics and control of laser-accelerated proton ( ion ) beams," *Physica Medica*, vol. 30, no. 3, pp. 255–270, 2014.

[119] W. Liang, Y. Li, M. Xu, X. Yuan, Z. Zheng, Y. Zhang, F. Liu, Z. Wang, H. Li, Z. Jin, Z. Wei, W. Zhao, Y. Li, and J. Zhang, "Study of hot electrons generated from intense laser-plasma interaction employing Image Plate," *Science in China Series G: Physics, Mechanics & Astronomy*, vol. 51, no. 10, pp. 1455–1462, 2008.

[120] G. Nave, C. J. Sansonetti, C. I. Szabo, J. J. Curry, and D. G. Smillie, "Use of phosphor image plates for measuring intensities in vacuum ultraviolet spectra," *Review of Scientific Instruments*, vol. 82, no. 013107, pp. 1–9, 2011.

[121] G. Fiksel, F. J. Marshall, C. Mileham, and C. Stoeckl, "Note : Spatial resolution of Fuji BAS-TR and BAS-SR imaging plates," *Review of Scientific Instruments*, vol. 83, no. 086103, pp. 1–3, 2012.

[122] Z. Li, D. Wen, D. Chen, S. Peng, L. Zhang, and K. Shi, "A study of dosimetry characteristics of GAF DM-1260 radiochromic films," *Radiation Physics and Chemistry*, vol. 57, no. 2, pp. 103–113, 2000.

[123] J. Sorriaux, A. Kacperek, S. Rossomme, J. A. Lee, D. Bertrand, S. Vynckier, and E. Sterpin, "Evaluation of Gafchromic EBT3 films characteristics in therapy photon, electron and proton beams," *Physica Medica*, vol. 29, no. 6, pp. 599–606, 2013.

[124] A. L. Palmer, D. A. Bradley, and A. Nisbet, "Evaluation and mitigation of potential errors in radiochromic film dosimetry due to film curvature at scanning," *Journal of Applied Clinical Medical Physics*, vol. 16, no. 2, pp. 425–431, 2015.

[125] S. Reinhardt, M. Würl, C. Greubel, N. Humble, J. J. Wilkens, M. Hillbrand, A. Mairani, W. Assmann, and K. Parodi, "Investigation of EBT2 and EBT3 films for proton dosimetry in the 4 – 20 MeV energy range," *Radiation and Environmental Biophysics*, vol. 54, pp. 71–79, 2015.

[126] Ashland International Specialty Products, "Gafchromic rdiotherapy films," 2016.

[127] A. Niroomand-Rad, C. R. Blackwell, B. M. Coursey, K. P. Gall, J. M. Galvin, W. L. McLaughlin, A. S. Meigooni, R. Nath, J. E. Rodgers, C. G. Soares, A. Niroomandrad, C. R. Blackwell, B. M. Coursey, K. P. Gall, J. M. Galvin, and W. L. Mclaughlin, "Radiochromic film dosimetry : Recommendations of AAPM Radiation Therapy Committee Task Group 55," *Medical Physics*, vol. 25, no. 2093, pp. 1–23, 1998.

[128] M. T. Bahreyni Toossi, F. Khorshidi, M. Ghorbani, N. Mohamadian, and D. Davenport, "Comparison of EBT and EBT3 RadioChromic Film Usage in Parotid Cancer Radiotherapy," *Journal of Biomedical Physics adn Engineering*, vol. 6, no. 1, pp. 1–12, 2016.

[129] Ashland International Specialty Products, "Gafchromic Dosimetry Media, Type EBT-3," tech. rep., 2016.

[130] O. Ettlinger, J. S. Green, D. Neely, D. Parker, and S. Green, "A comparison of different radiochromic film types," *Central Laser Facility Annual Report 2011-2012*, pp. 4–8, 2012.

[131] D. Kirby, S. Green, H. Palmans, R. Hugtenburg, C. Wojnecki, and D. Parker, "LET dependence of GafChromic films and an ion chamber in low-energy proton dosimetry," *Physics in Medicine and Biology*, vol. 55, pp. 417–433, 2010.

[132] L. Pecorino, *Molecular Biology of Cancer: Mechanisms, Targets, and Therapeutics*. Oxford University Press, 2nd ed., 2008.

[133] R. J. King, *Cancer Biology*. Harlow: Longman, 1st ed., 1996.

[134] E. LaTorre Travis, *Medical Radiobiology*. St. Louis: Mosby-Year Book, Inc, 2nd ed., 1989.

[135] P. Dendy and B. Heaton, *Medical Science Series: Physics for Diagnostic Radiology*. Bristol: Institute of Physics Publishing, 2nd ed., 2002.

[136] International Commision on Radiation Units and Measurements, "Average Energy Required to Produce an Ion Pair (Report 31)," tech. rep., International Commission on Radiation Units and Measurements, 1979.

[137] K. Bethge, G. Kraft, P. Kreisler, and G. Walter, *Medical Applications of Nuclear Physics*. Berlin: Springer Verlag, 1st ed., 2004.

[138] N. Dyson, *Radiation Physics with applications in Medicine and Biology*. Chichester: Ellis Horwood Limited, 2nd ed., 1993.

[139] E. J. Hall and A. J. Giaccia, *Radiobiology for the Radiologist*. Philadelhpia: Lippincott Williams and Wilkins, 6th ed., 2006.

[140] S. Amador Kane, *Introduction to Physics in Modern Medicine*. Taylor and Francis, 1st ed., 2003.

[141] J. Itzhaki, "DNA damage recognition: keeping the right players on board," 2012.

[142] Columbia University Centre for Radiological Research, "Interactions of Radiation with Matter," 2013.

[143] A. V. Akleyev, *Chronic Radiation Syndrome*. 2014.

[144] K. Hiom, "Coping with DNA double strand breaks," *DNA Repair*, vol. 9, no. 12, pp. 1256–1263, 2010.

[145] M. Valko, M. Izakovic, M. Mazur, C. J. Rhodes, and J. Telser, "Role of oxygen radicals in DNA damage and cancer incidence.," *Molecular and cellular biochemistry*, vol. 266, pp. 37–56, Nov 2004.

[146] J. M. Matés and F. M. Sánchez-Jiménez, "Role of reactive oxygen species in apoptosis: implications for cancer therapy.," *The international journal of biochemistry & cell biology*, vol. 32, pp. 157–70, Feb 2000.

[147] T. Yamamori, H. Yasui, M. Yamazumi, Y. Wada, Y. Nakamura, H. Nakamura, and O. Inanami, "Ionizing radiation induces mitochondrial reactive oxygen species production accompanied by upregulation of mitochondrial electron transport chain function and mitochondrial content under control of the cell cycle checkpoint," *Free Radical Biology and Medicine*, vol. 53, no. 2, pp. 260–270, 2012.

[148] E. I. Azzam, J.-P. Jay-Gerin, and D. Pain, "Ionizing radiation-induced metabolic oxidative stress and prolonged cell injury," *Cancer Letters*, vol. 327, pp. 48–60, 2012.

[149] L. Pecorino, *Molecular Biology of Cancer: Mechanisms, targets and Therapeutics*. Oxford: Oxford University Press, 3rd ed., 2012.

[150] J. K. Leach, G. Van Tuyle, P.-S. Lin, R. Schmidt-Ullrich, and R. B. Mikkelsen, "Ionizing Radiation-induced , Mitochondria-dependent Generation of Reactive Oxygen / Nitrogen 1," *Cancer Research*, no. 61, pp. 3894–3901, 2001.

[151] American Cancer Society, "The Science Behind Radiation Therapy," tech. rep., 2014.

[152] W. K. Sinclair and R. A. Morton, "X-Ray and Ultraviolet Sensitivity of Synchronised Chinese Hamster Cells at Various Stages of the Cell Cycle," *Biophysical Journal*, vol. 5, pp. 1–25, 1965.

[153] T. Terasima and L. J. Tolmach, "Variations in several responses of HeLa cells to X-irradiation during the division cycle," *Biophysical Journal*, vol. 3, no. 1, pp. 11–33, 1963.

[154] C. Hennequin, N. Giocanti, and V. Favaudon, "Interaction of Ionizing Radiation with Paclitaxel (Taxol) and Docetaxel (Taxotere) in HeLa and SQ2OB Cells," *Cancer Research*, vol. 56, pp. 1842–1850, 1996.

[155] S. Wang, C.-y. Guo, A. Castillo, P. Dent, and S. Grant, "Effect of Bryostatin 1 on Taxol-induced Apoptosis and Cytotoxicity in Human Leukemia Cells ( U937 )*," *Biochemical Pharmacology*, vol. 56, pp. 635–644, 1998.

[156] W. Zoli, L. Ricotti, F. Barzanti, M. Dal Susino, G. L. Frassineti, C. Milandri, D. Casadei Giunchi, and D. Amadori, "Scehdule-Dependent Interaction of Doxorubicin, Paclitaxel and Gemcitabine in Human Breast Cancer Cell Lines," *International Journal of Cancer*, vol. 80, pp. 413–416, 1999.

[157] T. M. Pawlik and K. Keyomarsi, "Role of Cell Cycle in Mediating Sensitivity to Radiotherapy," *International Journal of Radiation Oncology Biology Physics*, vol. 59, no. 4, pp. 928–942, 2004.

[158] E. J. Bernhard, A. Maity, R. J. Muschel, and W. G. Mckenna, "Effects of ionizing radiation on cell cycle progression.," *Radiation and Environmental Biophysics*, no. 34, pp. 79–83, 1995.

[159] I. Watanabe, "Radiation Effects on DNA Chain Growth in Mammalian Cells," *radiation Research*, vol. 58, no. 3, pp. 541–556, 1974.

[160] F. Makino and S. Okada, "Effects of Ionizing Radiations on DNA Replication in Cultured Mammalian Cells," *Radiation Research*, vol. 62, no. 1, pp. 37–51, 1975.

[161] P. M. Busse, S. K. Bose, R. W. Jones, and L. J. Tolmach, "The Action of Caffeine on X-Irradiated HeLa Cells: III. Enhancement of X-Ray-Induced Killing during G2 Arrest," *Radiation Research*, vol. 76, no. 2, pp. 292–307, 1978.

[162] T. Samuel, H. O. Weber, and J. O. Funk, "Linking DNA Damage to Cell Cycle Checkpoints," *Cell Ccyle*, vol. 1, no. 3, pp. 161–167, 2002.

[163] S. J. Collis, M. J. Swartz, W. G. Nelson, and T. L. Deweese, "Enhanced Radiation and Chemotherapy-mediated Cell Killing of Human Cancer Cells by Small Inhibitory RNA Silencing of DNA Repair Factors 1," *Cancer Research*, vol. 63, pp. 1550–1554, 2003.

[164] M. S. Meyn, "Ataxia-Telangiectasia and Cellular Responses to DNA Damage," *Cancer Research*, vol. 55, pp. 5991–6001, 1995.

[165] Y. Shiloh, "ATM and ATR : networking cellular responses to DNA damage," *Current Opinion in Genetics and Development*, vol. 11, pp. 71–77, 2001.

[166] L. H. Hartwell and T. E. D. A. Weinert, "Checkpoints : Controls That Ensure the Order of Cell Cycle Events," *Science*, vol. 246, pp. 629–634, 1989.

[167] L. H. Hartwell and M. B. Kastan, "Cell Cycle Control and Cancer," *Science*, vol. 266, pp. 1821–1828, 1994.

[168] B. Xu, S.-t. Kim, D.-s. Lim, and M. B. Kastan, "Two Molecularly Distinct G 2 / M Checkpoints Are Induced by Ionizing Irradiation," vol. 22, no. 4, pp. 1049–1059, 2002.

[169] R. J. Reynolds and J. A. Schecker, "Radiation, Cell Cycle, and Cancer," *Los Alamos Science*, no. 23, pp. 51–89, 1995.

[170] X. Li and W.-D. Heyer, "Homologous recombination in DNA repair and DNA damage tolerance.," *Cell research*, vol. 18, pp. 99–113, Jan 2008.

[171] A. Tutt, D. Bertwistle, J. Valentine, A. Gabriel, S. Swift, G. Ross, C. Griffin, J. Thacker, and A. Ashworth, "Mutation in Brca2 stimulates error-prone homology-directed repair of DNA double-strand breaks occurring between repeated sequences," *The EMBO Journal*, vol. 20, no. 17, pp. 4704–4716, 2001.

[172] M. R. Lieber, Y. Ma, U. Pannicke, and K. Schwarz, "Mechanism and regulation of human non-homologous DNA end-joining.," *Nature reviews. Molecular cell biology*, vol. 4, pp. 712–20, Sep 2003.

[173] R. Taleei, M. Weinfeld, and H. Nikjoo, "Single strand annealing mathematical model for double strand break repair," *Journal of Molecular Engineering & Systems Biology*, pp. 1–10, 2012.

[174] J. Xing, Y. Zhang, K. Han, A. H. Salem, S. K. Sen, C. D. Huff, Q. Zhou, E. F. Kirkness, S. Levy, M. A. Batzer, and L. B. Jorde, "Mobile elements create structural variation : Analysis of a complete human genome," *Genome Research*, vol. 19, no. 9, pp. 1516–1526, 2009.

[175] M. Frankenberg-Schwager, A. Gebauer, C. Koppe, H. Wolf, E. Pralle, and D. Frankenberg, "Single-Strand Annealing, Conservative Homologous Recombination, Nonhomologous DNA End Joining, and the Cell Cycle-Dependent Repair of DNA Double-Strand Breaks Induced by Sparsely or Densely Ionizing Radiation," *Radiation Research*, vol. 171, no. 3, pp. 265–273, 2009.

[176] G. Kraft, "Tumor therapy with heavy charged particles," *Progress in Particle and Nuclear Physics*, vol. 45, no. Supplement 2, pp. S473—-S544, 2000.

[177] Z. Chunxiang, D. E. Dunn, and R. Katz, "Radial Distribution of Dose and Cross-Sections for the Inactivation of Dry Enzymes and Viruses Inactivation of Dry Enzymes and Viruses," 1985.

[178] J. T. Bushberg and J. M. Boone, *The Essential Physics of Medical Imaging*. Lippincott Williams and Wilkins, 1st ed., 2011.

[179] C. Grassberger, A. Trofimov, A. Lomax, and H. Paganetti, "Variations in linear energy transfer within clinical proton therapy fields and the potential for biological treatment planning.," *International journal of radiation oncology, biology, physics*, vol. 80, pp. 1559–1566, Aug 2011.

[180] U. Linz, "Physical and Biological Rationale for Using Ions in Therapy," in *Ion Beam Therapy: Fundamentals, Technology, Clinical Applications* (U. Linz, ed.), ch. 4, pp. 45–59, Berlin: Springer Verlag, 1st ed., 2012.

[181] R. G. Bristow and R. P. Hill, "Hypoxia and metabolism. Hypoxia, DNA repair and genetic instability.," *Nature reviews. Cancer*, vol. 8, pp. 180–192, Mar 2008.

[182] P. Martenka and A. Roszak, "Tumour hypoxia as a predictive factor for radiotherapy," *Gin Onkol*, vol. 4, no. 2, pp. 99–107, 2006.

[183] T. Wenzl and J. J. Wilkens, "Modelling of the oxygen enhancement ratio for ion beam radiation therapy," *Physics in Medicine and Biology*, vol. 56, no. 11, pp. 3251–3268, 2011.

[184] J. C. Walsh, A. Lebedev, E. Aten, K. Madsen, L. Marciano, and H. C. Kolb, "The Clinical Importance of Assessing Tumor Hypoxia : Relationship of Tumor Hypoxia to Prognosis and Therapeutic Opportunities," *Antioxidants and Redox Signalling*, vol. 21, no. 10, pp. 1516–1554, 2014.

[185] T. Wenzl and J. J. Wilkens, "Theoretical analysis of the dose dependence of the oxygen enhancement ratio and its relevance for clinical applications.," *Radiation oncology (London, England)*, vol. 6, p. 171, Jan 2011.

[186] A. L. Harris, "Hypoxia–a key regulatory factor in tumour growth.," *Nature Reviews Cancer*, vol. 2, pp. 38–47, Jan 2002.

[187] L. H. Gray, A. D. Conger, M. Edbert, S. Hornsey, and O. C. Scott, "Concentration of oxygen dissolved in tissue at the time of irradiation as a factor in radiotherapy," *British Journal of Radiology*, vol. 26, no. 312, pp. 638–648, 1953.

[188] A. Wright and P. Howard-Flanders, "The influence of oxygen on the radiosensitivity of mammalian tissues," *Acta. Radiol*, vol. 48, no. 1, pp. 26–32, 1957.

[189] M. C. Brahimi-Horn, J. Chiche, and J. Pouysségur, "Hypoxia and cancer.," *Journal of Molecular Medicine (Berlin, Germany)*, vol. 85, pp. 1301–1307, Dec 2007.

[190] W. R. Wilson and M. P. Hay, "Targeting hypoxia in cancer therapy.," *Nature Reviews Cancer*, vol. 11, pp. 393–410, Jun 2011.

[191] R. Hirayama, Y. Furusawa, T. Fukawa, and K. Ando, "Repair kinetics of DNA-DSB induced by X-rays or Carbon Ions under Oxic and Hypoxic Conditions," *Journal of Radiation Research*, vol. 46, pp. 325–332, Sep 2005.

[192] J. M. Brown and W. R. Wilson, "Exploiting tumour hypoxia in cancer treatment.," *Nature Reviews Cancer*, vol. 4, pp. 437–47, Jun 2004.

[193] N.-Y. Ma, W. Tinganelli, A. Maier, M. Durante, and W. Kraft-Weyrather, "Influence of chronic hypoxia and radiation quality on cell survival.," *Journal of radiation research*, vol. 54 Suppl 1, pp. i13–22, Jul 2013.

[194] W. Tinganelli, N.-Y. Ma, C. Von Neubeck, A. Maier, C. Schicker, W. Kraft-Weyrather, and M. Durante, "Influence of acute hypoxia and radiation quality on cell survival.," *Journal of radiation research*, vol. 54 Suppl 1, pp. i23—-30, Jul 2013.

[195] D. Vordermark, D. R. Menke, and J. M. Brown, "Similar Radiation Sensitivities of Acutely and Chronically Hypoxic Cells in HT 1080 Fibrosarcoma Xenografts," *Radiation Research*, vol. 159, no. 1, pp. 94–101, 2003.

[196] L. Antonovic, E. Lindblom, A. Dasu, N. Bassler, Y. Furusawa, and I. Toma-Dasu, "Clinical oxygen enhancement ratio of tumors in carbon ion radiotherapy: The influence of local oxygenation changes," *Journal of Radiation Research*, vol. 55, no. 5, pp. 902–911, 2014.

[197] S. R. McKeown, "Defining normoxia, physoxia and hypoxia in tumours-implications for treatment response.," *The British Journal of Radiology*, vol. 87, no. 1035, pp. 20130676(1–12), 2014.

[198] G. L. Wang, B.-H. Jiang, E. A. Rue, and G. L. Semenza, "Hypoxia-inducible factor 1 is a basic-helix-loop-helix-PAS heterodimer regulated by cellular O2 tension," in *National Academy of Sciences of the United States of America*, vol. 92, pp. 5510–5514, 1995.

[199] M. Y. Koh and G. Powis, "Passing the baton : The HIF switch," *Trends in Biochemical Science*, vol. 37, no. 9, pp. 364–372, 2012.

[200] S. K. Burroughs, S. Kaluz, D. Wang, K. Wang, E. G. V. Meir, and B. Wang, "Therapeutics," vol. 5, no. 5, pp. 1–31, 2014.

[201] G. L. Semenza, "Hypoxia-Inducible Factors in Phsiology and Medicine," *Cell*, vol. 148, no. 3, pp. 399–408, 2013.

[202] J. Zhou, T. Schmid, S. Schnitzer, and B. Brüne, "Tumor hypoxia and cancer progression.," *Cancer letters*, vol. 237, pp. 10–21, Jun 2006.

[203] H. Yasuda, "Solid tumor physiology and hypoxia-induced chemo/radio-resistance: Novel strategy for cancer therapy: Nitric oxide donor as a therapeutic enhancer," *Nitric Oxide - Biology and Chemistry*, vol. 19, no. 2, pp. 205–216, 2008.

[204] H.-P. Kubis, N. Hanke, R. J. Scheibe, and G. Gros, "Accumulation and nuclear import of HIF1 alpha during high and low oxygen concentration in skeletal muscle cells in primary culture.," *Biochimica et biophysica acta*, vol. 1745, no. 2, pp. 187–195, 2005.

[205] R. P. Hill, D. T. Marie-Egyptienne, and D. W. Hedley, "Cancer Stem Cells, Hypoxia and Metastasis," *Seminars in Radiation Oncology*, vol. 19, no. 2, pp. 106–111, 2009.

[206] C. Befani, I. Mylonis, I.-M. Gkotinakou, P. Georgoulias, C.-J. Hu, G. Simos, and P. Liakos, "Cobalt stimulates HIF-1-dependent but inhibits HIF-2-dependent gene expression in liver cancer cells," *International Journal of Biochemistry and Cell Biology*, vol. 45, no. 11, pp. 1–18, 2008.

[207] D. M. Stroka, T. Burkhardt, I. Desbaillets, R. H. Wenger, D. a. Neil, C. Bauer, M. Gassmann, and D. Candinas, "HIF-1 is expressed in normoxic tissue and displays an organ-specific regulation under systemic hypoxia.," *The FASEB journal : official publication of the Federation of American Societies for Experimental Biology*, vol. 15, no. 13, pp. 2445–2453, 2001.

[208] S. N. Thomas, Z. Liao, D. Clark, Y. Chen, R. Samadani, L. Mao, D. K. Ann, J. E. Baulch, P. Shapiro, and A. J. Yang, "Exosomal Proteome Profiling: A Potential Multi-Marker Cellular Phenotyping Tool to Characterize Hypoxia-Induced Radiation Resistance in Breast Cancer.," *Proteomes*, vol. 1, no. 2, pp. 87–108, 2013.

[209] M. S. A. Okail, "Cobalt chloride , a chemical inducer of hypoxia-inducible factor-1 $\alpha$ in U251 human glioblastoma cell line," *Journal of Saudi Chemical Society*, vol. 14, no. 2, pp. 197–201, 2010.

[210] J.-P. Piret, D. Mottet, M. Raes, and C. Michiels, "CoCl2, a Chemical Inducer of Hypoxia-Inducible Factor-1, and Hypoxia Reduce Apoptotic Cell Death in Hepatoma Cell Line HepG2," *Annals of the New York Academy of Sciences*, vol. 973, pp. 443–447, 2002.

[211] A. Triantafyllou, P. Liakos, A. Tsakalof, E. Georgatsou, G. Simos, and S. Bonanou, "Cobalt induces hypoxia-inducible factor-1alpha (HIF-1alpha) in HeLa cells by an iron-independent, but ROS-, PI-3K- and MAPK-dependent mechanism.," *Free Radical Research*, vol. 40, no. 8, pp. 847–856, 2006.

[212] U. Linz and J. Alonso, "What will it take for laser driven proton accelerators to be applied to tumor therapy?," *Physical Review Special Topics - Accelerators and Beams*, vol. 10, p. 094801, Sep 2007.

[213] E. Fokas, G. Kraft, H. An, and R. Engenhart-Cabillic, "Ion beam radiobiology and cancer: time to update ourselves.," *Biochimica et biophysica acta*, vol. 1796, pp. 216–29, Dec 2009.

[214] T. I. Yock, B. Y. Yeap, D. H. Ebb, E. Weyman, B. R. Eaton, N. A. Sherry, R. M. Jones, S. M. MacDonald, M. B. Pulsifer, B. Lavally, A. N. Abrams, M. S. Huang, K. J. Marcus, and N. J. Tarbell, "Long-term toxic effects of proton radiotherapy for paediatric medulloblastoma: a phase 2 single-arm study," *The Lancet Oncology*, vol. 17, no. 3, pp. 287–298, 2016.

[215] NHS Choices, "Proton beam therapy 'effective' and 'causes fewer side effects'," 2016.

[216] J. P. C. Grutters, A. G. H. Kessels, M. Pijls-Johannesma, D. D. Ruysscher, M. A. Joore, and P. Lambin, "Comparison of the effectiveness of radiotherapy with photons, protons and carbon-ions for non-small cell lung cancer: A meta-analysis," *Radiotherapy and Oncology*, vol. 95, no. 1, pp. 32–40, 2010.

[217] R. D. Riley, J. P. T. Higgins, and J. J. Deeks, "Interpretation of random effects meta-analyses," *British Medical Journal*, vol. 342, no. 549, 2010.

[218] K. Peach, J. Cobb, T. Yokoi, I. Gardner, S. R. A. L. Isis, E. Stfc, R. A. L. Ppd, M. Poole, S. Astec, D. Uk, J. Pozimski, I. College, B. Cywinski, B. Jones, G. Mckenna, B. Vojnovic, M. Folkard, K. Kirkby, R. Webb, R. Barlow, A. Elliott, and B. O. Centre, "PAMELA – A Model for an FFAG Based Hadron Therapy Machine," in *PAC*, pp. 2880–2882, 2007.

[219] D. Schardt, "Tumor therapy with high-energy carbon ion beams," *Nuclear Physics A*, vol. 787, pp. 633–641, May 2007.

[220] W. Enghardt, J. Pawelke, M. Bussmann, T. Cowan, F. Fielder, U. Schramm, R. Sauerbrey, M. Kaluza, A. Tunnermann, and M. Baumann, "A technology platform for translational research on laser driven particle accelerators for radiotherapy," *Society of Photo-Optical Instrumentation Engineers*, vol. 8079, 2011.

[221] V. Malka, S. Fritzler, E. Lefebvre, E. D'Humieres, R. Ferrand, G. Grillon, C. Albaret, S. Meyroneinc, J. Chambaret, A. Antonetti, and D. Hulin, "Practicability of proton therapy using compact laser systems," *Medical Physics*, vol. 31, no. 6, pp. 1587–1592, 2004.

[222] P. Antici, M. Migliorati, a. Mostacci, L. Picardi, L. Palumbo, and C. Ronsivalle, "A compact post-acceleration scheme for laser-generated protons," *Physics of Plasmas*, vol. 18, no. 7, p. 073103, 2011.

[223] CERN Courier, "INFN and industry to build new cyclotron for hadron therapy," 2005.

[224] M. Murakami, Y. Hishikawa, S. Miyajima, Y. Okazaki, K. L. Sutherland, M. Abe, S. V. Bulanov, H. Daido, T. Z. Esirkepov, J. Koga, M. Yamagiwa, T. Tajima, and H. Daido, "Radiotherapy using a laser proton accelerator," *AIP Conference Proceedings*, vol. 1024, pp. 275–300, 2008.

[225] S. Auer, V. Hable, C. Greubel, G. a. Drexler, T. E. Schmid, C. Belka, G. Dollinger, and A. a. Friedl, "Survival of tumor cells after proton irradiation with ultra-high dose rates.," *Radiation oncology (London, England)*, vol. 6, p. 139, Jan 2011.

[226] M. Borghesi, S. Kar, R. Prasad, K. F. Kakolee, K. Quinn, H. Ahmed, G. Sarri, B. Ramakrishna, and B. Qiao, "Ion source development and radiobiology applications within the LIBRA project," *Society of Photo-Optical Instrumentation Engineers*, vol. 8079, 2011.

[227] D. Doria, K. F. Kakolee, S. Kar, S. K. Litt, F. Fiorini, H. Ahmed, S. Green, J. C. G. Jeynes, J. Kavanagh, D. Kirby, K. J. Kirkby, C. L. Lewis, M. J. Merchant, G. Nersisyan, R. Prasad, K. M. Prise, G. Schettino, M. Zepf, and M. Borghesi, "Biological effectiveness on live cells of laser driven protons at dose rates exceeding 109 Gys," *AIP Advances*, vol. 2, no. 1, p. 011209, 2012.

[228] E. Fourkal, I. Velchev, C.-M. Ma, and J. Fan, "Linear energy transfer of proton clusters.," *Physics in medicine and biology*, vol. 56, pp. 3123–36, May 2011.

[229] K. Zeil, M. Baumann, E. Beyreuther, T. Burris-Mog, T. E. Cowan, W. Enghardt, L. Karsch, S. D. Kraft, L. Laschinsky, J. Metzkes, D. Naumburger, M. Oppelt, C. Richter, R. Sauerbrey, M. Schürer, U. Schramm, and J. Pawelke, "Dose-controlled irradiation of cancer cells with laser-accelerated proton pulses," *Applied Physics B*, vol. 110, pp. 437–444, Nov 2012.

[230] C. Ma, I. Veltchev, E. Fourkal, J. Fan, T. Lin, W. Luo, and S. Stathakis, "Laser-accelerated proton therapy: target chamber design and shielding requirements," *Medical Physics*, vol. 33, no. 6 2117, 2007.

[231] I. Hofmann, J. Meyer-ter Vehn, X. Yan, A. Orzhekhovskaya, and S. Yaramyshev, "Collection and focusing of laser accelerated ion beams for therapy applications," *Physical Review Special Topics - Accelerators and Beams*, vol. 14, p. 031304, Mar 2011.

[232] V. Malka, J. Faure, and Y. a. Gauduel, "Ultra-short electron beams based spatio-temporal radiation biology and radiotherapy.," *Mutation research*, vol. 704, no. 1-3, pp. 142–51, 2010.

[233] A. Yogo, K. Sato, M. Nishikino, M. Mori, T. Teshima, H. Numasaki, M. Murakami, Y. Demizu, S. Akagi, S. Nagayama, K. Ogura, A. Sagisaka, S. Orimo, M. Nishiuchi, a. S. Pirozhkov, M. Ikegami, M. Tampo, H. Sakaki, M. Suzuki, I. Daito, Y. Oishi, H. Sugiyama, H. Kiriyama, H. Okada, S. Kanazawa, S. Kondo, T. Shimomura, Y. Nakai, M. Tanoue, H. Sasao, D. Wakai, P. R. Bolton, and H. Daido, "Application of laser-accelerated protons to the demonstration of DNA double-strand breaks in human cancer cells," *Applied Physics Letters*, vol. 94, no. 18, p. 181502, 2009.

[234] S. D. Kraft, C. Richter, K. Zeil, M. Baumann, E. Beyreuther, S. Bock, M. Bussmann, T. E. Cowan, Y. Dammene, W. Enghardt, U. Helbig, L. Karsch, T. Kluge, L. Laschinsky, E. Lessmann, J. Metzkes, D. Naumburger, R. Sauerbrey, M. Schürer, M. Sobiella, J. Woithe, U. Schramm, and J. Pawelke, "Dose-dependent biological damage of tumour cells by laser-accelerated proton beams," *New Journal of Physics*, vol. 12, p. 085003, Aug 2010.

[235] E. P. Rogakou, "DNA Double-stranded Breaks Induce Histone H2AX Phosphorylation on Serine 139," *Journal of Biological Chemistry*, vol. 273, pp. 5858–5868, Mar 1998.

[236] M. Belli, F. Cera, R. Cherubini, M. Dalla Vecchia, a. M. Haque, F. Ianzini, G. Moschini, O. Sapora, G. Simone, M. a. Tabocchini, and P. Tiveron, "RBE-LET relationships for cell inactivation and mutation induced by low energy protons in V79 cells: further results at the LNL facility.," *International journal of radiation biology*, vol. 74, pp. 501–9, Oct 1998.

[237] P. Wilson, B. Jones, T. Yokoi, M. Hill, and B. Vojnovic, "Revisiting the ultra-high dose rate effect: implications for charged particle radiotherapy using protons and light ions.," *The British journal of radiology*, vol. 85, pp. e933–9, Oct 2012.

[238] A. Giulietti and T. Tajima, "Lasers Offer New Tools to Radiobiology and Radiotherapy," in *Laser-Driven Particle Acceleration Towards Radiobiology and Medicine* (A. Giulietti, ed.), ch. 1, p. 320, Springer, 2016.

[239] R. G. Harrison, "Experiments in transplanting limbs and their bearing upon the problems of the development of nerves," *Journal of Experimental Zology Part A*, vol. 4, no. 2, pp. 239–281, 1907.

[240] Coriell Institute for Medical Research, "What is Cell Culture?," 2016.

[241] Gibco Life Technologies, *Cell culture basics*. Thermo Fisher Scientific Inc., 2014.

[242] Abcam Technical, "Cell culture guidelines," tech. rep., 2016.

[243] Coriell Institute for Medical Research, "AG01522 Fibroblast from Skin, Foreskin," 2016.

[244] M. Abercrombie, "Contact inhibition in tissue culture," *In Vitro*, vol. 6, no. 2, pp. 128–142, 1970.

[245] S. Gaillard, D. Pusset, S. M. de Toledo, M. Fromm, and E. I. Azzam, "Propagation distance of the $\alpha$-Particle-Induced Bystander Effect: The Role of Nuclear Traversal and Gap Junction Communication," *Radiation Research*, vol. 171, no. 5, pp. 513–520, 2009.

[246] C. Shao, Y. Furusawa, Y. Kobayashi, and T. Funayama, "Involvement of gap junctional intercellular communication in the bystander effect induced by broad-beam or microbeam heavy ions," *Nuclear Instruments and Methods in Physics Research B*, vol. 251, pp. 177–181, 2006.

[247] N. Autsavapromporn, S. M. de Toledo, M. Buonanno, J.-P. JAay-Gerin, A. L. Harris, and E. I. Azzam, "Intercellular Communication Amplifies Stressful Effects in High-Charge, High-Energy (HZE) Particle-Irradiated Human Cells," *Journal of Radiation Research*, vol. 52, no. 4, pp. 408–414, 2011.

[248] Beckman Coulter, "Z Series Coulter Counter: State of the Art Instrumentation," tech. rep., Fullerton, California, 2004.

[249] A. Cappione, E. Crossley, N. Thirumalapura, and D. Hoover, "Application Note: Immuno-monitoring using the Scepter™ 2.0 Cell Counter and Software Pro," tech. rep., 2011.

[250] Merck Millipore, "Scepter™ 2.0 Cell Counter - How it Works," 2016.

[251] D. R. Caprette, "Using a Counting Chamber," 2006.

[252] Public Health England, "Cell Counting Using a Haemocytometer," 2013.

[253] M. Fuentes, "Hemocytometer square size," 2013.

[254] Merck Millipore, "Scepter™ 2.0 Handheld Automated Cell Counter," 2016.

[255] H. G. Drexler and C. C. Uphoff, "Mycoplasma contamination of cell cultures: Incidence, sources, effects, detection, elimination, prevention," *Cytotechnology*, vol. 39, pp. 75–90, 2002.

[256] InvivoGen, "Mycoplasma Contamination of Cell Cultures - Review," 2016.

[257] Lonza, "Mycoplasma - Products for Detection and Removal," 2017.

[258] E. Burnett, L. Penn, and D. Finley, "Mycoplasma Detection and Elimination," *Biofiles*, vol. 8, no. 18, p. 1, 2013.

[259] L. Nikfarjam and P. Farzaneh, "Prevention and Detection of Mycoplasma Contamination in Cell Culture," *Cell Journal*, vol. 13, no. 4, pp. 203–212, 2012.

[260] D. Taylor-Robinson and C. Bebear, "Antibiotic susceptibilities of mycoplasmas and treatment of mycoplasmal infections," *J Antimicrob Chemother.*, vol. 40, no. (5), pp. 622–30, 1997.

[261] M. Podhorecka, A. Skladanowski, and P. Bozko, "H2AX phosphorylation: its role in DNA damage response and cancer therapy," *Journal of nucleic acids*, vol. 2011, 2010.

[262] A. Ivashkevich, C. E. Redon, A. J. Nakamura, R. F. Martin, and O. a. Martin, "Use of the $\gamma$-H2AX assay to monitor DNA damage and repair in translational cancer research.," *Cancer letters*, vol. 327, pp. 123–133, Dec 2012.

[263] N. Hamada, G. Schettino, and G. Kashino, "Histone H2AX phosphorylation in normal human cells irradiated with focused ultrasoft X rays: evidence for chromatin movement during repair," *Radiation Research*, vol. 166, pp. 31–38, 2006.

[264] L. J. Kuo and L.-X. Yang, "$\gamma$-H2AX - a novel biomarker for DNA double-strand breaks.," *In vivo (Athens, Greece)*, vol. 22, no. 3, pp. 305–9, 2008.

[265] M. Löbrich, A. Shibata, A. Beucher, A. Fisher, M. Ensminger, A. A. Goodarzi, O. Barton, and P. A. Jeggo, "$\gamma$ H2AX foci analysis for monitoring DNA double-strand break repair," *Cell Cycle*, vol. 9, no. 4, pp. 662–669, 2010.

[266] I. Rajagopal, "Genome Organisation (Chapter 5, p 155-165: 167-175)," 2009.

[267] L. Anderson, C. Henderson, and Y. Adachi, "Phosphorylation and rapid relocalization of 53BP1 to nuclear foci upon DNA damage.," *Molecular and Cellular Biology*, vol. 21, no. 5, pp. 1719–29, 2001.

[268] Z. Xia, J. C. Morales, W. G. Dunphy, and P. B. Carpenter, "Negative cell cycle regulation and DNA damage-inducible phosphorylation of the BRCT protein 53BP1.," *The Journal of Biological Chemistry*, vol. 276, pp. 2708–18, Jan 2001.

[269] B. Wang, S. Matsuoka, P. B. Carpenter, and S. J. Elledge, "53BP1, a mediator of the DNA damage checkpoint.," *Science (New York, N.Y.)*, vol. 298, pp. 1435–8, Nov 2002.

[270] I. Rappold, K. Iwabuchi, T. Date, and J. Chen, "Tumour Suppressor p53 Binding Protein 1 (53BP1) Is Involved in DNA Damage – signaling Pathways," *Journal of Cell Biology*, vol. 153, no. 3, pp. 613–620, 2001.

[271] O. Fernandez-Capetillo, H. Chen, and A. Celeste, "DNA damage-induced G2–M checkpoint activation by histone H2AX and 53BP1," *Nature Cell Biology*, vol. 4, no. December 2002, pp. 993–998, 2002.

[272] L. B. Schultz, N. H. Chehab, A. Malikzay, and T. D. Halazonetis, "p53 binding protein 1 (53BP1) is an early participant in the cellular response to DNA double-strand breaks.," *The Journal of Cell Biology*, vol. 151, pp. 1381–90, Dec 2000.

[273] A. Wilson, "U.S. Court upholds Status Quo on Gene Patents," 2013.

[274] T. T. Paull, E. P. Rogakou, V. Yamazaki, C. U. Kirchgessner, M. Gellert, and W. M. Bonner, "A critical role for histone H2AX in recruitment of repair factors to nuclear foci after DNA damage.," *Current biology : CB*, vol. 10, no. 15, pp. 886–95, 2000.

[275] F. Hoff, "How to Prepare Your Specimen for Immunofluorescence Microscopy," 2015.

[276] Duke University, "Introduction to sample preparation: immunofluorescence," 2016.

[277] G. Rolls, "Process of Fixation and the Nature of Fixatives," 2016.

[278] D. Davies, "Fixation and flow cytometry," 2014.

[279] Z. Darzynkiewicz, "Formaldehyde-paraformaldehyde," 1997.

[280] ThermoFisher Scientific, "Blocking Strategies for IHC," 2016.

[281] K. W. D. Ledingham, P. R. Bolton, N. Shikanzono, and C.-M. C. Ma, "Towards Laser Driven Hadron Cancer Radiotherapy: A Review of Progress," *Applied Sciences*, vol. 4, pp. 402–443, 2014.

[282] D. Wu and P. Yotnda, "Induction and testing of hypoxia in cell culture.," *Journal of Visualized Experiments*, vol. 54, p. e2899, 2011.

[283] M. Achison and T. R. Hupp, "Hypoxia attenuates the p53 response to cellular damage," *Oncogene*, vol. 22, no. 22, pp. 3431–3440, 2003.

[284] M. A. Esteban and P. H. Maxwell, "Manipulation of oxygen tensions for in vitro cell culture using a hypoxic workstation," *Expert Review of Proteomics*, vol. 2, no. 3, pp. 307–314, 2005.

[285] S. Reinhardt, M. Hillbrand, J. J. Wilkens, and W. Assmann, "Comparison of Gafchromic EBT2 and EBT3 films for clinical photon and proton beams," *Medical Physics*, vol. 39, no. 8, pp. 5257–5262, 2012.

[286] M. S. Kreipl, W. Freidland, and M. G. Paretzke, "Interaction of ion tracks in spatial and temporal proximity," *Radiat. Environ. Biophys*, vol. 48, no. 4, pp. 349–59, 2009.

[287] A. Yogo, T. Maeda, T. Hori, H. Sakaki, K. Ogura, M. Nishiuchi, A. Sagisaka, H. Kiriyama, H. Okada, S. Kanazawa, T. Shimomura, Y. Nakai, M. Tanoue, F. Sasao, P. R. Bolton, M. Murakami, T. Nomura, S. Kawanishi, and K. Kondo, "Measurement of relative biological effectiveness of protons in human cancer cells using a laser-driven quasimonoenergetic proton beamline," *Applied Physics Letters*, vol. 98, no. 5, p. 053701, 2011.

[288] F. Fiorini, D. Kirby, M. Borghesi, D. Doria, J. C. G. Jeynes, K. F. Kakolee, S. Kar, S. Kaur, K. J. Kirby, M. J. Merchant, and S. Green, "Dosimetry and spectral analysis of a radiobiological experiment using laser-driven proton beams.," *Physics in medicine and biology*, vol. 56, pp. 6969–82, Nov 2011.

[289] D. Habermehl, K. Ilicic, S. Dehne, S. Rieken, L. Orschiedt, S. Brons, T. Haberer, K.-J. Weber, J. Debus, and S. E. Combs, "The Relative Biological Effectiveness for Carbon and Oxygen Ion Beams Using the Raster-Scanning Technique in Hepatocellular Carcinoma Cell Lines," *PLoS ONE*, vol. 9, no. 12, 2014.

[290] M. Borghesi, D. Doria, S. Kar, M. Zepf, K. Prise, P. McKenna, D. Neely, Z. Najmudin, and G. Schettino, "High dose-rate effects in cell radiobiology employing ultrashort ion bursts: An A-ASAIL consortium proposal," tech. rep., Queen's University Belfast, Belfast, 2015.

[291] S. Raschke, S. Spickermann, T. Toncian, M. Swantusch, J. Boeker, and U. Giesen, "Ultra-short laser-accelerated proton pulses have similar DNA-damaging effectiveness but produce less immediate nitroxidative stress than conventional proton beams," *Scientific Reports*, vol. 6, pp. 32441(1–9), 2016.

[292] R. Kumareswaran, O. Ludkovski, A. Meng, J. Sykes, M. Pintilie, and R. G. Bristow, "Chronic hypoxia compromises repair of DNA double-strand breaks to drive genetic instability.," *Journal of cell science*, vol. 125, pp. 189–99, Jan 2012.

# Appendix A

# Research Publications

## A.1 Peer Reviewed Publications

- **Modified Thomson spectrometer design for high energy, multi-species ion sources.**
  D. Gwynne, S. Kar, D. Doria, H. Ahmed, M. Chercehz, J. Fernandez, R. J. Gray, J. S. Green. F. Hanton, D. A. MacLellan, P. McKenna, Z. Najmudin, D. Neely, J. A. Ruiz, A. Schiavi, M. Streeter, M. Swantusch, O. Willi, M. Zepf and M. Borghesi.
  Review of Scientific Instruments 83, 033304, 2014.

- **Recent developments in the Thomson Parabola Spectrometer diagnostic for laser-driven multi-species ion sources.**
  A. Alejo, D. Gwynne, D. Doria, H. Ahmed, D. C. Carroll, R. J. Clarke, D. Neely, G. G. Scott, M. Borghesi and S. Kar.
  Journal of Instrumentation $4^{th}$ International Conference Frontiers in Diagnostics Technologies 2016.

- **Optimisation of laser driven proton beams by an innovative target scheme.**
  H. Ahmed, S. Kar, G. Cantono, D. Doria, A. L. Giesecke, D. Gwynne, C. L. S. Lewis, A. Macchi, G. Nersisyan, K. Naughton, O. Willi, and M. Borghesi.

Journal of Instrumentation 12(06):C06025-C06025, 2017.

- **Investigations of ultrafast charge dynamics in laser-irradiated targets by a self probing technique employing laser driven protons.**
  H. Ahmed, S. Kar, G. Cantono, G. Nersisyan, S. Brauckmann, D. Doria, D. Gwynne, A. Macchi, K. Naughton, O. Willi, C. L. S. Lewis and M. Borghesi.
  Nuclear Instruments and Methods in Physics Research Section A: Accelerators, Spectrometers, Detectors and Associated Equipment 829:1, 172-175, 2016.

- **The radiobiology of laser-driven particle beams: focus on sub-lethal responses of normal human cells.**
  L. Manti, F. M. Perozziello, M. Borghesi, G. Candiano, P. Chaudhary, P. G. A. Cirrone, D. Doria, D. Gwynne, R. Lenaza, K. M. Prise, L. Romagnani, F. Romano, V. Scuderi and A. Tramontana.
  Journal of Instrumentation 12(03):C03084-C03084, 2017.

## A.2 Non-peer Reviewed Publications

- **Laser-Driven Ion Acceleration in a Hybrid RPA-TNSA Regime**
  D. Gwynne, S. Kar, H. Ahmed, D. Doria, F. Hanton, M. Cherchez, M. Swantusch, O. Willi, J. Fernandez, J.A. Ruiz, J.S. Green, D. Neely, R.J Gray, D.A. MacLellan, P. McKenna, Z. Najmudin, M. Streeter, M. Zepf and M. Borghesi.
  Central Laser Facility Annual Report 2013-2014.

- **Laser accelerated ultra high dose rate protons induced DNA damage under hypoxic conditions**
  P. Chaudhary, D.Gwynne, D. Doria, L. Romagnani, C. Maiorino, H. Padda, A. Alejo, N. Booth, D. C. Carroll, S. Kar, P. McKenna, M. Borghesi and K. M. Prise.
  Radiotherapy and Oncology 118 Supplement 1 24, 2016.

- **Polarisation dependence of ion acceleration from ultrathin foils.**

  C. Scullion, D. Doria, F. Hanton, D. Gwynne, K. Naughton, S. Kar, L. Romagnani, A. Sgattoni, A. Macchi, P. McKenna, D. R. Symes, M.Zepf and M. Borghesi.

  Central Laser Facility Annual Report 2013-2014.

- **Cell Irradiation with Laser-Driven Proton and Carbon Ions**

  F. Hanton, D. Doria, P. Chaudhary, D.Gwynne, L. Romagnani, C. Scullion, K. Naughton, T. Marshall, S. Kar, P. McKenna, G.Schettino, K. M. Prise and M. Borghesi.

  Central Laser Facility Annual Report 2013-2014.

## A.3 Publications in Preparation

- **A Compact Portable Hypoxia Chamber for use with Laser-Driven Ion Sources**

  D.Gwynne, P. Chaudhary, D. Doria, C. Maiorino, L. Romagnani, A. Alejo, N. Booth, H. Padda, S. Kar, P. McKenna, K. M. Prise and M. Borghesi.

  In preparation for publication in Biotechniques.

- **DNA DSB Repair Dynamics Following Irradiation with a Laser-Driven Proton Source at Ultra-High Dose Rates**

  F. Hanton, P. Chaudhary, D. Doria, D.Gwynne, L. Romagnani, T. Marshall, C. Scullion, K. Naughton, G.Schettino, S. Kar, M. Zepf, K. M. Prise and M. Borghesi.

  In preparation for publication in Radiation Research.

- **Narrow Energy Band, Narrow Divergence Ion Beams From Laser Driven Ultrathin Foils.**

  S.Kar, F. Hanton, A. Macchi, D.Gwynne, H. Ahmed, D. Doria, M. Cherchez, J. Fernandez, P. McKenna, D. A. MacLellan, D. Neely, J.A. Ruiz, O. Willi, M. Zepf and M. Borghesi.

  In preparation for publication in Physical Review Letters.

# Appendix B

# Immunofluorescence Protocol

**Materials**

- ((no. of dishes x 2) + 1) ml if using 4% PFA solution
- ((no. of dishes x 2) + 1) ml of permeabilisation buffer (0.5% Triton X-100 in PBS)
- ((no. of dishes x 5 x 10) + 1) ml of PBS
- ((no. of dishes x 2) + 1) ml of blocking buffer (10% Goat Serum, 0.1-0.25% Triton X-100 in PBS)
- ((no. of dishes) +1) ml of blocking buffer with correct concentration of primary antibody/antibodies
- ((no. of dishes) +1) ml of blocking buffer with correct concentration of secondary antibody/antibodies
- ((no. of dishes x 3 x 5) + 1) ml of washing buffer (0.1% Triton X-100 in PBS)
- (no. of dishes x 2) drops of DAPI
- Superglue

- Clear nail varnish
- 50 ml centrifuge tubes for mixing the fixative, permeabilisation and washing buffers
- 15 ml centrifuge tubes for mixing the blocking buffer and preparing the antibody solutions
- Aluminium foil
- Coverslips (22 x 40 mm are best for the cell dishes used)
- Glass slides (standard microscope slides can be used but they must be cut to size)
- Diamond pen
- Permanent marker
- Scalpel

1. Seed the cells at least 12-24 hours prior to irradiation and store in the incubator.

**Fixation**

2. Remove all media from the dish.
3. Wash twice with 5 ml of PBS.
4. Remove all the remaining PBS from the samples.
5. Fix the cells by adding 2 ml per dish of 4% PFA solution to each sample for 10 to 12 minutes at room temperature.
6. Remove the fixing solution and wash three times with 5 ml of PBS.
7. Store the samples in the fridge covered with at least 5 ml of PBS until after the 24 hour time point has been fixed.

8. Never let the sample dry out at any point; top up the PBS if necessary.

**Permeabilisation**

9. Remove any remaining PBS.

10. Permeabilise the cells with 2 ml per dish of the permealisation buffer (Triton X-100 in PBS) for 10 minutes at room temperature.

11. Remove any remaining buffer and wash three times for 5 minutes with 5 ml of PBS.

**Blocking**

12. Discard PBS and add 2 ml per dish of blocking buffer (10% Goat Serum, 0.1% Triton X-100 in PBS) and incubate at 37°C or room temperature for 1 to 2 hours.

13. Remove blocking buffer. No need to wash the samples after this step.

**Primary Antibody Reaction**

14. Add 1 ml per dish of the primary antibody/antibodies at the correct dilutions in blocking buffer, 3BP1(rabbit) primary antibody at 1:1000 and HIF-1(mouse) at 1:500, and incubate at 37°C for 2 hours.

15. Wash the dishes thrice with 3 ml of washing buffer (0.1% Triton X-100 in PBS), then once with PBS.

16. Remove all remaining solution.

**Secondary Antibody Reaction**

17. Add 1 ml per dish of the secondary antibody/antibodies at the correct dilutions in blocking buffer, GAR488 for 53BP1 secondary and GAM594 for HIF-1 secondary, both 1:1000 and incubate at 37°C for 1 hour.

18. Wash the dishes twice with 3 ml of washing buffer (0.1% Triton X-100 in PBS), then once with PBS.

19. Remove all remaining solution.

**Mounting Samples**

20. Remove the DAPI from the freezer 30 minutes before mounting.

21. Ensure the samples are as dry as possible.

22. Mark the back of the sample with any relevant information (such as the position of an energy line) using a marker and seal with clear nail varnish.

23. Add 2 drops of DAPI to each sample and attach a coverslip.

24. Remove the excess with a tissue and leave to dry for 24 hours in the dark.

25. Seal the edges of the coverslip with clear nail varnish once dry.

26. Attach a glass slide to the other side of the sample using Superglue. Once the glue is dry, cut the sample from the dish using a scalpel and label with any more relevant information (time point, cell line etc.).

27. Store at 4°C in the fridge or -20°C in the freezer until you wish to count the foci.